THE UNIVERSITY OF QUEENSLAND

AUSTRALIA

Towards a low-cost and portable ultra-low field magnetic resonance system based on permanent magnets and room temperature detectors

Ruben Pellicer Guridi

M.sc biomedical engineering

A thesis submitted for the degree of Doctor of Philosophy at

The University of Queensland in 2018

Queensland Brain Institute

Centre for Advanced Imaging

Abstract

Nuclear magnetic resonance has become a key medical tool for clinical diagnosis, monitoring, and intervention. This foremost imaging modality is routinely used to assess a broad range of pathologies which include breast cancer, glioblastoma brain tumours, neurodegenerative diseases, and knee lesions. In contrast to other imaging modalities such as computed tomography (CT) or X-ray, magnetic resonance does not utilise ionising radiation. Thereby, avoiding harm to patients. Its non-invasive character and excellent soft tissue contrast allow detecting diseases earlier and with higher precision than ever.

However, access to magnetic resonance is restricted to a large extent because, to increase sensitivity, systems tend to employ high magnetic fields. Strong fields create compatibility conflicts with metallic implants and other medical instrumentation. More importantly, increasing the static magnetic field makes this technology more expensive and difficult to site due to higher upfront and maintenance costs, and increased safety concerns. Its use is therefore limited to advanced hospitals, making the technology beyond the reach of many patients throughout the world. Even major hospitals have constrained magnetic resonance resources, forcing them to prioritise their usage and exploiting only a fraction of benefits afforded by magnetic resonance technology.

Ultra-low field magnetic resonance promises to be a more cost-effective alternative to conventional magnetic resonance systems as its hardware is simpler. Moreover, it is a good candidate for a mobile solution due to its smaller size, lower power consumption, lower weight, and reduced safety concerns. It is also more compatible with other instruments and can assess patients with implanted or lodged metals. Moreover, its frequency of operation provides unique resonance conditions which can open up novel applications to elucidate chemical or biological processes, such as directly mapping neuronal activity.

The main components of conventional ultra-low field magnetic resonance systems are a shielding box that reduces interference with foreign magnetic fields, resistive coils to generate a range of magnetic fields, detectors to sense the magnetic resonance signal, and a console that governs the system. Generated magnetic fields are a strong pre-polarisation field to increase the intensity of the signal received, an adjustable measurement field which defines acquisition conditions, a radio frequency field to induce the signal, and a spatially varying linear gradient field which encodes the signal in space to produce images. Yet, although the power required to generate these fields is lower in an ultra-low field system than in a high field counterpart, the energy requirement of ultra-low field systems is still

significant and require pricey power amplifiers, which constrain systems' portability and increase their costs. Besides, ultra-low field systems intrinsically suffer from a smaller signal, which has motivated the use of sophisticated sensors such as superconducting quantum interference devices or atomic magnetometers. Notably, superconducting quantum interference devices require cryogenics, and atomic magnetometers have to be carefully isolated from strong pulsating magnetic fields. These sensing technologies are fragile, bulky, and expensive, hindering system portability, versatility, and affordability.

This PhD project aims to develop methods leading towards a ‘truly' portable and low-cost ultra-low field magnetic resonance instrument. Current work focuses on the generation of the magnetic fields and the signal detection as these two major parts set the lower boundary for achievable signal quality, contrast versatility, and system dimensions, and delimit the requirements of the remaining parts.

First, instead of using resistive coils to generate magnetic fields, we propose employing permanent magnets which can be dynamically repositioned. We arrange the permanent magnets forming a cylindrical configuration which can generate an adjustable measurement field and a switchable strong pre-polarisation field. This field versatility has been validated empirically with a static prototype. We also study the possibility of generating gradient fields through additional permanent magnets. Results suggest that it is possible to generate a 3D magnetic resonance image with a minimal number of magnets moved along simple trajectories.

The second hardware development is comprised of methods to design inexpensive and robust detectors with exquisite sensitivity and rapid activation. High sensitivities are achieved by optimising the detectors with more accurate numerical models, exploring a more extensive range of arrangements, and considering most significant elements. These detectors traditionally delay acquisitions in the presence of the pulsed magnetic fields employed in magnetic resonance experiments. Here, this drawback is significantly attenuated through the combination of hardware and software solutions contributing to higher acquisition efficiency. A prototype resulting from these methods has empirically been tested, which validates the proposed models.

Proposed magnets design provides required quasi-static magnetic fields in a compact and energy efficient manner without compromising system safety or decreasing field versatility. In addition, the detector methods developed provide perhaps the highest acquisition efficiency value amongst ultra-low field magnetic resonance sensors, allowing for room

temperature imaging with inherently robust detectors. Here presented novel methods pave the way towards a clinically relevant, low-cost, and portable ultra-low field magnetic resonance system.

Declaration by author

This thesis is composed of my original work, and contains no material previously published or written by another person except where due reference has been made in the text. I have clearly stated the contribution by others to jointly-authored works that I have included in my thesis.

I have clearly stated the contribution of others to my thesis as a whole, including statistical assistance, survey design, data analysis, significant technical procedures, professional editorial advice, financial support and any other original research work used or reported in my thesis. The content of my thesis is the result of work I have carried out since the commencement of my higher degree by research candidature and does not include a substantial part of work that has been submitted *to qualify for the award of any* other degree or diploma in any university or other tertiary institution. I have clearly stated which parts of my thesis, if any, have been submitted to qualify for another award.

I acknowledge that an electronic copy of my thesis must be lodged with the University Library and, subject to the policy and procedures of The University of Queensland, the thesis be made available for research and study in accordance with the Copyright Act 1968 unless a period of embargo has been approved by the Dean of the Graduate School.

I acknowledge that copyright of all material contained in my thesis resides with the copyright holder(s) of that material. Where appropriate I have obtained copyright permission from the copyright holder to reproduce material in this thesis and have sought permission from co-authors for any jointly authored works included in the thesis.

Publications included in this thesis

Peer-reviewed papers

- Vogel MW, Giorni A, Vegh V, Pellicer-Guridi R, Reutens DC. Rotatable Small Permanent Magnet Array for Ultra-Low Field Nuclear Magnetic Resonance Instrumentation: A Concept Study. PloS one. 2016 Jun 6;11(6):e0157040 – incorporated as Chapter 3.

- Pellicer-Guridi R, Vogel MW, Reutens DC, Vegh V. Towards ultimate low frequency air-core magnetometer sensitivity. Scientific reports. 2017 May 23;7(1):2269 – incorporated as Chapter 5.

Submitted manuscripts included in this thesis

- Vogel MW, Pellicer-Guridi R, Su J, Vegh V, Reutens DC. 3D-Spatial encoding with permanent magnets for ultra-low field magnetic resonance imaging. Submitted to Scientific reports – incorporated as Chapter 4.

Other publications during candidature

Conference abstracts

- Pellicer-Guridi R, Vogel MW, Reutens DC, Vegh V. Towards ultimate air-core magnetometer sensitivity for ultra-low field MRI: A design method. ISMRM 2017-Abstract #2678

- Arndt F, Aussenhofer S, Behrens E, Blücher C, Blümler P, Brand J, Ettinger KM, Fillmer A, Grissom W, Gruber B, Guerin B, Haas S, Han H, Hansen M, Hasselwander CJ, Hodge R, Hoffmann W, Ittermann B, Jakubowski M, Kühne A, Klein S, Kroboth S, Ladd M, Layton K, Leiva B, Littin S, López-Aranguren Blázquez B, Marstal K, Mekle R, Moritz M, Moritz R, Niendorf T, Pellicer-Guridi R, Pendse M, Polimeridis A, Redlich T, Reiman H, Seemann R, Seifert F, Starke L, Stockmann J, Stoecker T, Takeda K, Thiele L, Uecker M, von Knobelsdorff-Brenkenhoff F, Wahlstedt R, Webb A, Winkler S, Winter L, Yu H, Zaitsev M. Open Source Imaging Initiative (OSI²) – Update and Roadmap. ISMRM 2017, Abstract # 4463

- Carey A, Pellicer-Guridi R, Vogel MW, Crozier S, Reutens DC, Vegh V. Ambient Electromagnetic Noise Reduction for Ultra-Low Field NMR. ESMRMB-2017

- Broche L, Pellicer-Guridi R, Winter L. The value of Open Source for Research, Education and Global Health – Open Source Imaging Initiative. ESMRMB 2017- Views Abstract #3

Contributions by others to the thesis

Chapter 3 - The numerical study was done by Vogel, Giorni, Vegh, and Reutens. Vogel and Giorni wrote an initial incomplete part of the draft.

Chapter 4 - The finite element simulations that estimate the fields for the different permanent magnet locations were done by Vogel. He performed the analysis of the different encoding trajectories through the minimisation of the condition number. Vogel was also the lead writer of the manuscript presented here. Vegh and Reutens were involved with the creation of the concept and the validation of the results as well as with the writing of the manuscript. The reconstruction program was partially developed by Su, who implemented the Kaczmarz method which solves the pseudo-inverse of a matrix.

Chapter 5 – Vegh, Reutens and Vogel contributed with critically revising the manuscript.

Statement of parts of the thesis submitted to qualify for the award of another degree

No works submitted towards another degree have been included in this thesis

Research Involving Human or Animal Subjects

No animal subjects, including humans, were involved in this research.

Acknowledgements

I consider myself very fortunate of having shared bits of life with inspiring people during this PhD candidature. I cannot thank Viktor Vegh enough for the outstanding guidance and support he has provided me. Working with him has offered me as much insight through his clever suggestions to navigate the sea of academia as it has through his daily grounded, and humorous attitude to sail in the ocean of life. I am very grateful to David Reutens for the invaluable time he has spent to ensure I would stay on track, and the effort he makes to transform technical manuscripts and grant applications into masterpieces of literature. Ignorance would have a hard time if we all would have the eagerness he shows to learn. I am very thankful to Michael Vogel for the abundant discussions which forced to strengthen my foundations. I appreciate his uplifting sense of humour which tried in vain to mask his great humbleness. I also want to thank Jiasheng Su for keeping up with the strenuous sprint to help me building the pre-amplifier. I highly value his willingness and patience to share his remarkable knowledge and creativity.

I also want to transmit my gratitude to Rainer Körber, and Jan-Hendrik Storm from the PTB in Berlin for their openness to collaborate with us, which has greatly facilitated the completion of this work. Thanks also to Ian Brereton and Miguel Fuentes for their kind assistance as PhD panel overseeing the evolution of the project. I also want to thank Alan Pringle and Don Maillet for their help with building mechanical and electronic hardware at the highest standards. Their “think twice, build once” philosophy has paid off in the long run. I thank Xiaoyong Xu for allowing me to use the coil winding machine. I also extend my gratitude to the attentive CAI staff members which have taken off from me heavy bureaucratic and organisational burden allowing me to focus on the research. My sincere appreciation to Lesley Green for making arranging meetings, travels, and bills seamless. I also want to thank Lorine Wilkinson for her prompt assistance to help me and the kind summer/master students successfully filling the right forms. Thanks also to Alani Winter for helping me troubleshooting last-minute issues such as package deliveries and payments. I would also like to thanks Gail Durbridge for giving me the chance of imparting tutorials in the magnetic resonance imaging technology masters course.

It has been a pleasure to sit next to Peter Caradonna, who has been a great example of respect and consideration. I don’t know how it would have felt to share office with the greatest scientist in the history, but it must have been similar as I do not think passion for physicist can get any bigger than his. I appreciate the help provided by the summer/master

students Aiden Carey, Jared Loi, Chirag Baheti and David Romero. Special thanks to Aiden for his enthusiasm and the interesting conversations we have had together. My sincere thanks to Viktor Vegh, Michael Kennedy, Martin Arnold, Andrew McLean and Mathilde Vlieg for their priceless help proofreading sections, or the whole, of this thesis. I would like to acknowledge the pleasant working atmosphere created by the colleges at CAI. Sharing this journey with them has been an enjoyment.

I am indebted to Lukas Winter for fueling the beautiful Open Source Imaging Initiative (OSI^2). My sincere thanks to him and the generous community of people that work to help other beings regardless of their condition.

I also want to thanks my dear housemates for immensely enriching my stay. I am very grateful to my dear friends at Dorothy Day house and Food-No-Bombs. They are like a spicy curry with lots of affection, humbleness, and critical thinking, which they admirably serve with coherence between words and actions. I address my final thanks to my mother, father and close family. Their unconditional love and support are the foundation of my life. I consider myself very fortunate of having done this journey with the caring companion and support of Mathilde Vlieg. I cannot put into words how much I love your compassion and appreciate your great efforts for the better.

Financial support

This research was supported by the University of Queensland through an International Postgraduate Research Scholarship (IPRS), and a University of Queensland Centennial Scholarship (UQCent).

This work was also supported by the Australian Research Council Discovery Early Career Research Award No. DE140100229 (M. W. Vogel) and the Australian National Health and Medical Research Council program grant No. 628952 and No. 631352 (D. C. Reutens).

Keywords

ultra-low field, nmr, mri, magnetic resonance, permanent magnet, halbach array, optimisation, magnetometer, ultra-low noise pre-amplifier, open source.

Australian and New Zealand Standard Research Classifications (ANZSRC)

ANZSRC code: 090304, Medical Devices, 50%

ANZSRC code: 029903, Medical Physics, 50%

Fields of Research (FoR) Classification

FoR code: 0903, Biomedical Engineering, 50%

FoR code: 0299, Medical Physics, 50%

List of figures & tables

List of Abbreviations used in the thesis

Acronym	Meaning
1D/2D/3D	1/2/3 dimensional
AC	alternating current
AM	atomic magnetometer
BJT	bipolar junction transistor
BS-SET	Bloch-Siebert spatial encoding
CAI	Centre for Advanced Imaging
CNR	contrast to noise ratio
CT	computed tomography
CW	continuous wave
DC	direct current
DNP	dynamic nuclear polarisation
EMF	electromotive force
ESR	equivalent series resistance
FEM	finite element method
FID	free induction decay
FOV	field of view
GMR	giant magnetoresistance mixed magnetometer
MCG	magnetocardiography
MDF	medium density fibreboard
MIT	magnetic induction tomography
MMPA 0100	Standard Specifications for Permanent Magnet Materials
MR	nuclear magnetic resonance
MRI	magnetic resonance imaging
MRSI	magnetic resonance spectroscopy imaging
NF	noise factor
NMR	magnetic resonance spectroscopy
PTB	Physikalisch-Technische Bundesanstalt
PatLoc	parallel imaging technique using localised gradients
Q	quality factor
ROI	region of interest
Rf	radio frequency
Rx	receive
SAR	specific absorption rate
SNR	signal to noise ratio
SPMA	small permanent magnet array
SQUID	superconducting quantum interference devices
TRASE	transient array spatial encoding
Tc	critical-temperature
Tx	transmit
ULF	ultra-low field
dB	decibel
EM	electromagnetic
jFET	junction field effect transistor
ppm	part per million

Chapter 1- Introduction

Nuclear magnetic resonance (MR) has become the gold standard for an ever-growing number of applications[1,2]. Its imaging modality, magnetic resonance imaging (MRI), is routinely used in hospitals for a vast range of pathologies which include breast cancer screening, detection of glioblastoma brain tumours, and knee lesions[3-5]. The abundant information embedded in the MR signal, its exquisite tissue contrast, and its high spatial resolution allow early and reliable pathology detection[3-5]. Importantly, unlike other imaging modalities such as X-rays, computed tomography, and positron emission tomography, it does not use ionising radiation, hence avoiding patient harm[1].

However, owning an MR system is very expensive as higher sensitivity is achieved by using strong magnetic fields, which require sophisticated and power-hungry electronics and scarce materials, such as superconducting metals and liquid helium[6]. Hence, aside from system acquisition costs, maintenance costs of high field systems are also exorbitant. Moreover, high field systems impose a considerable siting constraint due to the safety concerns associated with strong magnetic fields. These demands place this valuable medical tool out of the reach of most of the people around the world[7]. MR resources are constrained even in most advanced hospitals, compelling them to prioritise its use and to limit its applications to a small fraction of what MR has been shown capable of[8].

The MRI community is well aware of the need to make this technology more cost-effective and to increase patient throughput[9,10]. This interest in developing more affordable MR systems has prompted research into lower field systems. Such MR systems with lower field strength can be categorised into two major groups according to their field strength. Generally, systems employing measurement fields down to 10 mT are considered low field MR; while systems covering the rest of the lower range are termed ultra-low field (ULF) MR. Although both low field and ULF systems are good low-cost MR candidates, ULF can have distinct complementary benefits given that the resonance frequency is orders of magnitude lower. The field dependence of MR mechanisms has shown to improve the detectability of some pathologies through an enhanced tissue contrast at ULFs[11]. Conveniently, with ULF MR it is possible to adjust the measurement field. This feature can be used to combine MR signals acquired at different measurement fields to extract information relevant for diagnosis through an effect known as T_1 dispersion[12,13]. Moreover, these systems operate in the kHz frequency range, the effect of which is an enhancement of the coupling of the MR signal

with chemical or biological processes occurring on similar timescales. This effect can potentially provide new tools, such as direct imaging of neuronal activity[14].

Besides, ULF MR can be compatible with applications that would conflict with higher field systems due to magnetic field susceptibility or field strength related safety concerns[15]. For example, imaging in the vicinity of ferromagnetic materials produces large image artefacts and increases the risk of harmful heat deposition in patients[15]. These hazards exclude a considerable number of patients with metallic implants from being assessed by MRI. Similarly, despite the help MR could provide with time-critical decisions, victims of accidents at risk of having metals lodged in the body cannot undergo standard field strength MR because of potential hazards related to mechanical forces and heat deposition. The weaker magnetic fields employed in ULF MR systems make them also safer to operate in conjunction with other medical instruments, facilitating their presence in interventional scenarios where they could, for example, aid with image-guided surgeries[16].

System portability would further unleash the benefits and increase access to MR. For example, such a system could bring periodic breast cancer screening to rural and remote areas. Similar to ultrasound systems, portable MR systems could be used in rapid “point-of-care” assessment. This facilitated access would reduce work overhead from multiple appointments and increase treatment success ratio through timely personalised treatments. It could also be deployed in disaster zones allowing for time-sensitive decisions following brain injuries or strokes, which can be decisive for treatment outcome. Reduced weight, lower power consumption, and weaker stray fields make the ULF approach a compelling candidate for portable MR.

ULF MR systems have significant power requirements as fields are generated with resistive coils, which also limits achievable pre-polarisation field strengths[15]. Generating required fields with permanent magnets would considerably reduce the power consumption[17]. In this regard, permanent magnet based cylindrical Halbach configurations have been proven efficient in low field systems[18,19]. Further, ULF MR systems have to face an intrinsically low signal to noise ratio (SNR)[15]. To increase the sensitivity, sophisticated detectors such as Superconducting Quantum Interference Devices (SQUIDs)[12,16,20-31] or Atomic Magnetometers (AMs) are often employed. However, to the detriment of the affordability and portability of ULF MR systems, these detectors are expensive, bulky, and fragile. Additionally, SQUIDs, which are perhaps the most employed detectors in high-end ULF MR systems, are dependent on cryogenics, which further hinders maintenance, portability, and

costs. The ideal portable ULF MR detector should be highly sensitive, affordable and robust. Therefore, air-core magnetometers have found application in ULF MR as they are robust and inexpensive, and can reach high sensitivity if carefully designed. Yet, existing methods proposed for the design of air-core magnetometers are based on simplified models and simulations using a reduced number of variables, potentially leading to sensitivity that is suboptimal. Moreover, air-core magnetometers cannot acquire signals quickly after strong magnetic field changes intrinsic to MR experiments, thereby significantly reducing their MR signal acquisition efficiency.

This thesis reflects my work developing two key hardware components towards a portable and low-cost ULF MR: a versatile permanent magnet based ULF MR system and inexpensive yet highly sensitive detectors.

1.1 Thesis outline

This dissertation consists of this introductory chapter, a chapter discussing the background to the research, and then four chapters in article format describing the work regarding the permanent magnets and the detectors. There is then a final chapter offering an outlook on current and prospective work. The content of each subsequent chapter is presented here.

Chapter 2 provides background information regarding signal and noise in MR, and associated hardware necessary to establish a framework for the present work.

In Chapter 3 we study the feasibility of substituting traditional resistive coils with dynamically adjustable permanent magnets to generate an adjustable measurement magnetic field and a strong switchable pre-polarisation field suitable for ULF MR. A manual prototype is simulated and built to verify the magnetic field generation and validate the numerical approach.

Chapter 4 provides a framework for 3D imaging based on the concepts introduced in Chapter 3. Thereby, we explore the possibility of generating a range of gradient fields through simple stepped translations of additional satellite permanent magnets. The path and orientation of these magnets are numerically optimised for different helical paths, for both one and two small permanent magnets.

Chapter 5 presents a numerical method to facilitate the customisation of ULF MR coils and improve their sensitivity. This is achieved by means of more accurate numerical models and exploring a more extensive range of arrangements than previously proposed methods. The

accuracy of the numerical models is empirically validated through four different detector configurations. A global optimisation method is employed to solve for the larger number of decision variables.

In Chapter 6 the work from Chapter 5 is furthered to gain sensitivity to MR signal and expedite signal acquisition. Unlike in Chapter 5 where the signal source was simplified to be far from the coil, here the sensitivity is optimised for a given volume of interest better representing the ULF MR scenario. Additionally, an ultra-low noise pre-amplifier design is proposed for enhanced sensitivity. Detector dead-time is also reduced by combining novel hardware and post-processing solutions. Proposed methods and designs are empirically verified with ULF MR experiments.

Chapter 7 concludes the thesis, summarising the achievements of presented work, discussing the contribution of proposed methods towards an affordable and portable ULF MR system and its implications, and proposing future work lines.

Chapter 2- Theoretical foundation of ULF MR

Magnetic resonance systems combine static and alternating magnetic fields to extract information from the nuclear spins present in the body or sample. The same physical principles apply from ULF to ultra-high field instruments. The theoretical foundation of MR is provided here forth. The first section describes the MR phenomenon, its dependence on externally applied magnetic fields, and its practical use through MR instruments. The second section describes the specific magnetic fields involved in MR experiments, disclosing common hardware approaches to their generation or detection. The third section portrays the noise sources present in MR experiments. The implications of the presence of noise in MR experiments is explained in section four. Section five presents methods aiming to reduce the limitations imposed by the noise. The chapter concludes with a description of commonly used ULF MR hardware configurations for in-vivo human experiments.

2.1 MR signal

The atomic nucleus has mass, electric charge, and angular momentum. The nucleus generates a magnetic dipole as a result of the electric charge distribution and the spin. Each nucleus has an intrinsic magnetic moment to angular momentum ratio, which is called the gyromagnetic ratio γ. When exposed to an external magnetic field $\vec{B}$, nuclei with non-zero magnetic moment precess about the axis of $\vec{B}$ at a frequency proportional to the magnitude $|\vec{B}|$ such that $\omega = -\gamma|\vec{B}|$. The hydrogen nucleus ^{1}H is the most sensitive and stable MR element in the human body due to its high concentration (62% atomic per cent) and high gyromagnetic ratio γ = 42.577e6 Hz/T. Hence, ^{1}H is a good candidate for an extensive range of applications such as human tissue imaging.

The nature of the MR phenomenon is presented next. The evolution of this phenomenon in the presence of an external magnetic field is then explained. The section concludes describing the methods employed to extract different information through the MR signal.

2.1.1 Net magnetisation

Each nucleus has a set of allowed spin states which can be derived from its nuclear spin quantum number. The number of spin states = 2 I + 1 defines the number of possible energy levels that a nucleus can have under an external magnetic field. Here, I is the spin quantum number. The spin quantum number of a nuclei is zero when its number of neutrons and protons is even, integer (I = 1, 2, 3, 4 …) when its number of neutrons and the protons is

odd, and half-integer (I = 1/2. 3/2, 5/2 …) when the sum of its neutrons and protons is odd. The last is the case of ^{1}H with I =1/2.

Thereby, when hydrogen is placed in an external magnetic field, the nuclear magnetic field can either be aligned with or be opposing the external magnetic field due to the Zeeman interaction. The energy difference between this two states depends upon the external magnetic field according to

$$\Delta E = \gamma B \hbar, \tag{1}$$

where $\hbar$ is Planck's constant 1.05457×10^{-34} J·s.

With protons capable of generating magnetic fields in two opposing directions, the net magnetisation is defined by the difference between both populations. Spins have a preference for the lower energy state, what tends to increase the spin population in the lower state. However, the thermal energy $E_{Thermal} = kT$, which at room temperature is larger than the magnetic energy, decreases the spin distribution ratio. Here *k* is Boltzmann's constant and *T* is the absolute temperature. At equilibrium, this probability ratio follows the Boltzmann distribution[32]

$$n^{+}/n^{-} = e^{\Delta E/kT}. \tag{2}$$

Here n^{+} is the high energy state, n^{-} is the low energy state. In the absence of an external magnetic field, the nuclear spins are randomly oriented. In the presence of an external magnetic field, the net magnetisation can be approximated by manipulating the Boltzmann distribution equation to give

$$M_0{}^{1_H} = \frac{\Delta n \hbar \gamma}{2} \approx \frac{(\Delta E/kT) n_s}{2} \frac{\hbar \gamma}{2} = \frac{n_s \hbar^2 \gamma^2 B}{4kT}. \tag{3}$$

According to Equation (3), the magnetisation is proportional to the external field strength B and the number of protons n_s present in the sample. This value is 0.0325 A·T/m for water at room temperature (300 °K). Similarly, the steady state net magnetisation of any nucleus as a function of spin quantum number can be calculated by the more generic expression

$$M_0 = \frac{n_s \hbar^2 \gamma^2 I(I+1)B}{3kT}. \quad (4)$$

2.1.2 Temporal evolution of the net magnetisation

The temporal evolution of the magnetisation moment $M(t)$ under the field manipulations employed in MR can be modelled through Bloch's equation such that[33]

$$\frac{dM(t)}{dt} = M(t) \times \gamma B(t), \quad (5)$$

where interaction between spins is assumed to be negligible. However, the opposite is true, and spins are affected by a large number of processes what vastly enriches the information that can be extracted from the MR signal. The dominant spin interactions generate relaxation mechanisms which dampen excited spin states towards equilibrium. To accommodate for these mechanisms, Equation (5) needs to be extended to incorporate two main relaxation phenomena: the longitudinal relaxation T_1 and the transverse relaxation T_2. The T_1 relaxation is also termed the spin-lattice as it originates from a stimulated energy exchange of the spin with the surrounding lattice. T_1 characterises the return to equilibrium in the direction of the external magnetic field as follows:

$$\frac{dM_{\parallel}(t)}{dt} = -\frac{M_{\parallel}(t) - M_0(t)}{T_1(t)}. \quad (6)$$

The transverse relaxation T_2 is also called spin-spin relaxation and characterises the decay of the magnetisation in the plane perpendicular to the external magnetic field $M_{\perp}$. Collisions, diffusion and magnetic field inhomogeneities on a microscopic level are responsible for this effect. The time course of $M_{\perp}$ in the presence of T_2 relaxation can be described by

$$\frac{dM_{\perp}(t)}{dt} = -\frac{M_{\perp}(t)}{T_2(t)}. \quad (7)$$

Combining Equations (5-7) the general Bloch equation becomes

$$\frac{dM(t)}{dt} = M(t) \times \gamma B(t) - \frac{M_{\parallel}(t) - M_0(t)}{T_1(t)} - \frac{M_{\perp}(t)}{T_2(t)}. \quad (8)$$

It should be noted that the relaxation parameters T_1 and T_2, and the equilibrium magnetisation M_0 are a function of the magnetic field strength that the spins experience, as shown in Figure 1[34]. In traditional MR systems, the transient fields are much smaller than the static magnetic field B_0 so that variations in T_1, T_2 and M_0 can be neglected.

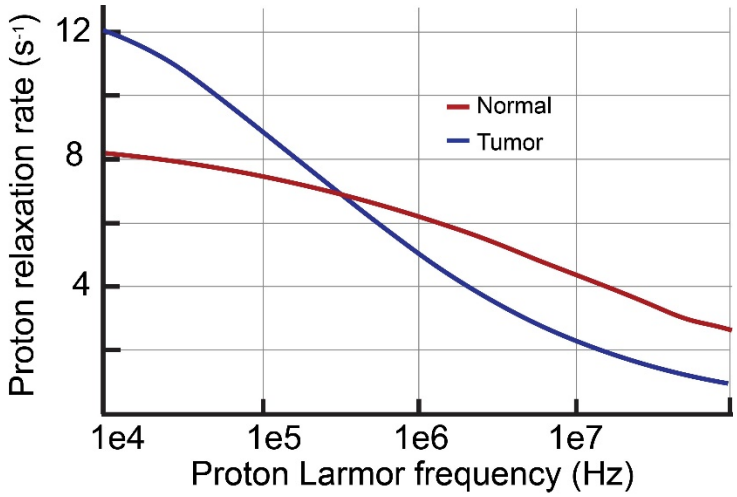

Figure 1: Normal (red) and tumour (blue) human breast tissue relaxation rates ($1/T_1$) for different frequencies. Data from[34].

In practice, the transverse magnetisation decays faster than would be predicted by the T_2 decay. This observed faster relaxation rate is known as T_2* which may be produced by inhomogeneities intrinsic to the instrument or from field distortions induced by the magnetic susceptibility of the sample. The three relaxation parameters follow the relation $T_2^* < T_2 < T_1$. Table 1 shows representative T_1 and T_2 values for 3 T, 1.5 T and 46 uT[31,35].

Table 1: Representative T_1 and T_2 measured values at 3 T, 1.5 T and 46 uT[31,35].

		***3 T*[35]**	***1.5 T*[35]**	***46 uT*[31]**
White Matter	T_1 (ms)	1084	884	75
	T_2 (ms)	69	72	79
Grey Matter	T_1 (ms)	1820	1124	103
	T_2 (ms)	99	95	106

2.1.3 Exploiting the MR signal: spectroscopy and imaging

The MR signal contains abundant information, which can be exploited in different ways leading to two main modalities: nuclear magnetic resonance spectroscopy (NMR) and nuclear magnetic resonance imaging.

Nuclear magnetic resonance spectroscopy provides insight by studying the frequency distribution of MR signals, typically evolving in a highly homogeneous magnetic field. Molecular information can be derived from the analysis of spectral features such as frequency shifts between resonances and peak amplitudes. The information can be used, for example, to deduce molecular structures and molecular dynamics, such as protein folding, reaction states, and chemical environments. Varying specific parameters in an NMR sequence incrementally provides multidimensional spectra, which are especially useful for determining molecular structures. Nonetheless, spectral information is often highly convoluted requiring a consolidated understanding of the effects involved.

NMR experiments demand low static magnetic field inhomogeneity and high field stability. Reducing sample volume reduces homogeneity requirements. However, smaller samples generate smaller MR signals, what is often compensated by increasing acquisition time or by employing higher field strength systems. The latter also facilitates the relative increase in spectral resolution as many spectral features are proportional to the field strength.

Magnetic resonance imaging generates contrast-rich images that can be used to depict the influence of diseases. Unlike NMR, MRI generally trades intravoxel information for spatial information. MRI image contrast can be modified by manipulating the influence of the different effects affecting the signal, such as proton density, T_1, T_2 or T_2^*.

Typically, images are reconstructed from sets of MR signals which encode the location of contributing spins. The encoding is achieved by inducing different precessional frequencies on each of the contributing spins by means of applying spatially varying magnetic fields. The phase difference accumulated between spins defines the resolution of the image. Spin phase can be manipulated either by changing the strength of employed gradient field or by varying the duration of the signal acquisition.

The majority of commercially available MRI systems employ gradient coils that generate three linearly varying gradient fields in a 3D Cartesian framework, which are controlled independently. This condition allows for using the k-space formalism and the computationally efficient Fourier-based imaging[36].

The use of nonlinear gradient fields has also been proposed, which showcases a number of advantages: it can reduce the risk of inducing peripheral nerve stimulation by reducing the field transients generated outside of the FOV, it can accelerate image acquisition by reducing the image resolution out of the region of interest, and it can increase the SNR by producing a tighter bandwidth signal[37-40]. Besides, producing linear fields requires large amounts of power and space as longer coils are needed[41]. Hence, more portable systems can be made if linear fields are not required[19,42,43]. The nonlinear gradient fields can be generated by custom built transmit coils or by static permanent magnets[37,38].

However, reconstructing an image encoded with nonlinear gradients is computationally expensive, as it is commonly done by iterative methods which solve for the pseudo-inverse of the encoding matrix[19,40,44]. This problem is especially problematic with 3D images given the large dimensionality of the encoding matrix. A transformation of the encoding matrix has been proposed for some specific gradient shapes to reduce the computational load and, to be able to exploit the convenience of the k-space formalism[37].

Magnetic resonance spectroscopic imaging (MRSI) combines the benefits of 1D MR spectroscopy and MR imaging[45]. It has generated interest in the recent years due to its clinical potential to analyse metabolites. However, its long acquisition times and the demanding user expertise required are limiting its broad application.

2.2 Basic hardware components of MR systems

MR systems are often capable of doing both imaging and spectroscopy as both methods largely overlap in their hardware needs. The main components of an MR system can be explained by following the steps of a simple “pulse and collect” experiment. The first step in this sequence is to create a net magnetisation in the sample which will generate an MR signal. This magnetisation is achieved by applying a strong static magnetic field to the sample externally. The net magnetisation is altered through a radio frequency induction field to induce a detectable MR signal. Spatially varying magnetic fields can be superposed onto abovementioned magnetic fields to generate a spatial dependency to the induction and of the signal. This spatial dependency is used to reconstruct an image of the sample or to interrogate the MR signal in a delimited volume. Figure 2 shows a typical arrangement of the hardware employed to generate these three external magnetic fields in a high field MR instrument with all the fields being generated by coils. The polarising coils are depicted in red, the gradient coils in blue, and the induction coils in pink. The different magnetic fields

can be generated or detected by a variety of manners. Existing means of producing and sensing such fields are described in what follows.

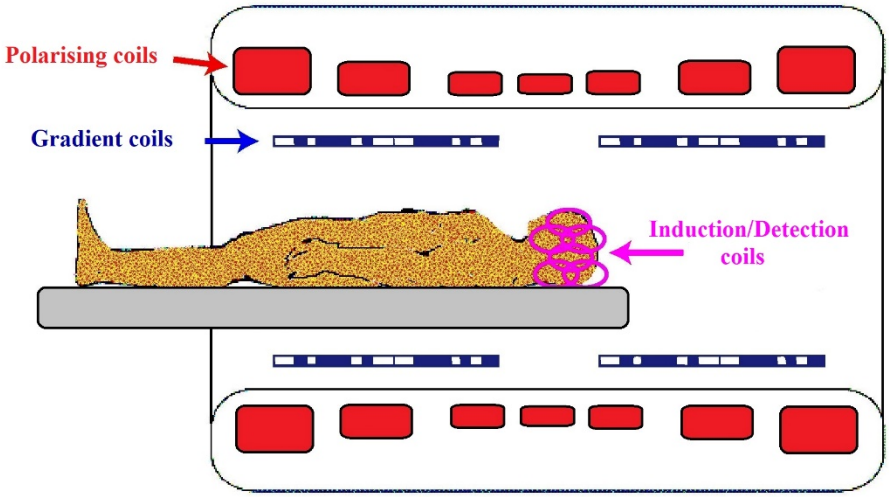

Figure 2: Cross-section of the hardware coils employed to generate the different fields in a typical high field MR system. Visualised coils are the polarising superconducting coil inside the cryostat, the gradient coils, and the induction and detection coils.

2.2.1 Polarising field

This magnet produces the static magnetic field (B_0) which defines the steady state net magnetisation and the central resonant frequency of the system. This field should be as homogenous as possible in strength and direction within the volume to be analysed, i.e. the field-of-view (FOV). The polarising magnet is aided by shimming elements to decrease field inhomogeneity. This field is the largest magnetic field source of the system. Polarising magnets generally weight several tones due to the numerous windings and passive shimming plates employed. Furthermore, they require large safety zones to protect from the hazards of their large stray magnetic fields.

Depending on the field strength and the desired system geometry, the polarising magnetic field is generated either by current circulating through coils or by permanent magnets. Generally, superconducting coils are needed to generate the strong fields required for the high and ultra-high field MR systems. Permanent magnets are mainly employed in low field systems. Resistive coils are mostly limited to ULF MR and some low field systems where associated power losses and heat dissipation are still practical. These different technologies are detailed in the following.

Polarising coils: Superconducting electromagnets comprise the technology which can generate the strongest static magnetic fields. For this reason, they are used in high and ultra-high field MR systems. This technology is found, for example, in typical clinical whole-body high field MR systems which employ field strengths between 1 T and 3 T. Commercial MR systems working at 7 T and higher also exist, but these are generally reserved for research or laboratory purposes. This approach to generating the magnetic field requires a delicate temperature regulation system with high electrical power demands and employs cryogenics, being the expensive liquid helium the most extensively used cooling agent.

Resistive coils are also common means of inducing magnetic fields. Although resistive coils can be used to generate strong magnetic fields, the heat dissipation and power consumption associated with their electrical resistivity discourages their use in high field systems. These coils are however commonly used to generate very low magnetic fields, such as the ones employed in ULF MR systems. Resistive coils generating field strengths up to few hundreds of microteslas can be thermo-regulated with forced-air cooling[46]; ULF MR instruments employing several tens of microteslas often can dispense with sophisticated cooling[15,30,47].

Polarising permanent magnets: As an alternative to polarisation coils, permanent magnets are a less conventional way of generating the polarisation field which is increasingly gaining attention. Achievable field strength has limited their application mainly to low field systems. Their main advantage is that the can generate considerably strong field strengths requiring neither superconducting cryogenic setups nor power hungry current amplifiers. Yet, achieving high field homogeneity in permanent magnet systems requires active shimming with resistive coils. Most clinical permanent magnet based low field MR systems are designed to offer a more open space for the patient, improving patient comfort and facilitating access to the patient in interventional scenarios.

Different arrangements have been proposed to build custom low field MR systems with permanent magnets. Various single sided or unilateral MR systems have been prototyped, which feature either a small region with reduced inhomogeneity or a region with a linearised magnetic field gradient[43,48-58]. Although these systems have the advantage of facilitating the access to the sample, existing designs are constrained by a reduced field of view. A more compact magnet size can be achieved by placing the magnets in Halbach configuration as this concentrates the field strength in a given region while keeping the stray fields relatively low[59]. The cylindrical Halbach configuration, in particular, has found application in MR[18,19,60-68]. The most exploited Halbach configuration generates a magnetic field perpendicular to its

axis as shown in Figure 15a. The Halbach configuration can be modified to achieve a desired field homogeneity level or a field gradient[46,48,63].

2.2.2 Induction field

To allow for its detection, the net magnetisation has to be transferred to the plane perpendicular to B_0, which is achieved by applying an alternating magnetic field transversal to the polarising field. This field is called the induction magnetic field, also known as radio frequency (Rf), transmission (Tx), or B_1^+ field. To reduce required power, this field is typically oscillating at frequencies near spin resonance. Two different main forms of acquisition strategies exist which are continuous wave[69,70] (CW) acquisition and pulsed acquisition. The stochastic excitation is a less common technique which uses randomised low-energy induction[71,72].

In CW, the induction happens concurrently to the acquisition. The spectral information is harvested by sweeping either the induction frequency or the external magnetic field. The signal is determined from complex impedance changes experienced in the excitation coil. The power required to generate the excitation field in this modality is low (milliwatts).

Contrarily, in pulsed MR the spectral information can cover the whole bandwidth of interest in a single acquisition. The signal can then be decomposed into different frequency components by the Fourier transform[73]. The MR signal is acquired quickly after the pulse. The pulsed excitation employs short power hungry pulses (kilowatts). A dead-time between excitation and acquisition is needed for the receiver electronics to recover from the strong voltages induced by the pulse.

In pulsed MR, the signal can be detected either with the same coil used for the induction (Tx/Rx) or with a receiving exclusive coil (Rx). Good transmit coils are power efficient and provide a homogeneous B_1^+ field. The second requirement facilitates the control of the spin dynamics, reducing image artefacts such as inhomogeneous image intensity or slice to slice interference. Differently, sensitivity is generally the most valued feature in receive coils; leading to the common practice of using independent transmit and receive coils. Employing multiple receivers in parallel can also improve the SNR and reduce imaging times[74-77]. Phased array coils wherein the currents can be controlled independently of each channel are more recently finding application to reduce heat deposition and increase B_1^+ homogeneity in ultra-high field systems [78,79].

Although CW has been around since the inception of MR techniques, it was soon superseded by pulsed techniques. This decrease in the popularity of CW was mainly because, while CW facilitates the study of very sort T2 samples, the pulsed counterpart can capture multiple resonances in parallel increasing the SNR per acquisition time[73]. Furthermore, the pulsed technique provides a large range of sequences and contrasts.

2.2.3 Gradient fields

The spatial information required to generate an image in MRI is attained by using gradient coils which generate a range of spatially varying magnetic fields. These magnetic fields generate a correspondence between the spatial position and the resonance frequency. These gradients are switched rapidly by applying large currents in resistive coils, which produce strong forces in the coils. Therefore, gradient coils have to be firmly held in place. Yet, they tend to wear out earlier than other parts[80]. To achieve rapid switching, high fidelity power amplifiers able to provide 500-600 A and 1500-2000 V are commonly employed.

Gradient fields are also used to restrict MR signal induction to a specific region of the body. In this way, the image from a limited volume, such as a 1 mm slice, can be reconstructed independently without needing to solve for the whole 3D volume. This excitation selectivity is the principle of slice selection in 2D MRI sequences.

MRI imaging has also been achieved by using the intrinsic magnetic field gradient of permanent magnets in a Halbach configuration, which is a less common alternative to generating the gradient fields using coils[60]. In this case, the system is rotated to vary its relative position with respect to the sample, thereby encoding the sample with 2D information. Encoding of the 3rd dimension is done via a special transmit array (TRASE)[81] which generates an Rf field that linearly varies its phase in the 3rd dimension.

Differently to static permanent magnet arrangements, Halbach array configurations that can be dynamically reconfigured have also been described. Blümler has recently proposed a variety of cylindrical Halbach configurations that generate relatively linear gradient fields. These arrangements can be combined with a set of concentric Halbach arrays to produce a variety of magnetic fields useful for MRI[67,82].

Although ideally gradient fields should only vary the magnitude of the resultant magnetic field without affecting its angle, Maxwell's equations state that this is practically not possible[83-86]. The difference between the ideal field and the generated field is called the concomitant field. This unwanted effect is negligible for high field systems as the static

magnetic field is orders of magnitude larger than the gradient fields. In ULF MRI, however, concomitant fields can substantially reduce the linearity of the resultant fields resulting in artefacts and signal loss[84,87].

2.2.4 Detectors

The wide range of existing MR applications has benefited from employing a plurality of tailored detectors that sense the magnetic field in the near-field. A description of the detectors most commonly used in ULF MR is presented in the following.

Faraday coil magnetometers, also known as air-core magnetometers, exploit the electromagnetic induction effect to sense magnetic fields. When a conductive loop is placed in the vicinity of a rotating magnetic dipole, the free electrons in the loop will experience a force proportional to the rate of change of the magnetic flux through the loop. This force represents a voltage, also known as electromotive force or *EMF*. The *EMF, ξ,* can be calculated by applying the principle of reciprocity such that[88]

$$\xi(t) = -\frac{d\phi(t)}{dt} = -\frac{d}{dt}\int_{VOI} \beta_{\perp}(s)\ M(s,t)ds. \tag{9}$$

As can be inferred from Equation (9), the *EMF* increases proportionally with frequency and sample magnetisation, reason why higher magnetic field systems can achieve higher sensitivity. Equation (9) also suggests that the coil is only sensitive to the component of the dipole $M(s,t)$ parallel to the magnetic field that current passing through the coil would generate at the point in the space s. In conventional MRI this effective magnetic field can be assumed to be the magnetic field normal to the plane of the coil $B_{\perp}$. This magnetic field $B_{\perp}$ can be obtained using Biot-Savart's law, and by integrating over the circular current loop, the following equation results[89]

$$B_{\perp} = \frac{\mu_0}{2\pi}\frac{1}{\sqrt{(a+r)^2+(z)^2}}\left[K(k) + \frac{a^2-r^2-z^2}{(a-r)^2+z^2}E(k)\right]; \tag{10}$$

$$k = \sqrt{\frac{4ra}{z^2+(a+r)^2}}. \tag{11}$$

Here a is the distance from the axis of the loop to the point in space s, z is the distance along the axis of the loop to s, r is the radius of the loop, μ_0 is the permeability of free space (4π x 10^{-7} h/m), $E(k)$ is the elliptic integral of the 2nd kind, and $K(k)$ is the elliptic integral of the 1st kind.

The *EMF* is a very small voltage which can easily be hindered by other noise sources. Therefore, it is essential to amplify the *EMF* before it is transmitted through the rest of the detection path for its discretisation. However, the noise contribution from the pre-amplifier itself can be significant. Pre-amplifier noise is often presented as the voltage noise referred to the input e_n and the equivalent current noise referred to the input i_n. The contribution of these two noise sources is minimised for a specific source impedance, which is the impedance of the coil in this case.

The optimal source impedance of a pre-amplifier is generally different from the impedance of the coil, necessitating the need for an impedance transformation. Accomplishing the impedance matching with electrical transformers is possible. However, transformer insertion losses are typically substantial and introduce considerable noise. Therefore, it is common practice to match with a matching network consisting of high quality lumped elements, which introduce fewer losses. Irrespective of the approach, the transformation ratio achievable through matching networks can only be maintained for a narrow bandwidth[90-93]. For this reason, matching with lumped elements has optimal performance only within a narrow frequency band. Higher transformation ratios generally increase the insertion losses of the matching network and reduce the acquisition bandwidth.

There exist many different matching configurations, some of which are shown in Figure 3, where *X* represents the reactance of either a capacitor or an inductor. Well-known arrangements include the “L” (Figure 3A-B), “π” (Figure 3C) and “T” (Figure 3D) configurations. The “L” matching network provides the widest bandwidth for a certain transformation ratio. The drawback is that for a given transformation ratio *m*, the “L” matching network only offers one possible choice of lumped element values. This confinement can lead to impractical or inefficient values. The “π” and “T” configurations allow for more freedom when choosing lumped element values. They can be seen as two back-to-back “L” networks with opposite transformation direction, i.e. one increases the impedance while the other one decreases it. The resultant transformation ratio is the multiplication of the two transformation ratios. The bandwidth of the matching network is mainly defined by the narrowest bandwidth from the two “L” sections.

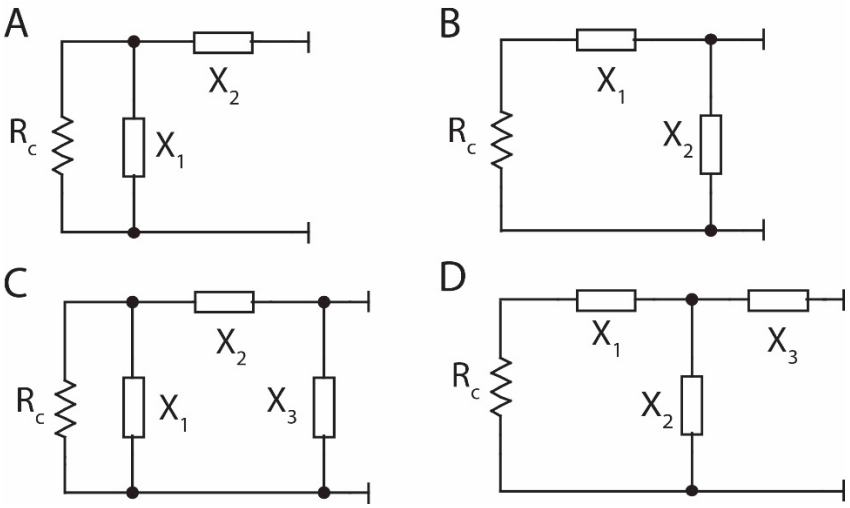

Figure 3: Different possible matching network configurations. The "L" matching networks offer impedance reducing (A) or boosting possibilities (B). The "π" configuration (C) and the "T" configuration (D) provide flexibility at the time of choosing the components and the transformation ratio. In the case of coils, the inductance of the coil readily provides a reactive element in series with the resistance of the coil.

In the "L" network, the impedance transformation and voltage transformation provided by the matching networks can be expressed by the quality factor (Q) of the network as in Equations (12)-(15). Here, the source resistance (R_c) and voltage source (V_c) are amplified or diminished according to the configuration shown in Figure 3A (R_a; V_a) or Figure 3B (R_b; V_b). Q is calculated by knowing the equivalent series resistance (ESR) introduced by the lumped elements. Note that in Equations (16)-(17) Q is calculated differently depending on whether the element is a capacitor or an inductor of value C and L respectively. It is difficult to achieve coil-network setups with high Q factors as the coil has a very low inductance to resistance ratio. The Q is especially low at low frequencies given its proportionality with frequency. It should be emphasised that there is an optimal transformation ratio for a given coil/pre-amplifier arrangement. This means that increasing Q above a specific value will reduce the SNR. The explanation of this lies in the equivalent current noise from the amplifier, which generates a voltage noise proportional to the impedance presented to the amplifier.

$$R_A = R_C(Q^2 + 1); \tag{12}$$

$$R_B = \frac{R_C}{(Q^2 + 1)}; \tag{13}$$

$$V_A = V_C\sqrt{Q^2 + 1;} \tag{14}$$

$$V_B = \frac{V_C}{\sqrt{Q^2 + 1}}; \tag{15}$$

$$Q_{inductor} = \frac{\omega L}{ESR}; \tag{16}$$

$$Q_{capacitor} = \frac{1}{\omega C \cdot ESR}; \tag{17}$$

The matching network creates a resonant tank circuit that stores energy, which can be particularly problematic in pulsed sequences, where the acquisition is made after strong magnetic field fluctuations (e.g., Rf. or pre-polarisation pulses). Large magnetic field fluctuations can induce a strong *EMF* in the coil, which is orders of magnitude higher than the *EMF* generated by the MR signal. Such high voltages are out of the dynamic range of the pre-amplifier and can damage the electronics. To prevent malfunction or damage, the energy stored in the coil and reactive elements needs to be dissipated before the signal is presented to the pre-amplifier. Stored energy dissipates through an exponentially decaying resonant process known as ring-down. Although data acquisition can start once the voltage of the ring-down is within the dynamic range of the pre-amplifier, the remaining ring-down signal generally contains frequency components which overlap with the MR signal, the result of which is severe artefacts in the data. Thus, signal acquisition is often further delayed reducing the sensitivity to the MR. This SNR loss is particularly pronounced in rapidly decaying MR signals.

At low frequencies, the ring-down can be particularly long due to a slower energy dissipation and a higher energy intake by the coil. The energy dissipation rate is proportional to the resonant frequency. The higher energy storage ($W_{inductor}$) arises from the increased inductance (L) of using multiple loop coils such that

$$W_{inductor} = \frac{1}{2}Li^2. \tag{18}$$

Here *i* is the current flowing though the coil. A standard way of protecting the pre-amplifier is by placing at its input a pair of diodes connected to ground in antiparallel. The diodes short-circuit the entrance to the pre-amplifier when the voltage across them exceeds their forward voltage, which is about 0.5 V. Even with the diodes in place, the power delivered to

the pre-amplifier can still be large enough to blind it for a considerable amount of time. This blinding is mostly related to biasing capacitors getting charged and temporally changing the DC bias conditions of the pre-amplifier[94]. Replacing the diodes with actively controlled PIN diodes can add extra protection, but the biasing circuit of the pin diodes has to be adequately designed to minimise insertion losses[95]. This protection scheme can be activated manually[96] or semi-automatically[94], adding the latter additional safety against user errors. To further protect the pre-amplifier, the diodes can be placed at a quarter wavelength ($\lambda/4$) distance from the coil. This additional transmission line length effectively converts the short circuit at the diodes into an open circuit at the coil, reflecting a large part of the power away from the pre-amplifier. At low frequencies, this would be impractical because a $\lambda/4$ cable would be extremely long, bulky and lossy. In this case, it is more convenient to use lumped elements to reproduce the same effect[96,97]. Detector dead-time constant can be estimated from the signal ring-down by

$$\tau = \frac{2Q}{\omega_0} ln \frac{V_p}{V_n}. \quad (19)$$

Here, the dead-time is the time the ring-down needs to decrease down to the noise floor level[98]. Different designs have been proposed to reduce this dead-time. *Q*-switching is a technique where the *Q* is temporarily reduced during the energy dissipation phase[99,100]. Shifting of the resonance frequency of the coil has also been proposed[101].

Superconducting quantum interference device (SQUID) is an extremely sensitive detector based on superconducting loops containing Josephson junctions. In MR applications SQUIDs employ a cryogenic flux transformer, which increases the sensitivity area of the SQUID by "transporting" the magnetic flux from a large area near the body to the smaller area of the SQUID. The flux transformer has a constriction where the supercurrent creates a highly localised strong magnetic field which is detected by the SQUID. The sensitivity of SQUIDs is not frequency dependent up to around 10 MHz[26]. The latest improvements in micro-fabrication technology have allowed the miniaturisation and commercialisation of SQUIDs, making them the most used signal detector for high-end ULF MR systems[12,24,26,87].

However, SQUIDs are expensive to buy and have maintenance overheads associated with the cryogenics[24]. Furthermore, the cryogenic enclosure can limit their geometry and reduce their effective sensitivity in ULF MR[24].

Atomic magnetometer (AM) is a state-of-the-art detector which can reach sensitivities in the same order of magnitude as a SQUID. AMs provide accurate magnetic field measurements by measuring the precession frequency of certain high-density vapour of alkali metal atoms, such as rubidium or caesium. These atomic spins are optically pumped using a resonant laser beam. For MR applications they have been combined with room temperature flux transformers.

Several experiments have been performed using this detector for anatomical ULF-MRI[102,103]. Unlike SQUIDs, they do not require cryogenics, but they must also be isolated in a careful manner from the pre-polarisation field and from external electromagnetic fields. Still, the bulkiness and complexity of current AM MR setups advocate for the more mature SQUID technology.

Giant magnetoresistance (GMR) mixed magnetometer detectors combine two thin layers of slightly distant different materials: a magnetic film with constant magnetisation, and a magnetic material that changes the orientation of its magnetic field under the presence of an external magnetic field. They have been used in ULF MR with the help of a superconducting flux transformer[104,105]. GMR mixed sensors can withstand strong magnetic fields up to 10 mT. The sensitivity that GMR mixed sensors have reached in MR applications has been lower than that of SQUIDs and AMs.

2.3 Noise in MR

Having portrayed the basis for estimating the voltage generated in a loop by the MR experiment we now address what the limits are to distinguish such a small signal. Unfortunately, the MR signal is not the only signal that is recorded in an MR experiment. The rest of signals which are not of interest compose what is called noise, and obscure the MR signal. The noise can be characterised by its nature, origin and spectral composition. In the following, we will introduce the noise sources relevant to MR with particular emphasis on the ones concerning the kHz regime.

2.3.1 Body noise

Conductive structures such as the human body couple noise to the MR signal if they are above 0 °K. The thermal energy makes electrons experience random displacements which follow principles of Brownian motion[106]. The precise trajectories and speed of the electrons in a determined time cannot be predicted. However, electric potential and current generated by this electron displacements have a known statistical distribution. The spectral distribution

of thermal noise is approximately white, and it can be characterised by having a Gaussian amplitude distribution when analysed over a delimited bandwidth.

Human tissue is considered to be a “poor conductor” due to its low electrical conductivity[107], and consequently, electromagnetic radiation is little attenuated up to the Gigahertz regime. Yet, tissue conductivity allows for energy exchange with MR coils. This interaction generates losses which can be classified as inductive or dielectric depending on their nature. These losses can be expressed as an additional resistance added in series to the equivalent circuit of a coil. Not surprisingly, this resistance characterises the noise induced by the corresponding phenomenon. Thus, losses and noise offer a different perspective on the same process. The corresponding noise can be expressed either in the form of a voltage source in series with the resistance or in the form of a current source in parallel with the resistance such that

$$e_{noise} = \sqrt{4kT\Delta f R}; \tag{20}$$

$$i_{noise} = \sqrt{\frac{4kT\Delta f}{R}}. \tag{21}$$

Here, *k* is Boltzmann’s constant, *T* is the absolute temperature, Δf is the frequency bandwidth, e_n is the voltage noise and i_n is the current noise. Figure 4 shows a schematic with different noise sources existing in a tuned coil detector. To calculate the total of the noise, it is common practice to reflect the noise sources to a same point. This point is usually the coil or the input of the amplifier. Once the noise sources are referred to the same point, the noises can be added together. If the noises are uncorrelated, as it is often the case, they are added as a square root of sums.

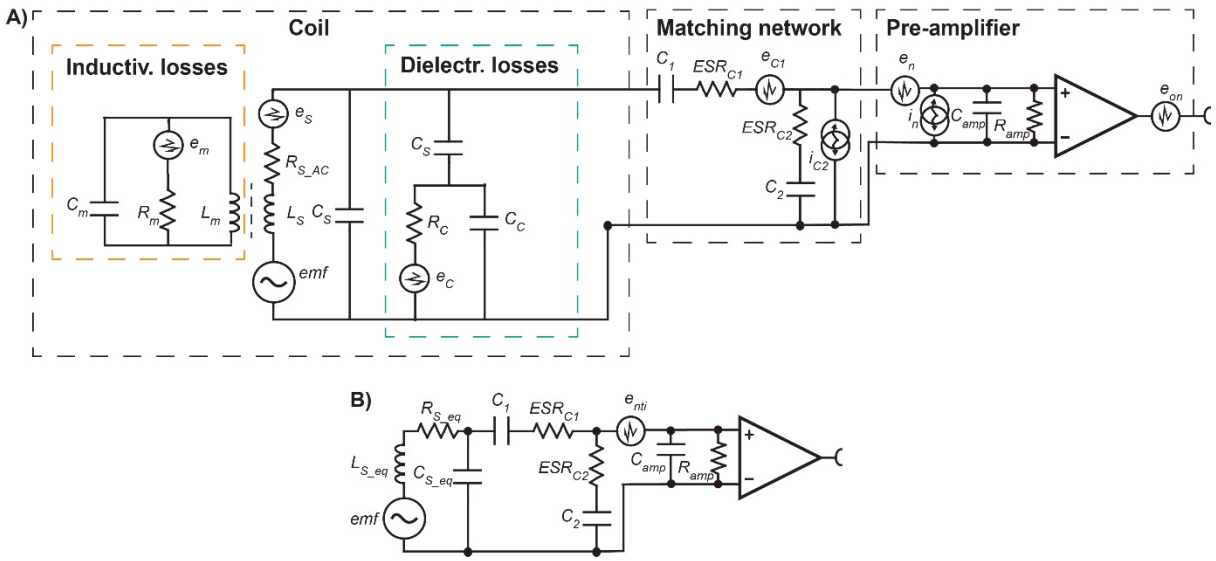

Figure 4: Schematic showing the equivalent circuit diagram of a tuned coil detector with different noise sources. Here, the thermal noise from the coil, the inductive losses, the dielectric losses, and the losses of the matching network have been represented, as well as the equivalent voltage and current noise from the pre-amplifier (A). emf *represents the electromotive force, and L_S, C_S and R_S the inductance, parasitic capacitance and conductor resistance of the coil. Additional inductive and dielectric losses experienced by the coil are captured in corresponding equivalent circuits. The inductive losses are modelled as a coupled inductor L_m in parallel to resistor R_m and a capacitor C_m. The dielectric losses are represented by a capacitor C_S, which represents the parasitic capacitance between the coil and the body, and a resistor R_C in parallel with the equivalent distributed capacitance C_C of the body. Capacitor losses are accounted through their equivalent series resistances ESR_{C1} and ESR_{C2}. The equivalent input current (i_n) and voltage (e_n) noise of the pre-amplifier is also included. To estimate the total equivalent noise (e_{nti}), noise sources are referred to one same point in the equivalent circuit, in this case to the input of the pre-amplifier (B).*

Dielectric Losses: The electric charge distribution in the coil generates electric lines of force in the body through a distributed capacitive effect between the coil and the body (C_S), and the equivalent resistance (R_C) and capacitance (C_C) across the body[108]. The equivalent circuit is shown in Figure 4A. Exact calculation of the parasitic capacitances and resistance is very complex. The value of C_S can roughly be expected to change proportionally with coil diameter, to decrease slowly with increasing coil length, and to be independent of the number of turns. The values of R_C and C_C vary with frequency as tissue conductivity and permittivity depend on it. The equivalent conductance of the coil due to dielectric losses can be calculated by

$$Y = Y_{real} + jY_{imag} = \frac{\omega_0^2 R_c C_s^2}{1 + \omega_0^2 R_c^2 (C_s + C_c)^2} + j\frac{\omega_0 C_s + \omega_0^3 R_c^2 C_s C_c (C_s + C_c)}{1 + \omega_0^2 R_c^2 (C_s + C_c)^2}. \quad (22)$$

The non-conservative part of Equation (22), i.e. the real part, represents the losses. The equivalent series resistance that represents the power loss of this dielectric effect is[109]

$$R_e = \omega^2 L^2 Y_{real}, \quad (23)$$

which at low frequencies approximates to

$$R_e \approx \omega^4 L^2 R_C C_S, \quad as \quad R_C \ll 1/\omega C_S. \quad (24)$$

At higher frequencies, the equivalent series resistance tends towards

$$R_e \approx \frac{\omega^2 L^2 C_S^2}{R_C (C_s + C_c)^2}, \quad as \quad R_C \gg 1/\omega C_S. \quad (25)$$

Changing the conductivity of the body to reduce dielectric losses is not an option. However, a similar effect can be achieved by shielding the coil, which in essence reduces the series resistance. This effect can be understood as the electrons from the shield mobilising to reduce the electric lines of force that the coil generates in the body and vice versa, depending on if one is on transmission or reception mode. This shield also reduces radiation resistance, although this is negligible for most MR detectors as the dimensions of the coil are much smaller than the wavelength.

Another strategy to reduce dielectric losses is to split the coil with capacitors symmetrically. This segmentation reduces the voltage drop across each section and minimises the effect of the parasitic capacitance. Similarly, the matching network can be balanced so the net electric potential of the coil is zero[110].

Dielectric losses are more prominent when the coil is operated near its self-resonance frequency or at high frequencies where the wavelength approaches the length of the coil. These losses become negligible in the kHz range.

Inductive losses: Similarly to dielectric losses, inductive losses can be interpreted from the transmission or the reception point of view. For the first case, the alternating transmission field (B_1^+) dissipates power by inducing eddy currents in the ions present in the body. For the reception point of view, thermal motion of ions in the body induce an *EMF* in the coil. According to the fluctuation-dissipation theorem, both cases should lead to the same result. Several analytical expressions have been derived to approximate the value of the equivalent series resistance generated by this effect (R_m) depending on the shape of the object[26,111]. For a solenoidal coil of radius *a*, length 2*g*, and *n* turns, on a spherical sample of radius *b* placed in the centre of the coil[111]

$$R_m = \frac{\pi\omega_0^2\mu_0^2 n^2 b^5 \sigma}{30(a^2+g^2)}. \quad (26)$$

In the case of a cylindrical sample of length 2*g* and radius *b* the above would be[111]

$$R_m = \frac{\pi\omega_0^2\mu_0^2 n^2 b^4 g \sigma}{16(a^2+g^2)}. \quad (27)$$

For also a cylindrical sample placed coaxially out of the coil[26]

$$R_m = \omega_0^2\mu_0^2\sigma V_{loss} = 2\pi\omega_0^2\mu_0^2\sigma b^2 g. \quad (28)$$

Unlike dielectric losses, inductive losses are not easily reduced as they are related to the magnetic field necessary for signal induction and detection. Separating the coil from the body by some millimetres, known as “lift-off” effect, has been shown to reduce dielectric[112] and inductive[113] losses. Hardware gradiometry has also been shown to reduce the inductive

noise of surface coils by attenuating inductive coupling between coil and body parts away from the region of interest[113]. Inductive losses are negligible in ULF MR.

It should be noted that dielectric and inductive losses introduce not only a real impedance but also an imaginary impedance. In practice, this results in a frequency shift of the resonant frequency of the detector. In some cases, this will require re-tuning of the matching network for optimal results.

2.3.2 Detector noise

Body noise is often the dominant noise source in large coils, especially in high field MRI. Contrarily, detector noise can become the dominant noise source when using smaller coils or lower field systems. In the following, the primary noise sources of a Faraday coil detector are presented for each of its elements.

Coil: The resistance of a room temperature coil can be a major noise contributor through the thermal noise. This noise depends on the resistance of the coil, which varies in frequency. The resistance of a coil is estimated in two steps. First, the so-called direct current (DC) resistance is calculated by[114]

$$R_{DC} = \frac{\rho l}{A}. \tag{29}$$

Here the resistivity ρ (ohms·m) is the inverse of the conductivity σ (siemens m^{-1}), l is the wire length, and A is the cross-sectional area of the wire (m^2). The second step is the calculation of the AC resistance, which accounts for the interactions between electrons resulting in a non-uniform current distribution across the cross-section of the conductor due to eddy currents. The corresponding decrease in the effective area increases conductor resistance as compared to the DC resistance. The AC resistance is dominated by two main effects: the proximity effect and the skin effect. The skin effect accounts for the forces generated and experienced by the electrons within an isolated wire, while the proximity effect does it for forces generated from neighbouring wire sections.

The skin effect is related to the skin depth which is defined by $\delta = \sqrt{\rho/\pi f \mu}$, where f is the frequency (Hz), and μ is the magnetic permeability of the material ($4\pi \times 10^{-7}$ H m^{-1} for copper). The skin effect starts being significant when wire radius is not bigger than the skin depth.

The proximity effect increases wire resistance when several conductors are close to each other. Unlike the skin effect, this effect not only depends on the frequency but also on the ratio of the self and mutual inductances of the neighbouring conductors, i.e. in the geometry of the coil. This effect is prominent in multiple turn coils. Multiple turn coils are used to raise the *EMF* above amplifier noise when body noise is not dominant, which happens at low frequencies or with small coils.

For the most common cylindrical coil shapes, AC resistance models exist which provide a reliable estimation up to the low MHz range[103]. Contrarily, finite element solvers are most often used to predict coil properties at frequencies above few MHz.

Matching network: Most matching networks are composed of capacitors and inductors. Although ideally reactive elements only store energy, in practice they also dissipate part of it. This energy dissipation can be described to a reasonable level of accuracy through an equivalent resistance in either series or parallel with the ideal element. The ratio of stored to dissipated energy is quantified by the *quality factor Q* such that

$$Q = 2\pi\left(\frac{maximum\ energy\ stored}{energy\ loss\ per\ cycle}\right) = \omega_r\left(\frac{maximum\ energy\ stored}{average\ power\ dissipated}\right). \quad (30)$$

As can be inferred from Equation (30), the quality factor depends on the resonant frequency ω_r.

Existing matching network topologies can generate different insertion losses depending on their arrangement. Inductors are generally much lossier than capacitors[115]. Therefore, the use of entirely capacitive matching networks, such as in the example of Figure 4, can reduce losses[116].

Pre-amplifier and semiconductors noise: For practical purposes, datasheets of commercial pre-amplifiers often summarise all the noise sources as input equivalent current and voltage noises. However, when designing a discrete pre-amplifier, knowing the nature of the different noises is essential to minimise their contribution, as this depends on variables such as biasing currents. Semiconductors experience additional spontaneous fluctuations in current and voltage other than the *thermal noise*[117-120]. Probably the most important noise types are the shot noise, the 1/f noise or flicker noise, the avalanche noise, and the generation-recombination noise.

Shot noise occurs due to the liberation of charge carriers in a discrete structure such as the p-n junction of diodes. They are associated with electrons with high enough energy to cross a barrier. It is described by the current noise

$$i_{shot} = \sqrt{2qI\Delta f}. \tag{31}$$

Thus, it depends on the forward junction current *I,* the electron charge *q*, and it is frequency and temperature independent. According to Equation (31), its power density distribution corresponds to white noise.

The *1/f noise*, also known as flicker noise, often dominates in the low-frequency range and gets its name from its spectral distribution. It arises from conductivity fluctuations in contact imperfections between two materials conducting DC. Therefore, it is present in biased semiconductor devices. Different models have been proposed for different semiconductor devices.

Reverse-biased junctions present *avalanche noise*, which arises from leakage current colliding with the crystal lattice of the semiconductor. This collision pulls out additional electrons which will flow in the same direction. This noise is also frequency independent.

Generation-recombination noise is caused by the fluctuation of the number of carriers due to device conductance changes. Its spectral density is relatively constant up to the frequency f=1/(2ττ) and decreases proportionally to $1/f^2$ beyond that frequency such that

$$S_{g-r} = \frac{\overline{(\Delta N)}^2 4\tau}{1 + (2\pi f\tau)^2}. \tag{32}$$

Here $\overline{(\Delta N)^2}$ is the variance of the number of carriers and τ is the carrier lifetime.

In the following, we will detail the dominant noise relevant to bipolar transistors (BJT) and junction field effect transistors (jFET), which are the most suitable transistor types for low noise pre-amplification applications.

The primary noise sources of *BJT transistors* are the thermal noise e_{th_rb} of the base-spreading resistance r_b, the shot noise i_{sh_b} and the flicker noise i_{1/f_b} of the base bias current I_B, and the shot noise i_{sh_c} of the collector current I_C, as represented in Figure 5.

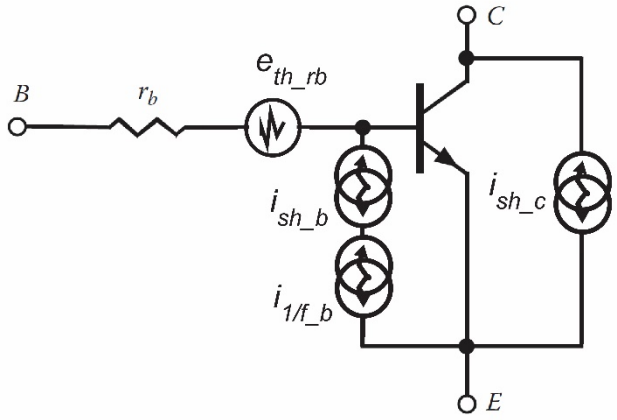

Figure 5: Schematic representing the noise sources of a bipolar transistor. The noise sources are the thermal noise e_{th_rb} of the base spreading resistance, the shot noise i_{sh_b} and the flicker noise i_{1/f_b} of the base bias current, and the shot noise i_{sh_c} of the channel bias current.

The equivalent total noise can be estimated by small signal models like the one shown in Figure 6. This model includes the parasitic capacitances, which are particularly relevant for high-frequency estimations. In this representation, the channel resistance and the load resistance have been combined in parallel into R_L. Likewise, C_L encompasses the capacitance of the next stage and the parasitic collector-emitter capacitance.

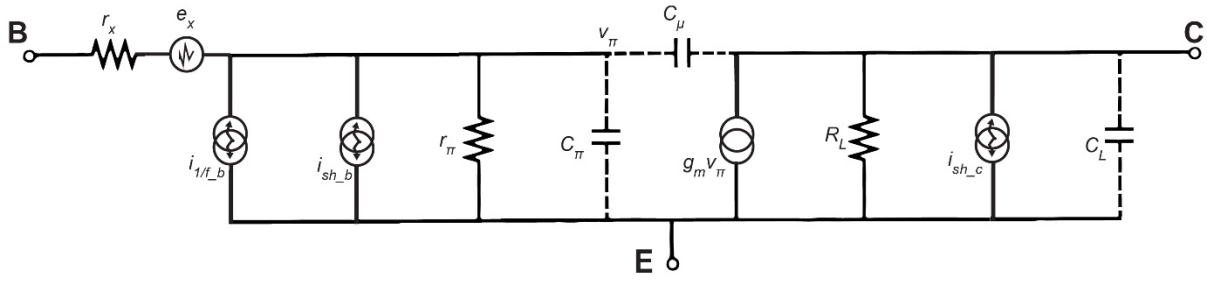

Figure 6: Small-signal model for BJT transistors with dominant noise sources.

n-p-n transistors have higher levels of flicker noise than p-n-p transistors. A commonly used flicker noise model used in BJT is

$$i_{1/f\_b} = \sqrt{\frac{k_f I_B^{\alpha} \Delta f}{f^{\gamma}}}, \tag{33}$$

where the coefficients γ and α are almost 1 in modern quality BJTs. K_f is the flicker noise coefficient and is measured experimentally.

For low frequencies where parasitic capacitances can be neglected the equivalent input referred voltage and current noises of BJT are[120]

$$e_n = \sqrt{e_{th\_rb}^2 + i_{sh\_c}^2 \left(\frac{V_T}{I_C}\right)^2} = \sqrt{4kTr_b + \frac{2(kT)^2}{qI_c}}; \tag{34}$$

$$i_n = \sqrt{i_{sh\_b}^2 + i_{1/f\_b}^2 + \frac{i_{sh\_c}^2}{\beta^2}}, \tag{35}$$

being β the common-emitter current gain, and $V_T = kT/q$ the thermal voltage.

Differently, the dominant noise sources in modern *jFETs* are the channel thermal noise i_{th_d}, the flicker noise i_{1/f_d} of drain current I_D, and the shot noise in the gate caused by the gate leakage current I_G, as shown in Figure 7. The flicker noise of jFETs is usually higher than that of BJT. The channel thermal noise i_{th_d} can be estimated by

$$i_{th\_d} = \sqrt{4kT\gamma g_m \Delta f}, \tag{36}$$

where g_m is the small signal transconductance. The gate current noise is approximated such that

$$i_{sh\_g} = \sqrt{2qI_c \Delta f}, \tag{37}$$

and the flicker noise of the drain current as

$$i_{1/f\_d} = \sqrt{\frac{k_f I_D^{\alpha} \Delta f}{f^{\gamma}}}. \quad (38)$$

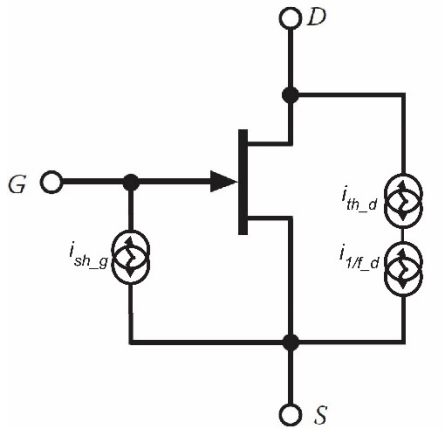

Figure 7: Schematic representing the primary noise sources of a jFET. Main noise sources are i_{sh_g} shot noise of the gate, and thermal and flicker noise of drain current.

Figure 8 shows the equivalent small signal circuit of a jFET with the dominant noise sources. The channel resistance and the load resistance have been combined in parallel in R_L. Similarly, C_L is the sum of the capacitance of the next stage and the parasitic drain-source capacitance. The parasitic capacitance C_{gd} plays a critical role by coupling channel noise to the input and limiting the gain bandwidth. Its effect can be calculated by applying Miller's theorem[121].

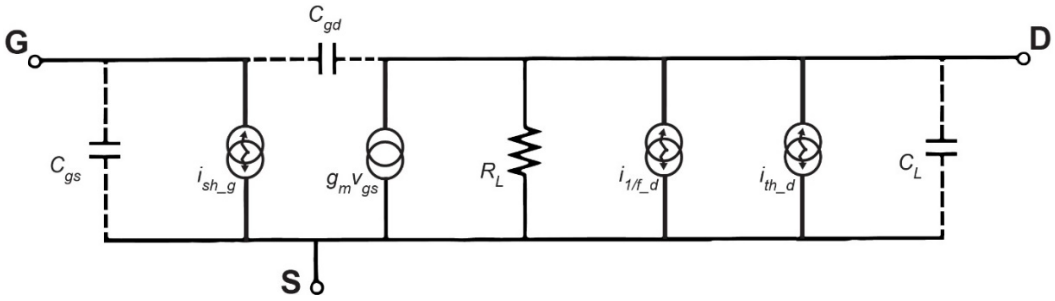

Figure 8: jFET small signal equivalent circuit with noise sources.

The equivalent input voltage and current noises in jFETs can be estimated by[122]

$$e_n = \frac{\sqrt{i_{th\_d}^2 + i_{1/f\_d}^2}}{g_m} = \frac{\sqrt{4kT\gamma g_m \Delta f + \frac{k_f I_D^\alpha \Delta f}{f^\gamma}}}{g_m}; \quad (39)$$

$$i_n = \sqrt{i_{sh\_g}^2 + \frac{e_{th\_Req}^2}{Z_{eq}^2}} = \sqrt{2qI_{Gss}\Delta f + \frac{4kTR_{eq}\Delta f}{Z_{eq}^2}} = \sqrt{2qI_{Gss}\Delta f + 4kT(Re\, Y_1)\Delta f}, \quad (40)$$

where

$$Y_1 = \frac{\omega^2 g_m R_L^2 C_{gd} C_L}{1 + \omega^2 R_L^2 C_L^2} + j\frac{\omega C_{gd}(1 + g_m R_L + \omega^2 R_L^2 C_L^2)}{1 + \omega^2 R_L^2 C_L^2}. \quad (41)$$

Looking into the elements contributing to the input referred equivalent voltage and current noises of Equations (39) and (40), it is possible to see that they feature both frequency independent and frequency dependent regions. In the low frequency region, the voltage noise is dominated by the *1/f* noise, decreasing with frequency until channel thermal noise takes over. Conversely, the low frequency region of the current noise is flat defined by the shot noise of the gate. This is surpassed as frequency increases by thermal noise from the output, which couples to the input through the parasitic capacitance C_{gd}.

Given that the channel thermal noise has a significant contribution in both current and voltage noises at higher frequencies, there is a considerable correlation between current and voltage noise. Therefore, the level of correlation needs to be considered in the estimation of the total noise through the normalised correlation coefficient γ such that[123]

$$e_{n\_total} = \sqrt{e_n^2 + (i_n Z_S)^2 + 2\gamma\sqrt{e_n{}^2}\sqrt{(i_n Z_S)^2}}, \quad (42)$$

where Z_S is the impedance seen from the input of the pre-amplifier[123].

A standard way of quantifying the noise introduced by the amplifier, apart from input referred equivalent current and voltage noises, is by the division between the square of the SNR if the amplifier were noiseless and the square of the SNR with the real amplifier. This ratio is called the *noise factor F*. An equivalent term is the *noise figure NF*, which is the noise factor expressed in decibels as follows[124]

$$NF = 10log(F) = 10log\left(1 + \frac{V_n^2 + 2\rho V_n I_n R_s + I_n^2 R_S^2}{4kTR_s\Delta f}\right), \quad (43)$$

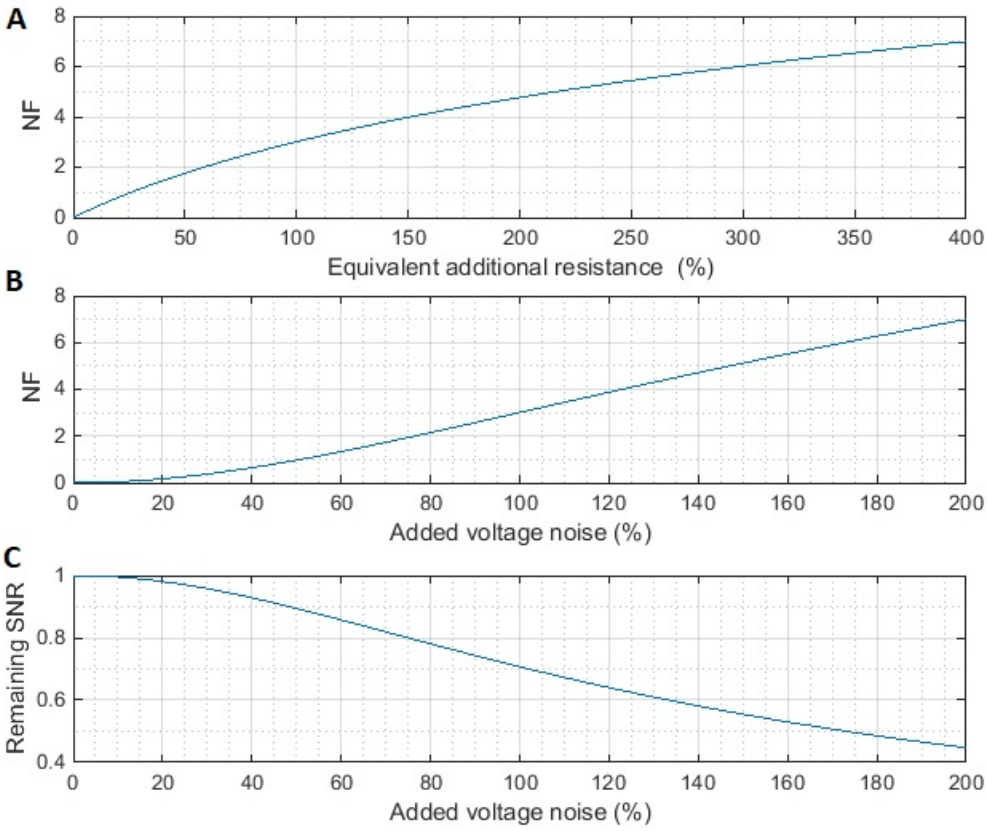

Figure 9: Influence of noise figure and SNR of the noise added by the pre-amplifier. The effect that the insertion losses of the amplifier have in the noise figure is plotted referred to the equivalent source noise resistance (A) and the percentage of additional voltage noise (B). The effects of the additional voltage noise on the normalised SNR as compared to the input SNR can be seen in (C).

and R_s is the source resistance. The source resistance that generates the optimum noise performance is typically calculated by $R_{s\_opt}=e_n/i_n$. Matching the source impedance to R_{s_opt} often requires of transforming the source impedance through a transformer or a matching network. One way of reducing the value of R_{s_opt} to facilitate the matching is by paralleling transistors. In this way, one reduces voltage noise trading it by current noise as

$$e_{n.par} = \frac{e_n}{\sqrt{n}}; \quad (44)$$

$$i_{n.par} = i_n\sqrt{n}, \tag{45}$$

while keeping the *NF* constant. The amplification of the signal in ultra-low noise amplifiers is most often done with multiple amplification stages. Multiple stages have to be carefully considered so the total noise of the pre-amplifier is minimised. The first stage is typically designed so that its noise is kept as low as possible. The first stage gain does not usually need to be large but high enough to minimise the noise contribution from the next stages. Often Friis formula can be used to estimate the noise factor contribution of each amplification stage such that[125]

$$F_{tot} = 1 + (F_1 - 1) + \frac{F_2 - 1}{G_1} + \frac{F_3 - 1}{G_1 G_2} + \cdots + \frac{F_n - 1}{G_1 G_2 \ldots G_{n-1}}, \tag{46}$$

where G_x is the average gain of the stage number "*x*". For this formula to hold, the output conductance of each stage has to be larger than zero and noise sources are assumed to be uncorrelated.

2.3.3 Ambient noise

Technology developed by humans is responsible for a large part of the electromagnetic (EM) background noise generated. This human-caused radiation strongly varies with the location, with rural areas on average having 20 to 30 dB less noise[126]. Typically, the electric power network generates the largest noises at 50 or 60 Hz and corresponding harmonics. Other strong sources are lighting, automobiles, motors, ignitions and other electronic devices[127]. In some cases, these sources can be long ranged and can be estimated as a plane wave.

Non-human induced natural sources also exist[126]. Earth magnetic field, ion, plasma and solar wind oscillations generate drifts at ultra-low frequencies around 1 mHz to 3000 mHz. Other electromagnetic noise can be produced with particles striking the magnetosphere causing such phenomena as chorus emissions and white noise aural hisses which range in frequencies from 500 Hz to 10 kHz. Electromagnetic perturbations from lightning can range from 1 Hz to 300 MHz travelling over a distance of 60,000 km[128].

The most common means for environmental noise reduction is by passively shielding the system. MR measurements are performed in a shielded room. Unlike at medium to high frequencies where copper Faraday cages (eddy current shielding) are employed[129,130], at low frequencies high permeability materials such as μ-metal, an extremely high permeability

alloy, are more efficiently used[131]. The associated material costs associated with high permeability shielding are, however, prohibitive. Such an approach to shielding from external influences also hinders system portability.

Active shielding has been used to replace the heavy and expensive passive enclosures in urban scenarios[27,132,133]. It aims to reduce environmental field fluctuations below 100 Hz that affect the small amplitude measurement field (B_m) by generating a counteracting field through a set of peripheral coils. Such an approach necessitates the need for additional sensors to accurately measure the environmental magnetic noise at the periphery of the system and to be able to apply a compensating field to negate environmental magnetic noise. The frequency response of the sensors and the feedback amplifiers limit active compensation to very low frequencies in the range 0-100 Hz.

To attenuate the effects of the environmental magnetic noise in the ULF-MRI regime (i.e. kHz range) hardware gradiometers are routinely employed with SQUIDs as have demonstrated to be very efficient for this purpose. Here, a set of two or more coils are connected in series to compensate part of the noise of the signal before it is amplified. However, gradiometers take up additional space and raise the noise floor of the coil[22]. Another approach called software gradiometry uses extra magnetic field detectors to detect only the environmental noise and subtract it through post processing[134]. This signal de-noising approach provides hardware less bulky than that of physical gradiometers, although it requires a dynamic range considerably broader than what can typically be afforded by SQUIDs.

2.4 Sensitivity & SNR

The ratio between the signal and the noise defines the sensitivity of the MR experiment. We have seen how signal and noise are often frequency dependent. On the one hand, increasing the field strength increases the steady state net magnetisation. Also, increasing frequency increases the *EMF* generated between the ends of a coil. The ambient noise generally decreases with an increase in frequency. On the other hand, dielectric and inductive losses increase with frequency. Also, the thermal noise from the coil increases with frequency, as its AC resistance increases. The matching network and the pre-amplifier can be designed to have a ‘sweet spot’ where noise is moderately independent of frequency. In the pre-amplifier, the flicker noise usually sets the lower limit while the parasitic capacitive feedback does it for the upper end. Similarly, losses in inductors and capacitors are higher at low frequencies and high frequencies.

There are other variables that heavily affect the SNR of acquired data such as the imaging sequence and relaxation times. These dependencies make estimating the SNR along a wide range of frequencies difficult. There have been analytical expressions derived to capture the dependency of field strength on SNR[135,136], the most popular of which is[135]

$$\mathrm{SNR} = \frac{\xi}{\sqrt{\sigma_{body}^2 + \sigma_{coil}^2}} = \frac{B_0^2}{\sqrt{\beta B_0^2 + \alpha\sqrt{B_0}}}, \tag{47}$$

where ξ denotes the *EMF* generated in the coil, σ_{body} and σ_{coil} the body and coil noise, and β and α are constants that scale the corresponding noises depending on coil and tissue properties. The first dividing term in Equation (47) represents the inductive losses from the body, and the second term the thermal noise of the coil. This formula suggests that while body noise dominates, the SNR is proportional to the field strength. This body noise dominance often happens at high fields or with large coils. If the opposite is true, namely the body noise is smaller, the SNR scales with the magnetic field to the power of 7/4, which is usually the case at lower fields. Figure 10 depicts this effect for a large MRI coil.

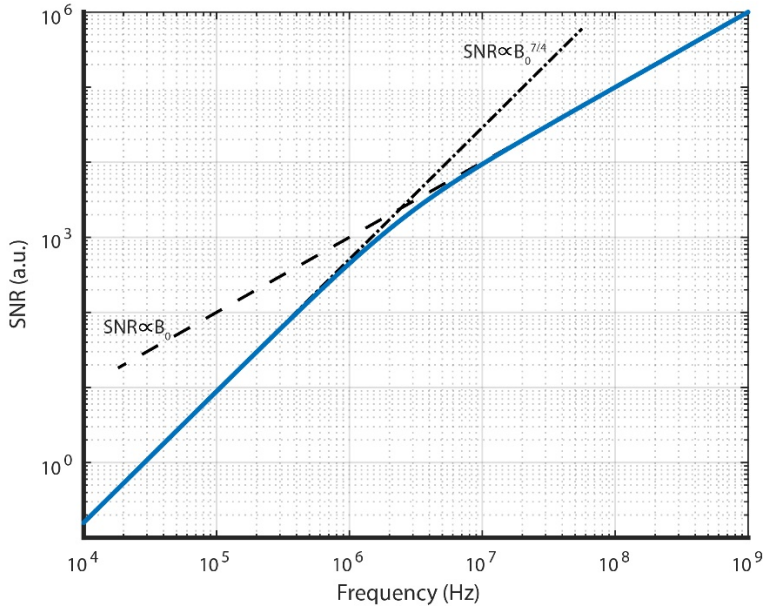

Figure 10: Plot of a typical estimation of SNR vs. frequency for an MRI coil. The low frequency region is dominated by the thermal noise from the coil, while the body noise dominates the higher frequencies. Other noise sources such as preamplifier noise and ambient noise are not considered here.

It is important to note that the SNR convention in the MR community is calculated from the voltage differences between signal and noise, unlike the standard definition in engineering where the powers are divided.

The SNR of a single acquisition is rarely high enough to be reliable for diagnosis. To increase the SNR, the signals from a repeated acquisition can be averaged. The SNR increases because signals from different acquisitions are correlated while noise is not. This feature improves the SNR by the square root of the number of acquisitions. Filling the k-space with different acquisitions also does increase the SNR through averaging. Averaging is often used in MR applications such as spectroscopy if the sample is not varying with time. In this case, the MR system has to be highly stable to maintain signal coherence between acquisitions. In human clinical applications, however, the number of acquisitions is limited as patient comfort and throughput advocate for quick scans.

In the case of MRI, SNR and image resolution are a trade-off. As a rule of thumb, for the same acquisition time, the SNR is proportional to the volume of the voxel. Besides, more samples need to be acquired to achieve higher resolution, which prolongs the acquisition time. The longer acquisition time can be compensated by stronger encoding gradients at the price of SNR, which decreases with the square root of the bandwidth. The reason for this is in the power density of the signal is spread across a broader frequency band, in turn reducing the energy of the signal per frequency bin whilst capturing additional noise from the extra frequencies. Therefore, to compare the performance of different systems, it is useful to estimate the SNR per unit of time (aka *imaging efficiency*). The SNR also depends on other variables such as tissue relaxation parameters and proton density. However, the SNR alone does not describe the capability of discerning between different tissue structures. This is better quantified by the ratio of the difference between the signals from the tissue of interest and the noise, commonly known as the contrast-to-noise ratio or CNR such that

$$CNR_{AB} = \frac{\xi_A - \xi_B}{\sigma_0} = \mathrm{SNR}_A - \mathrm{SNR}_B. \tag{48}$$

This definition is in the most of the cases more important than the SNR given that it is the difference between tissues what is routinely used for diagnosis. Matching sequence parameters to tissue properties can lead to improvements in CNR. This optimisation depends heavily on the sequence type. For example, Edelstein proposed estimating the CNR for a single-echo, saturation recovery pulse sequence by[135]

$$\mathrm{CNR} \propto V\rho\mathrm{SNR}_s\sqrt{t_{im}}\frac{\Delta T_1 T_R\sqrt{T_s}}{T_1^2}e^{-T_R/T_1}e^{-T_E/T_2}. \quad (49)$$

Here, SNR_s is the normalised SNR, T_s is the sampling time, t_{im} is the total imaging time, V is the volume of the signal source (voxel volume in the case of MRI), T_R is the pulse repetition time, and T_E is the echo time.

2.5 Signal enhancing techniques

Different techniques exist that increase SNR and imaging efficiency, some of which are presented in the following text.

2.5.1 Hyperpolarisation

Several methods that enhance the polarisation of the nuclear spins fall under the umbrella of what is called *hyperpolarisation*. Here, an enhancement of the net nuclear polarisation is achieved by either transferring spin order from another species or changing rapidly experimental conditions (e.g., temperature) between polarisation and detection stages. These methods include optical pumping, para-hydrogen-induced polarisation, and dynamic nuclear polarisation (DNP)[137-139].

In spin exchange optical pumping, an alkali metal vapour (e.g. R_b) polarises a noble gas (e.g. ^{3}He, ^{129}Xe, or ^{83}Kr) though spin-exchange collisions. Optical pumping has been used for spectroscopy and imaging the lungs with the noble gases ^{3}He and ^{129}Xe. In para-hydrogen-induced polarisation, higher nuclear spin order is achieved by means of a spin-conserved hydrogenation of an unsaturated substrate. DNP exploits the higher electron spin polarisation levels achievable in the solid state[140]. In most in-vivo situations, it requires the addition of a free radical rich substrate. One method of transferring the high electron polarisation to the nucleus is by keeping the sample in solid state and irradiate it at the right frequency, most commonly in the microwave range. This high transmission frequency, however, limits its application in humans. An alternative to the solid-state DNP is the dissolved-phase DNP where the hyperpolarised solid sample is rapidly brought to the liquid state and dissolved in a solution[141]. To be efficient, this solution contains a substance with long T_1. This substance can be used as contrast agent or target for a biomarker.

These methods usually require additional instrumentation to excite electron spins. They also require an extensive understanding of the energy levels and transition probabilities of the hyperpolarised substance to be used.

2.5.2 Cryogenics

According to Equation (4), cooling the sample/body increases the net magnetisation. Similarly, Equation (20) implies that cooling the detector also reduces its thermal noise. Cooling the patients is not an option, but it is possible to cool the detector[142]. It should be noted that the SNR can only be increased by cooling the detector when the body noise is not dominating. Also, there is a limit to the noise reduction in the sensor through this method. The conductivity of employed metals will decrease until it reaches a residual due to impurities within, a limit which is temperature independent. Additionally, the coil has to be enclosed in a dewar, increasing the distance between coil and sample. This separation reduces the filling factor and limits the improvement in SNR. In practice, the reduction in thermal noise by using cryoprobes at about 15K has reached sensitivity gains of only a factor of 4[142,143].

2.5.3 Pre-polarisation

The idea behind pre-polarisation is almost as old as MR research. In 1953 Packard and Varian[144] used a 10 mT pre-polarising magnetic field to enhance the net magnetisation of samples and observe their precession in the Earth's magnetic field. At the same time, Bloom and Mansir[145] used a similar pre-polarisation field to make measurements at around 0.2 mT. Pre-polarisation consists of pulsating a magnetic field B_p, which is stronger than the measurement field B_m, for a short period. During the time the pre-polarisation is active the nuclear spins tend towards a higher net magnetisation equilibrium state. Shortly after, the pre-polarisation field is removed and the MR signal is acquired at the lower field, as shown in Figure 11.

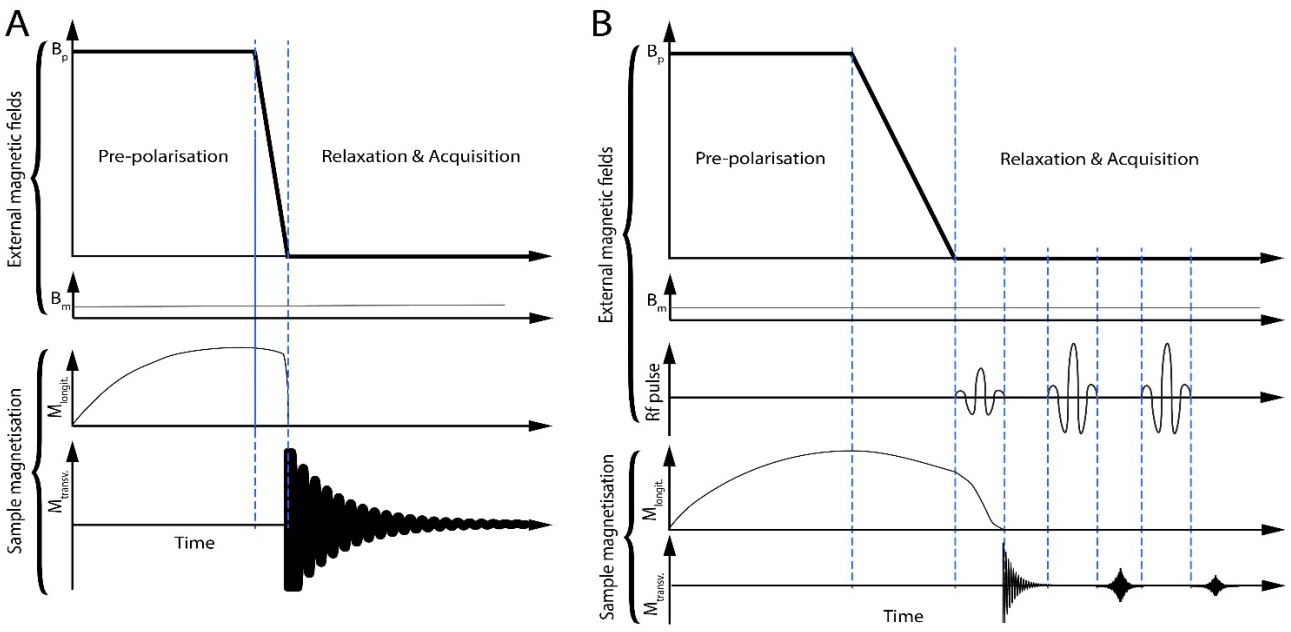

Figure 11: Schematic of typical pre-polarisation sequences. Direct acquisition of the FID is possible after a non-adiabatic removal of B_p (A). In this configuration, B_p is perpendicular to B_m. An adiabatic transition can be seen in (B). This configuration is independent of the alignment between B_m and B_p because the longitudinal magnetisation ends aligned with B_m after the transition. Rf pulses are used to induce the FID. A faster decay has been drawn visualising what would happen under the gradients of an imaging experiment. Echoes can refocus the transversal net magnetisation. Spin echoes are employed in this representation.

Pre-polarisation is a method to be used with weaker measurement fields to ideally increase the SNR from being proportional to $B_0^{7/4}$ to being proportional to $B_p \cdot B_m^{3/4}$. The SNR increase can be estimated by modifying Equation (47) and represent SNR as

$$\mathrm{SNR} = \frac{\xi}{\sqrt{\sigma_{body}^2 + \sigma_{coil}^2}} = \frac{B_0 B_P}{\sqrt{\beta B_0^2 + \alpha\sqrt{B_0}}} \propto \frac{\omega_0 M_0}{\sqrt{\zeta\omega_0^2 + \sqrt{\omega_0}}}. \qquad (50)$$

This ideal SNR improvement is lower in practice due to the signal decay during the transition from pre-polarisation to measurement. For this method to be efficient the acquisition needs to be performed before a significant amount of the net magnetisation is reduced by the MR relaxation mechanisms. To reduce these losses, the pre-polarisation field should be switched fast enough such that the spins do not follow the resultant external magnetic field (non-adiabatic transition), where B_p and B_m are perpendicular to each other, as shown in Figure 13. Figure 11A visualises the time sequence of this adiabatic induction. Nonetheless,

such a transition imposes a high demand on the electronics. Strong magnetic field changes can also induce eddy currents in neighbouring conducting surfaces and measurements result in additional noise. Inconveniently, the sequence becomes longer due to the need for pre-polarisation reducing imaging efficiency. Also, T_1 recovery times tend to be longer at higher fields, further prolonging pre-polarisation times. Moreover, there is no magnetisation growth during the readout time. This magnetisation decay makes sequences such as multi-slice or steady-state free precession imaging ineffective due to their reliance on longitudinal magnetisation recovery.

The potential benefits of the pre-polarisation technique are a decrease in magnet costs and power consumption. During pre-polarisation, the required field homogeneity is not critical. Therefore, the coils generating B_p can be smaller and can be placed closer to the patient. The result of which is a considerable reduction in the power requirements and less heat to dissipate from the coil.

Alternatively to acquiring the signal at a low magnetic field, one can leave the nuclear spins to experience the low fields for a limited time and then increase the field for the acquisition, as shown in
Figure 12[146]. This approach increases the sensitivity of the detector while still harvesting the benefits of the additional contrast mechanisms at low/ultra-low fields. This method is known as field cycling or fast field cycling. The method provides a mechanistic approach of exploring signals which evolve in a variety of fields without a need to retune the detector.

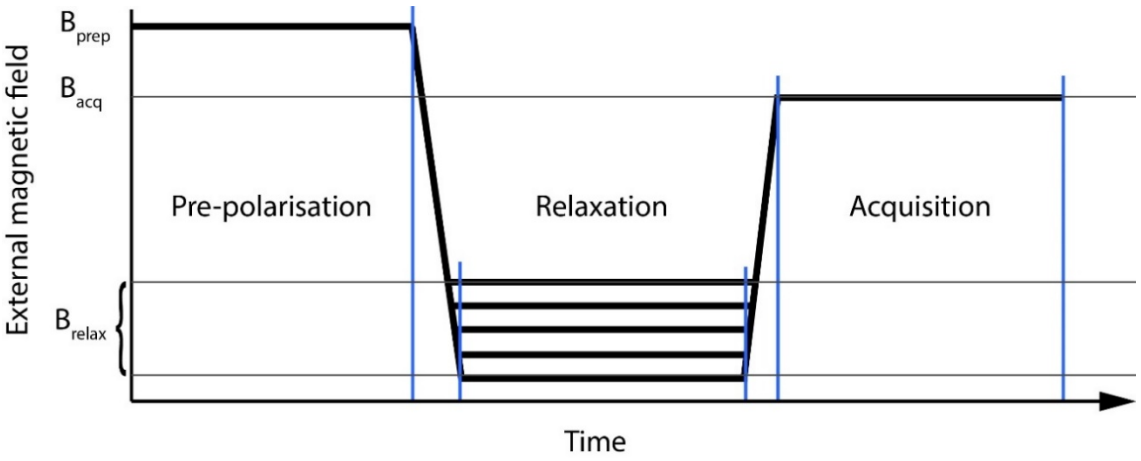

Figure 12: Simplified time diagram of typical field cycling MR sequence.

There are a variety of arrangements to generate the sequences presented in Figure 11. The main difference consists of how the pre-polarisation field is generated and oriented. For systems that produce B_p through permanent magnets, the sequence involves a physical translocation of the sample from the vicinity of the permanents magnets to the measurement

field B_m. This technique is not feasible for in-vivo ULF MR as the transportation time would be longer than the typical relaxation times of the nuclei. Therefore, existing human ULF MR systems employ resistive coils to generate both B_p and B_m. To reduce complexity, B_m is usually always on.

In some of the ULF MR arrangements, B_m and B_p generate parallel fields. This setup facilitates that the spins are aligned with B_m after the pre-polarisation regardless how B_p is removed. Nevertheless, in this arrangement B_m and B_p are highly coupled, which complicates the current control to maintain B_m stable as sudden changes in B_p will induce strong currents in the B_m coil[147].

The inductive coupling between coils can be significantly reduced by configuring the system in a way that B_m and B_p are perpendicular to each other. This arrangement has the advantage that if B_p can be removed fast enough to achieve a non-adiabatic transition, the most of the net magnetisation will be perpendicular to B_m, and the FID would immediately be measurable without the need for Rf pulses. To fulfil the non-adiabatic condition, the rotation of the resultant external magnetic field towards the final position, which in this case is parallel to B_m, has to be at all times substantially faster than the precession frequency of the spins. Therefore, a pure non-adiabatic transition through the removal of B_p is unfeasible because at the beginning of the B_p removal the angular frequency of the spins is very high and they can follow the rotation of the relatively slow resultant field generated by B_m and B_p. This will induce some signal loss. Differently, an adiabatic transition from B_p to B_m is easier to achieve as B_p is removed relatively slowly. Also, any eddy currents generated in nearby conductors are reduced. Conversely, the signal loss during the adiabatic transition due to T_1 relaxation can be significant, and Rf pulses are needed to tilt the net magnetisation away to generate transversal magnetisation.

In pre-polarised ULF MR, often a single FID will be acquired per pre-polarisation step. This acquisition scheme can be efficient as typically T_2* is as long as T_1 in this regime, making the most of the boosted net magnetisation. However, imaging involves the presence of gradients which shorten T_2*. In this case, acquiring multiple echoes per pre-polarisation cycle can help increase imaging efficiency.

2.6 Common ULF MR configurations

The variety of possible hardware arrangements to design a ULF MR system is large, as can be inferred from the diversity of the approaches that exist to generate magnetic fields, boost

the net magnetisation of the sample, and detect the MR signal. Practicality has, however, made some configurations more popular than others.

ULF MR systems typically use resistive coils to generate the measurement field and the gradient fields[11,15,20,24,30,46,47,102,132,147,148]. Measurement fields are generated by simple coil configurations, such as Helmholtz pairs, as the slower spin precession relaxes field homogeneity requirements. Instead of the cylindrical gradient coils common in high field systems, ULF MR systems often employ bi-planar coils, such as modified Maxwell pair configurations, to generate the gradient fields[46]. These open-access arrangements improve the accessibility to the system at the expense of reducing the power efficiency of the coils[46].

The pre-polarisation method is probably the most exploited signal boosting technique in in-vivo human ULF MR systems due to its simplicity and safety[15]. The pre-polarisation field is generated by relatively small but powerful resistive coils which are either cylindrically shaped or arranged in coil pairs[11,15,24,100,147]. This pre-polarisation field is often arranged perpendicular to the measurement field to reduce the coupling between the pre-polarisation and the measurement coils and facilitate the current control of the coils[15,24,100]. In cases involving small samples, generating the pre-polarisation field by permanent magnets placed away from the measurement field has been proposed. The sample is then sequentially transferred in a rapid manner from one field to the other[133,148,149]. In-vivo human imaging with no signal enhancing techniques other than optimised MR sequences extrapolated from high field systems has also been achieved recently employing a static field of 6.5 mT, which is towards the high field strength end of the ULF MR regime[46].

The magnetometers used for ULF MR largely depend on the application. SQUIDs are the dominant sensing technology used in most state-of-the-art human ULF MR systems[11,15,24,147]. This choice is driven by the high sensitivity of the SQUIDs in a broad frequency bandwidth, which opens up the possibility of concurrently acquiring magneto-encephalogram (MEG) and MR signals. These setups employ an array of SQUID detectors to increase the spatial resolution of MEG and exploit the reduction in acquisition time provided by parallel MRI. The complexity and costs of the SQUIDs have motivated the use of different room temperature resistive coil arrangements in systems aiming to provide an affordable solution[24,46].

Chapter 3 - Contributions *Vogel MW, Giorni A, Vegh V, Pellicer-Guridi R, Reutens DC. Rotatable Small Permanent Magnet Array for Ultra-Low Field Nuclear Magnetic Resonance Instrumentation: A Concept Study. PloS one. 2016 Jun 6;11(6):e0157040.*	
Contributor	Statement of contribution
Vogel MW	Conception and design (30%) Analysis and interpretation (35%) Drafting and production (40%)
Giorni A	Conception and design (20%) Analysis and interpretation (20%) Drafting and production (10%)
Vegh V	Conception and design (15%) Analysis and interpretation (5%) Drafting and production (15%)
Pellicer-Guridi R (Candidate)	Conception and design (15%) Analysis and interpretation (35%) Drafting and production (25%)
Reutens DC	Conception and design (20%) Analysis and interpretation (5%) Drafting and production (10%)

Chapter 3- Rotatable small permanent magnet array for ULF MR instrumentation: A concept study

3.1 Abstract

The feasibility of generating variable magnetic fields required for ultra-low field nuclear magnetic resonance relaxometry with dynamically adjustable permanent magnets is studied. The motivation is to substitute traditional electromagnets by distributed permanent magnets increasing system portability.

The finite element method (COMSOL®) is employed for the numerical small permanent magnet array design study to calculate achievable magnetic field strength and homogeneity, switching time and magnetic forces for ultra-low field relaxometry. A manual prototype is simulated and built to verify the magnetic field generation and validate the numerical approach.

A concentric small permanent magnet array can be used to generate strong sample pre-polarisation and variable measurement fields for ultra-low field relaxometry via simple prescribed magnet rotations. With the array it is possible to achieve a pre-polarisation field strength above 100 mT and variable measurement fields ranging from 20-50 µT with 200 ppm absolute field homogeneity within the field-of-view of 5 x 5 x 5 cubic centimetres.

A dynamic small permanent magnet array can generate the variety of multiple highly homogeneous magnetic fields required by ULF MR instruments. This design can significantly reduce the volume and energy requirements of traditional systems based on electromagnets considerably improving the portability.

3.2 Introduction

NMR and MRI are non-invasive and non-destructive investigative tools that can provide information from the molecular to the macroscopic scale. These techniques harness the phenomenon of magnetic resonance due to the interaction of precessing nuclear magnetic moments (nuclear spin systems) within a magnetic field with electromagnetic radiation. MR has a wide range of applications in areas including materials science, structural biology, chemistry and medical imaging[150-152].

Conventional MRI instruments comprise three main components: a permanent magnet to align the nuclear spins and generate net sample magnetisation; a transmitter/receiver coil system that radiates electromagnetic energy to the nuclear spin system and detects the MR

signal; and gradient coils that enable the encoding of spatial information allowing the generation of three dimensional images[151].

The signal-to-noise ratio (SNR) achieved in MR is proportional to the magnitude of net sample magnetisation. Hence, the quality of MR data is dependent on the strength and high absolute field homogeneity of the main magnetic field (commonly referred to as $\mathbf{B_0}$). Current efforts have concentrated on increasing field strength with superconducting coils that increase the bulk and cost of purchase, operation, and maintenance of MR instruments.

Partly in response to these drawbacks, over the last decade, there has been growing interest in ULF MR, which uses a main magnetic field strength of less than 10 mT[12,15,20,23,25,28,29,153-155]. Potential advantages of ULF over high field MR instruments include greater absolute magnetic field homogeneity, simple and low-cost instrumentation and low power consumption[156]. ULF MR offers the possibility of important new applications such as the ability to image in the presence of metal, for example in trauma, disaster and battlefield applications. Yet to be explored imaging paradigms based on the frequency overlap of the ULF instrument with the Eigenfrequencies may allow real-time interrogation of 'slow' kinetic processes in chemistry and biology, such as diffusion or protein folding and aggregation[15]. In addition, because superconducting magnets are not required, the instruments may be more portable allowing ULF instruments to be more readily transported to and operated in remote locations[15].

Although based on the same fundamental principles of magnetic resonance as high field MR, ULF instruments are set up differently. Prior to the measurement, sample magnetisation is generated by a pulsed magnetic field approximately three orders of magnitude higher than the Earth's field (~ 0.05-0.1 T). This technique is known as sample pre-polarisation and is one of the main strategies in ULF research (besides implementing highly sensitive magnetometers) to overcome low SNR which still severely restricts ULF-MR applications[15,23,29]. Radiofrequency pulses are not required to trigger the ULF-MR signal. Instead, the ULF-MR signal is generated and detected in the presence of a second magnetic field, the measurement field, and applied perpendicular to the pre-polarisation field.

Currently, the magnetic fields in ULF-MR instruments are generated using resistive coils, which high power consumption and heat production[15,20,28,157]. Moreover, the presence of highly conductive materials in resistive coils contributes to signal loss due to sample heating effects, residual coil noise, transients and eddy currents, and destructive interference

effects[15,20,158]. These problems motivate the search for alternative ways of generating strong magnetic fields with *Halbach* arrays.

Halbach arrays are a versatile arrangement of permanent magnets to generate highly homogeneous and strong magnetic fields generally achievable in small sample volume or field of view (FOV) compared to overall array volume[159-161]. This condition, however, is fulfilled for MR instruments and *Halbach* array technology has lead to the development of new generations of benchtop and handheld MR instruments, with field strength above 3T and inhomogeneity of less than 0.01 % (100 ppm)[62,159,162,163].

Permanent magnets do not require electric current flow to generate magnets fields. Hence, sample heating due to energy dissipation in the resistive material is avoided, cooling devices obviated and power consumption significantly reduced compared to resistive coil technology. Moreover, magnetic material conductivity is much lower compared to resistive coil material like copper, hence, eddy current effects induced by rapid magnetic field changes, and therefore, potential possible signal artefacts and noise are reduced.

Despite the FOV size restraints, a *Halbach* array has recently been introduced in a prototype portable MRI scanner suitable for human brains (FOV = 16 cm) to generate the low field ($\mathbf{B_0}$ = 77 mT)[19]. The static field $\mathbf{B_0}$ within the volume is quite inhomogeneous, almost 1% (~10000 ppm), due to the presence of fringe fields originating from both ends of the *Halbach* array (length and diameter ~ 36 cm) and the chosen FOV. However, the known field characteristics of $\mathbf{B_0}$ was exploited to encode spatial information, but it required the rotation of the *Halbach* array about the sample to acquire a 2D image[19].

The static nature of the magnetic fields generated by *Halbach* arrays implies that current flows, resistive coil technology, and radiofrequency (Rf) devices are still essential for triggering or generating signals and gradients in all current designs of MR instruments with *Halbach* arrays.

Our new approach is an extension of the concept of the *Halbach* array that obviates the need for resistive coils for low and ULF MR by introducing a dynamic adjustable small dynamic permanent magnet array (SPMA) to generate and switch between multiple magnetic fields. A variety of gradient fields is achieved by prescribed rotations of individual magnets which allows adjustments of magnetic field magnitudes and orientations.

In this study, we examine the potential of SPMAs for ULF-NMR relaxometry, an imaging and scanning paradigm to study the relaxation processes of samples. At ULF, this has the potential to allow the study of slow molecular dynamic processes in real time, for instance, to detect liquid explosives [15,164]. Aforementioned is enabled by the generation of highly homogeneous magnetic fields with moderately complex setups with the potential of possible control of magnetic field magnitude and hence, control of the Larmor frequency[15,164].

By applying the finite element method (FEM) to Maxwell's equation, we determined the magnetic fields generated by the dynamic SPMA and analysed it in terms of achievable field strength and field homogeneity. In addition, a manual operated SPMA was simulated and built to demonstrate the ability to generate the magnetic fields required for ULF relaxometry.

3.3 Materials and methods

3.3.1 ULF relaxometry

A ULF relaxometry instrument for measuring the sample longitudinal (T_1) and transversal relaxation (T_2) time, which depends on the applied magnetic field[150,151], requires *two* perpendicular and dynamic switchable magnetic fields: the pre-polarisation field $\mathbf{B_p}$ and the measurement field $\mathbf{B_m}$. A schematic representation of the application of $\mathbf{B_p}$ and $\mathbf{B_m}$ to perform a basic ULF relaxometry measurement is shown in Figure 13: The pulsed $\mathbf{B_p}$ (Figure 13A) with magnitudes typically ranging from 30 - 70 milliteslas (mT) generates the net sample magnetisation **M**, according to Curie's law (Figure 13A). The orientation and the magnitude of $\mathbf{B_m}$ define the precession axis of **M** and the Larmor frequency, respectively (Figure 13C). After $\mathbf{B_p}$ is switched off, the precession of **M** about $\mathbf{B_m}$ generates the sample signal known as free induction decay (FID) and is detected by the sensor (S) (Figure 13D). The duration and measurability of the FID depend on the demagnetisation characteristics of the sample and, on sensor location and orientation[158].

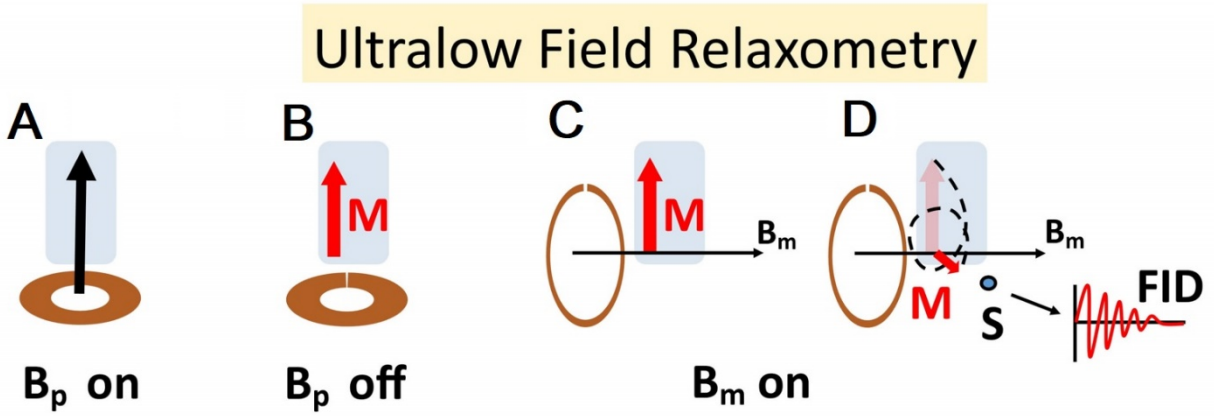

Figure 13: Schematic presentation of a ULF relaxometry measurement. (A) The pre-polarisation coil is switched on to generate $\boldsymbol{B_p}$*. (B) After switching off of pre-polarisation coil sample a net magnetisation* ***M*** *is induced. (C) The measurement field* $\boldsymbol{B_m}$*, perpendicular to* $\boldsymbol{B_p}$ *is switched on. (D) The net magnetisation vector* ***M*** *precesses about* $\boldsymbol{B_m}$ *and decays; the sample demagnetises. The localised magnetic field sensor (****S****) detects the sample signal (FID) during demagnetisation.*

3.3.2 SPMA design

The dynamic SPMA exemplified for ULF relaxometry presented in this manuscript is shown in Figure 14. It consisted of cylindrical magnets of finite length, transversely magnetised (i.e. in the *x-y* plane) arranged in three concentric cylindrical arrays as indicated in Figure 14A. Each magnet of array *A* was assumed to be pivot-mounted about the z-axis to allow the generation of various magnetic field configurations by prescribed rotations of each magnet. In contrast, the orientation of each magnet within array *B* and *C* was fixed but the two arrays can rotate about the z-axis, see Figure 14B.

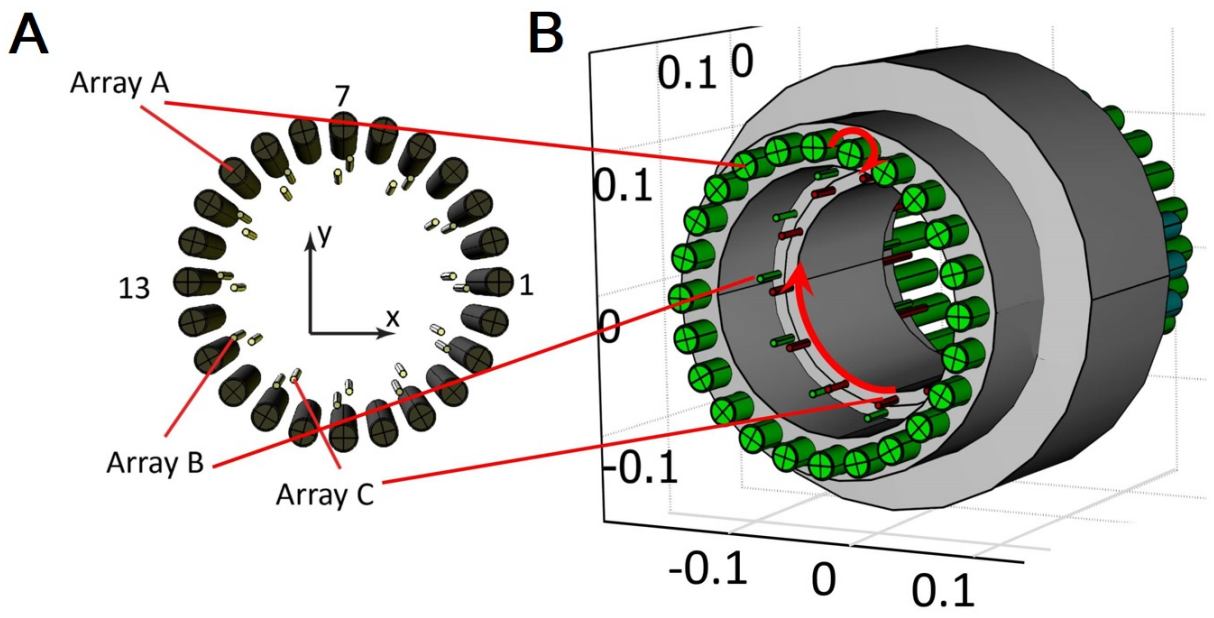

Figure 14: Setup of the dynamic SPMA model for ULF relaxometry. (A) The SPMA model consists of three concentric cylindrical arrays with transversally (x-y plane) magnetised rods. Array A, required for pre-polarisation, consists of 24 magnets; Arrays B and C, required for generating the variable measurement field, consist of 12 magnets each. The z-axis is parallel to the array symmetry axis. Numbering is counter-clockwise from the right-hand side. (B) Side view indicating the concentric SPMA setup and sizes. Array A is fixed but each magnet rotates individually about the z-axis (small red circular arrow). Arrays B and C (with fixed magnet orientation) rotate about the z-axis, indicated by the large red circular arrow.

Our SPMA design is based on the principle of generating highly homogeneous and strong magnetic field generation by a *Halbach* dipole cylinder or *Halbach* array [62]. The three concentric cylindrical arrays, *A*, *B,* and *C* generate the two mutually perpendicular magnetic fields required for ULF relaxometry measurements: $\mathbf{B_p}$ (array *A*) and $\mathbf{B_m}$ (array *B* and *C*). Throughout this paper, it is assumed that $\mathbf{B_p}$ is oriented along the *x*-axis and $\mathbf{B_m}$ along the *y*-axis. Each cylindrical magnet within the SPMA is transversally magnetised (x-y plane) with remanent magnetisation $\mathbf{B_r}$. The following parameters were used when designing the array: field of view (FOV) within the centre of the SPMA 5 x 5 x 5 cm^3; $\mathbf{B_p}$ magnitude >100 mT; $\mathbf{B_m}$ magnitude between 20-50 µT. The FOV was chosen to be sufficient both for ULF-NMR measurements and for a small ULF imaging device. $\mathbf{B_m}$ corresponds to the proton (^{1}H) Larmor frequency ω_L as determined by the Larmor equation

$$\omega_L = 2\pi f_L = \gamma B_m, \quad (51)$$

with the units for ω_L being rad/sec and f_L being Hz, respectively. And γ is the gyromagnetic ratio, 42.6 MHz/T or 2.678 x 10^8 rad/(T x sec) for protons.

3.3.3 Magnetisation pattern

Four different magnetisation patterns were considered in this study, created by prescribed rotations of each cylindrical magnet in the array *A* shown in Figure 16, with $\mathbf{B_r}$ of each magnet indicated by white arrows: *Halbach* (Figure 15A), *reverse Halbach* (Figure 15B), *transverse* (Figure 15C) and *radial* (Figure 15D). The *Halbach* pattern is known to achieve a strong homogeneous magnetic and directional field in the centre of the array *A*, while the lowest field strength or field cancellation (indicated by irregular field distribution in the centre) is achieved with the *reverse Halbach*, *tangential* or *radial* magnetisation patterns. Different magnetisation patterns and numbers of permanent magnets in the array lead to different magnetic field distributions, field strength, and homogeneity in the centre of the array. All of these variations affect suitability for ULF relaxometry measurements. A study on the impact of such effects is provided in the following sections.

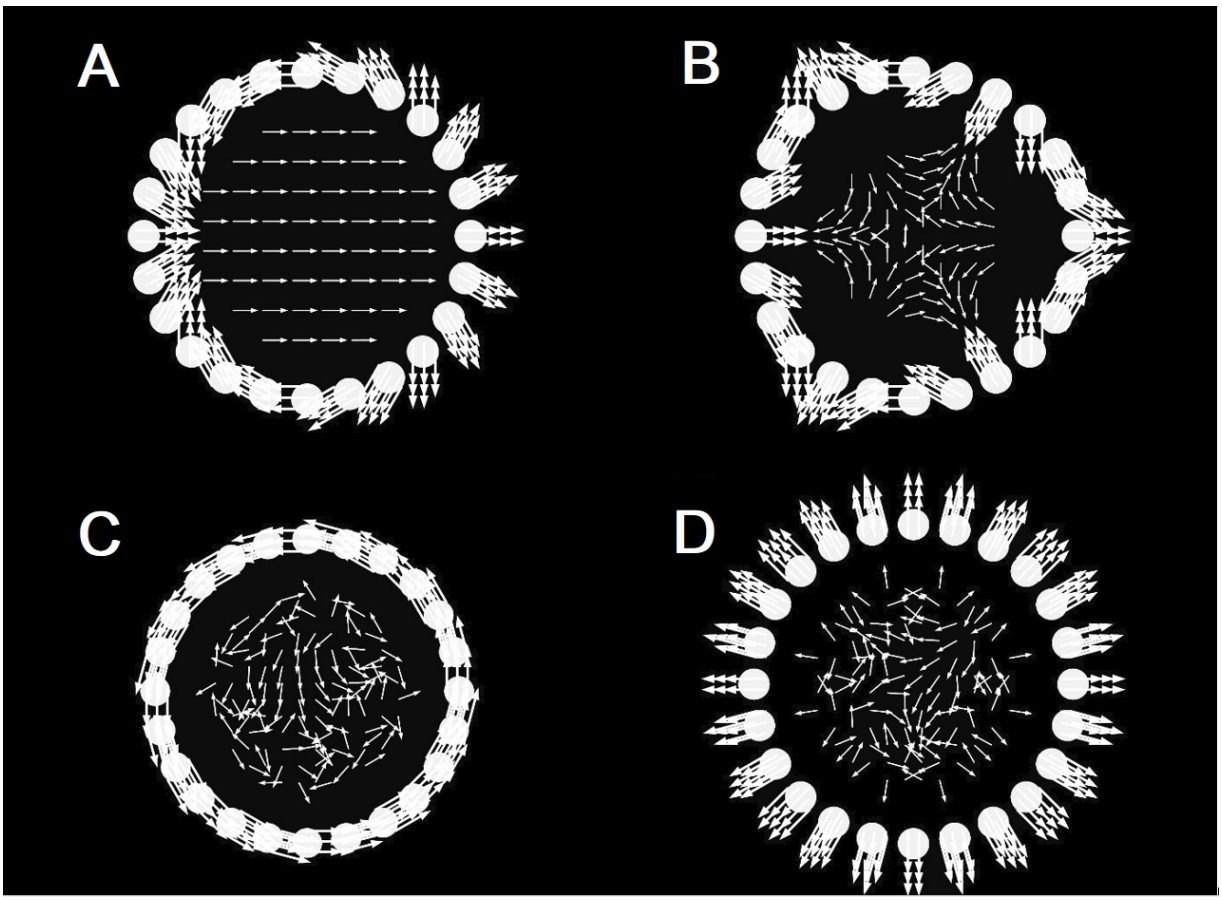

Figure 15: Definition and visualisation of the magnetisation patterns, formed by transversally magnetised cylindrical magnet array, considered in this study. (A) Halbach*, (B)* reverse Halbach*, (C)* tangential *and (D)* radial*. Shown as vector plots are the magnet remanent magnetisation (thick white arrows) and the normalised magnetic field distribution (thin white arrows) within the SPMA centre. The* Halbach pattern *leads to a highly directional and amplified magnetic field, while the other pattern leads to irregular, non-directional and nearly field cancellation. The detailed magnetic field characteristics for each magnetisation pattern are presented in Figure 19-Figure 22.*

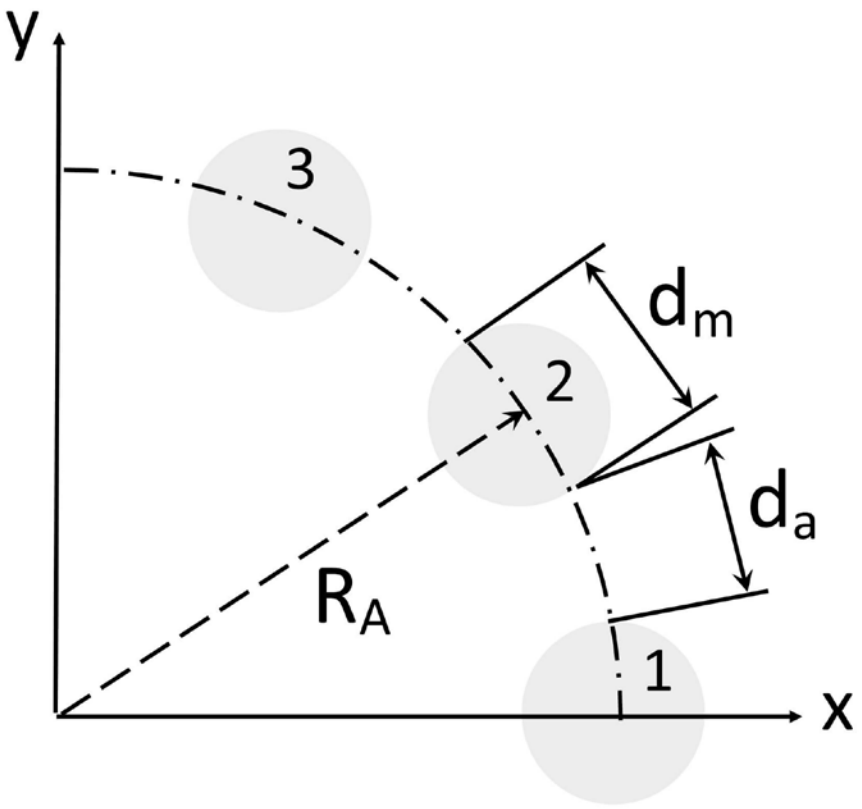

Figure 16: Section of an array with radius R_A. Each cylindrical magnet numbered counterclockwise and with diameter d_m, is evenly arranged along the circumference to ensure equidistant air gaps. The fill factor is defined as the ratio between d_m and d_a. In this example d_m equals d_a and the fill factor is 0.5.

3.3.4 Simulation environment

The complexity of the fields associated with different conformations of the SPMA precluded an analytical approach. Hence we undertook a rigorous numerical analysis using COMSOL® (version 4.3b, AC/DC module), a commercial finite element method (FEM) simulation environment with a computer-aided design interface for 3D model design. In the FEM simulation, the SPMA model was discretised in 3D-tetrahedral meshes within the computational window using a mesh distribution and density predetermined by COMSOL. The number of mesh points generally ranged between 40-50 million, to achieve sub-millimeter spatial resolution in the centre of the array and to ensure convergent and accurate results within reasonable time frames. The computational window was set at a size sufficient to minimise numerical errors due to discontinuities. Numerical boundary conditions were defined as magnetic shielding thickness d = 12 cm and material permeability μ_r = 5500,

corresponding to the shielding for the previously described ULF device developed at the Centre for Advanced Imaging [158].

3.3.5 Pre-polarisation array (array A) for ULF relaxometry

The outer Array *A* which generates $\mathbf{B_p}$, had an assumed fixed radius R_A = 11cm and array length *L* = 70 cm. It consisted of *n* identical cylindrical magnets each with a remanent magnetic field strength of 1 Tesla (T). Notably, other common and commercially available magnet cross-sections lead to the equivalent qualitative results provided that the magnet size is small compared to the distance to the centre of the array. An ideal *Halbach* array is characterised by a continuous change in azimuthal magnetisation vector direction, which at present cannot be achieved. Hence, cylindrical *Halbach* arrays are discretised by identical magnets with constant $\mathbf{B_r}$ with the approximation generally improved by increasing magnet numbers along the circumference. In this study *n* = 12, 16 and 24 magnets were considered.

The array radius R_A was chosen to be fixed to ensure that the SPMA fits within the magnetic shielding device developed at our centre for advanced imaging (CAI). Hence, to allow the SPMA performance to be compared with different numbers of magnets while keeping the overall size constant, a fill factor was introduced which quantifies the ratio of magnetic material to air gap (d_m to d_a) along the circumference (see Figure 16). A fill factor of 0.75, for instance, corresponds to 75% occupation by the magnet (d_m) and 25% by air (d_a) along the circumference, as seem from the centre. This implies that the magnet diameter d_m is dependent on the total magnet number *n* and is approximately

$$d_m = 2\pi \frac{Fillfactor \cdot R_A}{n}. \quad (52)$$

3.3.6 Measurement array (arrays B and C) for ULF relaxometry

The measurement field $\mathbf{B_m}$ was generated by superimposing two magnetic fields generated by arrays *B* ($\mathbf{B_B}$) and *C* ($\mathbf{B_C}$) with radii R_B = 8 cm and R_C = 9 cm, respectively, each with the fixed *Halbach* pattern. Similar nested bipolar Halbach array arrangements which generate adjustable static magnetic fields can be found in[165,166]. As with the pre-polarisation array *A*, this arrangement ensured a highly directional and homogeneous magnetic field along the y-axis. The total magnetic field magnitude within the FOV was almost compensated when (a) the magnetic field magnitudes $\mathbf{B_B}$ and $\mathbf{B_C}$ are matched and (b) the directions are opposite (Figure 17A). By rotating arrays *B* and *C* simultaneously clockwise and counter clockwise

about the *z*-axis, the *x*-components of the magnetic field near the centre was still cancelled, but a net y-component was generated representing the measurement field $\mathbf{B_m}$ (Figure 17B).

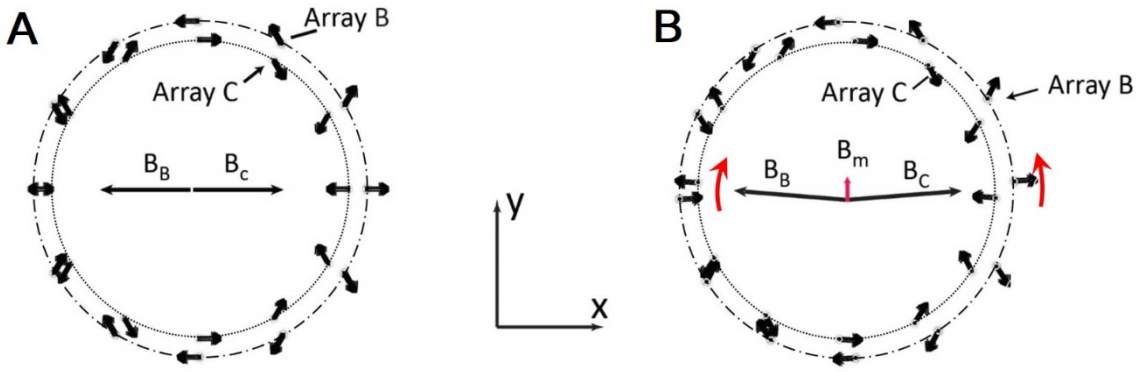

Figure 17: Principle of generating B_m simulated with COMSOL. (A) Two concentric arrays B *and* C *(R_B = 9 cm and R_C = 8 cm), each with Halbach magnetisation pattern (see Figure 15A), generate the opposite magnetic fields $\boldsymbol{B_B}$ and $\boldsymbol{B_C}$ at the centre. If their magnitude is matched, the field in the centre is nearly cancelled. (B) By rotating array* B *and* C *simultaneously clockwise and counterclockwise about the SPMA symmetry axis (see red arrows), the x-component of the magnetic field is still cancelled but the y-component, $\boldsymbol{B_m}$, is generated.*

The accuracy of ULF relaxometry measurements depends strongly on achievable magnetic field strength, its directionality and absolute field homogeneity which determine signal strength, quantified by the signal-to-noise ratio (SNR) [20]. Qualitative targets to optimise the performance of the ULF relaxometer are:

- highly directional and maximum magnitude of $\mathbf{B_p}$ during sample pre-polarisation (*switched on*).
- minimum magnitude for $\mathbf{B_p}$ during the measurement period.
- highly directional and homogeneous *variable* measurement field $\mathbf{B_m}$ (arrays *B* and *C*).

3.3.7 Manual SPMA

A manually operated SPMA was built to demonstrate the generation, cancellation and regulation of $\mathbf{B_p}$ and $\mathbf{B_m}$. Like the SPMA for ULF relaxometry in the numerical study, the prototype consisted of three concentric arrays to generate the pre-polarisation field, $\mathbf{B_p}$ (array *D*), and the measurement field, $\mathbf{B_m}$ (array *E* and *F*), see Figure 18. The manually adjustable arrays were composed of ferrite permanent magnets of rectangular cross-section (ferrite grade Y30BH, B_{rem} = 0.39 T, AMF Magnetics, Australia) chosen for their cost-

effectiveness, availability and simpler alignment abilities. Array *D* (Figure 18A, array I and II) had a radius R_D = 15 cm consisting of 12 magnets (15L x 2.5W x 2.54H cm) equally spaced around the circumference achieving a fill factor of 0.32. Twelve magnets (15L x 1.2W x 0.6H cm) composed the array *E* (R_E = 10.5 cm, Figure 18A, array III) and 6 magnets (15L x 1.2W x 0.6H cm) the array *F* (R_F = 7.5 cm, Figure 18A, array IV), leading to fill factors of 0.16 and 0.11, respectively. For each array, the magnets were pressure fitted in pairs of interconnected medium density fibreboard (MDF) rings that hold the bar magnets from both extremes of their length. The moderate magnetisation of the ferrite magnets allowed safe manual rotations of the arrays, and the fitting of the different diameter MDF rings kept the relative position of each array in place (Figure 18B). Two manually interchangeable frames for array *D* were built to hold the magnets for two different configurations: *tangential* (for measurement state) and *Halbach* (for sample pre-polarisation), see Figure 18A, arrays I and II.

A Gaussmeter (F.W. Bell, model 5080, Milwaukie, USA) mounted on a custom built 3-axis adjustable Cartesian holder was used for the magnetic field measurements, taken equidistantly in a grid (5 x 5 x 3, *x*,*y*,*z*) covering the FOV (5 x 5 x 5 cm^3) for 3 different angular settings (α = 0°, 5°, and 10°, see Figure 18B). The values obtained at each point were averaged for each angular setting.

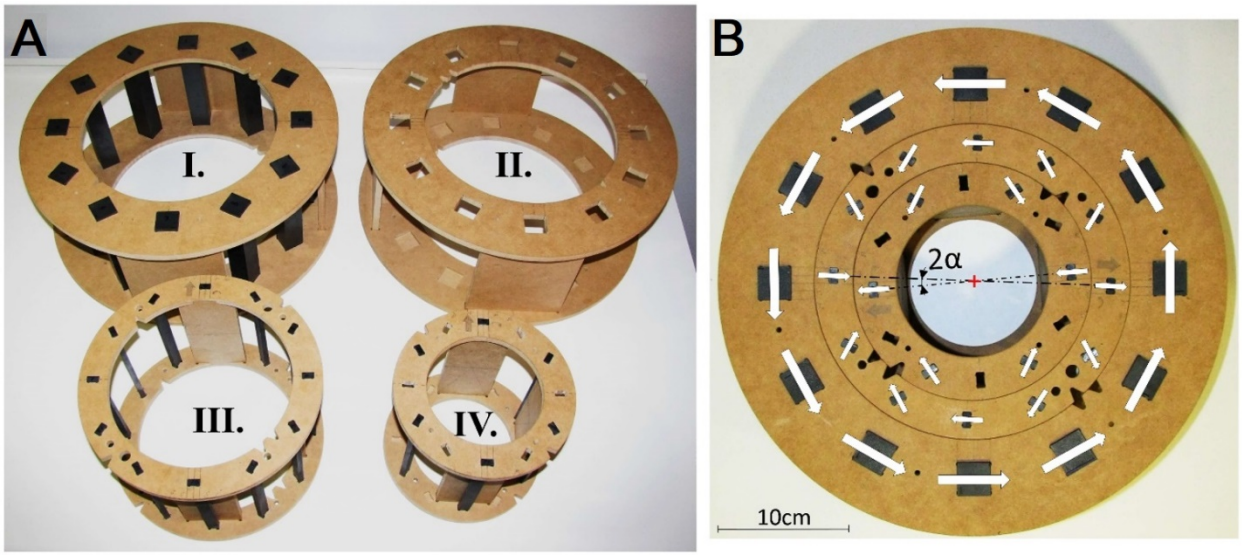

Figure 18: Built SPMA prototype. (A) Elements of the SPMA prototype shown separately: Array D *with* Halbach *pattern (I) and* tangential *pattern (II), array* E *(III) array* F *(IV) each with* Halbach *pattern. Array* D *magnets are fitted in the MDF frame I or II to achieve* $\boldsymbol{B_p}$ *ON or* $\boldsymbol{B_p}$ *OFF configurations, respectively. (B) Arrays* E *(III) and* F *(IV) fitted inside array* D *with* tangential *pattern (II).* $\boldsymbol{B_m}$ *magnitude control is achieved by rotating arrays* E *(III) and* F *(IV)*

in opposite directions with prescribed angles α. The white arrows indicate the magnetisation direction of each magnet

3.4 Results

3.4.1 SPMA for ULF relaxometry – Numerical simulation

Array A during pre-polarisation ('switched on'): The magnetic flux density distribution of Array *A* during pre-polarisation ($\mathbf{B_p}$) generated with the *Halbach* pattern (see Figure 15A) is presented as *x-y* cross-section surface plot in Figure 19A. Regions of high field intensities are indicated by white, regions of low field intensity by black, and light grey disks visualise the FOV. In the same figure, an arrow plot shows the local field direction of $\mathbf{B_p}$ along the x-axis. In this surface plot arrays *B* and *C* are not visible since $\mathbf{B_p}$ produced by array *A* is more than 1000 times larger than $\mathbf{B_m}$.

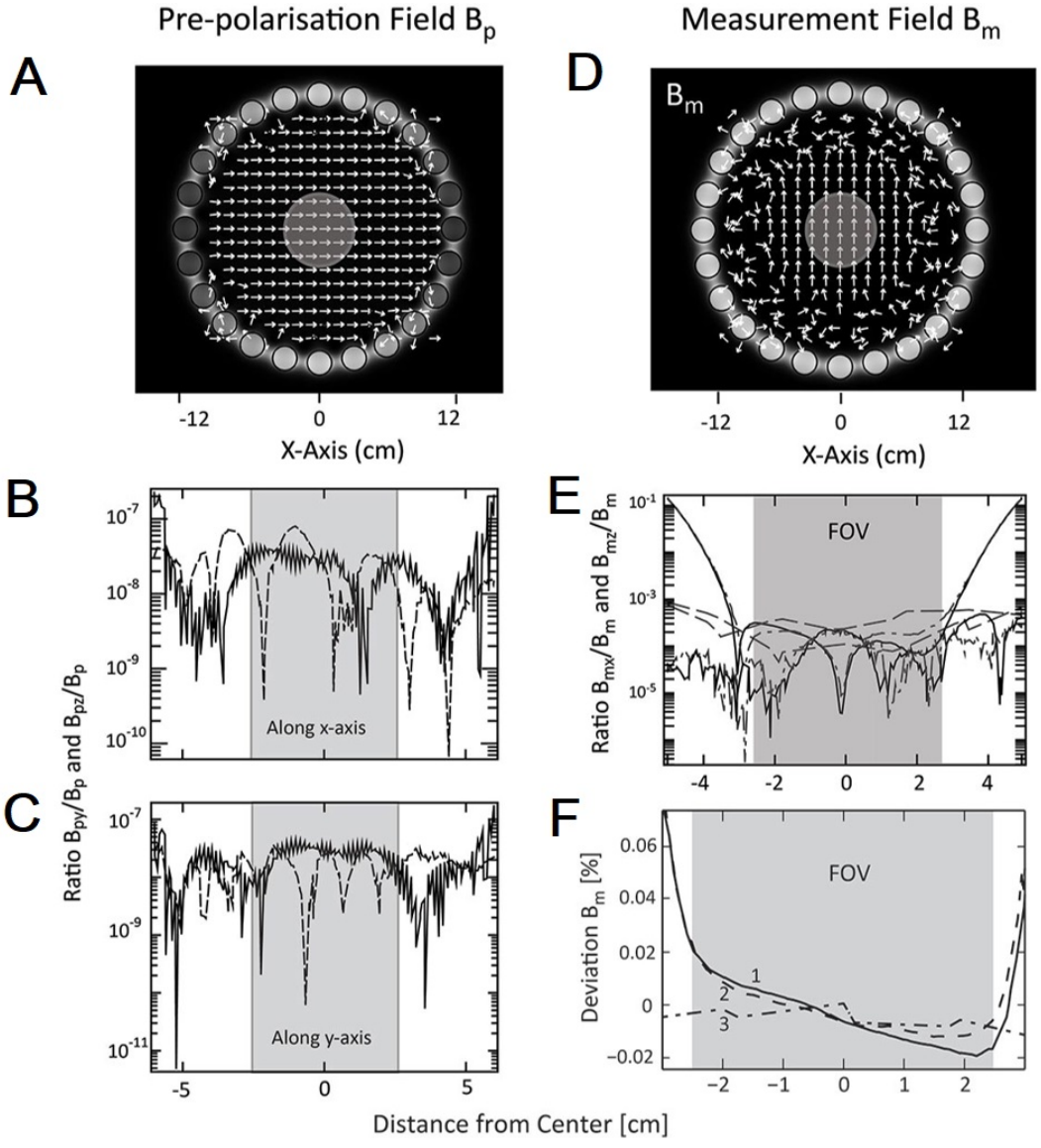

Figure 19: Surface plot magnitude and direction of the magnetic flux density of an SPMA. Magnetic flux (A) during pre-polarisation ($\boldsymbol{B_p}$) and (D) measurement state ($\boldsymbol{B_m}$). Regions of high and low field intensity are shown as white and black. Cross-section plots through the point of origin along the x-axis (B) and y-axis (C) of the ratio $\boldsymbol{B_{py}/B_p}$ (solid line) and $\boldsymbol{B_{pz}/B_p}$

(dashed line). B_{py} and B_{pz} are the y- and z-components of the pre-polarisation field B_p (= B_{px}). B_{py} and B_{pz} are at least six orders of magnitude smaller in all directions within the FOV. Plots along the z-axis were omitted since all ratios are well below 10^{-9}. (E) Cross-sections of all ratios B_{mx}/B_m and B_{mz}/B_m along the x-axis (solid line), y-axis (dashed line) and z-axis (dash-dotted line) demonstrating the x and z-component of the resultant magnetic field, generated by arrays A, B *and* C*, are at least three orders of magnitude smaller than B_m (F). Deviation in per cent from measurement field magnitude of B_m, plotted along the x-axis (curve 1, solid line), y-axis (curve 2, dashed line) and z-axis (curve 3, dash-dotted line). Arrays* B *and* C *were rotated by ~4.5° to achieve a magnitude of 40 µT.*

The directionality and homogeneity of $\mathbf{B_p}$ were assessed by the ratio of the minor field component ($\mathbf{B_{py}}$, $\mathbf{B_{pz}}$, along *y*- and *z*-axes) to the main component of $\mathbf{B_p}$ (along the *x*-axis). Figure 19B-C show cross-section plots of the magnetic flux density ratios $\mathbf{B_{py}/B_p}$ (solid lines) and $\mathbf{B_{pz}/B_p}$ (dashed lines) along *x* and *y*, validating that $\mathbf{B_{py}}$ and $\mathbf{B_{pz}}$ were at least six orders of magnitude smaller, hence demonstrating the high directionality of $\mathbf{B_p}$ along the *x*-axis. The plots along the z-axis were omitted since the ratios and the minor components are even smaller.

Table 2: Achievable magnetic field strength at the centre of array A and field inhomogeneity within the field of view (FOV) during pre-polarisation for varying number of magnets and fill factors calculated with COMSOL.

Number of magnets	Fill factor	Centre Field strength [mT]	Field inhomogeneity within the FOV [%]
12	0.75	214.58	Less than 0.02 (200 ppm)
16	0.75	162.56	Less than 0.02 (200 ppm)
24	0.75	109.15	Less than 0.02 (200 ppm)
16	0.5	76.29	Less than 0.02 (200 ppm)
12	0.375	54.51	Less than 0.02 (200 ppm)

Twelve, 16 and 24 magnets with a fill factor of 0.75, 12 magnets with a fill factor of 0.375 and 16 magnets with a fill factor of 0.5 were analysed to study the effect of these parameters on achievable pre-polarisation field inhomogeneity and magnitude variation across the FOV. The results are summarised in Table 2 and shown as cross-section plots in Figure 20. The solid line plots correspond to 12 magnets, dashed line plots to 16 magnets and dash-dotted plots to 24 magnets. For a constant fill factor of 0.75, the achievable field strength increases with decreasing magnet number, as illustrated in Figure 20A, because of the greater magnet surface and volume, according to Equation (52). In contrast, by reducing the fill factor, or

equivalently the number of magnets, the achievable pre-polarisation field strength decreased assuming constant magnet size, as shown in Figure 20B. However, in all cases, the magnetic field variation of $\mathbf{B_p}$ remains below 0.02% (200 ppm), as demonstrated in Figure 20C-D. The high field homogeneity is due to the combination of a small FOV compared to the large volume of the SPMA and the increased number of permanent magnets. Figure 21 illustrates the relative magnitude variation of $\mathbf{B_p}$ in three dimensions for n = 24 magnets (fill factor 0.75) with respect to the magnitude at the centre plotted along the *z*-axis in 2 cm steps on the *x*-*z* (Figure 21A) and *y*-*z* planes (Figure 21B) demonstrating the high field homogeneity within the whole volume of the FOV.

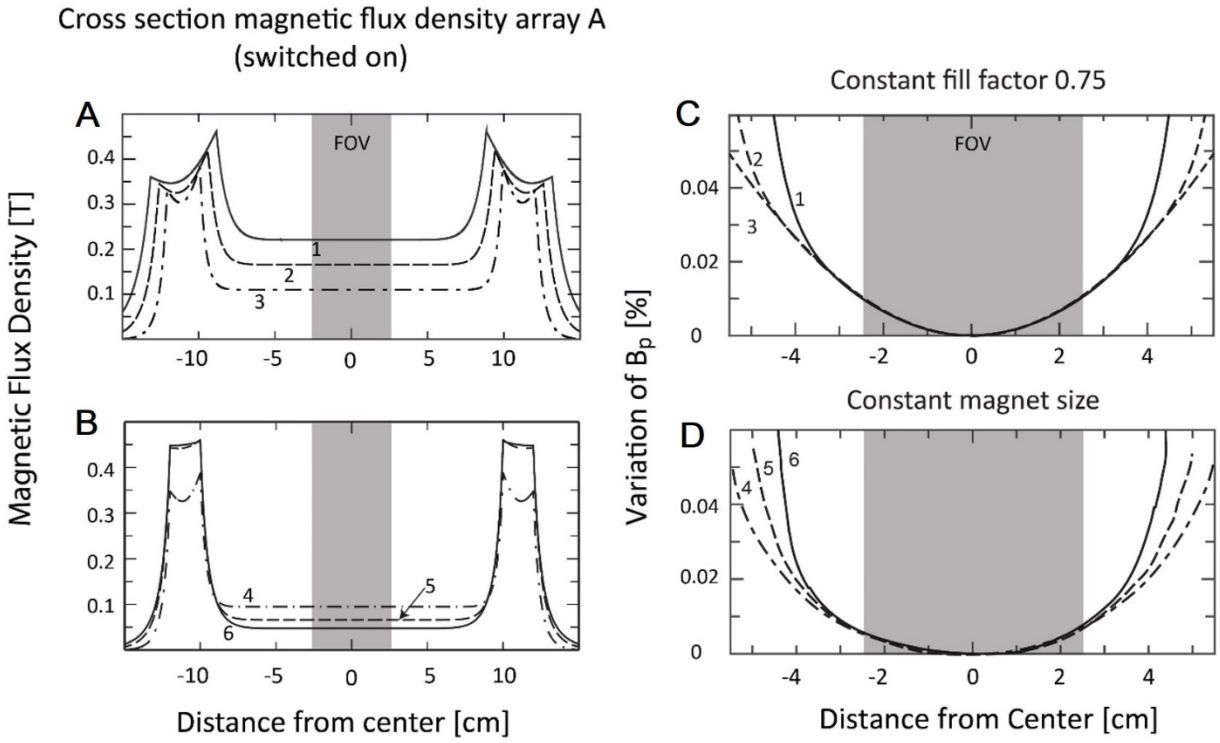

Figure 20: 2D-Cross-section plots of pre-polarisation field B_p along the x-axis (switched on). For array A *with constant fill factor, curve 1 (solid line) corresponds to 12 magnets, curve 2 (dashed line) to 16 and curve 3 (dash-dotted line) to 24 permanent magnets. For array* A *with constant magnet dimensions (L = 70 cm, d_m = 2.16 cm), curve 4 (dash-dotted line) corresponds to 24 magnets, curve 5 (dashed line) to 16 and curve 6 (solid line) to 12 permanent magnets. (A) In array A with constant fill factor 0.75, the field strength within the field of view (FOV) decreases with magnet numbers, since magnet volume and surface area increase. (B) For array* A *with constant magnet size, the field strength decreases with decreasing numbers of magnets. (C) Within the FOV the field inhomogeneity slightly decreases with decreasing magnet numbers for constant fill factor (C) and constant magnet size (D). In all cases, the field inhomogeneity within the FOV is well below 0.02 % (200 ppm).*

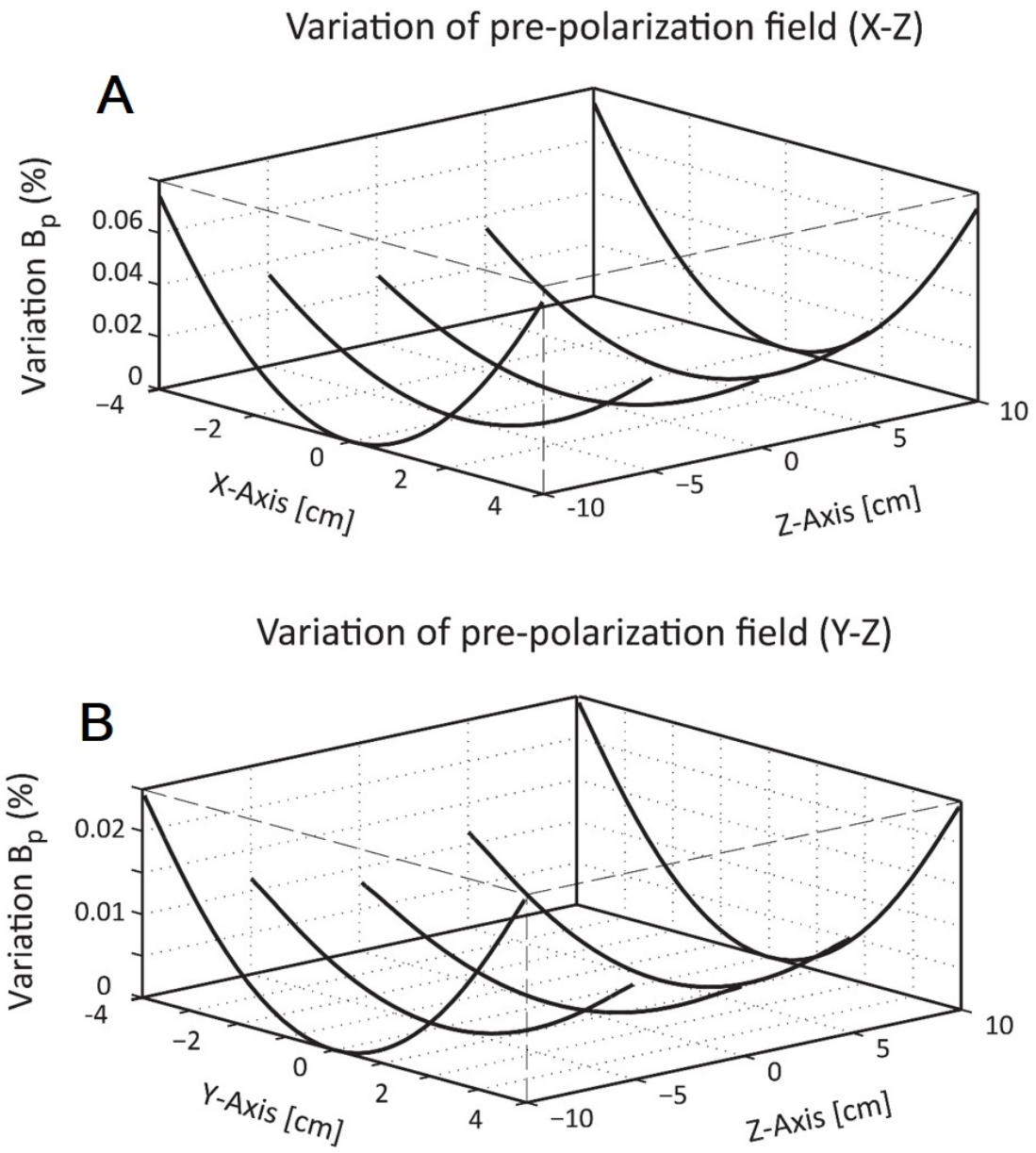

Figure 21: Relative magnitude variation of the pre-polarisation field, B_p, generated by array A *with 24 magnets. Field inhomogeneity shown as line plots in z = 2 cm steps along the x-axis (A) and y-axis (B). Plotted are magnitude deviations from the magnitude of* $\boldsymbol{B_p}$ *at the centre of the array in per cent. Within the chosen FOV of 5 x 5 x 5 cm³, the inhomogeneity is less than 0.02% in all cases.*

Array A after pre-polarisation ('switched off'): During the measurement period, the magnetic field within the centre of the SPMA produced by array *A* must be minimised to enable precession and relaxation of the sample magnetisation vector. This field cancellation was achieved by rotating each magnet of array *A* from the *Halbach* pattern (Figure 15A) to one of the three possible magnetisation patterns considered in this study, the *reverse Halbach* (Figure 15B), *radial* (Figure 15C) or *tangential* (Figure 15D). Figure 22 illustrates cross-section plots of the magnetic flux density generated by these magnetisation patterns with the FOV indicated by the grey shaded area. Only the *tangential* pattern enabled field cancellation to magnitudes below 1 µT within the FOV (Figure 22C). The residual magnetic field magnitude generated by array *A* is low enough ($< 10^{-8}$ T for 16 or 24 magnets, see Figure 22C) to ensure no interference with the measurement field $\mathbf{B_m}$ (20-50 µT). The area where the magnitude of the magnetic flux density generated by array *A* was below 1 µT, widens with the number of magnets (see Figure 22C). A similar effect was observed during pre-polarisation with the *Halbach* pattern (Figure 20) and is expected since the SPMA, as an approximation of an ideal *Halbach* array, generally improves as the number of magnets increases. From Figure 22C, it can be concluded that 16 (curve 2) or 24 cylindrical magnets (curve 3) are suitable to ensure minimum interference from array *A* during the measurement period.

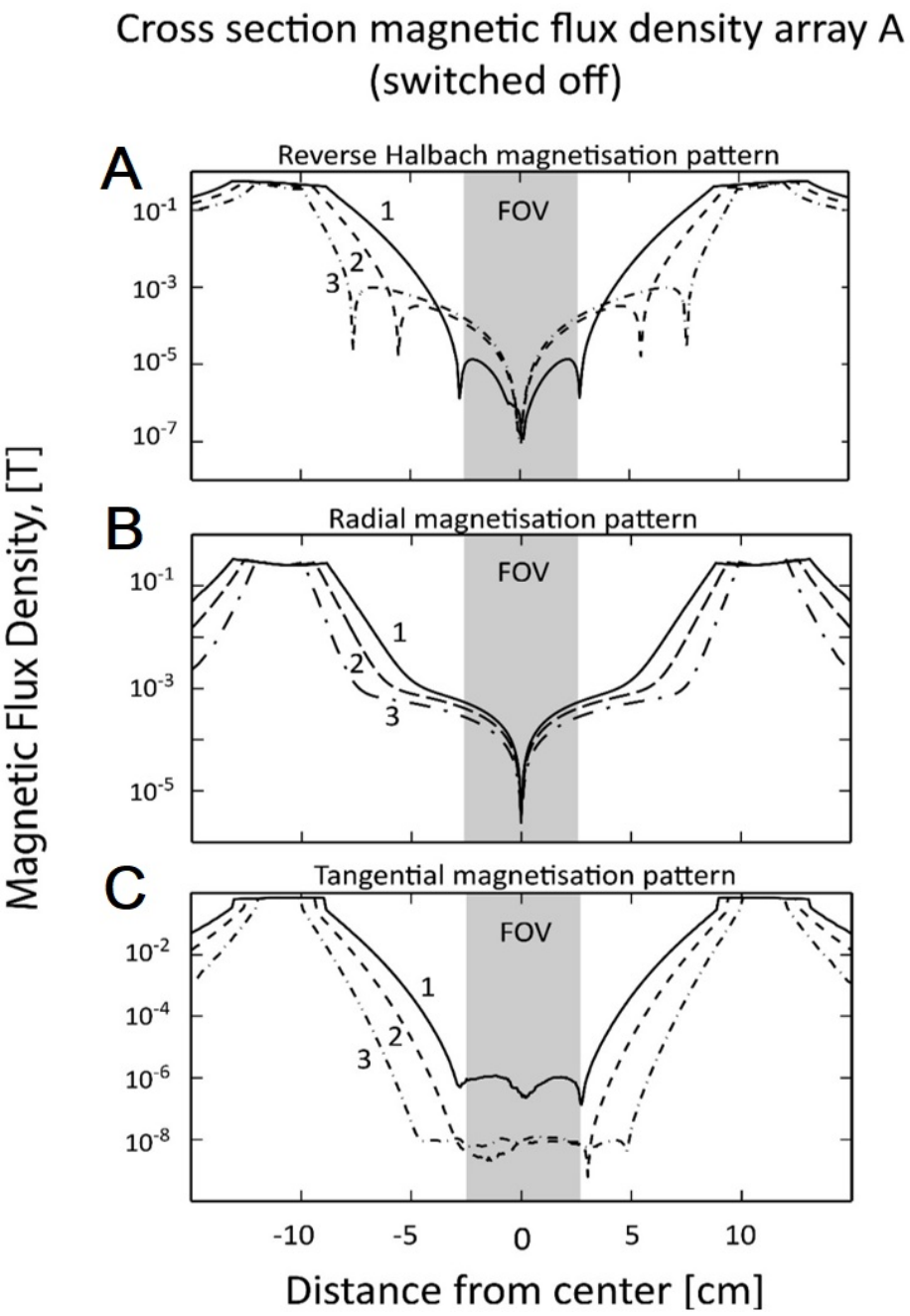

Figure 22: Transversal cross-section plots along the x-axis of the magnetic flux density for different magnetisation patterns, corresponding to Figure 16. In each array, 12 (solid line 1), 16 (dashed line 2) and 24 (dash-dotted line 3) magnets are considered. (A) Reverse Halbach, (B) radial, and (C) tangential pattern. The shaded area indicates the FOV. Only the tangential *pattern (C) is able to cancel the magnetic field within the FOV to magnitudes below µT.*

Energy considerations for array A: Strong permanent magnets arranged and fixed in different configurations cause considerable repulsive and attractive forces. We examined the total magnetic energy within array *A* as an index of how much energy was needed to change each permanent magnet in array *A* from pre-polarisation ('switched on') to measurement ('switched off'). This measure may also relate to the mechanical stability of the array and influence switching time. Since arrays *B* and *C* were much smaller both in terms of volume and the remanent magnetisation of the cylindrical magnets, their overall contribution to the forces and energy was not considered.

Table 3 lists the total magnetic energy contained in array *A* for different magnetisation patterns and amount of magnets. The total magnetic energy increased with decreasing magnet numbers due to the increased magnet volume and surface. The highest total magnetic energy for a given number of magnets was achieved with the *radial* pattern and the lowest with the *tangential* pattern. With the *radial* pattern, each magnet experienced repelling forces only (magnetisation vector parallel) whereas only attracting forces were present with the *tangential* pattern (magnetisation vector anti-parallel). This is similar to two bar magnets each fixed to an axis such that they can rotate freely, like a compass needle. Their opposite poles will attract each other (magnetisation vector anti-parallel) and form a stable configuration, which is the lowest possible total energy state.

Table 3: Total magnetic energy contained within array A for different magnetisation pattern and a varying number of magnets calculated with COMSOL.

	Total Magnetic Energy (Joule)			
Amount of magnets *n* in Array A	Halbach	Reverse Halbach	Tangential	Radial
12	2216	2220	1270	3104
16	1683	1689	955	2377
24	1134	1139	638	1614

Due to the complex arrangement of magnetisation vectors in the *Halbach* pattern, each magnet has different stored total magnetic energy, as highlighted in Figure 23A for 12, 16 and 24 magnets. Consequently, the energy required to rotate each magnet varies when array *A* switches from the *Halbach* pattern (pre-polarisation) to the *tangential* pattern (measurement field), which is illustrated in Figure 23B. As an example, the total magnetic energy difference for magnet number 7 of array *A* with 12 magnets (see Figure 14 for numbering) was -117 Joules (J) see Figure 23B, curve 1. The negative sign indicates energy

release when magnet number 7 rotates from pre-polarisation to measurement state and an energy amount of +117 J is required to switch from measurement to pre-polarisation state. This potential energy favours rapid switching from the pre-polarisation to the measurement state since the magnets of array *A* tend naturally towards the tangential magnetisation pattern due to the lower magnetic energy state. Moreover, since the transition time from measurement to pre-polarisation is not a critical factor, it can be chosen such that mechanical vibrations can be minimised.

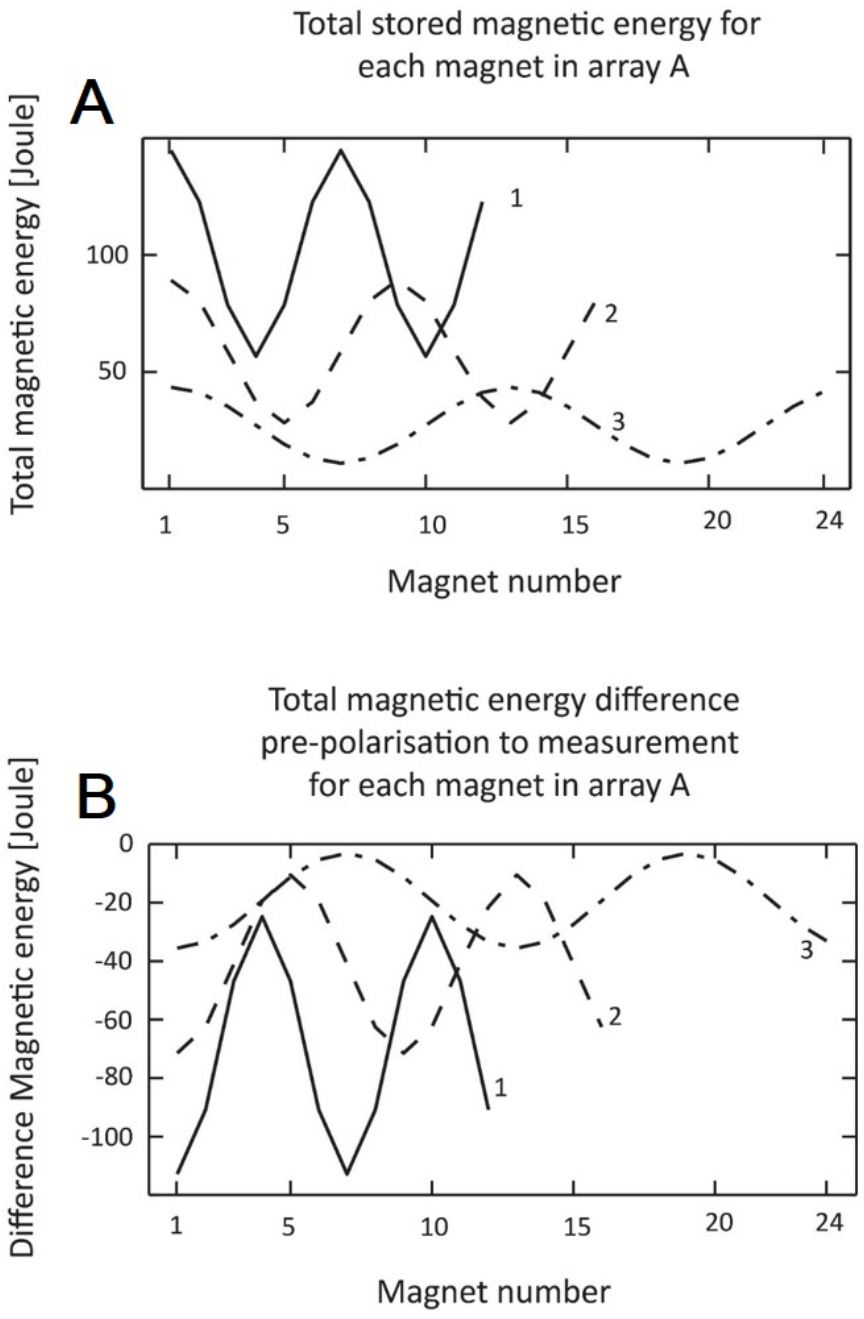

Figure 23: Total stored magnetic energy for each magnet in array A with a different number of magnets. The solid line (curve 1) corresponds to 12 magnets, the dashed line (curve 2) to 16 magnets and the dash-dotted line (curve 3) to 24 magnets in array A. Magnet

numbering follows Figure 14A. (A) Magnetic energy for each magnet in array A during pre-polarisation with Halbach magnetisation pattern (see Figure 15A). (B) The magnetic energy difference between pre-polarisation and measurement with tangential magnetisation pattern. Negative values in Figure 23B indicate that all the magnets move to a lower magnetic energy state.

The switching time from pre-polarisation to the measurement state was estimated in a simplified form by assuming that the difference in magnetic energy is predominantly released as rotational energy. Then, the rotational energy as a function of angular velocity (ω) is:

$$E_{rot} = \frac{1}{2}\omega^2 I \tag{53}$$

where I = 1/2 $m_{mag}{r_m}^2$ is the moment of inertia of the cylindrical magnet about the axis of rotation, and m_{mag} and r_m denote the mass and radius of the magnet, respectively.

The pre-polarisation field strength generated by array *A* with 24 magnets exceeded 100 mT, set as a target for our study (Figure 20A, Table 2) hence, the remainder of the study of magnetic forces in array A was performed with this configuration. The average total magnetic energy for array *A* was approximately +/- 20 J (curve 3, Figure 23B). With a magnet diameter r_m = 1.08 cm (refer to Equation (52), fill factor of 0.75), an average density of the rare-earth magnetic material of 7400 Kg/m^3, the angular speed yielded around 600 rad/sec or equivalently 10 ms for one revolution (100 Hz). Therefore, rapid switching of the pre-polarisation field can be achieved using SPMAs.

The mechanical force required to rotate each magnet from the measurement state to pre-polarisation state was calculated by relating torque (τ) to magnetic energy (E):

$$E = \tau\,\theta \tag{54}$$

with θ being the amount of rotation. Using Equation (54), assuming that the force *F* was applied tangentially to the magnet ($\tau = F \cdot r_m$), the average mechanical force was estimated to be around 300 N. Hence, as each magnet experiences about τ = 3.3 Nm, individual rotation of magnets could be achieved by commercially available hydraulic rotary actuators[167]. With the need for rapid switching in the presence of large forces, magnet

rotation must be controlled carefully through appropriate engineering design capable of minimising mechanical (torsional) vibrations in individual magnets and in the entire array of magnets.

Arrays B and C (measurement array): The measurement field $\mathbf{B_m}$ was generated by two concentric cylindrical arrays consisting of 12 magnets, each with the *Halbach* pattern. Figure 19D shows a surface plot of the magnetic field distribution across the *x*-*y* plane at $z = 0$ generated by array A with 24 magnets "switched off" by forming the *tangential* pattern, see Figure 15C, and by the *Halbach* pattern of arrays *B* and *C*. Regions of high and low field intensity are indicated by the white and black colour. In the same figure, an arrow plot in the central region indicates the local field direction of $\mathbf{B_m}$ along the y-axis. The measurement field magnitude $\mathbf{B_m}$ = 40 µT was generated by simultaneous rotation of arrays *B* and *C* clockwise and counter-clockwise about an angle of $\alpha = 4.5^{o}$. Similar to array A, the directionality and homogeneity of $\mathbf{B_m}$ was evaluated by assessing the ratio of the minor field components ($\mathbf{B_{mx}}$, $\mathbf{B_{mz}}$ along *x*- and *z*-axes) to the main component $\mathbf{B_m}$ (along *y*-axis), plotted in Figure 19E, along the x (solid line), y (dash-dotted line), and z-axis (dashed line). In all cases, the minor components of $\mathbf{B_m}$ were at least three orders of magnitude smaller within the FOV.

Figure 19F shows detailed line plots of $\mathbf{B_m}$ along the x-axis (curve 1), y-axis (curve 2), and z-axis (curve 3) through the centre of the SPMA. A relative magnitude variation of less than 0.02 % (200 ppm) was observed within the FOV. The absolute magnetic field variation was around 8 nT ($\mathbf{B_m}$ = 40 µT) corresponding to a line broadening in the NMR spectrum due to this field inhomogeneity of less than 0.2 Hz, according to Equation (51).

With the magnet parameters chosen (Ø = 0.3 cm, L = 70 cm and $\mathbf{B_r}$ = 0.2 T), for instance, rotation angles between 0 and 5^{o} led to variations of $\mathbf{B_m}$ from zero to 50 µT. Precise rotations of arrays *B* and *C* are thus necessary to control the magnitude and direction of $\mathbf{B_m}$. For instance, a small mismatch of the rotation angles of array *B* and *C* led to a tilt from the defined axis of precession (*y*-axis) and the creation of an additional *x*-component of $\mathbf{B_m}$. This tilt would result in a measurement field that is not perpendicular to sample magnetisation, resulting in a slight decrease in signal strength. However, since the angles are relatively small, the effect is likely to be negligible. On the other hand, a misalignment of 0.5^{o} of one array while others are aligned resulted in a significant magnitude variation in $\mathbf{B_m}$, which changed from 55.4 µT to 52.6 µT corresponding to a proton Larmor frequency change of 118 Hz. Furthermore, the field inhomogeneity increased from 0.02 % (200 ppm) to around

0.05 % (500 ppm) on average in all three directions. During a ULF experiment switching of $\mathbf{B_m}$ is not strictly necessary, since $\mathbf{B_p}$ is at least three orders of magnitude larger than $\mathbf{B_m}$. Therefore, arrays B and C can be adjusted and carefully controlled prior to experiments to minimise effects due to misalignment.

Matching the magnetic fields of two arrays with different radii but consisting of the same number of identical magnets cannot be achieved[62]. Hence, in our numerical study, we assumed that $\mathbf{B_m}$ was generated by arrays *B* and *C* for which the field matching was achieved by reducing $\mathbf{B_r}$ from 0.2 T to 0.16 T of the magnets in array *C*. This is a practical and cost-effective solution for the design of SPMAs, as off-the-shelf rare earth magnets have a wide range of standardised remanent magnetisations, as detailed in MMPA 0100 – Standard Specifications for Permanent Magnet Materials.

3.4.2 Manual SPMA measurement

The magnetic field distribution $\mathbf{B_p}$ and $\mathbf{B_m}$ generated by the manual SPMA prototype are presented for the pre-polarisation (Figure 24A) and the measurement state (Figure 24B). The direction of $\mathbf{B_p}$ and $\mathbf{B_m}$ within the FOV is qualitatively visualised by a custom-built array of small pivot-mounted needles. For comparison, a corresponding COMSOL® model was designed to simulate the magnetic fields within the FOV shown within the blue encircled inlets. The visualised magnetic field of the prototype is magnified within the red encircled inlets.

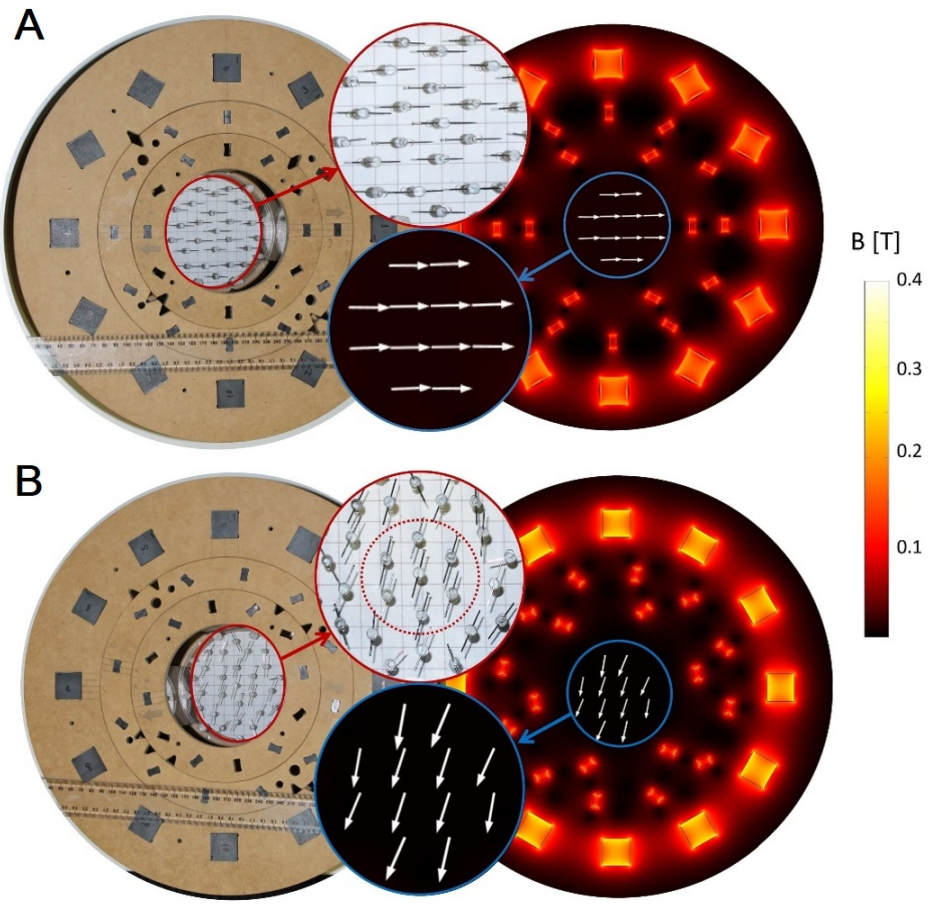

Figure 24: Comparison of pre-polarisation field Bp and measurement field Bm generated by an SPMA prototype (left-hand side) with numerical simulation (right-hand side). (A) Field direction of Bp indicated by an array of needles (top inset) and surface plot of COMSOL (bottom inset). (B) Field direction of Bm measured (top inset) and simulated (bottom inset).

Table 4 summarises the measured and calculated main field parameters for $\mathbf{B_p}$ and the measurement field $\mathbf{B_m}$ generated by arrays *E* and *F* with varying rotation angles (α = 0, 5 and 10 ^{O}). A non-zero magnitude of $\mathbf{B_m}$ = 0.4 mT is present for α = 0° because the magnetic field generated by each array individually ($\mathbf{B_E}$ and $\mathbf{B_F}$) is not matched, hence the direction of $\mathbf{B_m}$ is not parallel to the y-axis. The simulations correctly predicted the dependence of $\mathbf{B_m}$ on the rotation angle *α*. However, a slight deviation was caused by the presence of a residual field generated by array *D* for the *tangential* pattern, measured of 70 µT compared to the simulated 1 µT (Figure 18A, II). This deviation is due to uncompensated misalignment of individual magnets, variations of magnet dimensions or manufacturing imperfections which were not considered in the numerical model. Further structural optimisations of the manual SPMA (for instance, with shimming[19,159]) and detailed field homogeneity evaluation were not attempted since its primary purpose was to demonstrate the switching capabilities of $\mathbf{B_p}$ and the adjustability of $\mathbf{B_m}$.

Table 4: Comparison of simulated and measured magnetic fields generated by the SPMA prototype.

Field	Measurement [mT]	Simulation [mT]
$\mathbf{B_p}$	13.2	13.4
$\mathbf{B_m}$ Angle array E and F +/- 0°	0.44	0.42
$\mathbf{B_m}$ Angle array E and F +/- 5°	0.69	0.77
B_m Angle array E and F +/- 10°	1.30	1.36

3.5 Discussion

We introduced a small dynamic adjustable small permanent magnet array (SPMA) as a novel approach to generate multiple magnetic field configurations for ULF MR without resistive coil technology. As an advancement to *Halbach* arrays, the SPMA enables the generation of magnetic fields by a combination of forming multiple magnetisation patterns (see Figure 15) by prescribed rotations of individual pivot-mounted permanent magnets and rotations of permanent magnets arrays. Two magnetisation patterns were implemented, *Halbach* and *tangential* pattern to generate and cancel the pre-polarisation field $\mathbf{B_p}$ and two concentric arrays of permanent magnets were introduced to generate a variable measurement field $\mathbf{B_m}$ for ULF relaxometry.

Our simulation predicted pre-polarisation field magnitudes above 100 mT for the SPMA, higher compared to other ULF instruments with resistive cylindrical coil technology[15,21,164]. The simulation also predicted a magnetic field inhomogeneity for $\mathbf{B_p}$ better than 0.03 % (300 ppm) within a field of FOV of 5 x 5 x 5 cm^3. The SPMA field homogeneity is comparable to similar *Halbach* array designs with stacked rectangular magnets, known as NMR Mandhalas but the FOV is much larger compared to the array size[159,168]. Higher and more homogeneous sample pre-polarisation should provide better SNR in order to create an image successfully[20,29,155].

Variable measurement fields $\mathbf{B_m}$ ranging from near zero to 50 µT were generated by small rotations of two concentric cylindrical *Halbach* arrays *B* and *C* (while the outer array *A* forms the *tangential* pattern) with nominal magnitude deviations below 0.02 % or 200 ppm without shimming. This inhomogeneity is equivalent to spectral line broadening of less than 0.2 Hz for proton Larmor frequencies at ULF because the broadening (which limits resolution) relates to the absolute field inhomogeneity. For example, 300 ppm at $\mathbf{B_m}$ = 50 µT results in the equivalent line width broadening to 0.015 ppm at $\mathbf{B_m}$ = 1T, hence, very narrow spectral lines but with lower amplitude can be observed at ULF[15].

We emphasised the importance of precise rotational adjustments to achieve high field homogeneity and accurate control of $\mathbf{B_m}$ or the Larmor frequency ω_L. However, $\mathbf{B_m}$ does not need to be switched during an experiment since its magnitude is at least three orders of magnitude lower than $\mathbf{B_p}$. This simplifies motion control and adjustments for further enhancement of the field homogeneity.

Our model predicted fast switching capabilities within 6 ms from pre-polarisation to measurement state by utilising the total magnetic energy difference between the *Halbach* pattern and the *tangential* pattern. This rapid switching time is comparable to current ULF instruments with resistive coils and implemented customised switch boxes[20,29]. It is plausible that even faster switching can be achieved by implementing, for instance, additional hydraulic or pneumatic actuator systems. However, vibration and positioning of the permanent magnet will need to be recorded using encoders, and compensated via signal post-processing, which is beyond the scope of this study.

Without energy dissipation into heat due to high current flow in conductors sample heating is avoided and without the need for cooling devices energy consumption is significantly lower with the SPMA. Furthermore, undesired signal generation due to transient currents, induced in conductors by rapid switching, is reduced because the conductivity of magnet alloys is much lower compared to conductive materials like copper.

As a proof-of-principle to demonstrate the capability of generating varying magnetic fields and to evaluate the numerical approach (FEM) taken in this study, a manual SPMA was modelled and built in COMSOL®. All the main field parameters were correctly described with our computational model and experimentally verified. This good correspondence is in agreement with similar studies for simulating magnetic field parameters to optimise instrument designing based on *Halbach* arrays with COMSOL[19,160]. Any further optimisation steps to maximise field inhomogeneity, or match the magnetic fields generated by array B and C was not attempted here since the primary focus was to verify the new feature of the SPMA. Also, appropriate shimming techniques to improve field qualities were described elsewhere[19,159].

Although the SPMA study presented in this paper is limited to the application of ULF relaxometry, the flexible and modular design allows additional magnet arrays to be added, for instance, for generating dynamic gradient fields to achieve imaging with ULF-MRI. This is achievable since the absolute field homogeneity requirements for ULF instrumentation are quite moderate. Notably, despite the generation and switch between $\mathbf{B_p}$ and $\mathbf{B_m}$ with the

SPMA, sequences for signal generation and acquisition do not differ significantly from conventional approaches with instrumentation equipped with resistive magnets. Measuring strategies like iterative sample pre-polarisation leading to repeated signal acquisitions for enhanced signal-to-noise ratio through signal averaging can be applied with the SPMA similar to high field relaxometry applications.

Generating linear gradient fields with a permanent magnet at ULF is more challenging due to the presence of concomitant fields[84,87]. This difficulty is a consequence of Maxwell's equations since the gradient field gradients are comparable to the magnitude of $\mathbf{B_m}$[15], resulting in image distortion, which needs to be corrected during image reconstruction. As mentioned, a new approach for spatial signal encoding was introduced for a portable MRI scanner with a *Halbach* array utilising the intrinsic field inhomogeneity of the *Halbach* array and nonlinear image reconstruction methods[19]. However, the *Halbach* array used a static field distribution providing encoding only in 1D, which requires the system to be rotated about the sample to achieve 2D images. It is possible to further extend the acquisition to 3D through alternatives such as Bloch-Siebert Spatial Encoding (BS-SET) or TRansient Array Spatial Encoding (TRASE). These methods, however, require additional RF excitation hardware[60]. Alternatively, it is conceivable that 3D spatial encoding of the signal can be performed using additional dynamically adjustable SPMAs capable of achieving field properties similar to high field MRI[169]. This approach is the subject of our current ongoing research.

3.6 Conclusion

The proposed SPMA is substantially different from all the resistive coil-based approaches reported in the literature to date. Flexible magnetic field manipulations achieving very high field homogeneities has been demonstrated empirically by rearrangement of a concentric small permanent magnet array. We showed that it is possible to produce pre-polarisation and measurement fields relevant for ULF NMR via rotation of individual permanent magnets and rotation of *Halbach* arrays. Our findings may benefit future developments in ULF MR by eliminating the need for resistive coils for the generation of various magnetic fields. The consequence of which is a more compact system with lower energy requirement resulting in increased portability of instrumentation. It is also plausible that such SPMAs have application outside of ULF MR, where switching of magnetic fields is required.

3.7 Author contributions

The numerical study was done by Vogel, Giorni, Vegh, and Reutens. My contribution to this work was to design and build the physical prototype. Subsequently, I measured the magnetic

field generated by the prototype for a range of different configurations, which then I used to validate the corresponding numerical approach. Regarding the manuscript, in essence, I modified a draft paper based solely in simulations to accommodate for the empirical proof of concept achieved through the validations. Therefore, apart from writing the sections of the article on the construction and the empirical validation, I modified the abstract, introduction, discussion and conclusions to reshape the scope and accommodate the added value.

Chapter 4 - Contributions

Vogel MW., Pellicer-Guridi R, Jiasheng S, Vegh V, Reutens DC. 3D-Spatial encoding with permanent magnets for ultra-low field magnetic resonance imaging. Submitted to Scientific reports.

Contributor	Statement of contribution
Vogel MW	Conception and design (50%) Analysis and interpretation (45%) Drafting and production (60%)
Pellicer-Guridi R (Candidate)	Conception and design (30%) Analysis and interpretation (35%) Drafting and production (20%)
Jiasheng S	Conception and design (0%) Analysis and interpretation (10%) Drafting and production (0%)
Vegh V	Conception and design (5%) Analysis and interpretation (5%) Drafting and production (5%)
Reutens DC	Conception and design (15%) Analysis and interpretation (5%) Drafting and production (15%)

Chapter 4- 3D-Spatial encoding with permanent magnets for ultra-low field magnetic resonance imaging

4.1 Abstract

We describe the use of small permanent magnets moving along prescribed helical paths to enable 3D spatial encoding and imaging without sample adjustment in ULF MRI. A semi-analytical simulation method was developed to determine optimal magnet path and orientation for any given encoding magnet number and instrument architecture. We then describe a mechanically operated ULF-MRI instrument utilising permanent magnets for magnetic field generation; these obviate the disadvantages of resistive coil technology. For proof-of-concept, different helical magnet paths and lengths for one and two small magnets were considered to study spatial encoding efficiency. We demonstrate that a single small encoding magnet moving around the sample in a single revolution suffices for the generation of a 3D image by back projection.

4.2 Introduction

The conventional setup of MRI or NMR instruments comprises a static magnetic field to align the nuclear spins and generate net sample magnetisation; a transmitter/receiver coil system to perturb the nuclear spin system and detect the resultant MR signal, and a coil system to encode spatial information for image generation[170]. Image quality depends mainly on SNR which increases with the magnitude and homogeneity of the main magnetic field (commonly referred to as $\mathbf{B_0}$). This SNR advantage has been the primary motivation for increases in magnetic field strength in MR instruments[152,171]. However, superconducting magnets and advanced cryogenics are required to generate such high magnetic field strength, increasing the bulk and cost of purchase, operation and maintenance of these instruments.

The last decade has seen the development of ULF MR instruments with main magnetic fields below 10 mT[15,19,20,25,29,46,155,172,173]. The low field strength at ULF enables novel applications including imaging in the presence of metal offering important future applications for example in trauma, disaster and battlefield imaging[15]. Superconducting technology is not required for magnetic field generation, enabling portable, low power operation. Moreover, the Larmor frequency overlaps with a range of molecular and physiological processes such as protein folding, slow diffusion, molecular tumbling and enzyme catalysis potentially opening the way for novel imaging paradigms sensitised to these processes which are difficult to observe at high field[15,155]. Although based on the same fundamental principles of magnetic resonance as high field MR, signal generation and operation of ULF MR

instruments is different. A pulsed magnetic field, the pre-polarising field, approximately three orders of magnitude higher (~0.05-0.1 T) than the Earth's field is applied prior to the measurement to enhance net sample magnetisation according to Curie's law[15,150,158,172]. Instead of radiofrequency (RF) pulses, signals in ULF MR are generated by the switch to a second magnetic field, the measurement field, oriented perpendicular to the pre-polarisation field.

We have previously described the use of dynamically adjustable small permanent magnet arrays (SPMA) that exploit the advantages of Halbach arrays to generate and dynamically control the magnetic fields in ULF MR[172]. Recently, Cooley et al. harnessed the intrinsic static field inhomogeneity of a Halbach array for spatial encoding[19]. The Halbach array was rotated about the sample for 2D spatial encoding and RF pulses were required for 3D imaging[19,60]. Here, we report on the use of dynamically adjustable permanent magnets to generate 3D spatial encoding field configurations for ULF-MRI. A practical method to determine the most suitable magnet location and orientation to generate the encoding fields is described and demonstrated for a permanent magnet based ULF-MRI instrument.

4.3 Materials and methods

Figure 25 illustrates the design of a ULF MR instrument with SPMAs developed at the Centre for Advanced Imaging (CAI) at The University of Queensland. It comprises four concentrically arranged cylindrical magnet arrays: *Array A* with 12 individually rotatable magnets for switching the *pre-polarisation field* $\mathbf{B_p}$ to generate sample magnetisation; *Arrays B* and *C* with 24 and 36 magnets respectively for generating the *measurement field* $\mathbf{B_m}$[172]; and the *Encoding Array D* with two permanent magnets (a-b) that creates 3D spatial encoding fields $\mathbf{B_e}$ for image acquisition.

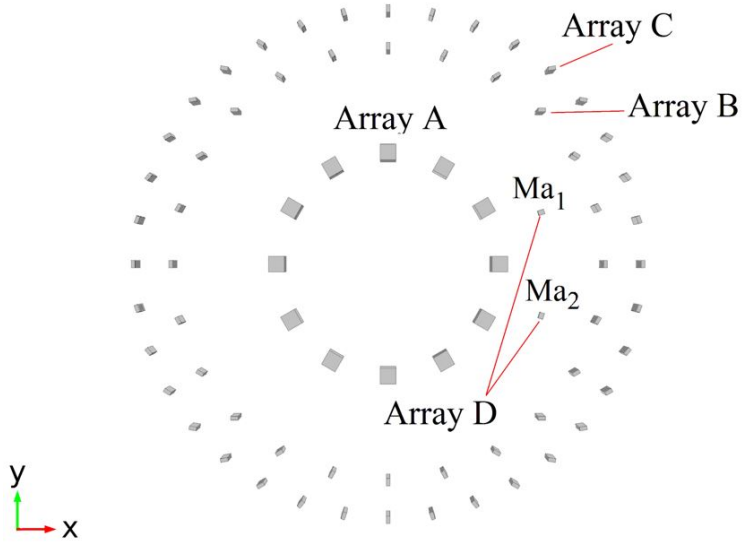

Figure 25: Concept design of ULF-MRI instrument with permanent magnet arrays, developed at the Centre for Advanced Imaging (CAI). Array A with 12 magnets switches the pre-polarisation field Bp by individual magnet rotation. Shown here is the tangential magnetisation pattern (Bp = off). Array B (24 magnets) and array C (36 magnets) generate the measurement field to define the Larmor frequency. Array D consists of two small permanent magnets (Ma1 and Ma2) for 3D spatial encoding moving in helical paths along a cylindrical surface.

4.3.1 Simulation environment

COMSOL©, a commercial finite element method (FEM) simulation environment, (version 5.0, modules AC/DC and Magneto-static, COMSOL Inc., Burlington, MA 01803, USA) was used for numerical analysis. The 3D model of the ULF-MRI instrument with the encoding array (Figure 25) was set up with a computer-aided design interface to simulate the temporal transition from the pre-polarisation to the measurement field, required for a virtual signal generation for which an in-house program was developed in MATLAB (MathWorks©, Natick, MA, USA). MATLAB routines were also used for image reconstruction and determining optimal magnet location and orientation for the instrument architecture. COMSOL simulations were carried out using an x64-based 16 core PC with 128 GB of RAM, while the MATLAB simulations were run on an x64-based 8 core PCs (DELL© Optiplex 9020) with 32 GB of RAM.

In the FEM simulation in COMSOL, the model was discretised in 3D-tetrahedral meshes using predetermined and optimised mesh distributions implemented. Mesh density was manually increased around the magnets of array A to achieve sub-millimetre spatial resolution in the centre of the array. The number of tetrahedral elements ranged between

27-28 million with each simulation taking 12-24 hours. A cylindrically shaped computational window size (diameter 1.3 m, height 1.56 m) with predetermined boundary conditions was set to be sufficiently large to model the instrument at 1:1 scale and to minimise numerical errors due to domain discontinuities. The relative permeability of the magnet material was set to a typical value of 1.05 (Ceramic, Neodymium alloys or Alnico magnets[174]) and for the surrounding environment (air) it was set at 1.

A 3D cubic cross-shaped digital phantom (see inlet in Figure 33) with an arbitrary spin density of 5 compared to a background spin density of 0 was modelled using typical soft tissue relaxation times at ULF of T_1 = 100 ms and T_2 = 80 ms [31]. Image size was chosen to be 8 x 8 x 8 voxels.

4.3.2 Signal generation in ULF-MRI

After the pre-polarisation period (~ $5 \cdot T_1$, T_1 = longitudinal relaxation time) $\mathbf{B_p}$ is switched off at $t = t_{pre}$, see Figure 26A. If $\mathbf{B_p}$ is switched off rapidly or *non-adiabatically* ($|dB_p/dt| >> \gamma^2|B_m|$ [15]) the magnetisation vector **M** will retain its original orientation[150] and precess about $\mathbf{B_{res}}$, the resultant magnetic field generated by $\mathbf{B_p}$ and $\mathbf{B_m}$ (Figure 26B). If $\mathbf{B_p}$ is removed slowly or *adiabatically* ($|dB_p/dt| << \gamma^2|B_m|$ [15]) **M** follows $\mathbf{B_{res}}$[150] and will be parallel to $\mathbf{B_m}$ after $\mathbf{B_p}$ is switched off (Figure 26C). As a result, no precession occurs, and additional RF pulses have to be applied to flip **M** away from $\mathbf{B_m}$ to trigger signals.

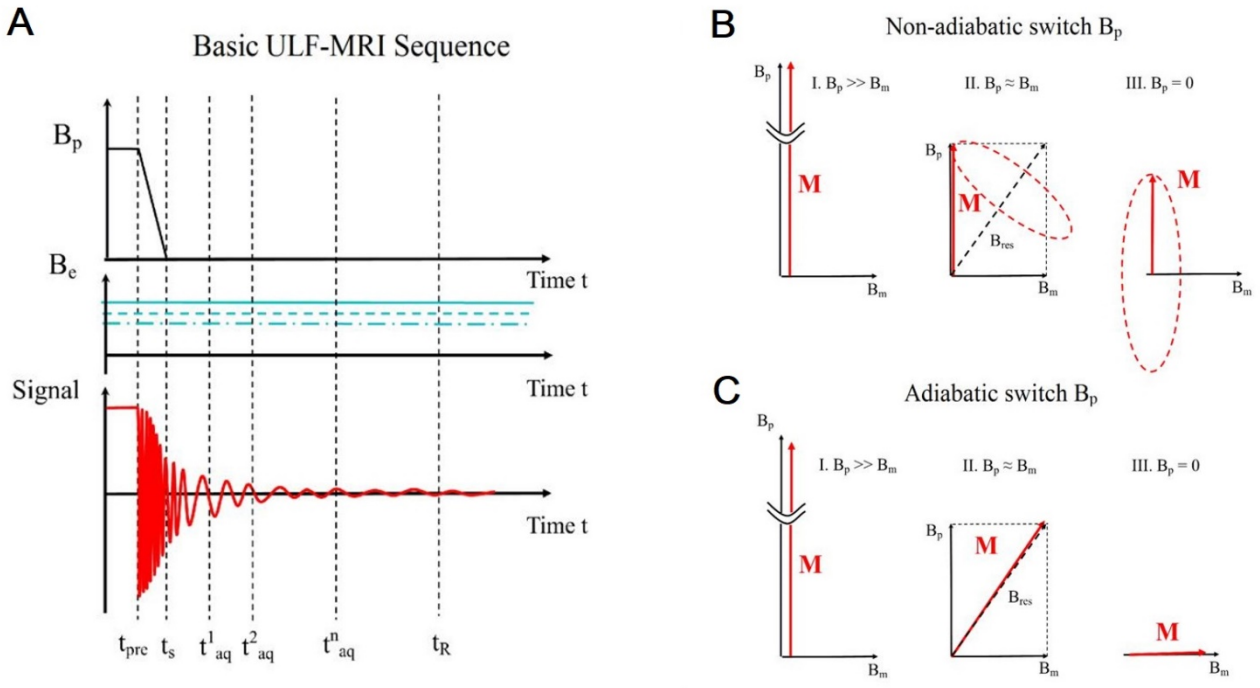

Figure 26: (A) Basic sequence for ULF-MRI with permanent magnet array and without RF used for signal simulation. The measurement field $\mathbf{B_m}$ (not shown here) is assumed to be

switched on permanently during the experiment. The encoding field $\boldsymbol{B_e}$ *changes only after* $t = t_R$ *during pre-polarisation.* $\boldsymbol{B_p}$ *is switched off at* $t = t_{pre}$*, and is assumed to be decayed at* $t = t_S$*. The signal is detected at* $t = t^k_{aq}$ *(*$k = 1$ *to* N*). The total signal acquisition number,* N*, is assumed to be 8 at constant interval* $\Delta t_{aq} = 100$ *µs. (B) Adiabatic vs non-adiabatic pre-polarisation switching. If the change* $d\boldsymbol{B_p}/dt$ *is non-adiabatic, the magnetisation vector* $\boldsymbol{M}$ *remains perpendicular to* $\boldsymbol{B_m}$ *and starts to precess. (C) If the changes are adiabatically,* $\boldsymbol{M}$ *follows* $\boldsymbol{B_{res}}$ *and aligns with* $\boldsymbol{B_m}$ *and no precession occurs, hence additional RF pulses are required for signal triggering.*

$\mathbf{B_m}$ was assumed to be static during the entire experiment since its magnitude (~ 100-200 µT) is at least three orders of magnitude lower than $\mathbf{B_p}$ and will not interfere with $\mathbf{B_p}$. The encoding field $\mathbf{B_e}$ remained constant within one measurement period ($t_S < t < t_R$) and transient effects during ramping up or down were not considered. $\mathbf{B_e}$ is changed only during the pre-polarisation period to avoid signal artefacts due to the movement of magnets or arrays. The temporal evolution of **M** is described by Bloch's equation and the signal induced in a single coil by Faraday's law[150,170]. In the signal simulation, spin-to-spin interactions were ignored as these are negligible in the low and ULF regime. It should be noted that the signal originates from the entire sample since no planar slice selections were implemented.

4.3.3 The encoding matrix

Since the magnetic fields produced by $\mathbf{B_m}$ and $\mathbf{B_e}$ are nonlinear, Fourier transform-based image reconstruction methods used in standard MRI are not suitable. This is because non-equidistant k-space filling due to nonlinearity, if uncorrected, results in distortions and inhomogeneous image resolution. Instead, we have applied a back projection-based image reconstruction method using the following general relation between the signal at time t, the sample at spatial locations denoted by $\mathbf{q}$ and an encoding matrix $\mathbf{E_{enc}}$:

$$\mathbf{S}(t) = \mathbf{E_{enc}}(\mathbf{q}, t) \cdot \mathbf{m}(\mathbf{q}) \,. \tag{55}$$

Each matrix element of $\mathbf{E_{enc}}$ describes the time-dependent phase accumulation of the precessing magnetisation vectors, which depends on the local magnetic field strength and the acquisition time[19,60].

4.3.4 Acquisition strategy

For spatial encoding, we used linearly independent encoding field configurations with signal measurement at multiple time points after pre-polarisation for each configuration, as

indicated in Figure 26A. The encoding field configurations are generated by Array D with each encoding magnet moving along a prescribed path in *discrete* steps. For a total of *Q* voxels in a sample and *N* time points, we used *Q*/*N* different encoding field configurations. Hence, each signal acquisition fills one row of the encoding matrix, with total row number *P* = *N*·*Q*. Spin echoes are not used due to the short measurement time, and accumulated phase is evaluated and included in the encoding matrix. The short time windows are due to short tissue T_1 and T_2 relaxation times at ULF (< 100 ms), weak signal amplitude, spin decoherence and other T_2^* effects caused by the nonlinear encoding fields. We used $N = 8$ signals per encoding field configuration starting at t_s = 10ms at intervals of 100 µs. This time interval, the dwell time, corresponds to a sweep width of 5 kHz or a measurement field magnitude of 117 µT.

At discrete sample locations *q* with magnetisation m_q, the signal *S(t)* acquired for the p^{th} encoding field configuration at time *t* after pre-polarisation is described as:

$$S_p(t) = \sum_{p=1}^{P} \sum_{q=1}^{Q} m_q e^{-j\omega_{qp}t}, \tag{56}$$

where $\omega_{p,q}$ (p = 1,2.. P, q = 1,2…Q) is the Larmor frequency for a voxel corresponding to location *q* and encoding field configuration *p*. The initial phase for each voxel is assumed to be 0. Using the Bloch's equations, Equation (56) can be recast as:

$$\begin{pmatrix} S_1(t) \\ S_2(t) \\ \vdots \\ S_p(t) \end{pmatrix} = \begin{pmatrix} e^{-j\gamma B_{11}t} & e^{-j\gamma B_{21}t} & \dots & e^{-j\gamma B_{q1}t} \\ e^{-j\gamma B_{12}t} & e^{-j\gamma B_{22}t} & \dots & e^{-j\gamma B_{q2}t} \\ \vdots & \vdots & \dots & \vdots \\ e^{-j\gamma B_{1p}t} & e^{-j\gamma B_{2p}t} & \dots & e^{-j\gamma B_{qp}t} \end{pmatrix} \begin{pmatrix} m_1 \\ m_2 \\ \vdots \\ m_q \end{pmatrix} \equiv \boldsymbol{E}_{enc} \cdot \boldsymbol{m} \tag{57}$$

4.3.5 Image reconstruction

Inverting $\mathbf{E}_{enc}$ is the most straightforward method to retrieve the image information from Equation (57). This operation, however, requires $\mathbf{E}_{enc}$ to be a square matrix. Matrix inversion using standard methods such as Gauss-Jordan elimination or LU decomposition is problematic for large matrix sizes required by high image resolutions or by acquisitions using multiple receiver coils[175,176].

4.3.6 Calculating encoding field configuration

Figure 27 shows the parameters used to calculate the local magnetic flux density $\mathbf{B}_{x,y,z}$ generated by one magnet dipole with magnetisation $\mathbf{m}$, located at $\mathbf{r}_{dp}$. The dipole approximation is applicable since the encoding magnets are much smaller than the distance to the sample. The far-field approximation yields the magnetic field of the dipole[177]:

$$\boldsymbol{B} = \frac{\mu_0}{4\pi}\left(\frac{3\left(\boldsymbol{r}_{pi}-\boldsymbol{r}_{dp}\right)\left(\boldsymbol{m}\cdot\left(\boldsymbol{r}_{pi}-\boldsymbol{r}_{dp}\right)\right)}{\left|\boldsymbol{r}_{pi}-\boldsymbol{r}_{dp}\right|^5}-\frac{\boldsymbol{m}}{\left|\boldsymbol{r}_{pi}-\boldsymbol{r}_{dp}\right|^3}\right) \qquad (58)$$

For *n* encoding magnets the resultant magnetic field is the sum of the fields generated by each magnet according to the superposition principle. The resultant is substituted into Equation (57) to generate the encoding matrix.

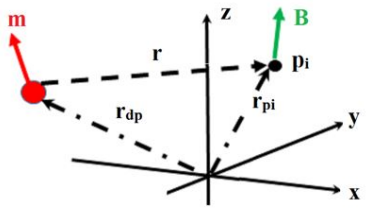

Figure 27: Magnetic field calculation at the sample point $\mathbf{r}_{pi}$ generated by a magnetic dipole with magnetisation $\mathbf{m}$ located at the point $\mathbf{r}_{dp}$.

4.3.7 Evaluation of encoding field configuration

We aimed to maximise the rank of the encoding matrix, which reflects the number of linearly independent rows. We also aimed for a low condition number, which determines the accuracy of the numerical matrix solvers. We examined encoding field configurations generated by magnet paths that were feasible for the ULF-MRI instrument design. Two encoding magnets, Ma_1 and Ma_2 (Figure 29) moving in cylindrical helical paths around the sample were simulated. Each magnet was assumed to be attached on separate rotatable cylinders within array D as illustrated in Figure 29A. The helical path of Ma_1 (Figure 30) is described by:

$$x_{Ma1} = R_{ad1}\cos(\alpha);\ y_{Ma1} = R_{ad1}\sin(\alpha);\ z(\alpha) = A\alpha^2 + B\alpha + C \qquad (59)$$

where α denotes the rotation angle with respect to the x-axis and the coefficients A, B and C are given by

$$\begin{bmatrix} A \\ B \\ C \end{bmatrix} = \begin{pmatrix} \alpha_1^2 & \alpha_1 & 1 \\ \alpha_2^2 & \alpha_2 & 1 \\ \alpha_3^2 & \alpha_3 & 1 \end{pmatrix}^{-1} \begin{bmatrix} z(\alpha_1) \\ z(\alpha_2) \\ z(\alpha_3) \end{bmatrix}, \tag{60}$$

α_1 are α_3 are the starting and final angular positions and α_2 is an intermediate angular position. The intermediate angle α_2 is defined where the curves intersect with $z = 0$. If $\alpha_2 = (\alpha_3 - \alpha_1)/2$, $z(\alpha)$ is a linear function of α. The equations describing the helical path of Ma_2 are obtained by substituting Rad_2 for Rad_1 and β for α in Equation (59).

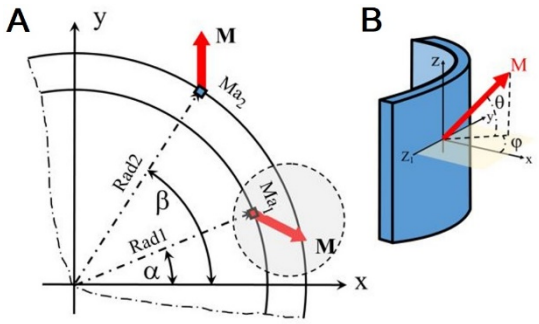

*Figure 28: (A) Transverse view of array D with two encoding magnets Ma_1 and Ma_2 each with magnetisation **M**. In this study Rad_1 and Rad_2 are constant. (B) 3D view showing a cylindrical frame segment with a fixed magnetisation vector **M** representing Ma_1. The optimisation parameters are the azimuthal angle φ, polar angle θ and height z(α).*

For all magnet motions considered in this paper, $z(\alpha_1)$ = -0.15 m and $z(\alpha_3)$ = 0.15m (i.e. total array height = 0.3 m). Figure 29A illustrates three different 3D helical paths for α_2 = 180º (red curve), 100º (black curve) and 240º (blue curve). We also evaluated different helical path lengths (Figure 29B) by selecting α_3= 180º (black curve), 240º (blue curve) and 360º (red curve).

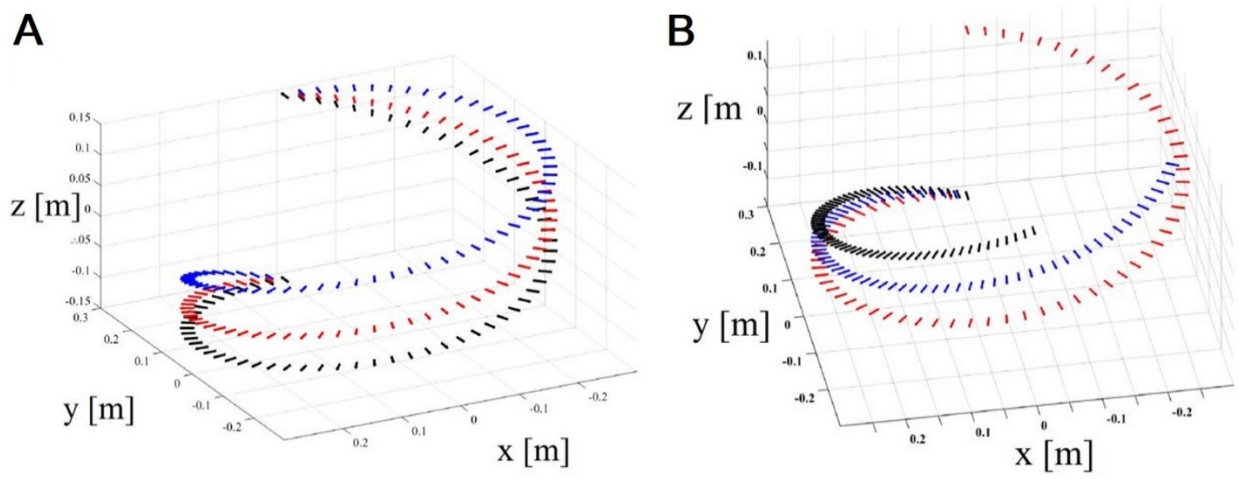

Figure 29: (A) Three examples of 3D helical paths with linear (α_2 =180°, red curve) and quadratic height variations z (α_2 =100°, black curve and α_2 =240°, blue curve) are shown, each starting from initial angle α_1 = 0° to final angle α_3 = 360°. The height varies from z(α_1) = -0.15m to z(α_3) = 0.15 m. Each line segment corresponds to one encoding step location and the magnet orientation, shown here for θ = 0 and φ = 0. (B) 3D helical paths with linear height variation (α_2 = 180°) but different final angles α_3 = 360° (red curve), α_3 = 240° (blue curve) or α_3 = 180° (black curve).

In Figure 29, the lines indicate the spatial magnetisation vector pointing outwards and perpendicular on the path at each encoding step.

The quality of the reconstructed image is evaluated using the standard deviation of voxel intensity at various cross sections after predetermined iteration steps.

4.4 Results

For all magnet configurations considered, the rank of the encoding matrix varied little. Here we present the results for condition number.

4.4.1 Configurations with one encoding magnet

Figure 30 shows the condition number of the encoding matrix versus the encoding magnet orientation, described by the azimuthal angle φ and polar angle θ (see Figure 28), as a grey scale surface plot for Ma_1 and α ranging from α_1 = 0° to α_3 = 360°. Three values for α_2 were selected: 180° (Figure 30A), 100° (Figure 30B) and 230° (Figure 30C). For α_2 =180° (i.e. α_2 = (α_3 – α_1)/2), $z(\alpha)$ is a linear function of α. In all cases, a region of lower condition number is present at θ = 0 and ϕ = 0, i.e. with the magnet oriented perpendicular to the path. Figure 31 depicts the dependence of the lowest condition number of each configuration on α_2, with path parameters α_1 = 0° and α_3 = 360°. The condition number is lowest for α_2 = 180°.

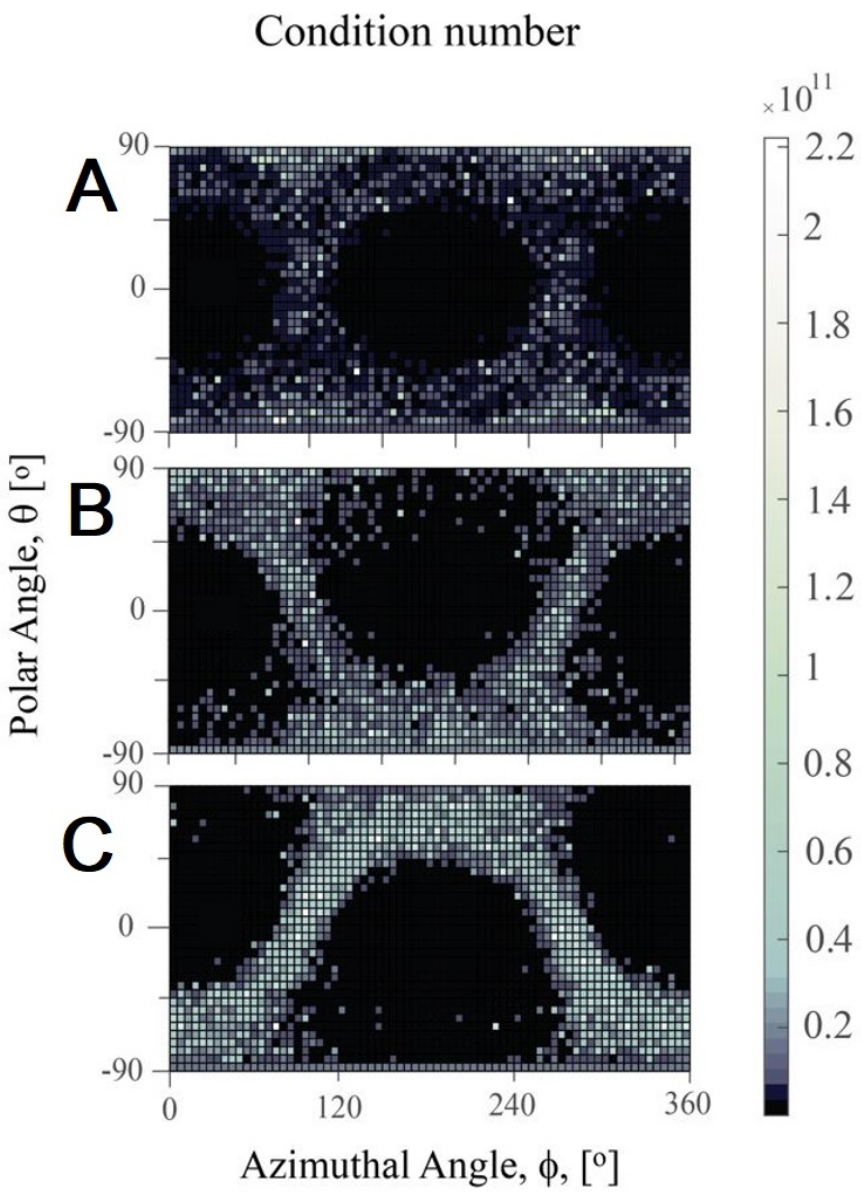

Figure 30: Condition number of the encoding matrix vs magnet Ma_1 orientation with helical path parameters $\alpha_1 = 0^o$ and $\alpha_3 = 360^o$ and height variation from $z(\alpha_1) = -0.15$ m and $z(\alpha_3) = 0.15$ m (A) Linear height variation ($\alpha_2 = 180^o$), (B) Nonlinear height variation ($\alpha_2 = 100^o$). (C) Nonlinear height variation $\alpha_2 = 230^o$.

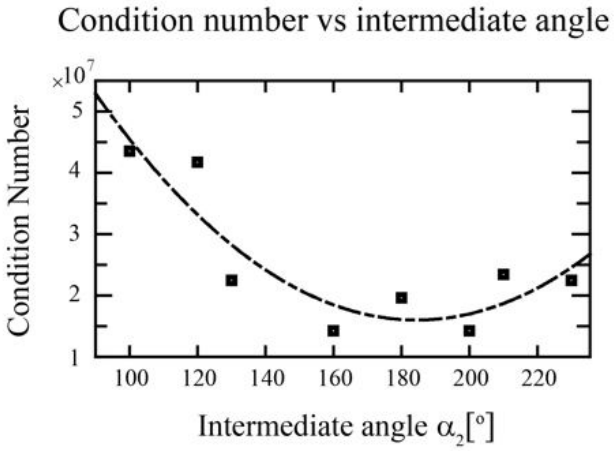

Figure 31: Minimum condition number vs intermediate angle α_2 with initial angle $\alpha_1 = 0^o$ and $\alpha_3 = 360^o$. The minimum condition number is located around $\alpha_2 = 180^o$, indicating an optimal spiral path with linear height variation.

Figure 32 illustrates the relationship between condition number and the length of the helical path for one encoding magnet with linear height variation. Condition number significantly increased as path length decreases but varies by less than one order of magnitude for α_3 between 240^o and 360^o. This may enable faster encoding without compromising efficiency.

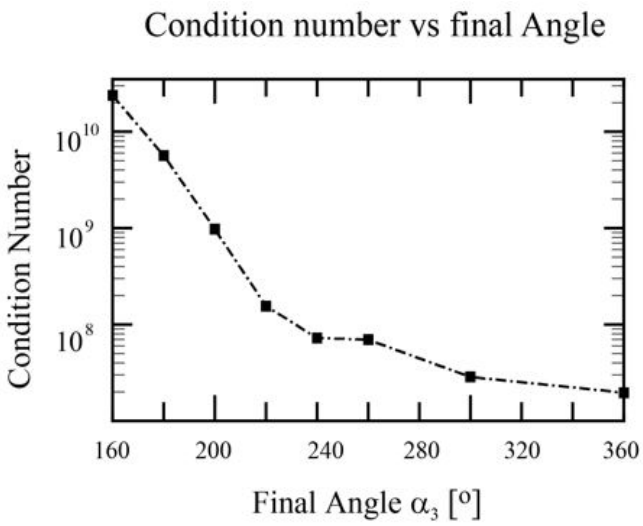

Figure 32: Condition number versus spiral path length and constant height variation from z = -0.15 – 0.15 m.

Figure 33 shows 2D cross-section images at z = 0.06 m, 0.045 m, 0.015 m, -0.015 m and -0.045 m achieved with a single encoding magnet Ma_1 and with path parameters $\alpha_1 = 0^o$, $\alpha_2 = 120^o$ and $\alpha_3 = 240^o$ (Figure 29A, blue path), reconstructed with the Kaczmarz method. Results for different iteration numbers are shown. Image quality improves rapidly within the

first few iterations and convergence occurs within 5-8 iterations. For further evaluation of the quality of reconstructed images we arbitrarily selected 10 iterations as the comparator against the digital phantom.

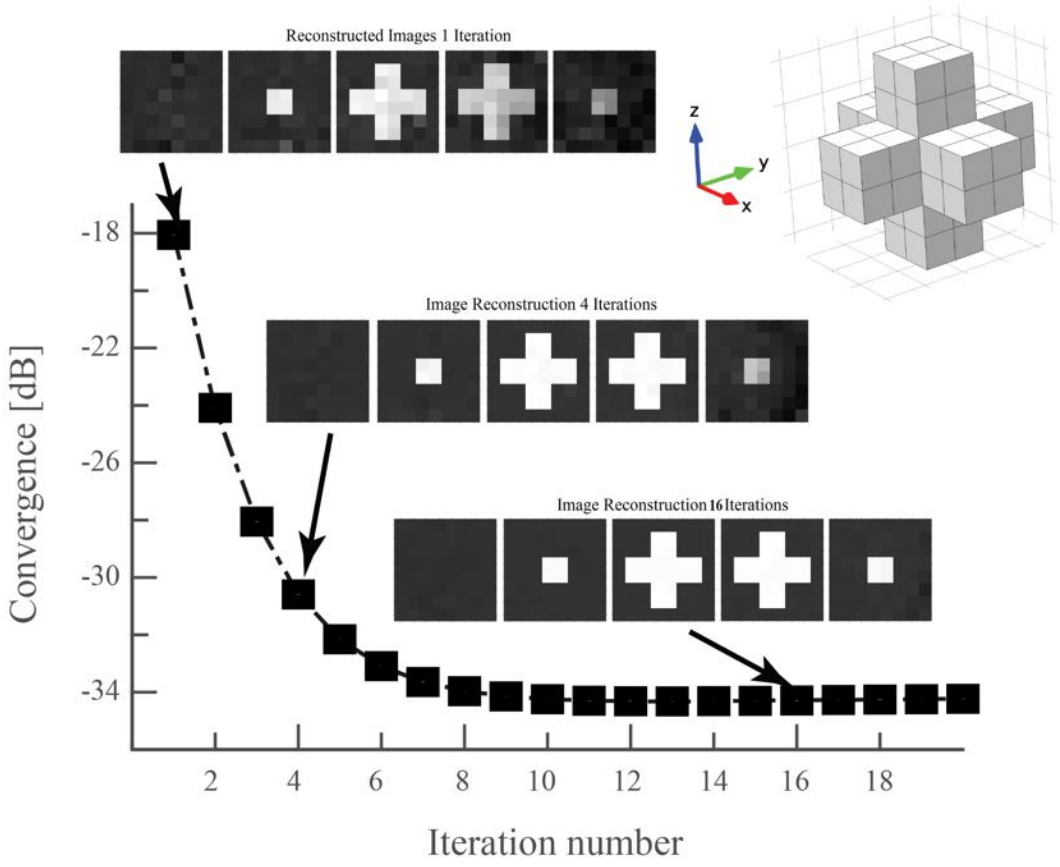

Figure 33: Calculated Image convergence with the iterative Kaczmarz-based reconstruction method for a 3D cross-shaped tissue sample (inlet) surrounded by another tissue. The spin density difference sample-surroundings was arbitrarily chosen to be five to one. The image converges after about 8 iterations.

The effect of path length on spatial encoding and image reconstruction quality is illustrated in Figure 34, which shows images in the *xy*-plane at z = 0 m. Greater path length results in a lower standard deviation between reconstructed and phantom images: standard deviation = 0.0231 for α_3=180°, 0.0221 for α_3=240° and 0.0200 for α_3=360°.

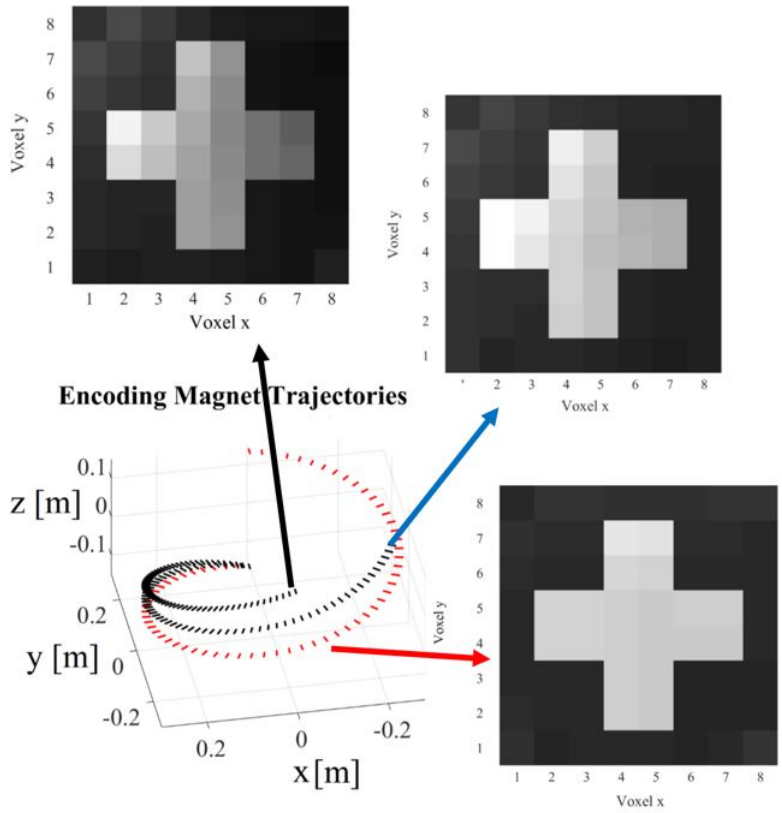

Figure 34: The image quality dependence on path length for one encoding magnet, shown for α_3=180° (black), α_3=240° (blue) and α_3=360° (red), with constant encoding step numbers. The height varies from z=-0.15m to z=0.15m. The image reconstruction with the Kaczmarz method is shown after 10 iterations. The standard deviations are 0.0231 (α_3 = 180°), 0.0221 (α_3=240°) and 0.0200 (α_3=360°).

4.4.2 Spatial encoding array - Optimisation and image reconstruction with two encoding magnet

We next considered the case of two identical magnets moving along two path configurations as shown in Figure 35. Configurations were examined in which magnet *Ma*$_1$ moves counterclockwise from the bottom to the top (Figure 35A, black curves and arrows) and magnet Ma$_2$ moves counterclockwise from the bottom to the top (Configuration 1, Figure 35A, left, red arrow) or from top to bottom (Configuration 2, Figure 35A, right, red curve and arrow). The magnets were separated by 180° at all times to reduce image inhomogeneity. The combined path lengths of both magnets were chosen to equal the circumference of *array D*.

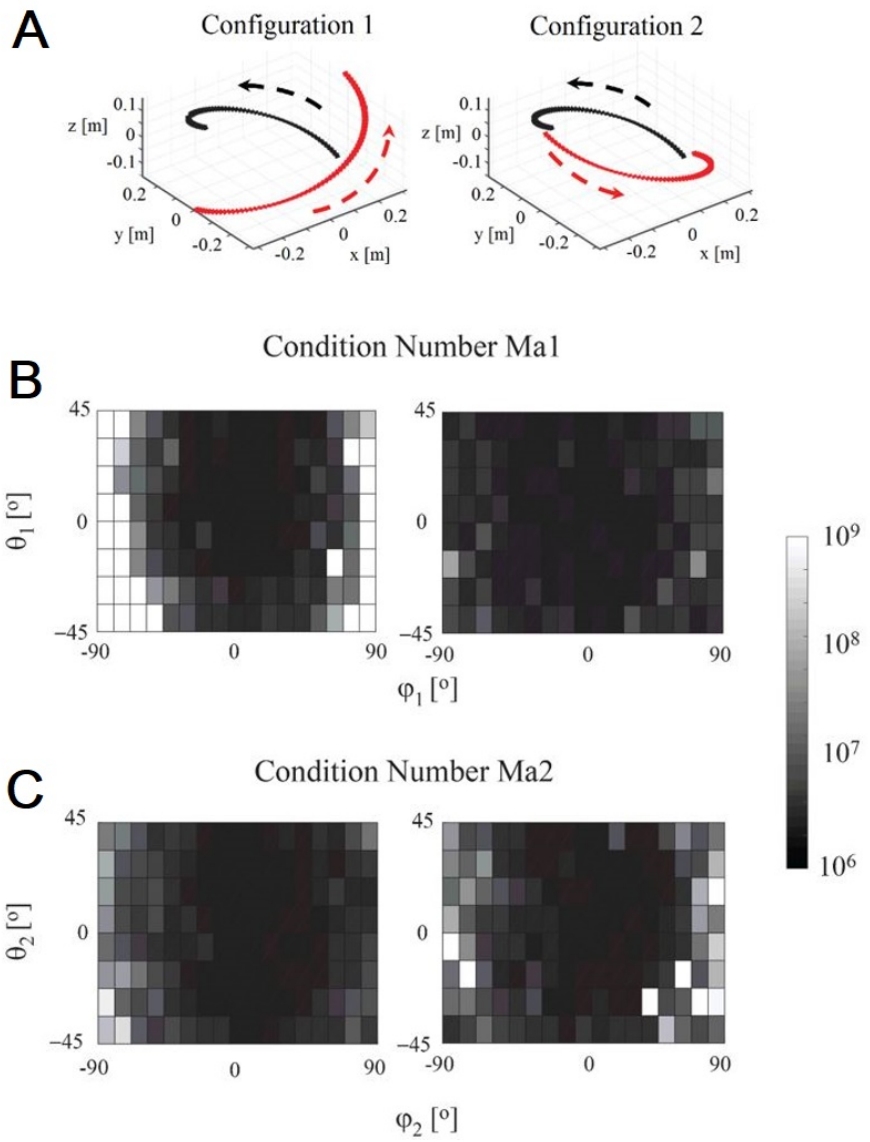

Figure 35: Encoding matrix condition number vs magnet orientations Ma*1 and* Ma*2 for configuration 1 (left column) and configuration 2 (right) column. (A) The paths and the arrows indicate the magnet motion. At each encoding step, the magnets are opposite to each other (xy-plane projection) and encircle the sample. (B) Condition number for* Ma*1 with optimal orientation of* Ma*2. (C) Condition number for* Ma*2 with optimal orientation for* Ma*1.*

The polar and azimuthal angles of the encoding magnets Ma_1 and Ma_2, were independently varied to determine the minimal condition number and optimal orientation. Figure 36B shows the condition numbers for Ma_1 for different combinations of φ_1 and θ_1 keeping φ_2 and θ_2 for Ma_2 at their optimum (left panel shows results for Configuration 1 and right panel shows results for Configuration 2. Figure 36C shows the condition numbers for Ma_2 for different combinations of φ_2 and θ_2 keeping φ_1 and θ_1 for Ma_1 at their optimum for each of the corresponding configurations. The optimal orientation angles for the two magnets are perpendicular to the magnet path (φ_1^{opt} and $\varphi_2^{opt} \sim 0^o$) and parallel to the xy-plane (θ_1^{opt} and

θ_2^{opt} ~ 0°). The reconstructed images for each configuration are shown in Figure 37. The standard deviations for configurations 1 and 2 were 0.0254 and 0.0287 respectively; image quality was higher in the former.

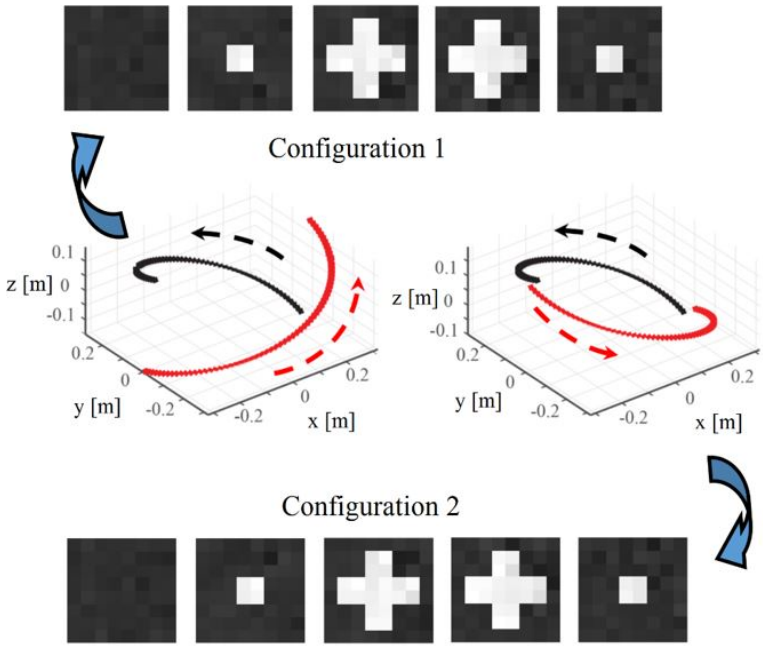

Figure 36: Image reconstruction for the encoding array with two magnets, Ma_1 *(black) and* Ma_2 *(red). The magnet motions are indicated by the arrows for two configurations. The height varies from z = -0.15m to z = 0.15m. The image reconstruction with the Kaczmarz method is shown after 10 iterations. The standard deviations are 0.0254 (configuration 1) and 0.0287 (configuration 2).*

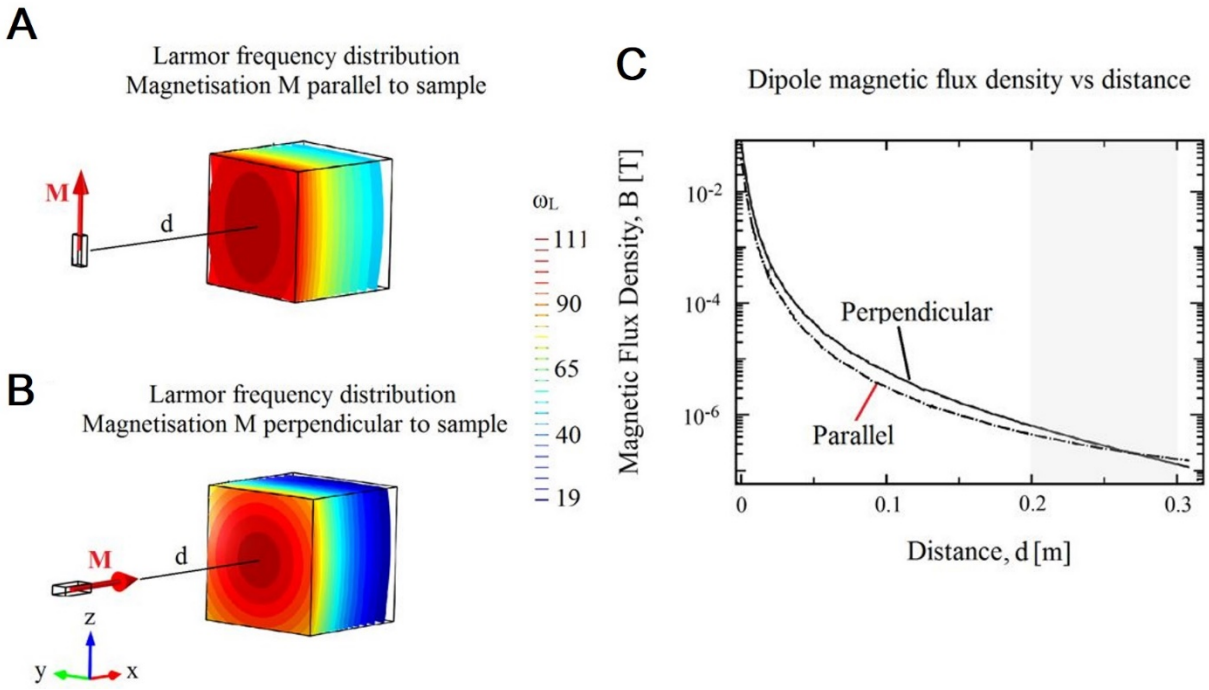

Figure 37: Larmor frequency distribution across the FOV generated by one encoding magnet, sized 6x12x25mm. (A) Encoding magnet is oriented parallel to the FOV which leads to a frequency variation of ~65 Hz. (B) Encoding magnet is oriented perpendicular, which results in a higher frequency variation of ~ 92Hz. (C) Magnetic flux density distribution along the x-axis for parallel encoding magnet orientation (dash-dotted curve) and perpendicular encoding magnet orientation (solid curve 1). In the far region between 0.2-0.3m (grey shaded area) the magnetic field variation is stronger for perpendicular magnet orientation leading to higher Larmor frequency variation and enhanced encoding efficiency since the resulting encoding matrix has a lower condition number.

4.5 Discussion

We introduce a novel 3D spatial encoding method using dynamic SPMAs for ULF-MRI. We developed an in-house simulation method to determine optimal magnet orientations and locations for prescribed path parameters depending on the instrument design. Our approach calculates the discrete magnetic field distribution analytically within the field of view generated by localised magnetic dipoles. The dipole approximation is applicable and accurate since the encoding magnet sizes are assumed to be much smaller compared to the characteristic distances. Our approach allows faster calculation since only feasible solutions are considered for specific construction designs. We describe an encoding array design with one or two magnets for a ULF MRI instrument we have developed, using simple helical magnet motions. Although only spiral paths with equidistant stopping points along a

cylindrical surface were considered, the semi-analytical method can be readily extended to include any number of magnets moving along any prescribed paths.

MATLAB's inbuilt functions *rank* and *cond* were employed to calculate rank and condition number, respectively, of the resulting encoding matrix. The rank is an estimation of the number of linearly independent rows and aimed to be maximised. The maximal rank equals the number of encoding field configurations, *q,* times signal acquisition number *N* per encoding field and determines the total voxel number. The condition number indicate the accuracy of a matrix inversion, with a high magnitude indicating an undesired ill-conditioned problem. A well-conditioned problem (e.g. matrix data) corresponds to a low condition number and hence, in conjunction with image reconstruction lead to higher encoding efficiency.

We applied the Kaczmarz method, an iterative algorithm for solving the linear Equation (57). Based on the results summarised in Figure 33 we assumed 10 iterations until image convergence before attempting image comparison using the standard deviation from the phantom image. This metric allows us to compare the resolving power of the different encoding fields and therefore the reconstructed image quality.

Magnet parameters of commercially available magnets were implemented for the simulation. The low magnet field ($\mathbf{B_r}$ = 0.2 T) of ferrite was chosen so that encoding field strength was comparable to $\mathbf{B_m}$. Bandwidth limitations of the magnetic field sensor were considered. With $\mathbf{B_m}$ of 200 µT (Larmor frequency ≈ 8.5 kHz) the superposition of two encoding magnets Ma_1 and Ma_2 results in an encoding field strength in the field of view ranging from 1-10 µT, corresponding to a frequency spread of 43-430 Hz, well within the bandwidth of our recently developed highly sensitive coil-based magnetometers[178].

Our simulations predict that with a single encoding magnet moving around the sample on a linear helical path 3D images can be acquired without moving the sample or applying additional encoding RF pulses using Bloch-Siebert spatial encoding (BS-SET) or transient array spatial encoding (TRASE)[60]. For the design studied, we found lowest condition numbers were achieved when $z(\alpha)$ was a linear function of α. This is attributed to the low helical path slopes for the nonlinear height variation near the bottom (black curve, $\alpha_2 = 100^o$) and the top (blue curve, $\alpha_2 = 240^o$; see Figure 30B) which lead to lower variation in the encoding field along the z-axis and hence increased linear dependencies and higher condition numbers.

Shortening the path length with constant height variation increased condition number and reduced the quality of the reconstructed image (Figure 35). This result is not unexpected because the step size decreases with reduced path length if the number of voxels is unchanged, leading to an increased linear dependence between encoding field configurations. Additionally, due to the drop in field strength with distance (see Figure 38C), variation in Larmor frequency in the sample is smaller at locations furthest from the magnetic dipole. Image quality is degraded if the encoding magnet does not revolve completely around the sample (see Figure 35, for $\alpha_3 = 180^o$ and $\alpha_3 = 240^o$). Increasing path lengths with one encoding magnet to enhance image quality increases acquisition time and may require more complex mechanical motion control. This acquisition time increase can be alleviated by introducing multiple encoding magnets, each controlled independently.

For the configurations considered, the optimal magnet orientations were perpendicular to both the motion path and the cylindrical surface of Array D. This is a consequence of the torus-shaped magnetic field distribution of a magnetic dipole[177]. Figure 37 schematically illustrates the magnetic dipole orientation and the Larmor frequency determined by the field generated within the sample region, evaluated with COMSOL. The remanent magnetisation of the encoding magnet is $\mathbf{B_r}$ = 0.2 T, and its distance to the sample centre equals 0.25 m. A magnet orientation parallel to the sample (Figure 37A) results in a Larmor frequency variation about 65 Hz, much lower compared to 92 Hz with the perpendicular orientation (Figure 37B). In the far-field region, the magnetic field of the dipole along its direction of magnetisation (Figure 37C, solid curve 1) drops off faster than in the direction orthogonal to this axis (Figure 38C, dash-dotted curve 2), leading to a larger frequency variation along the former axis. Broad regions of low condition number around the optimal angles indicate high tolerances to inaccuracy in encoding magnet alignment and position in these regions.

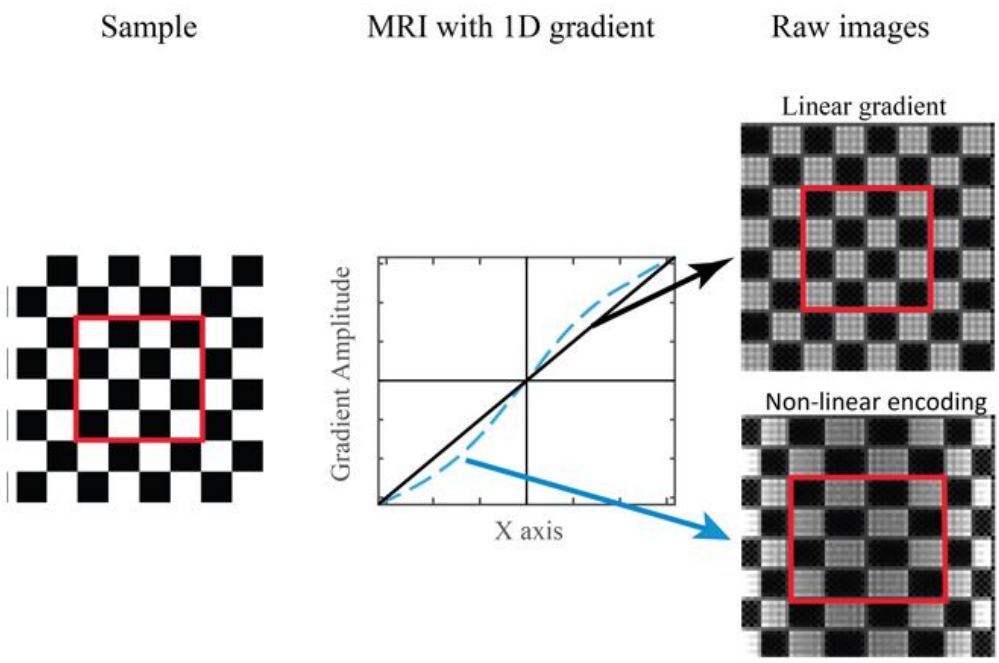

Figure 38: 1D MRI simulations of a 2D chessboard with a linear gradient (solid line) and a 1D nonlinear encoding field (dashed line).

An additional potential advantage of permanent magnet encoding arrays is the ability to control 3D field variations to locally enhance image resolution further. This is illustrated in Figure 38 with a raw image simulation of a 2D chessboard sample acquired with a linear 1D gradient and nonlinear 1D encoding field, respectively. The image resolution in a region of interest, indicated by the red box, is homogeneous for the gradient and depends on the gradient strength. In contrast, the image resolution in the region of interest is higher and depends on the slope of the local encoding field. This approach has been used is used in parallel acquisition technique with localised gradients (PatLoc) to better match the imaging geometry of interest in high field MRI[169]. However, the coil arrangement offers local image enhancements in 2D at fixed locations only. In principle, a flexible and modular permanent magnet encoding arrangement allows the resolution to be enhanced at any location within the sample by spatially varying the paths and magnet orientations to control the magnitude and the spatial encoding field distribution.

4.6 Author contributions

The finite element simulations that estimate the fields for the different permanent magnet locations were done by Vogel. He performed the analysis of the various encoding trajectories through the minimisation of the condition number. Vogel was also the lead writer of the manuscript presented here. Vegh and Reutens were involved with the creation of the

concept and the validation of the results as well as with the writing of the manuscript. I developed the simulation program that efficiently predicts the evolution of the spin magnetisation and its detection. I used this program to analyse the efficiency of the signal for different pre-polarisation transition speeds and encoding arrangements. I then proceeded to reconstruct phantom images, which I analysed to assess the resolving power of varying encoding arrangements. Additionally, I quantified the quality of reconstructed images and validated the matrix analysis performed by Vogel. I wrote the parts of the manuscript concerning my contribution above stated. The reconstruction program was partially developed by Su, who implemented the Kaczmarz method which solves the pseudo-inverse of a matrix.

Chapter 5 - Contributions *Pellicer-Guridi R, Vogel MW, Reutens DC, Vegh V. Towards ultimate low frequency air-core magnetometer sensitivity. Scientific reports. 2017 May 23;7(1):2269*	
Contributor	Statement of contribution
Pellicer-Guridi R (Candidate)	Conception and design (85%) Analysis and interpretation (85%) Drafting and production (80%)
Vogel MW	Conception and design (5%) Analysis and interpretation (10%) Drafting and production (0%)
Reutens DC	Conception and design (5%) Analysis and interpretation (0%) Drafting and production (5%)
Vegh V	Conception and design (5%) Analysis and interpretation (5%) Drafting and production (15%)

Chapter 5- Towards ultimate low frequency air-core magnetometer sensitivity: A design method

5.1 Abstract

Air-core magnetometers are amongst the most commonly used magnetic field detectors in biomedical instruments. They offer excellent sensitivity, low fabrication complexity and a robust, cost-effective solution. However, air-core magnetometers must be tailored to the specific application to achieve high sensitivity, which can be decisive in the accuracy of the diagnoses and the time required for the examination. Existing methods proposed for the design of air-core magnetometers are based on simplified models and simulations using a reduced number of variables, potentially leading to sensitivity that is suboptimal. To circumvent this, we chose a method with fewer assumptions and a larger number of decision variables which employed a genetic algorithm, a global optimisation method. Experimental validation shows that the model is appropriate for the design of highly sensitive air-core magnetometers. Moreover, our results support the suitability of a genetic algorithm for optimisation in this context. The new method described herein will be made publicly available via our website to facilitate the development of less costly biomedical instruments using air-core magnetometers with unprecedented sensitivity.

5.2 Introduction

Air-core magnetometers are preferred for many biomedical applications because of their high sensitivity, robustness and low construction cost. Although magnetometers with a ferromagnetic core can reach higher sensitivities than air-core magnetometers[179], they cannot be used in applications where the distortion of the signal or the magnetic field is not acceptable. Biomedical applications of air-core magnetometers include magnetic induction tomography (MIT)[180], ULF MR[24] and magnetocardiography (MCG)[181]. Customising coil design to specific biomedical applications may lead to a considerable improvement in sensitivity[179], enabling earlier diagnosis and more accurate monitoring of disease. Additionally, most applications use signal averaging to achieve the desired signal-to-noise ratio, and increasing coil sensitivity would confer the benefit of reduced acquisition time, in proportion to the square of the additional sensitivity.

Air core magnetometer sensitivity is determined by the ratio between the electromotive force (*EMF*) induced in the coil and the electronic noise of the detector. The noise floor of air-core magnetometers is dominated by the thermal noise of the coil, the noise of the pre-amplifier, and the noise of any lumped elements connected to the input of the pre-amplifier, such as

tuning capacitors. The task of optimal coil design is that of maximising the ratio between *EMF* and all other contributing noise sources. The primary design variables for air core magnetometers are the frequency range, coil size, pre-amplifier properties (gain, noise floor and pre-amplification mode), conductor diameter, and the number and location of loops. The application delimits some of these variables, such as the outer radius of the coil and its frequency range, whereas the most difficult variables to determine are often conductor diameter and the number of loops and their locations.

Various analytical solutions have been proposed to optimise the design of air-core magnetometers[182] and closely related ferromagnetic-core induction magnetometers[183,184]. Analytical solutions can offer a direct understanding of how different parameters affect the theoretical sensitivity of magnetometers. Furthermore, they provide a function that can be solved for optimal coil parameters[185]. However, a major challenge remains to solve the analytical problem maintaining accurate but more complex models of the electrical properties of the coil, i.e. resistance, inductance and parasitic capacitance. The accuracy with which these values can be specified affects the analytical solution.

Numerical methods have been described for the optimisation of air-core magnetometer designs[181,186-191]. These have the benefit of requiring fewer assumptions than analytic methods. However, it is essential to match the optimisation algorithm to the problem to mitigate against finding a local instead of a global solution[185]. Estola et al. simulated some magneto-cardiograms with non-rectangular coil cross-section for detecting a near-field source in the band 0.5-100 Hz[181]. Wire diameter was determined using a brute force strategy using simulated designs based on a simplified model for the magnetic source and employing an established computer-aided design methodology. Chen et al. described an optimisation method which maximised signal-to-noise ratio (SNR) and minimised coil diameter for coils operating in the range of tens of Hz to 71 kHz[186]. The upper limit on the frequency was determined by the constraint of magnetometer weight. Here, coil design was limited to a single layer, and the search for the optimal number and diameter of coil loops was deduced from a plot of sensitivity for different coil combinations. An optimal broadband air-core magnetometer, based on the Brooks coil, was later developed and its sensitivity was analysed in the absence of amplifier noise[192]. Subsequent work yielded the optimised minimum air-core coil size based on a fixed cut-off frequency and a specific type of amplifier[188]. Details about the optimisation algorithm used to obtain the parameters were, however, not provided. An air-core magnetometer has also been designed specifically for ULF-MRI[187]. The average coil diameter was optimised, and conductor thickness was chosen

based on skin depth for copper wire tuned to 3 kHz ULF-MRI applications. Additional work on ferromagnetic-core magnetometers has focused on maximising sensitivity with constraints on the weight and size of the coils[190,191].

Our approach to improving the design of air-core magnetometers is to relax the constraints on the optimisation process with the objective of increasing coil sensitivity. To achieve this goal, we use more accurate but more complex analytical expressions, the parameters of which are deduced using a global optimisation procedure. We allowed conductor diameter, distance between wires, number of coil layers and number of turns per layer to be free variables. A genetic algorithm was employed to search for the globally optimal solution. In what follows, numerical models for two popular pre-amplification modes are first presented, followed by an outline of non-tuned current-to-voltage and tuned voltage-to-voltage designs. The non-tuned current-to-voltage design, commonly known as the trans-impedance amplifier, is desirable in many applications due to the linear frequency gain response and excellent sensitivity below 1 kHz. The tuned voltage-to-voltage design has the potential to provide additional sensitivity with narrower bandwidths, most notably for higher frequency applications. Empirical measurements were used to validate the numerical models used for the optimisation of air-core magnetometers.

5.3 Methods

5.3.1 Numerical model

Individual components used in the numerical procedure have been described previously. Each model is outlined in detail without imposing assumptions.

5.3.2 Coil

The electrical properties of the coil are represented by the AC resistance (R_{S_AC}), inductance (L_S) and the parasitic capacitance (C_S) based on knowledge of conductor location and diameter. Assuming wires are equally distributed within the coil winding, individual locations are estimated based on coil outer diameter, number of layers and turns per layer, conductor diameter and wire spacing (see Figure 39). In the case of a single strand solid conductor with diameter d_i, the DC resistance R_{S_DC} is calculated for the total wire length l_{total} such that $R_{S\_DC} = \rho_{copper} \cdot l_{total}/(\pi \cdot (d_i/2)^2)$. The AC resistance can be calculated as[103]:

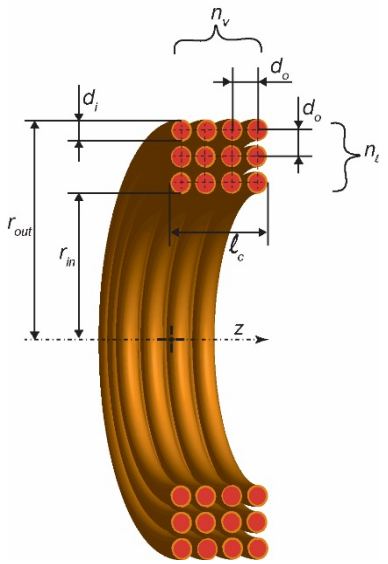

Figure 39: Cross-section of the coil showing its parameters that can be varied. Optimisation variables are shown in bold: d_i is the conductor diameter, d_o is the conductor spacing, n_l the number of layers and n_v the number of loops per layer. Inner and outer radius of the coil are represented as r_{in} and r_{out}, respectively.

$$R_{ac} = R_{dc}\left(1 + F(z) + u(N)\cdot\frac{d_i^2}{d_o^2}\cdot G(z)\right), \tag{61}$$

$$F(z) = \frac{z^2}{8} Im\frac{J_3\left(z\sqrt{-i}\right)}{J_1\left(z\sqrt{-i}\right)}, G(z) = \frac{z^2}{8} Im\frac{J_2\left(z\sqrt{-i}\right)}{J_0\left(z\sqrt{-i}\right)}, \tag{62}$$

$$z = \sqrt{\frac{d_i^2}{4}\omega\mu_0 \Big/ \rho_{copper}}, \tag{63}$$

where $F(z)$ and $G(z)$ are functions representing the skin depth and conductor proximity effects, respectively, and J corresponds to Bessel functions of the first kind. $u(N)$ depends on the separation of conductor centres (d_o in Figure 39), radius of individual loops (r_{loop}), z-axis offset of each loop (z_{loop}) and the number of loops (N). Thereby,

$$u(N) = \frac{1}{N}\sum_{i=1}^{N}\left\{\left(\sum_{j=1,j\neq i}^{N}\frac{r_{loop,j}-r_{loop,i}}{\left(r_{loop,j}-r_{loop,i}\right)^2+\left(z_{loop,j}-z_{loop,i}\right)^2}\right)^2 + \left(\sum_{j=1,j\neq i}^{N}\frac{z_{loop,j}-z_{loop,i}}{\left(r_{loop,j}-r_{loop,i}\right)^2+\left(z_{loop,j}-z_{loop,i}\right)^2}\right)^2\right\}. \quad (64)$$

In the case of Litz wires, the calculation of R_{S_DC} and R_{S_AC} is obtained via Equation (65) and Equation (66) with t_{yard} being the outer insulation of the wire, and with N_S, N_B and N_C defining the number of strands, number of bunching and cabling operations of the Litz wire respectively. The packing factor p was predefined: p = 1.25 for $N_S \leq 11$; p = 1.26 for $11 < N_S \leq 15$; p = 1.27 for $15 < N_S \leq 24$; and p = 1.26 for $24 < N_S < 400$. Hence,

$$R_{S\_AC} = R_{S\_DC}\left(1 + F(z) + (u(N)+2)\cdot\frac{N_S^2 d_i^2}{d_o^2}\cdot G(z)\right), \quad (65)$$

$$d_{i\_strand} = \frac{d_i - t_{yarn}}{p\sqrt{N_S}};\ R_{S\_DC} = R_{S\_DC\_strand}\cdot\frac{1.015^{N_B}\cdot 1.025^{N_C}}{N_S}. \quad (66)$$

Coil inductance and capacitance were calculated numerically using a previously described method[193]. The total inductance is a sum of self-inductance (L_0) and mutual inductance (M_0) such that $L_S = L_0 + M_0$. The self-inductance employs the argument $k_{L,i}^2 = 4r_{loop,i}\cdot(r_i - d_i/2)/(2r_i - d_i/2)^2$, where μ_0 is the magnetic permeability of air, and E and K the elliptic integrals of first and second kind, such that

$$L_0 = \mu_0\cdot\sum_{i=1}^{N}\left(2r_{loop,i} - \frac{d_i}{2}\right)\left\{\left(1-\frac{1}{2}k_{L,i}^2\right)K\left(k_{L,i}\right) - E\left(k_{L,i}\right)\right\}. \quad (67)$$

As for M_0, the arguments of k_L incorporate an extra dimension to capture the mutual coupling between conductors, hence $k_{L,i,j}^2 = 4r_{loop,i}\,r_{loop,j}/\left(r_{loop,i}+r_{loop,j}\right)^2 + \left(z_{loop,i}-z_{loop,j}\right)^2$. The mutual inductance is then estimated as

$$M_0 = 2\mu_0\cdot\sum_{i=1}^{N}\sum_{j=1,j\neq i}^{N}\frac{\sqrt{r_{loop,i}-r_{loop,j}}}{k_{i,j}}\left\{\left(1-\frac{1}{2}k_{L,i,j}^2\right)K\left(k_{L,i,j}\right) - E\left(k_{L,i,j}\right)\right\}. \quad (68)$$

The equation for stray capacitance:

$$C_s = \frac{8\pi\varepsilon_0\varepsilon_r l_c(n_l - 1)}{6{N_L}^2(1.26d_o - 1.15d_i)}\{2r_{in} + d_o\}, \quad (69)$$

was proposed by Martinez et al.[193], and is expressed here for the case of equally spaced conductors. Equation (69) is a function of the relative electrical permittivity of the coating layer (ε_r), coil length (l_c), number of layers (n_l) and coil internal radius r_{in}, and ε_0 is the electrical permittivity of free-space. *EMF* induced in the coil was calculated in volts per Tesla by Lorentz's principle of reciprocity: $emf/B_\perp = j2\pi\sum_{i=1}^{N}\pi r_{loop,i}^2$, where $B_\perp$is the component of the magnetic field normal to the *z*-axis.

<u>*Non-tuned current-to-voltage amplifier design*</u>: Trans-impedance amplification, as shown in Figure 40, is one of the most used pre-amplification modes with coil based magnetometers because of its good sensitivity at frequencies below 100 Hz and its wide linear gain range[181-184,186,188,190]. In this design, the *EMF* generates a current which is forced to pass through the feedback resistor (R_f) generating a voltage proportional to the *EMF* at the output of the amplifier.

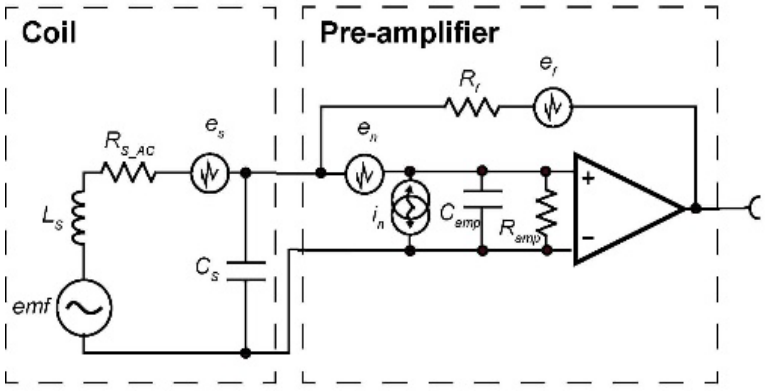

Figure 40: Schematic of the non-tuned current-to-voltage amplifier including noise sources. The equivalent circuit of the coil (left) and pre-amplifier (right) are shown. Depending on the pre-amplifier, the thermal noise of the feedback resistor (e_f) may be substituted by a minimum output voltage noise.

The noise floor of the setup is used to estimate magnetometer sensitivity (ζ) such that

$$\zeta(f) = \frac{emf(f)}{e_{nti}(f)}. \quad (70)$$

Here, $e_{nti}(f)$ measures the frequency dependent total voltage noise to the input of the amplifier, in units of v/√Hz. The noise itself is calculated using $e_{nti} = \sqrt{e_{ni}^2 + e_{ii}^2 + e_{si}^2 + e_{fi}^2}$, where e_{ni}^2 is the noise induced from the voltage noise of the pre-amplifier, e_{ii}^2 is the noise generated by the current noise of the pre-amplifier, e_{si}^2 is the thermal noise produced by the coil and e_{fi}^2 is the thermal voltage noise from the feedback resistor R_f. Noise sources at the input of the amplifier are expressed as

$$e_{ii} = i_{in} \cdot |Z_s|; \tag{71}$$

$$e_{si} = \sqrt{4k_b T R_s};, \tag{72}$$

$$e_{fi} = \sqrt{4k_b T R_f} \cdot \left|Z_s/\left(R_f + Z_s\right)\right|; \tag{73}$$

$$X_{Ls} = j2\pi f L_s; \tag{74}$$

$$X_{Cs} = \frac{1}{j2\pi f C_s}; \tag{75}$$

$$Z_s = \frac{(R_s + X_{Ls})X_{Cs}}{R_s + X_{Ls} + X_{Cs}}; \tag{76}$$

where Z_S is coil impedance, k_b is Boltzmann's constant (1.38e-23 J/°k), and T is the temperature (300 °K at room temperature). In this design, current and voltage noise sources are assumed to be uncorrelated. In the case of instrumentation amplifiers, such as INA217 for which the minimum noise to the output e_{o_min} is provided, the equivalent noise at the input (e_{i_on}) is substituted for noise from the feedback such that $e_{i\_on} = e_{on} \cdot \left|Z_s/\left(R_f + Z_s\right)\right|$.

Tuned voltage-to-voltage amplifier design: Tuned magnetometers use a resonant circuit to enhance the sensitivity at a specific frequency of operation. The tuned voltage-to-voltage amplifier is the most commonly used amplification design for this purpose. We chose the inverted-L matching network configuration since it uses a small number of capacitors and does not incorporate extra inductors which may lead to additional losses in signal, especially at low frequencies. The loss introduced by the parasitic resistance of the capacitors is calculated through their equivalent series resistance (ESR). The quality factor (*Q*) of the capacitor with capacitance (*C*) can be converted to ESR by

$$ESR = 1/2\pi fCQ. \tag{77}$$

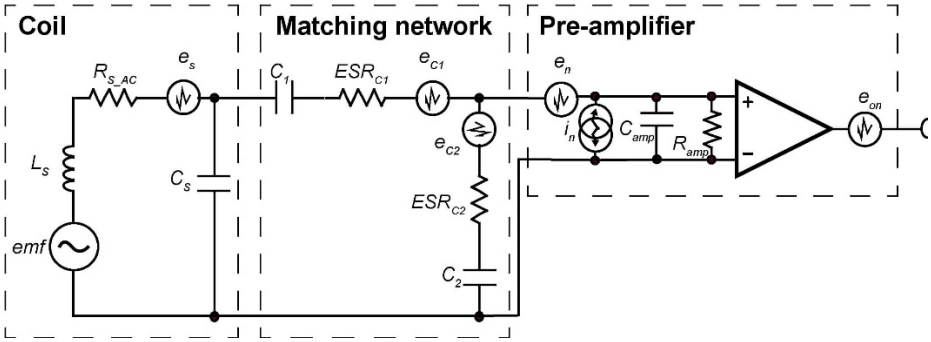

Figure 41: Equivalent circuit diagram for the tuned voltage-to-voltage pre-amplification design. Shown are individual equivalent circuits for the coil (left), matching network (centre) and pre-amplifier (right).

The tuning and matching network is necessary to set the frequency (f_0) of the coil as previously described[194]. At this frequency, the tuning and matching network transforms the coil impedance (Z_S) to the apparent source impedance (R_{match}) measured at the input of the amplifier, and the transformation ratio is $m = R_{match}/R_{S\_AC}$. For this transformation, the required quality factor Q_{req} of the resonant circuit comprising the coil and the tuning and matching network is first calculated using $Q_{req} = \sqrt{m-1}$. Then, the total reactance is obtained ($X_{S\_total} = Q_{req}R_S$). Additionally, the reactance of the series network capacitor C_1 is computed ($X_{s\_tun1} = X_{S\_total} - X_S$, where X_S is the imaginary part of Z_S). Finally, the equivalent parallel impedance, the conjugate of the impedance of the second tuning capacitor (C_2), is calculated ($X_{S_{total_p}} = X_{S_{total}} \cdot \left(1 + 1/Q_{req}^2\right)$). The input capacitance of the amplifier (C_{amp}) can contribute significantly in specific designs, and is therefore considered here. The values for the tuning capacitors are:

$$C_1 = \frac{1}{j2\pi f_0 \cdot (X_{S\_tun1})}, \tag{78}$$

$$C_2 = \frac{1}{j2\pi f_0 \cdot -(X_{S\_total\_p})} - C_{amp}. \tag{79}$$

Once the values for the tuning and matching capacitors have been established, their ESR is determined using a look-up table created from datasheets provided by the manufacturer. ESR is highly dependent on the operating frequency and capacitance, as shown in Figure 42; *Q* varies accordingly with capacitance and frequency.

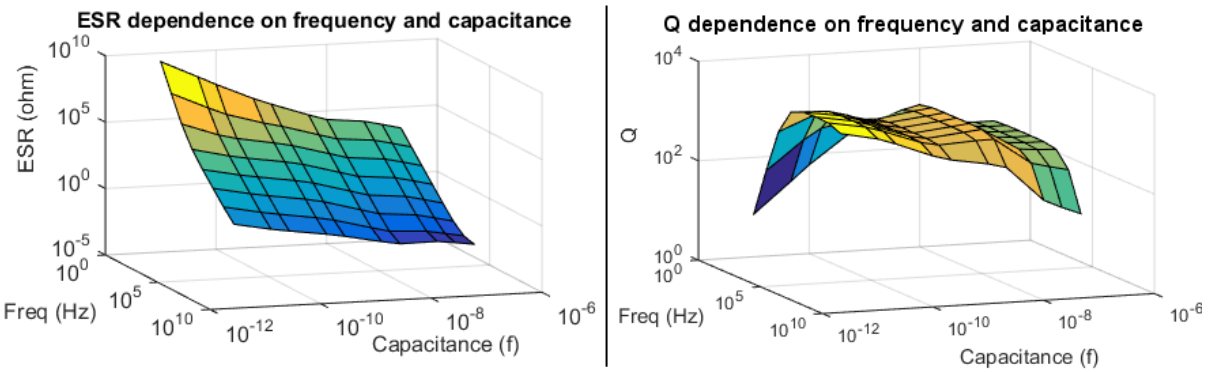

Figure 42: Plots of the interpolated look-up table employed to estimate the ESR of capacitors (left) and corresponding quality factor (right). The plots show that both ESR and Q are highly dependent on capacitance and frequency of operation.

The effective gain (G_{eff}) the *EMF* experiences has to take account losses due to the incorporation of the matching network capacitors. Additionally, thermal noise sources are added for each of the capacitors (e_{C1} for ESR_{C1} and e_{C2} for ESR_{C2}). The total voltage noise is then defined as $e_{nti} = \sqrt{e_{ni}^2 + e_{ii}^2 + e_{si}^2 + e_{C1i}^2 + e_{C2i}^2 + e_{oni}^2}$ measured at the amplifier input. In summary, the components of the tuned voltage-voltage design can be calculated as:

$$e_{ii} = i_n \cdot |Z_{th}|; \tag{80}$$

$$e_{si} = \sqrt{4k_bTR_s} \cdot |G_{eff}|; \tag{81}$$

$$e_{C1i} = \sqrt{4k_bT \cdot ESR_{C1}} \cdot |G_{C1}|; \tag{82}$$

$$e_{C2i} = \sqrt{\frac{4k_bT}{EPR_{C2}}} \cdot |Z_{th}|; \quad (83)$$

$$e_{oni}^2 = \frac{e_{on}^2}{G}; \quad (84)$$

$$Z_{th} = \frac{X_{a\_C1}(Z_s + X_{C1} + ESR_{C1})}{X_{a\_C1} + Z_s + X_{C1} + ESR_{C1}}; \quad (85)$$

$$G_{eff} = \frac{Z'_{a\_C1}}{Z'_{a\_C1} + X_{Ls} + R_s}; \quad (86)$$

$$G_{C1} = \frac{Z_{a\_C1}}{Z_{a\_C1} + Z_S + X_{C1} + ESR_{c1}}; \quad (87)$$

$$EPR_{C2} = \left(1 + \left(\frac{1}{2\pi f C_2 ESR_{C2}}\right)^2\right) \cdot ESR_{C2}; \quad (88)$$

$$Z_{a\_C1} = \frac{1}{\frac{1}{X_{C2} + ESR_{C2}} + \frac{1}{X_{Camp}} + \frac{1}{R_{amp}}}; \quad (89)$$

$$Z'_{a\_C1} = \frac{X_{Cs}\left(Z_{a\_C1} + X_{C1} + ESR_{C2}\right)}{X_{Cs} + Z_{a\_C1} + X_{C1} + ESR_{C2}}. \quad (90)$$

Z_{a_C1} is the impedance seen from the first capacitor towards the amplifier, Z_{th} is the equivalent Thevenin impedance of the coil and matching network measured at the amplifier input, G_{C1} is the gain experienced by the voltage noise from C_1 to the input of the amplifier, and G is the gain of the pre-amplifier. The noise floor can be stated as

$$\zeta(f) = emf(f) \cdot \frac{G_{eff}(f)}{e_{nti}(f)}. \quad (91)$$

5.3.3 Validation of numerical models

A small and a large coil (Figure 43) were built along with non-tuned and tuned amplifiers. We adapted the matching network to each coil. The small coil used 38 layers with 41 loops per layer, resulting in an outer radius of 19 mm and height of 10 mm. The copper conductor had a diameter of 0.2 mm and conductors were spaced 0.24 mm apart. The bigger coil had 5 layers with 21 loops per layer, resulting in an outer radius of 60 mm and height of 18 mm.

The copper conductor, in this case, had a 0.8 mm diameter and was spaced 0.86 mm apart (RS Components Pty. Ltd., Smithfield, Australia).

Figure 43: Coil prototypes. The small coil (left) comprises 38 layers, 43 loops per layer with an outer radius of 19 mm and height of 10 mm. The copper conductor had a diameter of 0.2 mm and conductors were spaced 0.22 mm). The big coil (right) is composed of 5 layers, 21 loops per layer with an outer radius of 60 mm and height of 18 mm. The copper conductor had a diameter of 0.8 mm and conductors were spaced 0.86 mm).

The instrumentation amplifier (INA217 from RS Components Pty. Ltd.) was used for both the non-tuned and tuned designs (see Figure 40 and Figure 41). Measured input voltage noise was 1.3 nV/√Hz, input current noise was 0.8 pA/√Hz, and output noise was 90 nV/√Hz. A second stage amplification step with a gain of 1000 was added to the non-tuned pre-amplifier to minimise noise floor and improve discretisation (NI6259, National Instruments, US). The gain of the tuned voltage-to-voltage pre-amplifier was 1000; a second stage amplification step was not required.

Coil sensitivity was determined using a combination of two measurements. First, a Helmholtz pair was used to assess the field-to-voltage conversion of the magnetometer. The magnetometer was located coaxially in the centre of the Helmholtz pair, and the field was calculated as $B_{\perp} = 8\mu_0 N_{Helm} I / 5\sqrt{5}\, a$, where μ_0 is free-space permeability ($4\pi \cdot 10^{-7}$ T·m/A), I is the current in the coils, a is coil radius, and N_{Helm} is the number of turns in each Helmholtz coil. A pre-determined current was applied to the Helmholtz pair at a selection of different frequencies to compute the field-to-voltage conversion in the frequency band of interest. Second, the electronic noise floor of the magnetometer was measured by placing the magnetometer in a magnetic shielding box (1.5 m^3) that attenuated background electromagnetic radiation to a level below magnetometer sensitivity. The sensitivity of the

magnetometer (T/√Hz) was then calculated by dividing the measured noise floor (V/√Hz) by the measured field to voltage conversion ratio (V/T).

5.3.4 Optimisation algorithm

The optimisation algorithm allowed the following decision variables to evolve: number of layers, number of loops per layer, and conductor diameter and spacing. Other variables, such as coil outer diameter, amplifier noise sources and ESR look-up table for the tuning and matching capacitors were user-defined.

Traditionally, adjusting the apparent coil impedance at amplifier input to equal $R_{match\_class} = e_{ni}/i_{ni}$ is found to give the optimum SNR when the noise sources i_{ni}, e_{ni} and e_{si} are the main contributors of the total noise and *EMF* increases proportionally with coil impedance. Since this conditions are not fulfilled here, noise matching was left to the optimisation algorithm. The search strategy for the optimum sensitivity is done differently for the tuned and the non-tuned configurations. In the case of the non-tuned design, the genetic algorithm searches for the optimum noise configuration because it has control over the impedance of the coil. The case of the tuned design is different because the matching network can influence the apparent impedance of the coil presented to the amplifier through effective adjustments to the transformation ratio. We performed this adjustment by calculating the sensitivity over a range of conversion ratios for each coil configuration evaluated by the genetic algorithm and selecting the conversion ratio achieving the best sensitivity. The range of R_{match} was chosen to be $e_{ni}/i_{ni} \leq R_{match} \leq 4k_bT/in^2$; the upper limit corresponds to where amplifier current noise matches coil thermal noise. The sensitivity was tabulated for 20 logarithmically equidistant values for R_{match}, and capacitor values achieving best sensitivity were selected.

To find optimal values for the decision variables, ga, an inbuilt MATLAB® function was employed. Equation (70) was used as the cost function for the non-tuned case, and Equation (91) for the tuned case. We used the following constraints: $d_i < d_o,\ 1 < n_v < 100,\ 1 < n_l < 100,\ 0.101 < d_i < 5\ (mm),\ 0.1 < d_o < 4.9\ (mm)$. A penalty was imposed to prevent solutions in which the self-resonant frequency of the coil (f_{self}) is close ($f_{self} \leq 10\ f_o$) to the frequencies of interest (f_0). The penalty was implemented by multiplying the sensitivity by a factor $p = 1 + (10f_0 - f_{self})/10f_0$. Cost function tolerance was set to be at least two orders of magnitude lower than the expected sensitivity value. First and second kind elliptic integrals were evaluated using, ellipke, another inbuilt MATLAB® function, and tolerance was changed from the default value to 1e-3 to speed up the calculations by up to a factor of

10. Simulations were executed on an eight core Intel computer with an i7-2600 3.4 GHz CPU and 16 GB RAM.

Reproducibility was assessed for a number of different magnetometer setups and computational times were recorded. Sensitivity curves for different configurations were analysed. The influence of the matching and tuning network, of lossy capacitors and of using Litz wires were also analysed. The optimal solutions obtained with the proposed method were compared with the Brooks coil design. The benefit of using Litz wires was evaluated as well.

5.4 Results

We first validate the numerical models against experimental measurements performed in two coils for the non-tuned current-to-voltage and tuned voltage-to-voltage amplification configurations. Afterwards, we evaluate the optimisation algorithm.

5.4.1 Numerical model

Table 5 quantifies the error between predicted and measured electrical properties of the in-house built air-core magnetometers. The simulated and measured DC resistance and AC resistance at 10 kHz, inductance, and capacitance of prototypes differed by only 2%, 3%, 4% and 15%, respectively.

Table 5: Comparison of the electrical properties between simulated and empirically measured values in two different in-house built coils. The parameters are number of layers (n_l), number of loops per layer (n_v), conductor diameter (d_i) and spacing (d_o), coil outer radius (r_{out}), DC resistance (R_{S_DC}), AC resistance at 10 kHz (R_{S_AC}), inductance and parasitic capacitance of the coil.

	Coil param. (u. & mm)					R_{S_DC} (Ω)		R_{S_AC} (Ω) 10 kHz		Induct. (mH)		Paras. Cap. (pf)	
	n_l	n_v	d_i	d_o	r_{out}	Theo	Meas	Theo	Meas	Theo	Meas	Theo	Meas.
Small coil	38	41	0.2	0.24	19	71.2	72.4	75.1	76.4	57.4	55.5	18	21
Big coil	5	21	0.8	0.86	60	1.29	1.31	2.14	2.2	2.15	2.16	258	261

The magnetic field sensitivity of the current-to-voltage and voltage-to-voltage coils is provided in Figure 44. The non-tuned current-to-voltage coil sensitivity in the range 1 kHz - 100 kHz is shown in Figure 44A. Respectively, the simulated and measured mean sensitivities are 544 fT/√Hz and 558 fT/√Hz for the small coil and 22.7 fT/√Hz and 22.3 fT/√Hz for the large coil. Figure 43 shows the sensitivities for the same coils but with tuned

voltage-to-voltage amplification at 10 kHz. For a 1 kHz bandwidth, the simulated and measured sensitivities for the small coil are 24.5 fT/√Hz and 23.7 fT/√Hz and simulation with ideal capacitor yields a sensitivity of 19.6 fT/√Hz. Corresponding peak sensitivities are 29.7 fT/√Hz, 30.3 fT/√Hz and 26.2 fT/√Hz. Similarly, for the larger coil, the mean values are 4.3 fT/√Hz for measured, 3.8 fT/√Hz simulated with lossy capacitors and 3.4 fT/√Hz simulated using an ideal matching network. Peak sensitivities are 3 fT/√Hz, 3.4 fT/√Hz and 4 fT/√Hz. By accounting for ESR in the simulations, the accuracy of the numerical model improves 80% for the small coil and by 40% for the big coil.

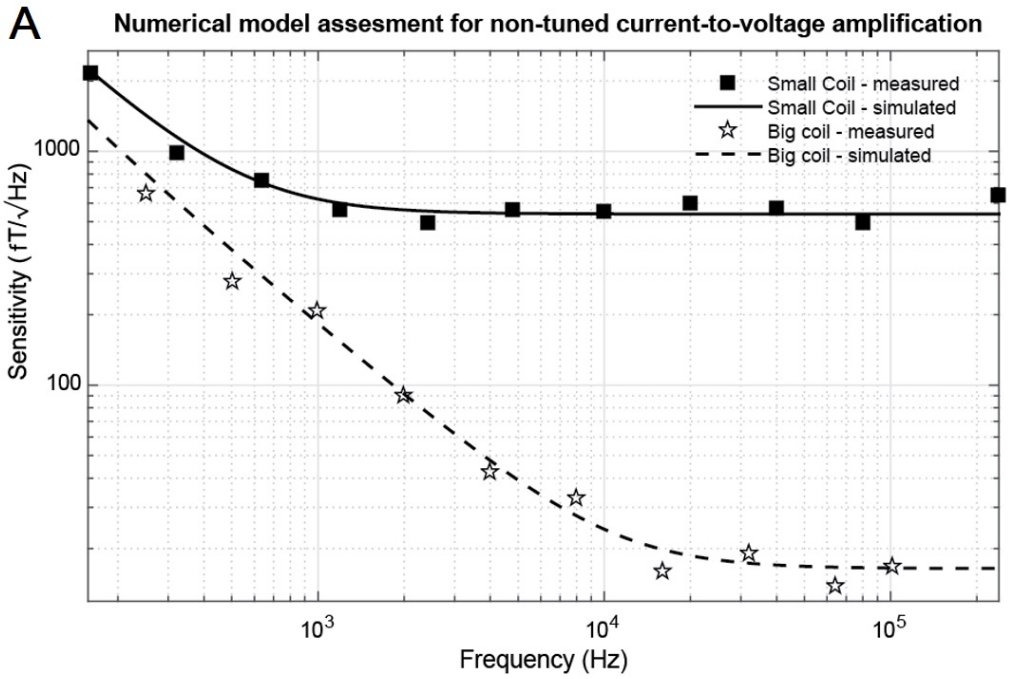

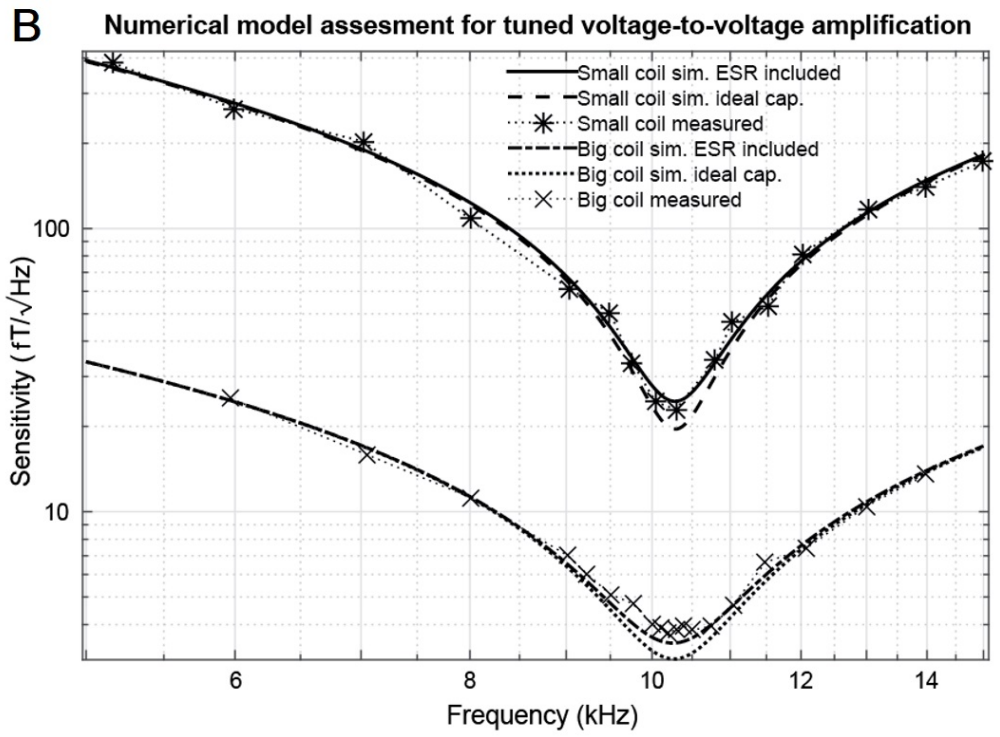

Figure 44: Sensitivity comparison between measured and estimated values for non-tuned current-to-voltage (A) and tuned voltage-to-voltage with ideal and lossy capacitors (B).

The reproducibility of the results obtained using the optimisation procedure for a specific case (r_{out} = 45 mm, f_0 = 10 kHz, bw = 1 kHz, INA127, $Q_{C1} \approx Q_{C2} \approx 200$) is provided in Figure 45. Multiple runs of the algorithm result in a coefficient of variation of 1.5 % for non-tuned current-to-voltage magnetometers and 0.6 % for the tuned voltage-to-voltage configuration. The average optimal sensitivity is 2.4% higher than the best solution found by the solver in the non-tuned case and 0.5% in the tuned mode. The time to reach a solution scales with the number of coil loops in the design. For example, it takes approximately one minute to optimise a 300 loop coil configuration whereas it may take as long as 60 minutes to find an optimal solution for a 5000 loop coil arrangement. In the latter case, about 85% of the computation time is associated with the computation of the elliptic integrals.

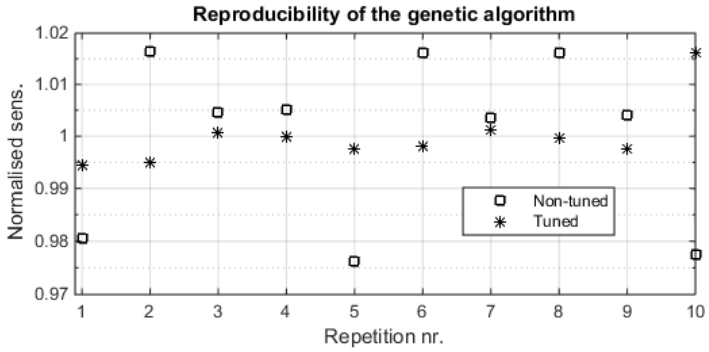

Figure 45: Reproducibility of the results obtaining using the optimisation algorithm for non-tuned current-to-voltage (squares) and tuned voltage-to-voltage (asterisks) designs. The sensitivities have been normalised to the mean sensitivity for each method.

5.4.2 Optimisation algorithm

The relationship between sensitivity and frequency differs between the non-tuned current-to-voltage and the tuned voltage-to-voltage configurations. For the non-tuned current-to-voltage configuration, the optimal sensitivity range is found at the inflexion point where the slope changes from a negative slope to a constant value as can be seen in Figure 46. In the bandwidth of interest, the sensitivity improves with increasing frequency. The tuned case has the best sensitivity in the vicinity of the resonant frequency as the iterative matching network algorithm tunes the peak voltage of the amplifier to be near the target resonant frequency. This sensitivity enhancement is highlighted in Figure 47A by the gain in *EMF* at the amplifier input. The corresponding sensitivity peak is shown in Figure 47B. Notably, the fact that the sensitivity peak is in the centre of the bandwidth does not necessarily mean

optimal sensitivity. This is corroborated in Figure 47C, where the mean sensitivity of a set of coils optimised for a bandwidth fixed between 9.5 kHz and 10.5 kHz with different offsets in the tuning frequency (r_{out} = 45 mm, f_0 = 10 kHz, bw = 1 kHz, INA127, $Q_{C1} \approx Q_{C2} \approx 200$), is shown. The horizontal axis represents the offset of the tuning frequency referred to the centre frequency of 10 kHz. Here, the sensitivity improvement is less than 1%.

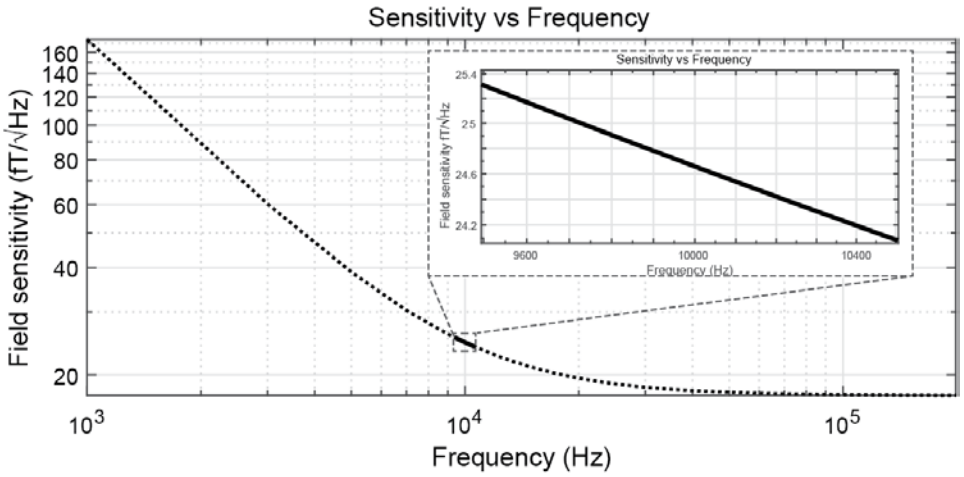

Figure 46: Sensitivity vs. frequency curve of a non-tuned current-to-voltage amplifier, with a zoom into the region for optimal sensitivity operation.

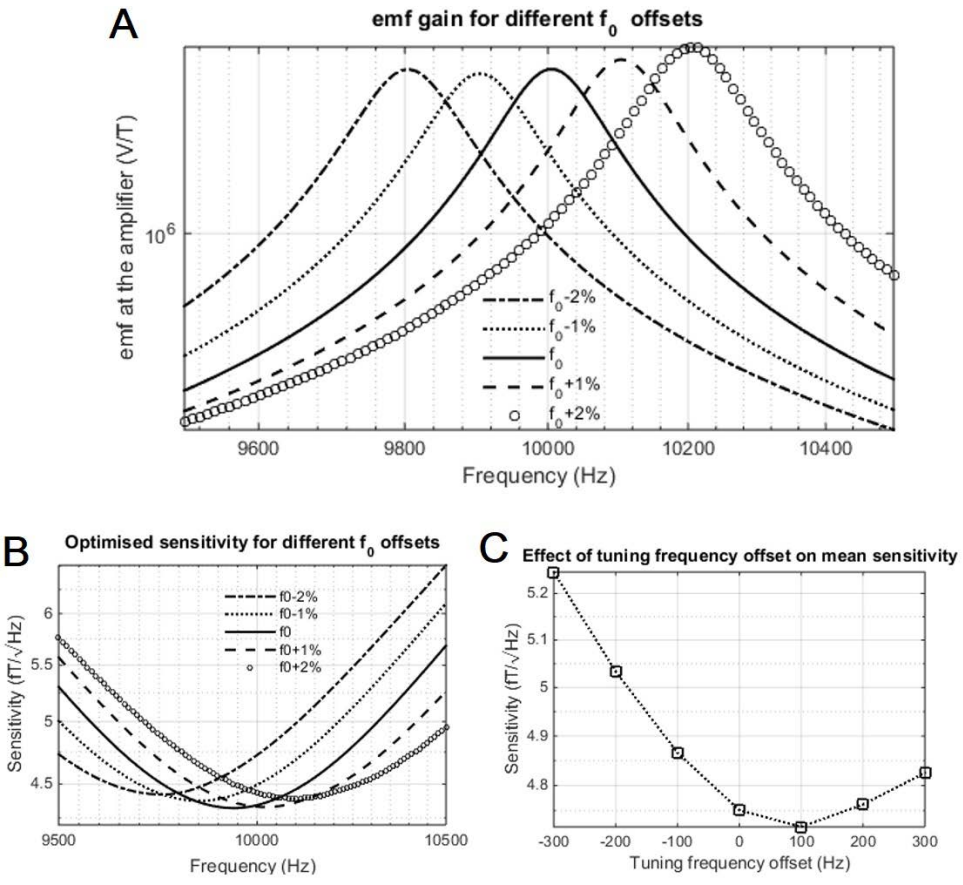

Figure 47: Plot of the EMF (A) at the input of the amplifier, the sensitivity (B) for an optimised coil tuned to 9.8, 9.9, 10, 10.1, and 10.2 kHz and the effect of tuning frequency on average sensitivity (C).

Optimised equivalent coil resistance at the centre frequency measured at the amplifier input (R_{match}) is within proposed search space for four cases evaluated (r_{out} = 45 mm, INA127, $Q_{C1} \approx Q_{C2} \approx 200$), all of which are shown in Figure 48. In two of the cases (solid line and broken line) the bandwidth (bw) is set to 0 Hz, that is, the coil is optimised to give the best performance at a single frequency, and the optimal solution lies near the classical value of $R_{match\_class} = e_n/i_n$. However, setting the bandwidth to 1 kHz shifts the optimal value for R_{match} higher (dotted line and dot-slash line). This improves sensitivity by 13% and 35% with respect to R_{match_class} for f_0 = 10 kHz and f_0 = 3.3 kHz respectively.

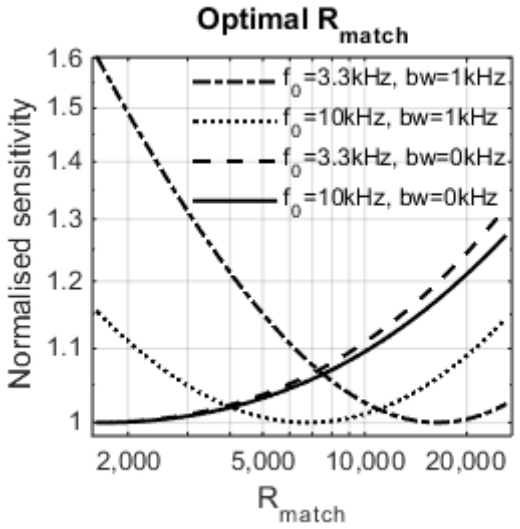

Figure 48: Mean sensitivity by different equivalent resistances R_{match} for different tuned voltage-to-voltage coils. Sensitivities are normalised to optimal sensitivity points for each configuration.

The simulation result provided in Figure 49 indicates that high-quality factor capacitors have a significant effect on sensitivity. For the tuned voltage-to-voltage configuration (r_{out} = 45 mm, f_0 = 10 kHz, bw = 1 kHz, INA217) with low quality capacitors (Q = 33), the average sensitivity is decreased by as much as 69% compared to the sensitivity with higher quality capacitors (Q = 1000). Notably, Figure 49 provides a clear indication of the relationship between the quality factor of the capacitors and achievable sensitivity, greatest impact below a quality factor of ~330. Beyond this level of capacitor Q, the improvement is reduced. Not unexpectedly, the effect of higher Q is greater on peak sensitivity than on mean sensitivity.

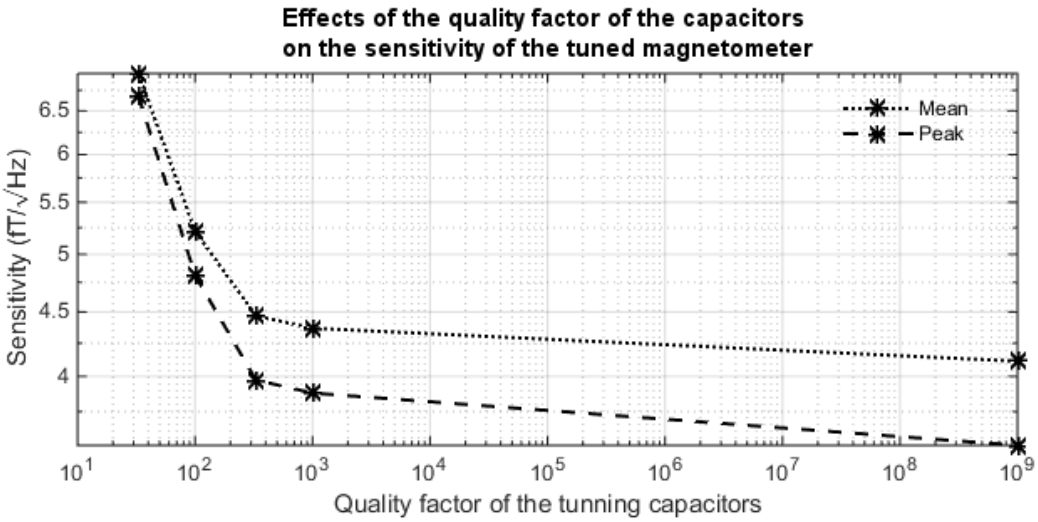

Figure 49: Effect of the quality factor of the capacitors on the sensitivity of the tuned voltage-to-voltage air-core magnetometer. Both the mean and peak results are shown.

We evaluated how much sensitivity can be gained through the self-resonance effect by examining the effect of removing in the optimisation algorithm the penalisation related to the self-resonance frequency of the coil. Figure 50 shows results for an example configuration (INA217, r_{out} = 45 mm, l_{max} = 20 mm, bw = 0 Hz, $Q_{C1} \approx Q_{C2} \approx 200$) for both the non-tuned and tuned configurations. An effect cannot be observed for the non-tuned configuration, whilst more than 30% increase in sensitivity was predicted above 10 kHz for the tuned configuration.

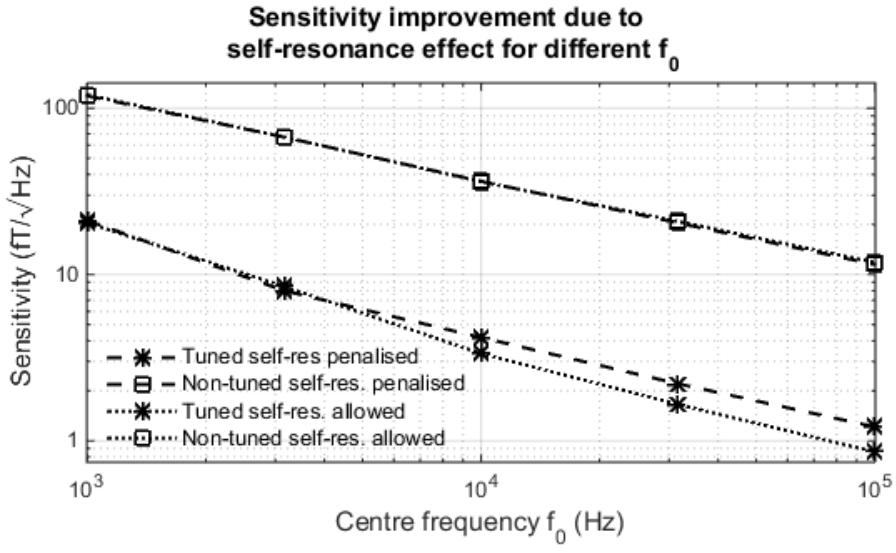

Figure 50: Comparison of the solutions from the optimisation algorithm with (broken lines) and without (dotted lines) self-resonant frequency penalisation.

Brooks coils have a particular shape consisting of a square cross-section with an outer radius twice the coil height. It has been suggested that this design maximises the sensitivity of non-tuned current-to-voltage configuration by maximising the ratio of inductance to resistance. In Figure 51 we compare the sensitivities for Brooks coils versus our proposed customised design method. The outer radius was constrained to be the same for both coils, but the height and inner radius was allowed to vary in the customised design. Optimised Brooks coils had 24x24, 19x19, 20x20, 17x17 and 18x18 turns, while the customised algorithm found 50x10, 50x8, 48x7, 47x6 and 44x6 to be the optimum turns per layer and number of layers for coils with outer radii of 10, 15, 20, 25 and 30 mm respectively. The corresponding inductance to resistance ratio are 7.1146e-04, 7.6895e-04, 5.9885e-04, 3.8542e-04, 3.5256e-04 H/Ω for the Brooks coil and 7.6636e-04, 6.5807e-04, 7.6774e-04, 5.8848e-04, 3.1220e-04 H/Ω for the customised coil. Restricting the optimisation algorithm to the Brooks coil layout, resulted in approximately 20% lower sensitivity than the use of customised shapes. Both designs had the following settings: LT1028 pre-amplifier [188], f_0 = 10 kHz and bw = 19000 Hz.

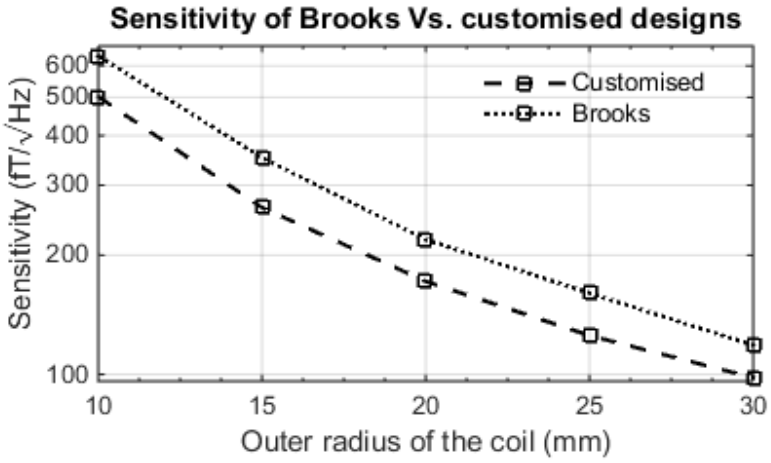

Figure 51: Mean sensitivity achieved by a Brooks coil (square cross-section) with non-tuned current-to-voltage amplification compared with rectangular cross-section non-tuned current-to-voltage configuration.

To evaluate the benefit of using a tuned voltage-to-voltage configuration as opposed to the non-tuned current-to-voltage configuration, we performed tests based on the INA217 (e_{ni} = 3.5 nV/√Hz (pink noise at 10 Hz) + 1.3nV/√Hz white noise, i_{ni} = 3 pA /√Hz (pink noise at 10 Hz) + 0.8 pA/√Hz white noise, e_{on} = 90 nV/√Hz) and LNA718A (e_{ni} = 2 nV/√Hz (pink noise at 10 Hz) + 0.7 nV/√Hz white noise, i_{ni} = 490 fA/√Hz (pink noise at 10 Hz) + 98 fA/√Hz, e_{on} = 13 nV/√Hz and R_f = 10 kΩ) amplifiers. In Figure 52, sensitivity is plotted against centre

frequency (f_0) for the four cases considered with r_{out} = 4.5 mm, l_{max} = 20 mm and bw = f_0*1.9. For INA217, the non-tuned configuration is predicted to be more sensitive than the tuned configuration only when the centre frequency is below 21 Hz. For the LNA718A, the tuned configuration is more sensitive than the non-tuned configuration at frequencies above 90 Hz. The sensitivity difference between non-tuned and tuned configurations increases with the frequency.

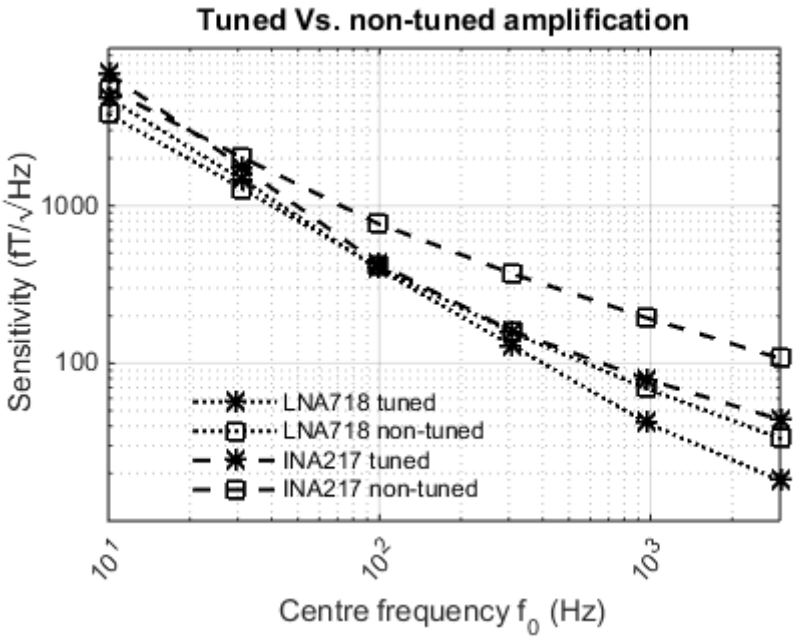

Figure 52: Mean sensitivity comparison in between optimised non-tuned current-to-voltage (squares) and tuned voltage-to-voltage (asterisks) amplification with two different pre-amplifiers: LNA718 (broken lines) and INA217 (dotted lines).

Considering the non-tuned current-to-voltage and tuned voltage-to-voltage configurations using the LNA718 pre-amplifier (r_{out} = 45 mm, l_{max} = 20 mm, f_0 = 100 kHz, bw = 10 kHz, Q_{C1} ≈ Q_{C2} ≈ 200), Figure 53 shows the effect of increasing the number of strands per wire. Results have been normalised against the case of a single strand wire. The use of a Litz wire does not appear to provide great benefits for the non-tuned case. For the tuned configuration, an improvement in sensitivity of around 21% can be achieved with around 500 strands per wire, while for the non-tuned case, a maximum of 5% improvement is achieved with 200 strands per wire. It is worth noting that thermal noise from the coil is dominant in the tuned setup whereas it is less than half of the other noise sources in the non-tuned case.

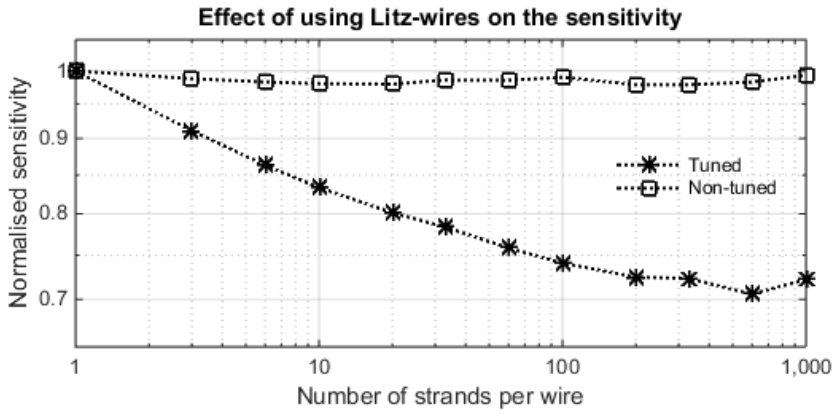

Figure 53: Normalised sensitivity as a function of number of strands per wire illustrated for the non-tuned current-to-voltage (squares) and tuned voltage-to-voltage (asterisks) configurations.

We used the numerical simulation environment to explore the effect of different noise sources on achievable sensitivity. In Figure 54 we show results for the non-tuned current-to-voltage and the tuned voltage-to-voltage configurations optimised to a centre frequency of 10 kHz (*bw* = 1 kHz, R_{out} = 45 mm, amplifier INA217, l_{max} = 20 mm). The dominant noise sources for the non-tuned configuration (Figure 54A) are the output (e_{i_on}) and input (e_{ni}) voltage noise of the amplifier. For the tuned coil (Figure 54B), thermal noise of the coil dominates (e_{Si}), closely followed by the thermal noise of the tuning capacitor in series with the coil (e_{C1}) and the current noise of the amplifier (e_{ii}). Input voltage noise of the amplifier (e_{ni}) affects mainly in frequencies far from the centre frequency in the tuned case.

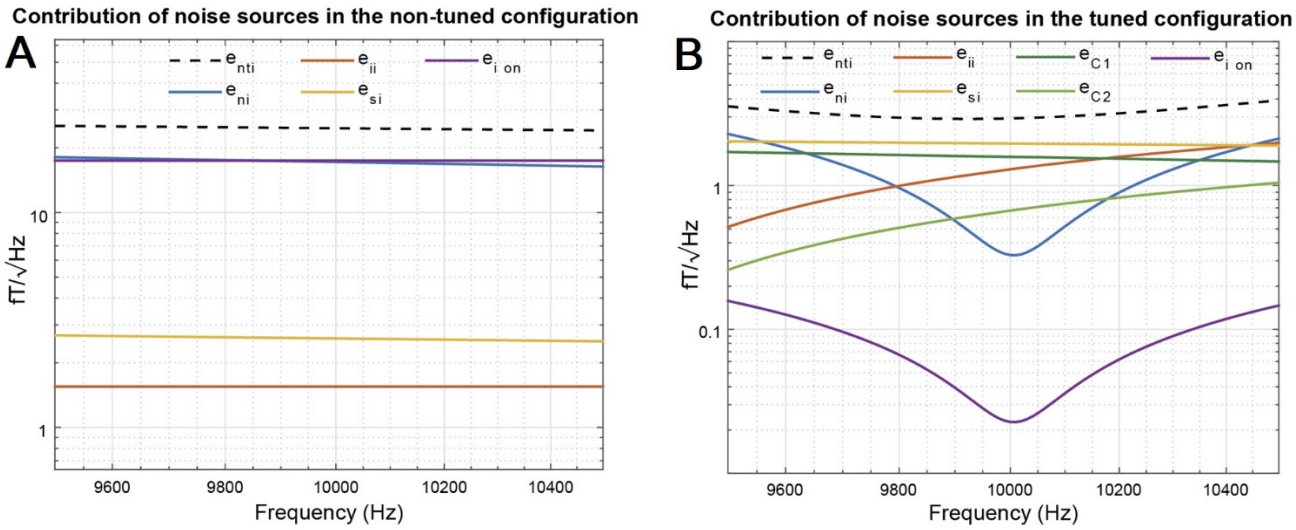

Figure 54: Assessment of the contribution of the various noise sources. Plots show the contribution of each noise source for the non-tuned current-to-voltage (A) and tuned voltage-to-voltage (B) configurations.

5.5 Discussion

We propose a more general model for the design of air-core magnetometers for both non-tuned current-to-voltage and tuned voltage-to-voltage pre-amplifier configurations. We demonstrate that tuning can offer higher sensitivity even on wideband applications. By considering a more flexible model, we can produce air-core magnetometer configurations with very high predicted sensitivities. In particular, the sensitivity predicted for our optimised design is higher than that thought to be achievable with the optimal Brooks coils. *Although* this coil geometry has been proposed because of its high inductance to resistance ratio, the results we report suggest that this ratio does not necessarily provide the highest sensitivity. We show that additional gains in sensitivity can be achieved with an optimisation process accounting for a larger number of decision variables.

Our experimental results used for validation are in close agreement with the predictions from our model. Accurate characterisation of air-core magnetometers requires accurate estimation of the equivalent resistance, inductance and *EMF*. The lower accuracy with which parasitic capacitance can be estimated is negligible, provided frequencies of interest are well below the self-resonant frequency of the coil. The model used to evaluate the field transformation (V/T) is verified for both the non-tuned and tuned configurations, alongside a validation for the noise floor. The good agreement between simulations and experimental findings is not unexpected since we employ prevailing numerical models. We provide results for frequencies below 100 kHz. However, here presented numerical models are valid up to the low MHz range. From few MHz on other tools, such as the finite element method, maybe better suited due to wavelength shortening at higher frequencies.

Concerning the optimal frequency for maximal sensitivity in non-tuned air-core magnetometers, it has previously been shown that the sensitivity in the linear region is proportional to the cut-off frequency [192]. Therefore, it follows that the optimal sensitivity for a given bandwidth is near the cut-off frequency, as shown in Figure 46. For the tuned voltage-to-voltage configuration, the optimal sensitivity appears at a frequency close to the tuning frequency as a consequence of resonance. However, an improvement in sensitivity can be gained by shifting the tuning frequency away from the centre frequency of the bandwidth (Figure 47C). The non-tuned current-to-voltage design only outperforms the tuned voltage-to-voltage design at ultra-low frequencies (< 100 Hz) in the configurations examined here (Figure 52).

The classical approach of optimising the air-core magnetometer sensitivity by matching the equivalent resistance R_{match} to e_n/i_n does not always apply [123]. This approach can be inaccurate for a number of reasons. The classical approach assumes that noise sources i_{ni}, e_{ni} and e_{si} are the main contributors of the total noise and *EMF* increases proportionally with coil impedance. In the non-tuned current-to-voltage configuration, minimum output voltage noise of the amplifier can be dominant depending on the feedback of the amplifier, and the *EMF* follows a nonlinear relationship with the impedance of the coil. In the tuned voltage-to-voltage configuration thermal noise of the tuning and matching capacitors can be dominant at very low frequencies. Additionally, most noise sources, as well as the equivalent source impedance, are frequency dependent in both configurations. Consequently, coil and network are not optimised to provide the best sensitivity at one single frequency, but the best sensitivity averaged over the frequency bandwidth of interest.

We have shown different possibilities to enhance the sensitivity, the outcome of which can be anticipated through plots of individual noise contributions. In the example of Figure 54, these noise contributions indicate that the minimum output noise and the voltage noise of the amplifier determine the noise floor of the non-tuned current-to-voltage magnetometer. Other noise sources are at least a factor of two smaller, reducing the benefit of using a Litz wire (Figure 53). Conversely, in the tuned voltage-to-voltage configuration it is possible to improve sensitivity through the use of Litz wire because the thermal noise from the coil is dominant. The quality of capacitors used in the design should be considered carefully as their thermal noise can be significant (see Figure 54B).

The use of lossy capacitors in the model confers notable benefits. First, the simulations are more reliable, showing a 40-80 % improvement in the accuracy with the prototypes built for this work. Second, the optimisation process is forced to converge to feasible capacitor values. Third, the simulation environment can, to some extent, compensate for undesirable effects introduced by low-quality capacitors via changes to the design.

Our results suggest a potential enhancement in air-core magnetometer sensitivity via exploitation of coil self-resonance in the tuned voltage-to-voltage configuration (see Figure 50). Any gains in sensitivity rely on being able to accurately predict the parasitic capacitance of the coil, which is problematic in the presence of densely packed loops. The parasitic capacitance is very susceptible to the manufacturing process and any material imperfections. In effect, slightly different distances between loops generate different parasitic capacitances between neighbouring coils. This parasitic capacitance spread

results in a broadening of the self-resonance peak and consequently reduces coil quality factor. We have avoided working with frequencies near the coil self-resonance to be able to build reproducible coils.

Our simulation environment could be modified to cater for design constraints not considered here. For example, linear sensitivity across frequencies may be desirable for some applications. For this case, any deviations in gain could be penalised in the optimisation process. Our results do, however, suggest that such a constraint will reduce sensitivity. In applications where the best noise performance is required, the gain could be linearised by adding a digital or analogue compensation step, such as the one used in[181]. In applications where a portable or lightweight solution is needed[183], bounds on magnetometer weight could be set as well. Additionally, a fully capacitive T matching network may be beneficial if a very selective narrow band is required, noticing the additional losses from the extra capacitor. Networks incorporating inductors should be avoided due to the associated substantial losses, particularly at frequencies considered here. The coil layout could also be changed to account for cases where anisotropic wire positioning or non-rectangular profiles are desired. In such cases, particular modules of the numerical model, such as calculation of the AC resistance and parasitic capacitance of the coil, would need to be adapted on a case-by-case basis.

5.6 Conclusions

We propose an optimisation method for the design of highly sensitive air-core magnetometers. Two popular amplification configurations are considered: non-tuned current-to-voltage and tuned voltage-to-voltage mode. We use a globally optimal method to maximise sensitivity by changing conductor diameter, spacing between conductors, number of conductor layers and loops per layer. Our findings suggest that the use of equations with fewer limiting assumptions and a higher number of decision variables yields air-core magnetometers which can significantly outperform existing designs such as the optimal Brooks coils.

The program used to generate the results is open source, and it is publicly available via our website to help facilitate the design of high-performance air-core magnetometers across a range of applications. The program can readily quantify the value added by the use of expensive electrical components such as high-end pre-amplifiers, high-quality capacitors and Litz wires. Additionally, it can facilitate the design of customised, highly sensitive and relatively cheap air-core magnetometers to substitute more expensive and fragile

technologies, such as SQUIDs, in applications like emerging low-cost fieldable ultra-low-field nuclear magnetic resonance systems[24,46,172].

Chapter 6- Air-core magnetometer optimisation for ULF MR

6.1 Abstract

ULF MR instruments are generating increasing interest due to their potential as low-cost portable technology and novel promising applications. However, state-of-the-art ULF instruments employ expensive and fragile detecting technologies often requiring cryogenics, which hampers portability and affordability. Alternatively, room temperature air-core magnetometers have been suggested as an inexpensive yet highly sensitive signal detector. Still, achieving required exquisite sensitivities relies on the air-core magnetometers to be optimised for each application. Here, a previously presented optimisation method is further developed and applied to design highly sensitive ULF MR surface and cylindrical coils. In conjunction with the new design, an ultra-low noise pre-amplifier design is proposed for enhanced performance. The detector is complemented with a novel low insertion loss *Q*-damping scheme and a post-processing method that reduce the long dead-times associated with pre-polarisation or radiofrequency pulses. Proposed methods and designs are empirically verified with a cylindrical detector at 2.5 kHz. The proposed sensor, which is inexpensive to make, can provide ULF MR with a robust and highly sensitive detector. The advance promotes the portability of ULF MR instruments.

6.2 Introduction

Thanks to the latest technological and post-processing advancements, lower field MR systems are gaining interest as they are cheaper to produce and can be made more accessible than 1.5T to 7T clinical instruments. The ULF MR approach is also of interest because proton resonant frequency approaches the timescale of many biological processes, which potentially can be inferred through their coupling to the MR signal. Biomolecular dynamics and neural activity are two examples of occurrences that could be studied through ULF MR. Besides, the reduced power requirements and stray fields of ULF MR systems facilitate their portability.

In general, ULF instruments consist of pre-polarisation and measurement fields, and a highly sensitive magnetometer for signal detection. The need to boost SNR at low frequencies has instigated the use of state-of-the-art detectors, which are expensive, require of complicated maintenance, and have to be very carefully handled. ULF systems have been tested with superconducting quantum interference devices (SQUIDs) [12,26,87], atomic magnetometers (AMs)[102,103] and Giant magnetoresistance (GMR) mixed magnetometers[104,105]. Highly sensitive miniaturised SQUIDs can currently be found in the market. However, they need

cryogenics and are most often found in bulky hardware gradiometry configurations. AMs have also been shown to be highly sensitive in ULF MR applications. Whilst AMs do not require of cryogenics, they are also not as effective as SQUIDs. GMR mixed magnetometers have also found use as detectors in ULF MR, but they have lower sensitivity than SQUIDs and AMs and require cryogenics for their superconducting flux transformers. All of these types of signal detectors are costly, complicated to operate and maintain, and limit instrument portability whilst increasing instrument complexity.

6.2.1 Air-core magnetometers in ULF-MRI

Air-core magnetometers are an attractive alternative signal detection in ULF MR as they are inexpensive, robust, and can be highly sensitive. However, their performance depends on how well they have been customised to the application. Although air-core magnetometers have been widely used in ULF MR[100,195], no method has been presented to date which optimises ULF MR coils with respect to measuring near-field signals from a region of interest. Savukov demonstrated in-vivo imaging of a hand at 83.6 kHz acquired with a tuned magnetometer based on an open wall solenoid coil, but offered minimal description of the coil design[196]. Matlashov and colleges reported that the practical sensitivity of surface coils in ULF MRI experiments at 3.3 kHz was relatively close to that of SQUIDs[24,75]. Interestingly, the theoretical 40 fold sensitivity advantage of SQUIDs over coils was measured to be only 3 in practice. Their setup consisted of 7 surface coils of 90 mm diameter reaching 20 fT/√Hz sensitivity each and suggested that their magnetometer could be optimised without providing specific details. Lin optimised a similar surface coil reaching 6 fT/√Hz and 2 fT/√Hz sensitivities at room temperature and 77 °K respectively[187]. However, the optimisation was done in view of far-field measurements, and the 3dB bandwidth of 88 Hz at 300 °K and 44 Hz at 77 °K is impractical for conventional MRI protocols. In the same line, it is worth mentioning the work of Suefke which, although at the higher end of the kHz range, proposed a method to increase the sensitivity by boosting the transformation ratio of the matching network with an external high-quality factor ferrite core inductor[197]. Likewise, its functional bandwidth is inconveniently narrow as already predicted by Pollak et al.[198]. In a previous work, we presented an algorithm to facilitate air-core magnetometer design for a large range of frequencies and dimensions, with optimisation based on far-field measurements. This work suggested that higher sensitivity can be reached by considering all detector components in the optimisation process. Typically, air-core magnetometers are composed of a coil, a pre-amplifier and a matching network, as they need to be tuned to a limited bandwidth to reach competitive sensitivities[199].

6.2.2 Pre-amplifier options for air-core magnetometers

The pre-amplifier aims to amplify the *EMF* to minimise its vulnerability to noise along the subsequent signal path. Off-the-shelf low noise operational amplifiers have often been employed[24,187]. Although these have been designed thoroughly, their noise performance is usually lower than that achievable by customised designs made of selected discrete components[119,123]. Most of the discrete MRI pre-amplifiers described in the literature are designed for frequencies in the MHz range and are not optimal for the low kHz range[94,97,200-202]. Nonetheless, low noise pre-amplifiers for lower frequencies have been extensively used in other areas such as astrophysical and geophysical exploration[203-206], mass espectrometry[207], audio applications[208,209], and other low frequency low noise applications[123,210,211]. A particular commercial model, the SR560 from Stanford Research Systems, has repeatedly been proposed due to its well-validated performance up to a few 100 kHz. The circuit diagram of this product was revealed recently[119].

6.2.3 Detector dead-time reduction

Apart from being highly sensitive, MR detectors need to be able to withstand and quickly recover from strong magnetic field transients. In the case of air-core magnetometers, different approaches have been suggested to dissipate this energy quickly and protect the pre-amplifier. PIN diodes are extensively used for this purpose in high frequency systems, but their control currents introduce noise that is difficult to filter out at low frequencies[95,212,213]. Transistor switches have also been suggested, which typically have lower feedthrough at the expenses of higher on resistance, increasing insertion losses. Electromechanical switches offer perhaps the lowest insertion losses at the drawback of slower transitions and shorter lifetime[214]. Another option is to inductively couple *Q*-damping circuits with low insertion losses[215,216]. Regardless of the technique used for switching, they all generate a considerable charge injection which makes the circuit ring after state changes[100,217]. Negative feedback has shown to reduce this effect at the cost of more complex coil specific pre-amplifier designs[94,218], but not without increasing the noise floor of the detector[100]. Therefore, the design of detector capable of rapid energy dissipation without affecting the noise performance during acquisition remains a challenge.

Other approaches have also been proposed to remove ring downs. These include the insertion of carefully calibrated inverse pulses for cancelling out the ring-down[94,219], the combination of equivalent acquisitions with opposite or different ring-down phases by software[220-222], and backward linear prediction which discards the data points corrupted by the ring-down and extrapolates their value from the remaining signal[223]. These methods

either increase the complexity of acquisition sequences or suffer from limited signal efficiency during the ring-down.

6.2.4 Optimisation of air-core magnetometers for ULF-MR

In this work, a complete ULF MR sensor solution is proposed. It is composed of an accurate surface and cylindrical coil design optimisation method, an ultra-low noise pre-amplifier design, an accelerated *Q*-damping circuit, and a post-processing approach to attenuate ring-down. The coil design method is an adaptation of a previously published method so that the sensitivity is optimised to the near-field instead to the far-field[178]. The pre-amplifier is based on the work of Pallottino with modifications to be able to accommodate for a lower noise jFET front end and to increase detector bandwidth[205]. The dead-time is accelerated by the combination of two methods. First, the dangerous high energy level stored in the coil is critically damped, process which is accelerated by temporarily increasing the resonant frequency of the tank circuit. Second, the coil re-excitement arising from changing the state of the electromechanical switches is attenuated by software. Here presented concepts and methods can facilitate the design of high-performance coils for a broad range of ULF NMR and MRI needs.

6.3 Methods

6.3.1 Coil design

Coil number of layers, number of turns per layer, wire diameter, and spacing between wires are optimised by a method that employs accurate numerical models, and a genetic algorithm that searches for the globally optimal sensitivity[178]. User input parameters are frequency range of interest, pre-amplifier input voltage and current noise properties, quality factor look-up table of desired matching capacitor series, location of the volume of interest with respect to the coil, and coil inner or outer diameter. This last feature allows for the design of cylindrical or surface coils respectively, as cylindrical coils usually allocate within the sample/body part, while the outer diameter of surface coils limits the arrangement of multiple detectors. A more detailed description of the optimisation method can be found in[178]. The optimisation process was performed using a desktop with an eight core Intel i7-2600 3.4 GHz CPU and 16 GB RAM.

The prior algorithm was optimised to achieve sensitivity to the far-field[178]. This algorithm has been modified to improve the sensitivity to a specific volume of interest near the coil relative to its wavelength, which is the case in MR where the signal originates near the coil. The *EMF* calculation has been replaced by the reciprocity principle, by numerically integrating

the axial magnetic field that 1 A current flowing through each of the coil loops would generate in the volume of interest such that[224,225]

$$EMF \propto S = \int_{z=h_{roi1}}^{h_{roi2}} 2\pi \int_{\rho=0}^{r_{roi}} \sum_{n=1}^{n_l} \frac{C}{2\alpha^2\beta}\left((a_n^2 - \rho^2 - z^2)E(k_n^2) + \alpha^2 K(k_n^2)\right), \quad (92)$$

with

$$\alpha_n^2 = a_n^2 - \rho^2 - z^2 - 2a_n\rho; \quad (93)$$

$$\beta_n^2 = a_n^2 + \rho^2 + z^2 + 2a_n\rho; \quad (94)$$

$$k_n^2 = 1 - \frac{\alpha_n^2}{\beta_n}; \quad (95)$$

$$C = \frac{\mu_0}{\pi}. \quad (96)$$

Here, S is the normalised sensitivity to the volume of interest, a_n is the radius of the *n*th loop, ρ is the radial distance of the point in the space, and z is the distance from the plane of the loop to the point in the space. K and E are the complete elliptic integrals of the first and second kind, respectively. μ_0 is the permeability of free space = 4π*1e-7. In Equation (92) the volume of interest is considered to be cylindrical of radius r_{roi}, elongating from h_{roi1} to h_{roi2}. Notice the proportionality symbol ∝ in Equation (92), as the actual *EMF* also depends on other parameters irrelevant for the optimisation, namely the net magnetisation of the sample, its relaxation parameters and acquisition sequence. Above estimation assumes that the measurement magnetic field is perpendicular to the axis of the coil so that the plane of the transversal magnetisation of the spins is parallel to the axis of the coil. It also assumes that, within the volume of interest, the acquisition bandwidth is much smaller than the resonance frequency.

Coil sensitivity is often reported in T/√Hz. However, this is a figure of merit to describe the sensitivity to the far-field, which is different from the near-field. Here, the sensitivity of the coil is more appropriately measured in the form of SNR so that it can be contrasted with an NMR experiment. The calculations to predict the SNR employ the reciprocity principle of Equation (92) such that[226]

$$EMF(t) = \omega \cdot S \cdot M_{net} \cdot V_{VOI}; \quad (97)$$

$$M_{net} = M_0 e^{-t/T_2} e^{-i\omega t}; \quad (98)$$

$$M_0{}^{1}{}_H = \frac{\Delta n \hbar \gamma}{2} \approx \frac{(\Delta E/kT) n_s}{2} \frac{\hbar \gamma}{2} = \frac{n_s \hbar^2 \gamma^2 B}{4kT}. \quad (99)$$

Here, *k* is Boltzmann's constant, *T* is the absolute temperature, $\hbar$ is Planck's constant, γ is the gyromagnetic ratio, B is the external magnetic field, and n_s is the proton density. We use a sample of 20 ml distilled water, which has a $T_2 \approx T_1 \approx$ 740ms at 59 μT measurement field. Estimated SNR is calculated by $SNR = EMF/detector\_noise\_floor$. Similarly, the SNR from the experiment is determined using a spectral difference measurement between the signal with and without the sample.

6.3.2 Pre-amplifier

The proposed pre-amplifier is based on Pallottino's design, which has been chosen because it achieves very low noise with a relatively simple design[205]. Its cascode configuration reduces the dynamic capacitance generated by the Miller effect, and its feedback lowers gain variations. Here, the original design has been modified with the aims of reducing the noise floor and expanding the functional frequency range. The detailed pre-amplifier schematic is provided in Figure 55.

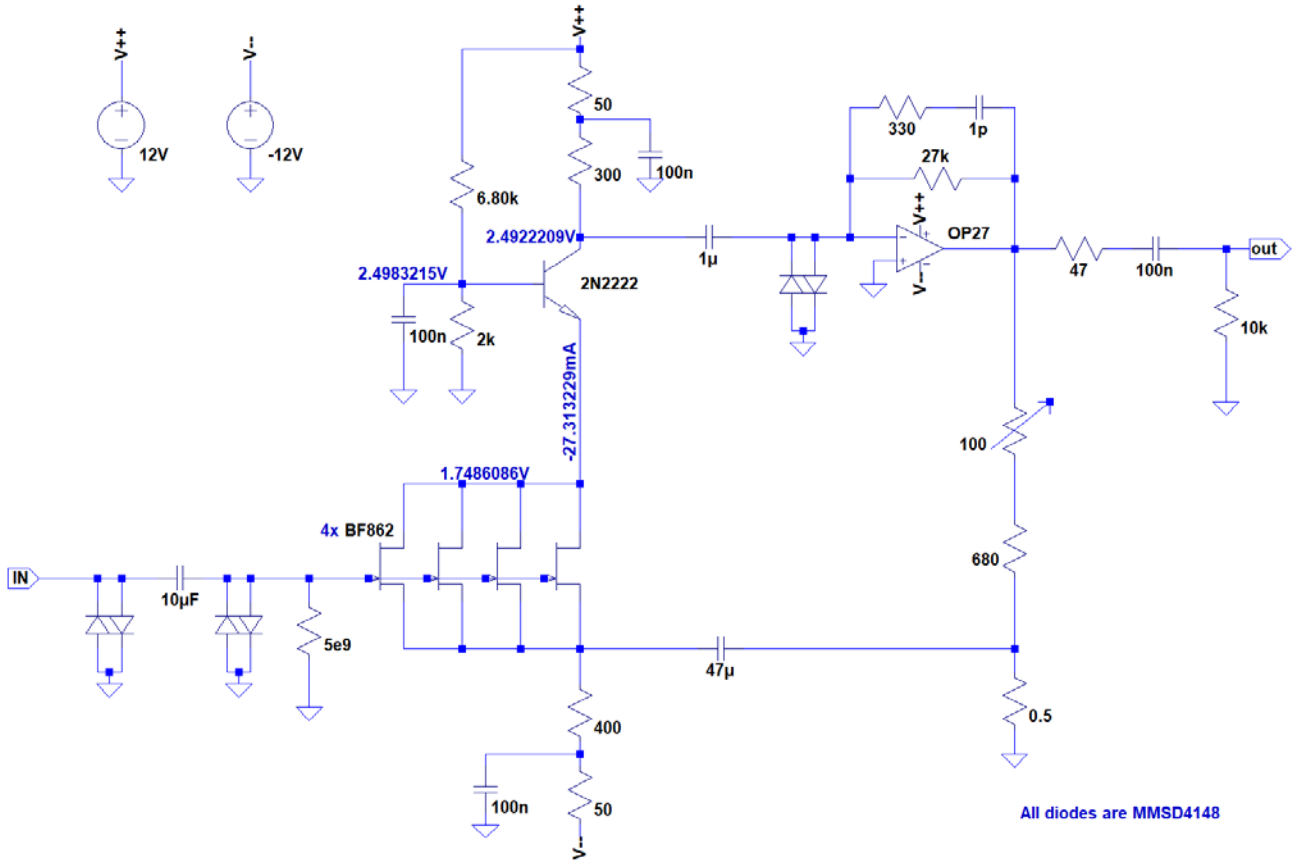

Figure 55: Schematic showing proposed pre-amplifier based on[205]. Some simulated bias voltages and jFET bias current are displayed. All diodes are MMSD4148.

The original 2SK162 jFET has been substituted by a better performing more modern jFET, the BF862 (NXP Semiconductors, Eindhoven, the Netherlands). It has low input voltage noise amongst jFETs (0.8 nV/√Hz). Although it has higher 1/f noise corner frequency than its predecessor, it is below 1 kHz which is typically out of the frequencies of interest. Following the original design, four jFETs have been incorporated in a parallel configuration to halve voltage noise further. Inevitably, this also increases input current noise by the same ratio, which is not problematic as it remains within a few fA/√Hz. Importantly, the BF862 has a relatively low input capacitance (10 pF), giving room for adding jFETs in parallel without running into instability issues or gain losses at higher frequencies. Besides, it has a reasonable transconductance (35 ≤ gm ≤ 45) to provide enough gain so that the SNR is not significantly degraded along the rest of the signal path. Component availability and affordability also advocate for this transistor, which may be subject to changes as this transistor has been recently discontinued.

Each BF862 is biased at about 7 mA, offering a good trade-off between thermal stability and low noise. The feedback capacitance of the operational amplifier was reduced to 1 pF to increase the operational bandwidth, and bypass capacitance was changed to 47 µF to

improve pre-amplifier recovery time. The pre-amplifier is simulated using LTspice (Analog Devices®, Massachusetts, United States) and amplifier noise floor, gain, bandwidth, and saturation recovery were estimated. Pre-amplifier stability is assessed using a general two-port-analysis[215]. A prototype of this pre-amplifier has been built to verify the simulations.

6.3.3 *Q*-damping

The fastest energy dissipation in a series RLC resonant circuit happens when the circuit is critically damped with a resistance $R_{crit} = \sqrt{4L/C}$. The energy is dissipated at an exponential decay with time constant $\tau = 1/2\pi f_0$, being the resonant frequency $f_0 = 1/2\pi\sqrt{LC}$. In the NMR field, the ring-down has often been considered damped after 20 time-constants at critically damping[227]. This definition ignores the initial condition of the ring-down, so here we assume the ring-down to have been damped when its voltage is under the noise floor of the detector. This frequency dependency of the energy dissipation implies that for frequencies in the low kHz range the ring-down time can be tens of milliseconds, which delays the acquisition time, and reduces SNR and acquisition efficiency. For ULF proton human imaging dead-times no longer than 1 ms would be desirable. Therefore, we propose to accelerate the energy dissipation by temporarily increasing the resonant frequency of the circuit, which is achieved by reducing C. Here, the circuit is retuned to the highest possible frequency, which is the self-resonant frequency of the coil, by removing all external capacitors. The parasitic capacitance of the coil is estimated with the same numerical model proposed for the optimisation algorithm. This capacitance is connected in parallel with the coil, so the damping resistance has to be placed in parallel as well, and is calculated by $R_{crit} = \sqrt{L/4C}$. This resistance is usually much larger than the resistance of the coil.

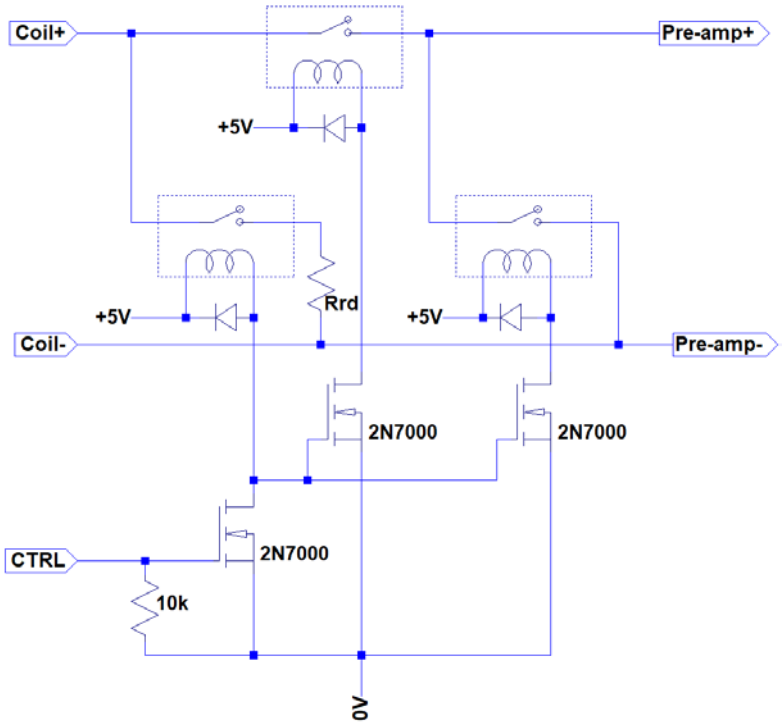

Figure 56: Circuit diagram of the Q-damping.

Component switching and pre-amplifier protection are achieved by a set of 3 reed relays which are synchronously controlled with a TTL signal, as shown in Figure 56. Relay coils are powered by one general purpose MOSFET each. Switching to the damping configuration shorts the pre-amplifier input to ground, opens the signal path between coil and matching network, and sets the damping resistor in parallel with the coil.

6.3.4 Software ring-down attenuation

The long ring-down re-induced by switching *Q*-damping states is attenuated using a software technique. The contribution of the ring-down to the total signal is estimated and subtracted. Three different variants of the ring-down estimation algorithms have been tested:

- mono-exponential fitting: A mono-exponential oscillatory decay has been fitted to the section where the ring-down is dominant over the signal and the noise according to Equation (100). Circuit resonant frequency and decay time where estimated form an averaged NMR signal free ring-down. Once the frequency and the ring-down time constant have been estimated, they are fixed in Equation (100), which is then used to estimate the phase and amplitude of the ring-down overlapped to the MR signal. The fitting is applied to only the early oscillations of the ring-down cycle where the ring-down signal dominates.

- recorded ring-down: A recorded ring-down is averaged and subtracted from the signal. In one variant, the averaged ring-down is directly subtracted. In contrast, in another variant, the magnitude and phase of the ring-down are estimated and adjusted in the subtracted ring-down for each acquisition. To estimate the phase and amplitude, a sinusoidal lobe is fitted to one of the first lobes where the ring-down voltage is the highest, to ensure ring-down dominance over MR signal, shown in blue in Figure 57. The amplitude is scaled according to the difference between the lobe of the averaged ring-down pattern and the actual MR acquisition. To adjust for the phase, the averaged ring-down pattern is first Fourier transformed to the frequency domain. Here, the phase is adjusted so that the dephasing in the bandwidth of interest is compensated. Figure 58 depicts the phase compensation, which follows a trapezoidal shape to adjust the phase in the frequencies of interest but maintain a real-valued time domain signal. For this same reason, the sign of the dephasing has opposite sign in the negative frequencies.

$$V_{rd} = A_{rd} e^{\frac{-t}{\tau_{rd}}} \cos(\omega_{rd} t + \varphi) \tag{100}$$

$$\frac{-1}{\tau_{rd}} = \alpha_{rd} = \frac{R}{2L}. \tag{101}$$

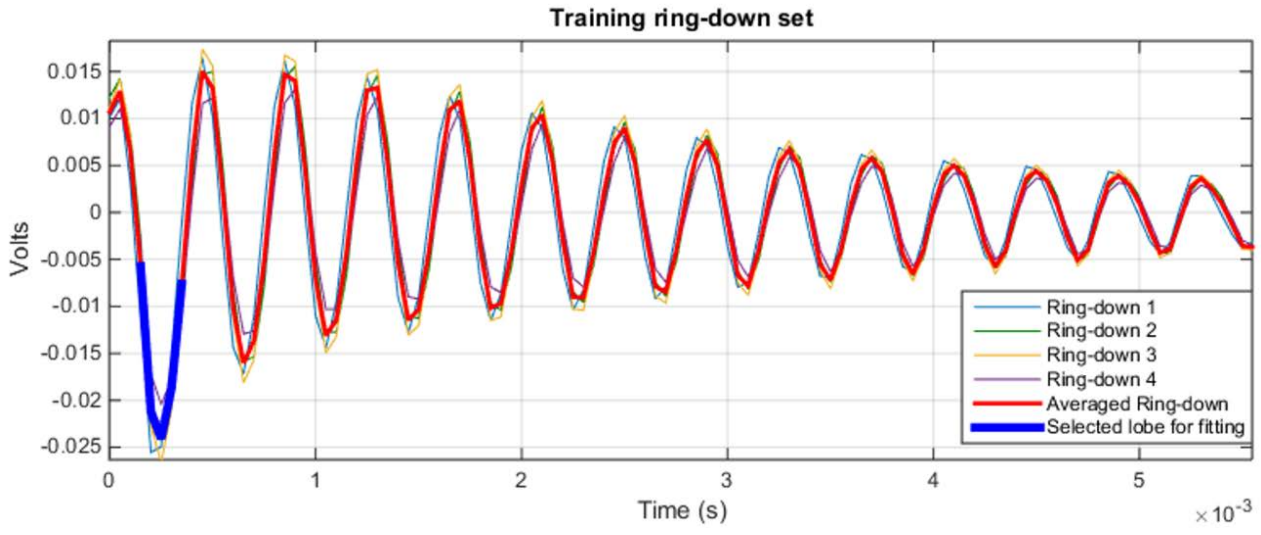

Figure 57: NMR signal free acquisitions used to characterise the ring-down. Signals are averaged to create the reference signal (red). One of the first lobes (blue) is used as a reference for adjusting the correction ring-down reference to each pulse.

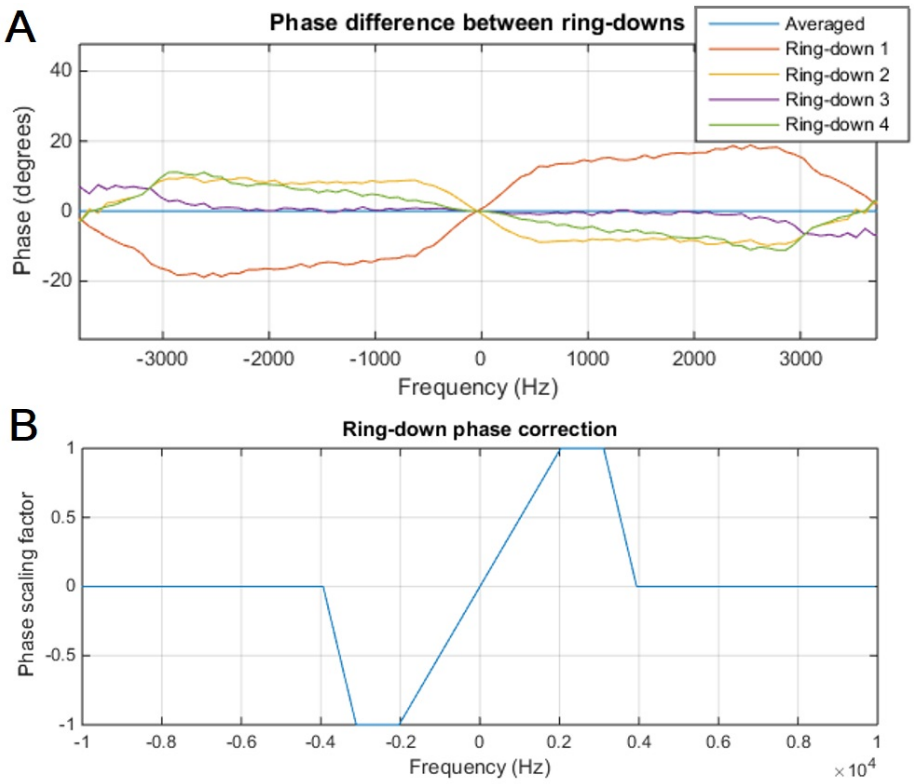

Figure 58: Ring-down phase correction. Ring-downs have slight phase variations shown in (A). These are estimated and adjusted according to the weighting shown in (B).

To improve the fitting, the DC offset is removed by a zero phase digital high-pass filter. Subsequently, A_{rd} and φ_{rd} are estimated for each ring-down event. Afterwards, the estimated ring-down voltage is subtracted from the original signal. The fitting is achieved by nonlinear least-squares minimisation with the trust-region-reflective algorithm[228].

6.3.5 NMR experiment

Detector performance is verified in the ULF MRI facilities at the Physikalisch-Technische Bundesanstalt (PTB, Berlin, Germany). The test coil was designed to be able to position a 20 ml NMR sample tube within the coil. The sample tube had an inner dimension 25 mm x 40 mm and outer dimension 27.5 mm x 58 mm, as shown in Figure 59. The coil had the following parameters: 25.6 Ω AC resistance at 1 kHz, 52.6 mH, 29 mm inner diameter, 48.1 mm outer diameter, 34 mm height, 0.4 mm copper conductor diameter, 0.45 mm wire diameter including coating, 22 layers and 40 turns per layer.

The *Q*-damping circuit employed three SIL05-1A72-BV669 reed relays (Standex-Meder Electronics, Massachusetts, United States), and a damping resistor of 20 kΩ. A single parallel matching capacitor of 77.9 nF with a *Q* of 188 was used. Unfortunately, logistic problems impeded performing this tests with here presented pre-amplifier. Nevertheless, we

were provided of another excellent ultra-low noise jFET pre-amplifier available at PTB, the LNAM-FBX (Magnicon GmbH, Hamburg, Germany) with 0.53nV/√Hz voltage noise, and 15fA/√Hz current noise. Although this commercially available pre-amplifier has slightly higher noise floor than the pre-amplifier proposed here, detector sensitivity should almost not be affected as the noise in the tested setup is primarily dominated by the thermal noise of the coil followed by the thermal noise of the capacitor. Also, given that in the experiments performed the *Q*-damping circuit protects the pre-amplifier from running into saturation, the slow recovery time of the LNAM-FBX (25ms) does not impede performance.

Signals from a 20 ml distilled water sample, an in-vivo human thumb, and a 20 ml $CuSO_4$ solution (0.079 wt%) with $T_1 \approx T_2 \approx 100$ ms comparable to some relevant human tissues were acquired, as displayed in Figure 59. NMR sequences consisted in FID acquisitions with a pre-polarisation field of 16.6 mT during 5 s preceding each FID. MRI experiments employed the same pre-polarisation field, but the pre-polarisation time was reduced to 0.5 s, and 4 gradient echoes were acquired per pre-polarisation cycle with 50 ms echo time. The resolution of the acquired 3D image was 4 mm isotropic. Measurement field inhomogeneity was about 100 ppm peak-to-peak across the imaging volume.

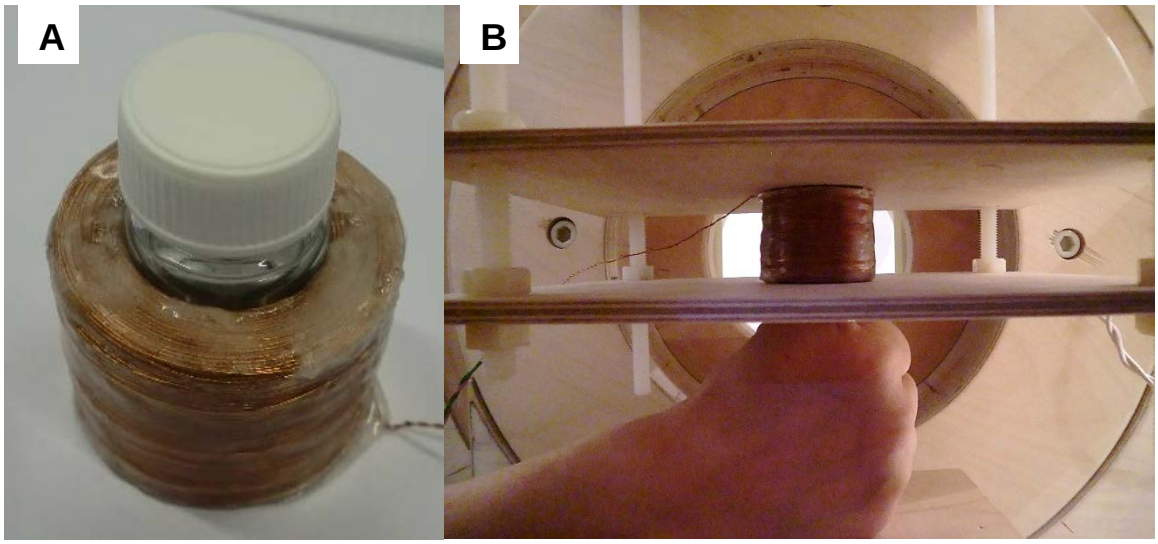

Figure 59: Setup of the ULF NMR and MRI experiments. (A) shows the employed coil, with the 20 ml sample holder in place. (B) shows a caption of the in-vivo human thumb acquisition.

Acquisitions without either the sample or the Rf pulses were performed to test the efficacy of the approach used for ring-down correction. In the experiments with Rf pulses but without sample, the active time of the *Q*-damping circuit was progressively reduced to observe the effectiveness of the energy removal of the *Q*-damping approach. As described above, the

Q-damping circuit changes the capacitance of the tank circuit to increase the resonant frequency. In this case, we opt to use the self-resonant frequency of the coil, which is about 85 kHz. Hence, the corresponding estimated decay time is 1.9 µs if critically damped with 20 kΩ.

6.4 Results

6.4.1 Pre-amplifier

The measured and predicted voltage noise floor of the pre-amplifier at 1-100 kHz is about 0.39nV/√Hz and 0.36 nV/√Hz respectively, which can be seen in Figure 60A. The noise floor is governed by that of the jFETs. A flat gain of 1000 is achieved from about 500 Hz up to 100 kHz, which is visualised in Figure 60B. The recovery time from saturation is around 6 ms, as shown in Figure 60C. The phase margins were 100° and 120° in the low and high frequency ends respectively, as shown in Figure 60D.

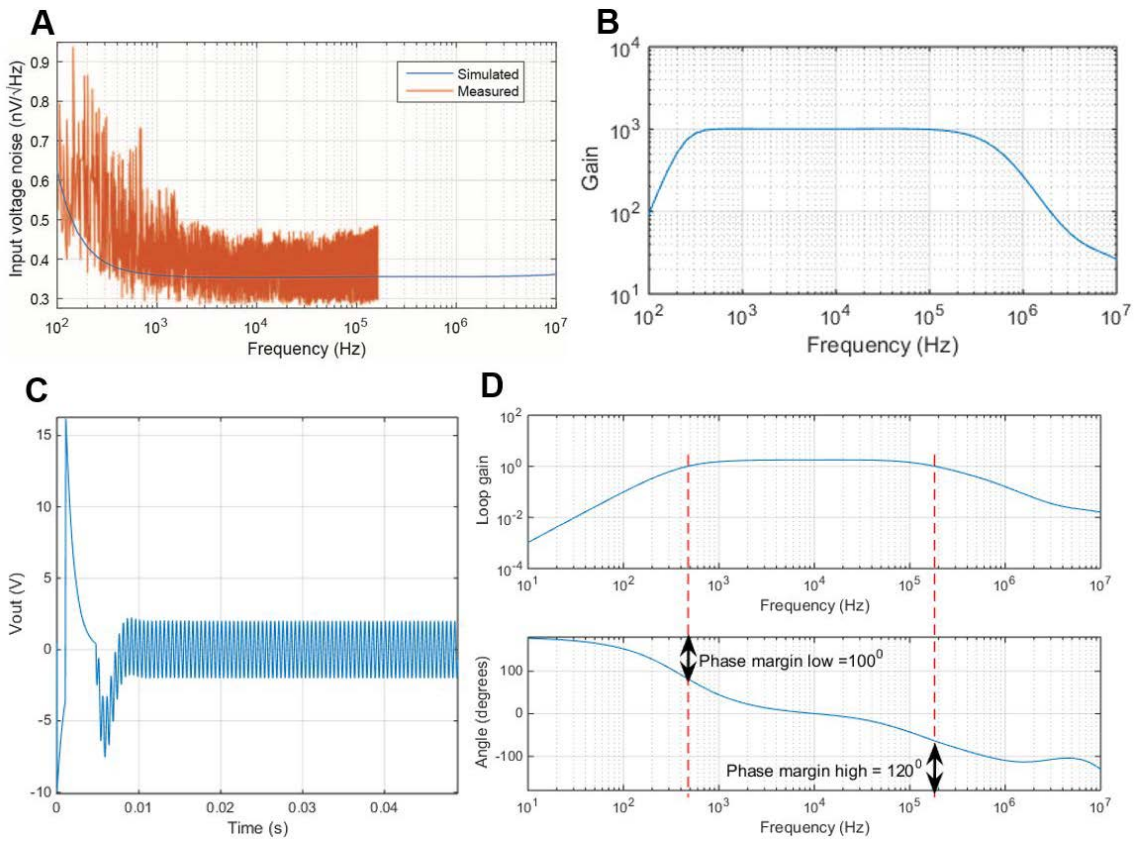

Figure 60: Pre-amplifier characteristics. Ultra-low voltage noise floor of about 0.39nV/√Hz is achieved (A) with a gain of 1000 from 5 Hz to 100 kHz (B). Recovery from saturation is achieved in about 6 ms (C). Phase margins also ensure stability at both low and high frequency ends (D).

6.4.2 NMR experiments

Sensitivity: The SNR of measured distilled water FID signal was calculated to be 82, whilst simulations suggested a value of 80. Figure 61A visualises the measured distilled water NMR spectrum showing a slight frequency shift, lower peak amplitude and a broadening as compared to the simulated one. The measured spectrum corresponds to a single FID acquisition shown in Figure 61B. Figure 62 shows the spectra of the distilled water sample with (A) and without averaging (B) and the averaged spectra of the in-vivo human thumb (C). Besides, acquired MRI image of the 20 ml $CuSO_4$ sample can be seen in Figure 63, with 4 mm isotropic image resolution.

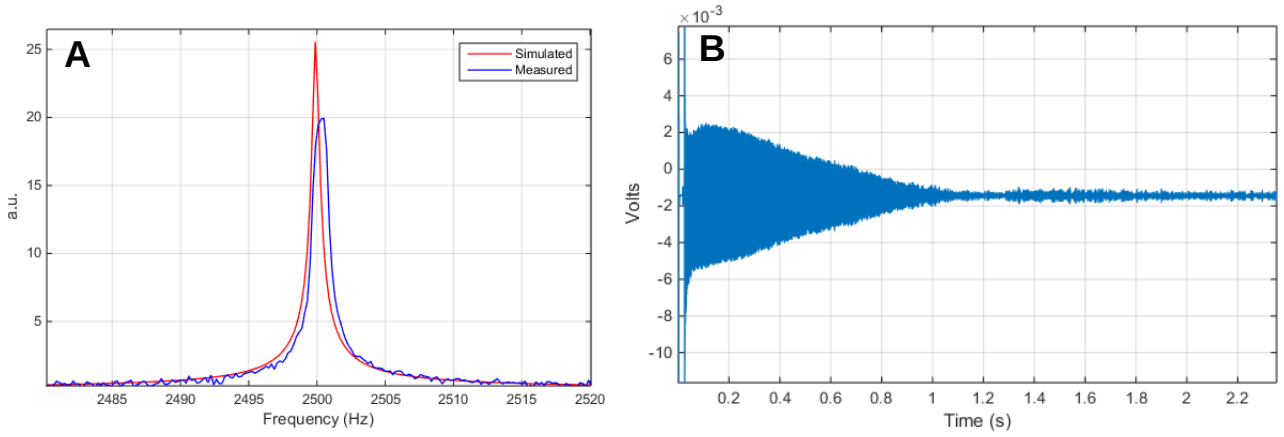

Figure 61: Spectrum and time domain signal of measured FID of the 20 ml distilled water at 59 μT. SNR similarity between measured and simulated signals can be inferred in (A). The initial ring-down obscuring the beginning of the FID is visible in (B).

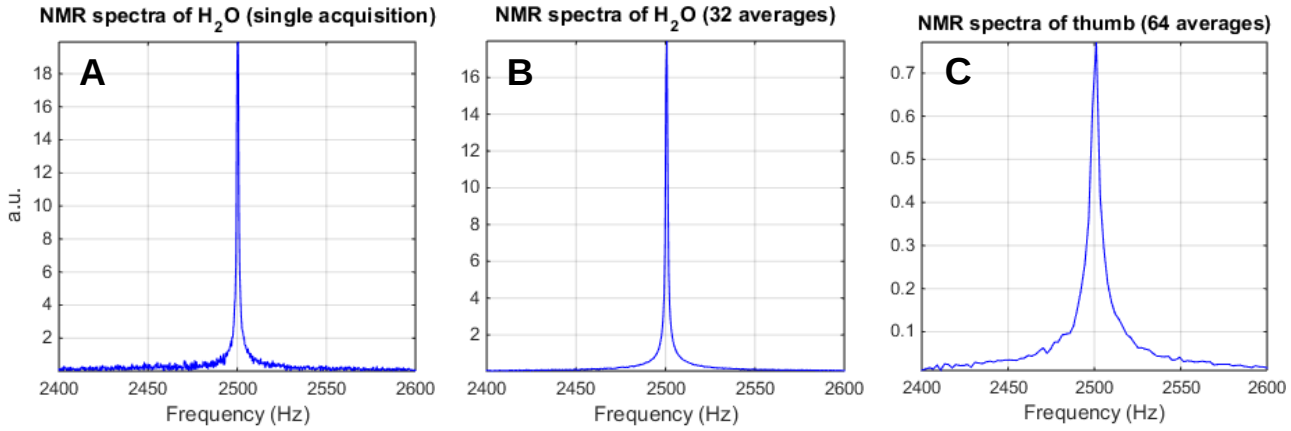

Figure 62: NMR spectra of water and thumb. The NMR of water is shown for a single acquisition (A), and a 32 times averaged acquisition (B). (C) shows the 64 time averaged human thumb spectrum.

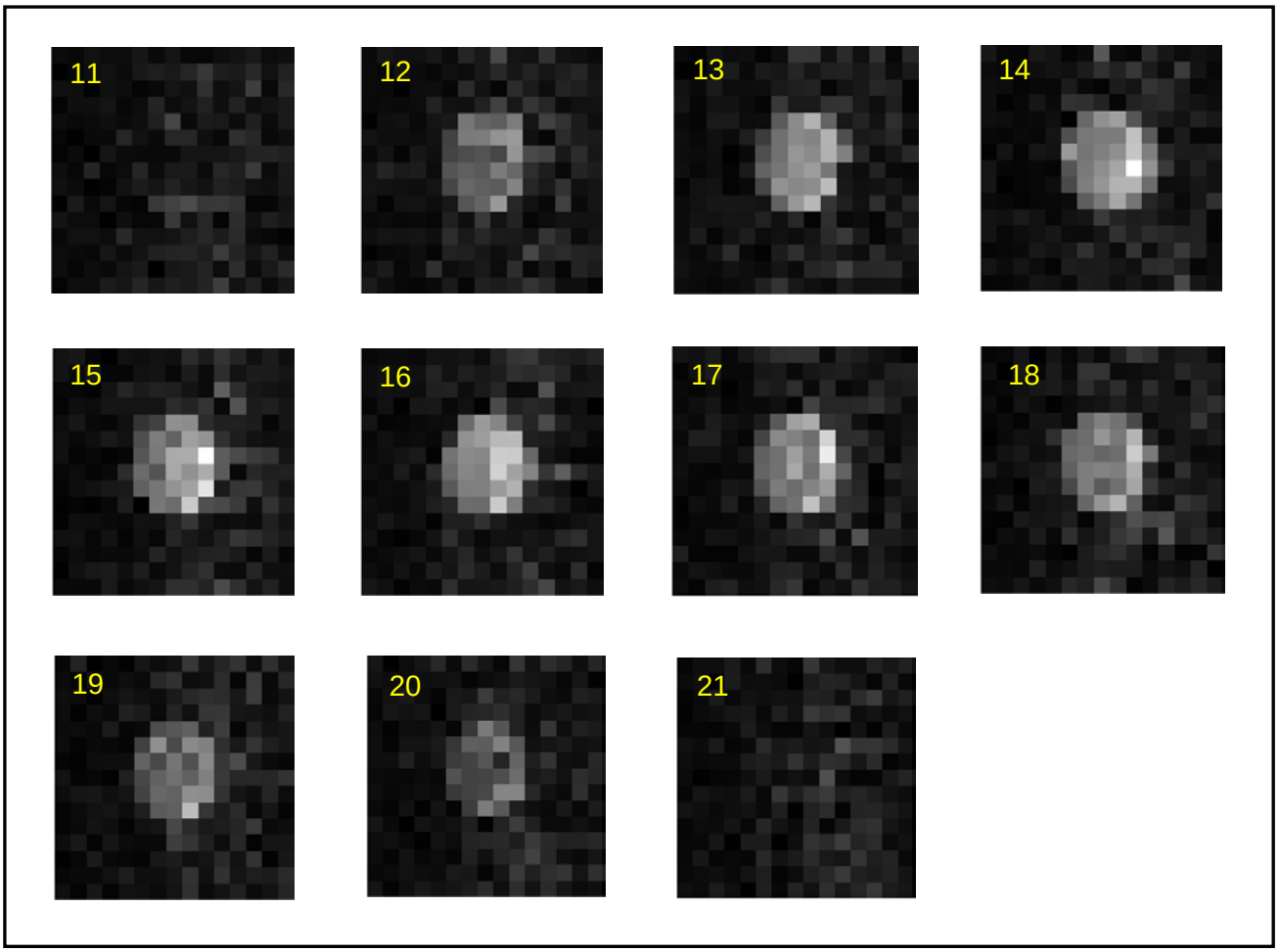

Figure 63: Image of the $CuSO_4$ 20 ml sample. Yellow numbers indicate slice number. Slides not covering sample are not shown.

Ring-down: Experimental acquisitions show that the ring-down started to be affected by the Rf pulses with damping times lower than 1 ms. The re-ringing of the coil needs 20 ms before it reaches noise floor levels. This re-ringing is reproducible as shown in Figure 64. Also, no differences can be seen between the ring-down from 0°, 90° or 180° pulses.

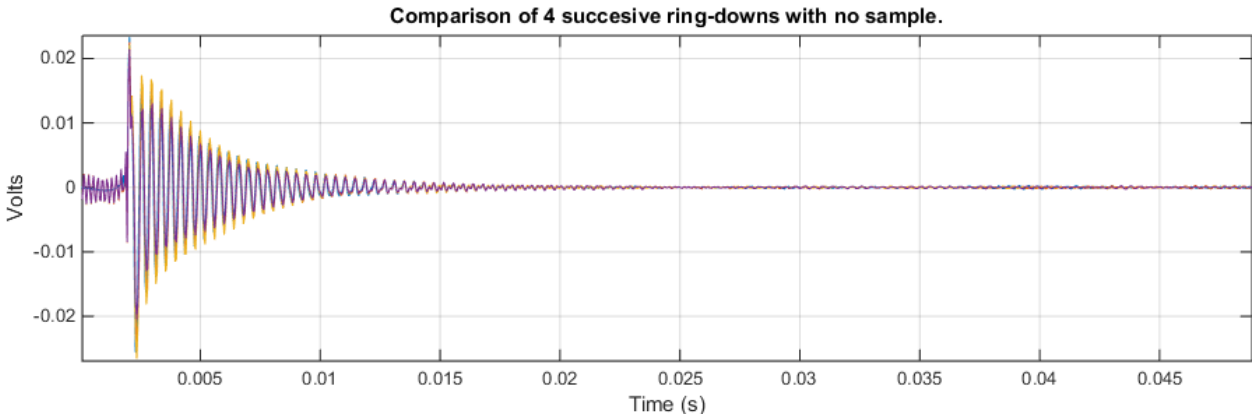

Figure 64: Superposition of 4 ring-downs. The ring-downs are similar with some variation in phase and amplitude.

Software ring-down attenuation: In all proposed methods a considerable reduction of the ring-down is achieved. In Figure 65 the resultant error of the three methods on the NMR free ring-down decay can be seen in the time domain. The ring-down suppression by the mono-exponential fitting can be seen in Figure 65A. The remaining error is related to the 2nd harmonic (5 kHz) of the ring-down, which is related to detector nonlinearities. Alternatively, directly subtracting the ring-down has lower performance than its adaptive version as can be observed in Figure 65B and C. Figure 66 shows the methods applied to distilled water and human thumb NMR FID signals. All three methods improve the spectrum considerably. Directly subtracting the averaged ring-down has the poorest performance, reducing the ring-down effects by about 60%. The exponential fitting and adaptive recorded ring-down subtraction methods reduce the presence of ring-down by 80%.

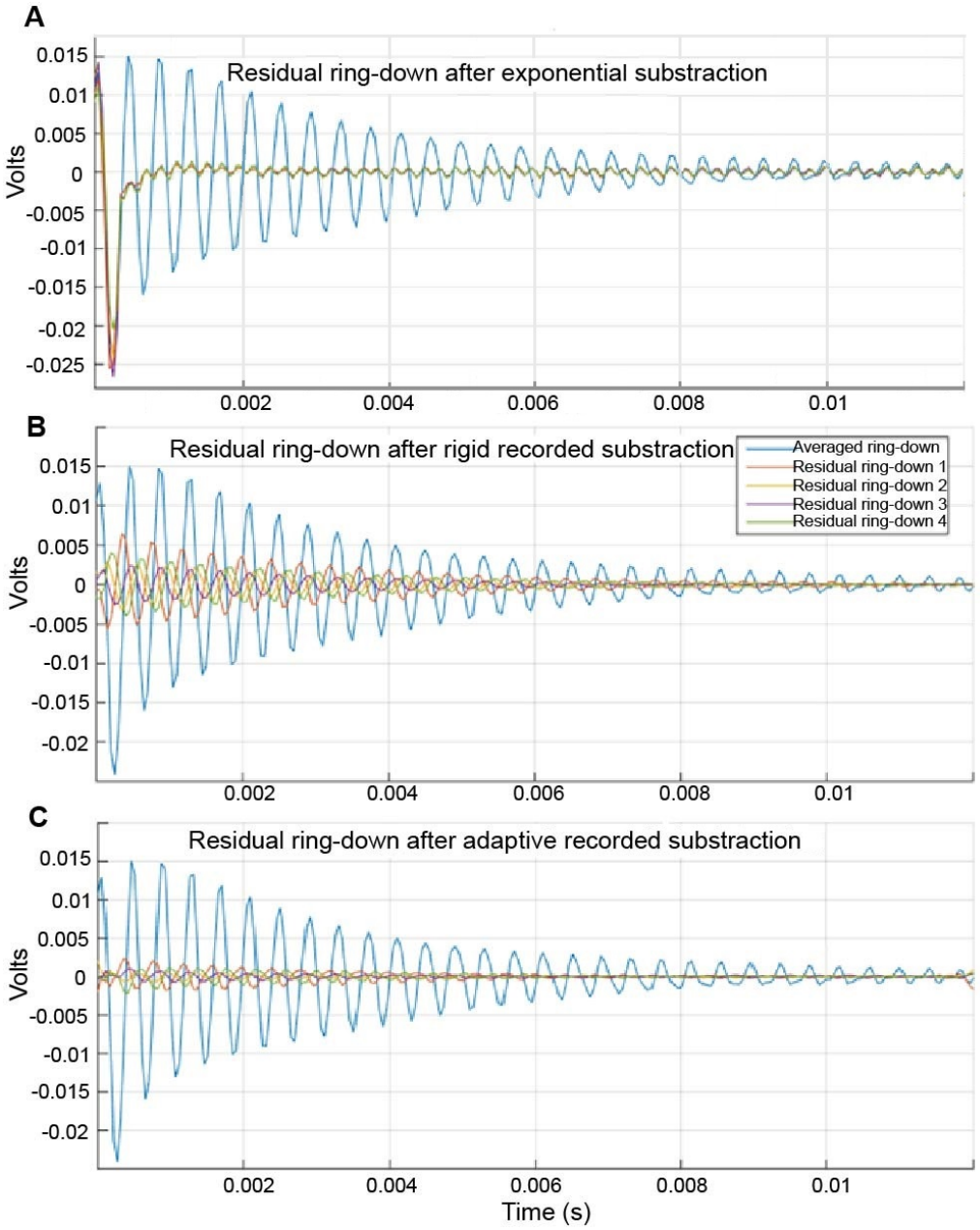

Figure 65: Residual ring-down signal of proposed algorithms. Figures show the effectiveness of the ring-down attenuation by plotting the residuals with the averaged ring-down as a reference. The residual after employing the exponential fitting algorithm is shown in (A). Note the second harmonic at 5 kHz dominates the residual. Direct subtraction of averaged ring-down shows considerably higher residual (B) unless it is compensated in phase and magnitude (C).

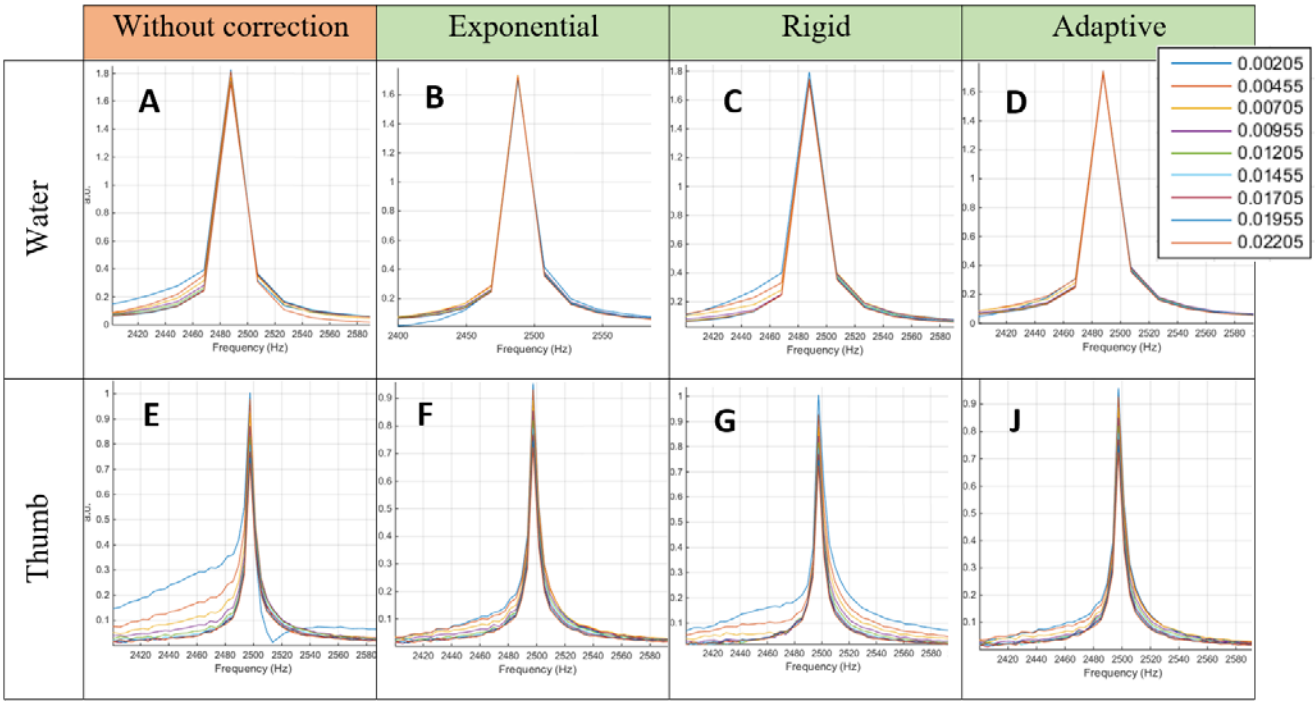

Figure 66: Visualisation of tested ring-down attenuation alternatives for different dead-times, represented in the legend in seconds. The first column shows the original signal without corrections for water (A) and thumb (E). The effect of the ring-down is more evident in the thumb spectrum than in the water sample. The exponential fitting (B & F) and adaptive recorded ring-down (D & J) methods reach similar results in both cases. The rigid recorded ring-down (C & G) method shows the weakest attenuation.

6.5 Discussion

We have proposed a comprehensive solution to facilitate the design of ULF MR detectors based on air-core magnetometers which leads to relatively fast and highly sensitive signal acquisition. Here, we have improved our previous work[178] by optimising the coils to a specific volume in the near-field, what advances coil sensitivity[26,181]. Additionally, we propose an inexpensive ultra-low noise pre-amplifier which showcases lower noise floor than previously

reported ULF MR pre-amplifiers, thereby improving magnetometer sensitivity[24,187]. Besides, we have been able to increase acquisition efficiency by reducing detector dead-time below 4 ms, which is less than half of what has been recently reported[100]. Results show that faster energy dissipation is achieved by increasing the resonant frequency of the *Q*-damping circuit. Consequently, this allows the ring-down to be independent of the Rf pulse, becoming more reproducible and improving its attenuation through prediction via data post-processing.

6.5.1 Coil design

The 2.5% SNR difference between estimation and measurement corroborates the accuracy of employed numerical models. In comparison to the far-field optimisation method described previously[178], the speed of the near-field optimisation algorithm is considerably slower. Computation times have increased by a factor of 3. Nevertheless, coils can be designed within reasonable times using a standard PC (a coil of few hundred loops in about 3 minutes, and 5000 loops in about 3 hours). Other than a reduction in computational performance, no other effect on algorithm performance was noticed.

Albeit the satisfactory results reported here, some improvements to the numerical model and optimisation algorithm can be envisioned. Currently, either coil inner or outer diameter is fixed, which can be a detrimental restriction in some scenarios. For example, not fixing neither inner nor outer coil diameter could benefit single surface coil arrangements where space is not a constraint. Likewise, higher SNR designs may be achievable with consideration towards other factors, such as reducing inductance to reduce ring-down with pulse sequences using short echo or repetition times.

Alternatively, if the frequencies of interest are extremely narrowband, an external high-*Q* inductor could be used which provides a very large voltage transformation[197]. For this strategy to improve the SNR, the inductance of the external high-permeability coil should be much higher than the inductance of the MR coil, while the resistance of the external coil should be somewhat smaller than the MR coil[198]. The functional bandwidth of this approach could be improved by applying negative feedback.

The proposed method can optimise cylindrical and surface coils, which are routinely used coil designs[24,187,197]. Cylindrical coils can be very sensitive as they can achieve large filling factors. Conversely, surface coils provide the versatility of limiting sensitivity to a smaller region of the sample. Currently, our approach has been to optimise individual coils. However, methods could be extended to optimise surface coil arrays to allow for faster acquisitions through parallel imaging[75].

6.5.2 Pre-amplifier

The proposed pre-amplifier is an important component to achieve a cost-effective solution for signal detection. Although its measured voltage noise is 8.3% higher than the simulated value of 0.36 nV/√Hz, this is still at least two times lower than values previously reported ULF MR pre-amplifiers[24,187]. The difference between measured and simulated value is reasonable as at such low noise floors any layout and manufacturing imperfections quickly become a source of additional noise. Also, the jFETs used have not been individually screened, which can increase noise floor if any of the four jFETs has higher noise figures than stated. Note, noise based on the four jFET design is quadratically additive. If a lower noise floor is desired, one can individually test and select the best performing jFETs from a batch, or add more jFETs in parallel. We have chosen to parallelise only four BF862 jFETs as they feature good stability and bandwidth for a wide range of source loads, i.e. potential coils.

Regarding the pre-amplifier topology, the cascode configuration reduces the dynamic capacitance generated by the Miller effect. Also, the negative feedback increases gain stability. Faster recovery times from saturation are possible by reducing the value of the bypass capacitor placed before the OP27 and the feedback bypass capacitor of 47 uF (refer to Figure 55). These changes, however, would reduce the bandwidth from the lower end of the frequencies. Conceivably, depending on the specific application, perhaps a differential input would be favoured due to its higher rejection to common mode and inherent gain stability. In such a case we recommend the reader to consider the SR560 design[119]. If noise performance is the priority, then the single cascode configuration would be favoured. Readers not interested in building a pre-amplifier may opt for commercially available high-performance solutions, such as the LNAM-FBX. Note that this approach would lead to significant increases in the cost of detectors.

6.5.3 *Q*-damping

Q-damping circuits traditionally critically damp the coil maintaining the original resonant frequency of the circuit. Here we show that switching the resonant frequency to higher frequencies can accelerate the energy dissipation by a factor proportional to the relative frequency change. We have opted for resonating the coil at its natural resonant frequency of 85 kHz as this offers a 34 fold increase in damping time reduction as compared to critically damping at the acquisition frequency of 2.5 kHz. This method has allowed us to completely dissipate energy within 1 ms, which is remarkably fast considering employed reed relays have a 0.2 ms response time. An alternative approach would be to estimate the parasitic

capacitance of the coil and include an externally dominating capacitor. In this way, the resonant frequency can be estimated more accurately, and a more optimal level of damping can be achieved. This may, however, reduce the dissipation speed as the *Q*-damping resonant frequency would be reduced.

Additionally, the state transition of the electromechanical switches makes the coil re-ring, ringing which slowly decays in the non-damped circuit with a decay time of 3.3 ms. With the current setup, this re-ringing needs 20 ms before it becomes smaller than the noise floor. Fortunately, ring-down characteristics seem to be independent of the Rf power used, which confirms the efficacy of the proposed damping approach. Once the ring-down has decayed, the negligible insertion loss of the *Q*-damping circuit helps conserve the high sensitivity of the detector. Thereby, the *Q*-damping circuit efficiently removes the energy and protects the pre-amplifier, but induces a considerable re-ringing.

6.5.4 Software ring-down attenuation

The software ring-down attenuation can considerably reduce acquisition dead-time. According to our results (see Figure 66), the direct subtraction of the averaged recorded ring-down can halve the dead-time. This limited attenuation efficiency implies that the reproducibility of the ring-down is somewhat limited in our setup; likely due to the use of electromechanical switches which are subject to mechanical vibrations. However, once the bouncing of the relays has settled, specific features of the resonant behaviour of the circuit are reproducible, i.e. the resonant frequency and the decay time remain constant. For this reason, adjusting the amplitude and phase of the averaged ring-down seems to improve the ring-down attenuation substantially (see Figure 66). Given that these two methods use a finite number of sample points of an acquired signal, part of the ring-down will not be removed if the number of sample points of the MR signal is larger, which is often the case. In this regard, choosing the right length of recorded ring-down will improve the attenuation. As a reference, one should aim to use as many reference ring-down sample points as possible prior to the signal reaching the noise floor. It should be noticed that the reference ring-down contains noise along the whole acquisition, which can be reduced by averaging over many ring-down signals. Averaging can also extend the usable length of the ring-down reference as it decreases the noise floor.

Contrarily, the exponential fitting method can attenuate the ring-down along the whole MR acquisition. Care must be taken in estimating the resonance frequency. A wrong frequency estimation would be less efficient with long MR signals as the ring-down suppression can

become an artificially increased ring-down. Fortunately, this effect is counteracted by the decaying nature of the signal. Similarly, inaccurate estimation of the decay time would reduce the attenuation power or even artificially add signal. Once an accurate characterisation of the ring-down has been achieved, a precise estimation of the amplitude and the phase of the ring-down in the acquired MR signal is desirable. The estimation is most reliable in the initial ring-down cycles as the tank circuit is still loading the MR signal, and the interference of the MR signal in the ring-down is at its minimum. Another factor to consider is that pre-amplifier nonlinearity after a pulse may alter the shape of the ring-down decay. It is therefore desirable to calibrate the ring-down decay time on a signal track where the pre-amplifier is working linearly. Pre-amplifier nonlinearity is better absorbed by the direct subtraction method, where the shape of the subtracted signal would inherently capture the nonlinearity. This feature can be observed in Figure 65, where the 5 kHz harmonic is not suppressed by the exponential fitting method (Figure 65A) as is the case with the recorded ring-down method (Figure 65B-C).

Short dead-times are more critical with short-lived signals, as shown in Figure 66. Multi-echo sequences also benefit from shorter echo times allowing the acquisition of more echoes per pre-polarisation cycle. Solid-state electronic switches have a more reproducible transition than electromechanical relays, what would allow for a more accurate estimation of the ring-down. This improved estimation would increase the efficiency of the methods presented here. However, care must be taken with the additional noise introduced by electronic switches as they can rapidly deteriorate the noise performance of the pre-amplifier. If the noise floor of the detector is increased, the dead-time is decreased as the ring-down disappears in the noise earlier. This is one of the reasons why it is difficult to compare the different *Q*-damping approaches proposed in the literature, as ring-down times are highly dependent on the noise floor, Rf pulse strength and coil properties.

6.6 Conclusions

We have presented a complete solution to provide air-core magnetometers with unprecedented sensitivity and acquisition efficiency, substituting current expensive, delicate, and bulky sensors for affordable and portable ULF MR systems. High sensitivities are achieved by optimising the coil to the volume of interest, and by considering pre-amplifier and matching network properties. The most popular coil types have been implemented here, i.e. the surface and the cylindrical coils. To further improve acquisition efficiency, coil energy dissipation is accelerated by a switched *Q*-damping configuration that critically damps the circuit at frequencies higher than the acquisition frequency. The re-excitation induced by the

Q-damping switching circuit follows a pattern and can be substantially attenuated by subtracting an estimation of the ring-down. A prototype coil resulting from these methods has been tested in NMR and MRI experiments to validate the numerical methods. To complete the detector system, an adaptation of an ultra-low noise pre-amplifier has been proposed, which provides the detector with high SNR while maintaining low upfront costs.

The optimisation algorithm, circuit schematics and PCB layouts will be made publically available to promote this exciting modality by facilitating the design of affordable, robust, and highly sensitive detectors.

Chapter 7- Discussion and conclusions

7.1 Summary of achievements

Presented concepts contribute to the ultimate goal of developing a ULF MR system with increased portability and reduced costs. We have proposed a novel design that improves system portability through the use of permanent magnets to generate a range of magnetic fields. Further, we have developed methods that facilitate the design of inexpensive but highly sensitive room temperature air-core magnetometers, providing them with probably the highest performance value amongst ULF MR sensors.

To substitute resistive coils with permanent magnets, while maintaining the field versatility required for ULF MR relaxometry, we have combined three concentric Halbach arrays, which can be mechanically reconfigured through rotations to some of its components (see Chapter 3). An adjustable measurement field is produced by two of the Halbach arrays, which coaxially rotate in opposite directions to vary the field. A switchable strong pre-polarisation field is generated by individual rotation of the permanent magnets of the third Halbach array. Predicted field versatility has been validated with a static SPMA prototype.

To produce the variety of linearly independent gradient fields needed for generating a 3D MRI image with permanent magnets, we have studied the possibility of stepping one or two magnets around the SPMA (see Chapter 4). A series of different satellite magnet configuration variants are analysed in the search for the optimal arrangement. Our simulations predict that it is possible to resolve 3D images with minimal encoding magnets moving around the sample on a simple linear helical path without the need to move the sample or to apply additional encoding RF fields[81,229].

To provide robust and inexpensive air-core magnetometers with high sensitivity, we have developed a computer program that facilitates their design (see Chapter 5). The proposed algorithm numerically optimises air-core magnetometers to specific target frequencies and dimension requirements. By maintaining a high number of design variables, this program finds optimal cylindrical coils from a larger pool of possibilities than previous works. Importantly, we have verified that the combination of accurate numerical models produces pragmatic results, which lead to realistic sensitivity figures.

To further augment detector imaging sensitivity and efficiency, we have modified a simple and inexpensive ultra-low noise pre-amplifier; we have developed a novel efficient *Q*-damping approach; and we have proposed a ring-down attenuation post-processing method

(see Chapter 6). The pre-amplifier features a remarkably low voltage noise and 1000 gain between 1 kHz and 100 kHz. The *Q*-damping circuit protects the pre-amplifier from overvoltage and promptly dissipates the energy of the coil by temporarily increasing the resonant frequency of the tank circuit and critically damping it. The post-processing method reduces by 80% the effects of the re-ringing created by *Q*-damping switching. The low insertion losses and fast energy dissipation capabilities of the *Q*-damping architecture, combined with the ring-down attenuation algorithm, help maintain the sensitivity of the detector and allow for prompt signal acquisitions.

7.2 Discussion

Specific system characteristics that have motivated our research path are power consumption, system size, safety, SNR, imaging efficiency, price, and application versatility. In the following, we discuss how the present work advocates for abovementioned features.

Low energy consumption is an important requirement for portability. Generating the quasi-static fields by permanent magnets allows for a considerable reduction in energy use as compared to fields generated with resistive coils. In our design, the main energy dissipation arises from the mechanical movements required for the pre-polarisation, which is significantly lower than the energy dissipated in resistive coils due to current flow. Similarly, air-core magnetometers do not require an uninterrupted power supply to maintain thermal regulation of the cryogen, which is the case of SQUIDs.

Reducing overall system siting requirements facilitates its portability. Producing proposed nonlinear image encoding gradients reduce system size by simplifying magnet arrangement. The ability to switch off the strong pre-polarisation field and the reduced stray magnetic field of the cylindrical Halbach configuration also facilitate the transportation of the system. Further, unlike most ULF MR SQUID-based detector setups, proposed air-core magnetometers are not configured in a hardware gradiometry configuration, conceding more compact coil arrangements and allowing for smaller systems.

Signal SNR and imaging efficiency are critical for the provision of reliable diagnoses and patient throughput. A stronger pre-polarisation quasi-proportionally increases signal SNR through increasing sample magnetisation. We predict that pre-polarisation fields higher than 100 mT are possible with the SMPA concept, which is higher than what is reached in existing resistive coil based ULF MR systems. The lower conductivity of the permanent magnets can also reduce system noise by decreasing eddy currents. Moreover, the high sensitivity and

shorter dead-times of presented magnetometers boost acquisition efficiency. Instead of specific coil designs, we have developed methods to easily design high-performance coils, because tailoring the coils to the application improves imaging efficiency drastically[230]. Proposed methods aid optimising the design of two popular coil designs, i.e. cylindrical coils and surface coils, providing the building blocks for coil array designs for applications such as parallel imaging. Achieved ring-down attenuation allows for coil designs with a large number of turns. Methods presented here also enable the optimisation of coils highly sensitive to ambient noise to attenuate it further through software gradiometry.

The price of the system has also been a design consideration. This cost effectiveness has perhaps been optimised to a greater extent with the detectors than with the SPMA array, as the detectors are a well-stabilised technology. The bill of materials for proposed air-core magnetometers is around $60 (AUD), although this is highly dependent on the type and length of wire employed for the coil. Proposed methods provide air-core magnetometers with unprecedented sensitivity/price ratio, making proposed detectors very competitive against other more sophisticated technologies that cost several thousands of dollars, such as SQUIDs and atomic magnetometers. Besides, the technical developments on permanent magnet production have considerably reduced their price over the last decade. At the current state of development, the mechanical actuation of the pre-polarisation array encompasses a considerable fraction of the overall system price. Hardware costs will likely be reduced after the proof-of-concept phase.

Proposed concepts and methods have been developed to cover a wide range of applications. The measurement field has been made adjustable so that the distinctive benefits of acquiring the MR signal in different measurement fields can be exploited. Accordingly, the developed detector design methods allow for customising coils for a broad range of frequencies and target shapes. This tailoring enables acquiring either NMR or 3D MRI data. Given current inner bore size, acquisitions are limited to samples or human extremities, but this could be upsized to allow for human heads or even human torsos.

7.3 Future directions

Further work is required to complete an SPMA ULF MR system. Fast and precise mechanical actuators need to be developed to accurately and reproducibly rotate the individual magnets of the pre-polarisation array. This precision is especially critical to achieving field cancellation in the pre-polarisation OFF configuration. Conveniently, the energetic state of the pre-polarisation ON arrangement assists with the fast movement

required for turning the field off and aligning the magnets. Still, mechanical vibrations and the capability of the mechanical actuators to accurately perform the rotations will determine transition times.

Image reconstruction relies on accurate mapping of the fields generated by the SPMA to prevent image quality loss. Therefore, pre-polarisation array magnet misalignments and temperature related drifts require periodic calibration and simultaneous monitoring of generated magnetic fields. The empirical field evolution of the pre-polarisation switching will also be studied, aided by a 3D array of detectors.

The image reconstruction will benefit from an algorithm that solves the pseudo-inverse faster and with higher accuracy than the Kaczmarz method here employed. The candidate algorithm should filter out inconsistent noise intrinsic to overdetermined matrices, like the ones concerning this project. Alternatively, deep convolutional neural networks can be good candidates to compensate for field infidelities and enhance SNR in image reconstruction tasks[231].

Although the presented method theoretically allows for 3D imaging without Rf pulses, higher imaging efficiency can be expected if multiple echoes are acquired within one pre-polarisation cycle. Gradient echoes and field echoes are challenging to achieve as magnetic fields are generated by permanent magnets. Therefore, spin echoes are probably the most reasonable solution, which would require an efficient Rf power amplifier that maintains power consumption as low as possible. Such a sequence would benefit from the reduced dead-time of the proposed sensors, which would allow faster echo trains. In this regard, substituting the reed relays of the *Q*-damping switch with transistors would generate a more reproducible ring-down which would considerably improve the efficiency of the proposed attenuation algorithm, further reducing the dead-time.

ULF MR systems require expensive, large, and heavy shielding to reduce ambient noise. The requirements of the shielding can be reduced through hardware gradiometry at the expense of increased detector size. Alternatively, software gradiometry can be performed by using additional far-field sensing detectors, which has shown promising results[232].

Interestingly, acquiring the MR signal in the ULF regime offers some features which are unique to this modality. For example, it allows imaging in the proximity of metals, which would allow screening of patients otherwise excluded from MR due to safety hazards and imaging artefacts[15]. Similarly, ULF MR systems impose fewer compatibility constraints to

operate in conjunction with other medical instruments, enabling their use in interventional scenarios such as in image-guided surgeries[16]. Some pathologies can benefit from enhanced contrast in ULF MR[233]. Similarly, ULF NMR can facilitate the study of relevant spectral features non-proportional to the measurement magnetic field, such as J-coupling.

Apart from the common MR applications, the ULF MR frequency of operation has the potential to elucidate chemical or biological processes occurring at similar timescales. For example, a biological activity that generates magnetic fields, like neural currents, could be inferred through its effect on the MR signal[14]. Our approach also allows for adjusting the field strength, which can be used to optimise the contrast for specific applications or to gain additional insight into tissues by looking to field dependent features such as the T_1 dispersion curves[12,13].

The methods developed here can find application beyond the MR area. The field versatility of the SPMA would facilitate field manipulation in applications such as guided drug delivery through magnetic nanoparticles[82,234]. Also, the proposed sensing solution can have extensive use in areas such as magnetocardiograpy[181] and magnetic induction tomography[180], for near-field sources, and astrophysical/geophysical exploration[203-206], mass spectrometry[207], and audio[208,209] applications for the far-field counterpart.

7.4 Conclusions

The proposed SPMA concept improves power efficiency without sacrificing the safety and the field versatility typical of coil-based ULF MR systems. The substitution of expensive and fragile sensing technologies like SQUIDs and atomic magnetometers by high-performance air-core magnetometers further improves system portability and affordability. The combination of proposed methods paves the way towards a truly portable low-cost ULF MR system. Such an instrument can complement conventional MR and significantly lower the economic barrier that restrains the majority of world's population from benefiting from the comprehensive healthcare value of MR.

References

1 van der Graaf, M. In vivo magnetic resonance spectroscopy: basic methodology and clinical applications. *European Biophysics Journal* **39**, 527-540 (2010).

2 Liney, G. *MRI in clinical practice / Gary Liney*. (London : Springer, 2006).

3 DeMartini, W. & Lehman, C. A review of current evidence-based clinical applications for breast magnetic resonance imaging. *Topics in magnetic resonance imaging* **19**, 143-150 (2008).

4 Bauer, S., Wiest, R., Nolte, L.-P. & Reyes, M. A survey of MRI-based medical image analysis for brain tumor studies. *Physics in Medicine & Biology* **58**, R97 (2013).

5 Phelan, N., Rowland, P., Galvin, R. & O'Byrne, J. M. A systematic review and meta-analysis of the diagnostic accuracy of MRI for suspected ACL and meniscal tears of the knee. *Knee Surgery, Sports Traumatology, Arthroscopy* **24**, 1525-1539 (2016).

6 Sferrella, S. Equipment Service: Total Cost of Ownership. (2012). <http://www.radiologybusiness.com/topics/technology-management/equipment-service-total-cost-ownership>.

7 World Health Organization. Baseline country survey on medical devices - Magnetic Resonance Imaging. . *Global Health Observatory data, Medical equipment* (2014). <http://www.who.int/gho/health_technologies/medical_devices/medical_equipment/en/>.

8 Petrou, M., Foerster, B. R. & Reich, D. S. Translational research in radiology: challenges and role in a patient-based practice. *Academic radiology* **16**, 593-596 (2009).

9 Open Source Imaging Initiative (OSI^2). Open Source Magnetic Resonance Imaging: From the Community to the Community. (2016). <http://www.opensourceimaging.org/>.

10 Pipe, J. in *Magnetic Resonance in Medicine Highlights* (2016).

11 Nieminen, J. O. *et al.* Improved contrast in ultra-low-field MRI with time-dependent bipolar prepolarizing fields: theory and NMR demonstrations. *Metrology and Measurement Systems* **20**, 327-336 (2013).

12 Lee, S. K. *et al.* SQUID-detected MRI at 132 μT with T1-weighted contrast established at 10 μT–300 mT. *Magnetic resonance in medicine* **53**, 9-14 (2005).

13 Ungersma, S. E. *et al.* Magnetic resonance imaging with T1 dispersion contrast. *Magnetic resonance in medicine* **55**, 1362-1371 (2006).

14 Burghoff, M. *et al.* On the feasibility of neurocurrent imaging by low-field nuclear magnetic resonance. *Applied Physics Letters* **96**, 233701 (2010).

15 Kraus Jr, R., Espy, M., Magnelind, P. & Volegov, P. *Ultra-Low Field Nuclear Magnetic Resonance: A New MRI Regime*. (Oxford University Press, 2014).

16 Körber, R. in *EMBEC & NBC 2017* 795-798 (Springer, 2017).

17 Florio, F., Sinha, G. & Sundararaman, R. Designing High-Accuracy Permanent Magnets for Low-Power Magnetic Resonance Imaging. *IEEE Transactions on Magnetics* **54**, 5300209 (2018).

18 Cooley, C. Z. *et al.* Design of Sparse Halbach Magnet Arrays for Portable MRI Using a Genetic Algorithm. *IEEE Transactions on Magnetics* **54**, 1-12 (2018).

19 Cooley, C. Z. *et al.* Two-dimensional imaging in a lightweight portable MRI scanner without gradient coils. *Magnetic resonance in medicine* **73**, 872-883 (2015).

20 Espy, M., Matlashov, A. & Volegov, P. SQUID-detected ultra-low field MRI. *J Magn Reson* **228**, 1-15 (2013).

21 Espy, M. A. *et al.* Progress Toward a Deployable SQUID-Based Ultra-Low Field MRI System for Anatomical Imaging. *IEEE Trans. Appl. Supercond.* **25**, 1-5 (2015).

22 Garachtchenko, A., Matlashov, A., Kraus Jr, R. H. & Cantor, R. Baseline distance optimization for SQUID gradiometers. *Applied Superconductivity, IEEE Transactions on* **9**, 3676-3679 (1999).

23 Matlachov, A. N., Volegov, P. L., Espy, M. A., George, J. S. & Kraus Jr, R. H. SQUID detected NMR in microtesla magnetic fields. *J Magn Reson* **170**, 1-7 (2004).

24 Matlashov, A. N. *et al.* SQUIDs vs. induction coils for ultra-low field nuclear magnetic resonance: experimental and simulation comparison. *IEEE Transactions on Applied Superconductivity* **21**, 465-468 (2011).

25 McDermott, R. *et al.* SQUID-detected magnetic resonance imaging in microtesla magnetic fields. *J. Low Temp. Phys.* **135**, 793-821 (2004).
26 Myers, W. *et al.* Calculated signal-to-noise ratio of MRI detected with SQUIDs and Faraday detectors in fields from 10μT to 1.5 T. *Journal of Magnetic Resonance* **186**, 182-192 (2007).
27 Qiu, L. *et al.* Magnetic field improved ULF-NMR measurement in an unshielded laboratory using a low-Tc SQUID. *Physics Procedia* **36**, 388-393 (2012).
28 Trahms, L. & Burghoff, M. NMR at very low fields. *Magn Reson Imag* **28**, 1244-1250 (2010).
29 Vadim, S. Z. *et al.* SQUID-based instrumentation for ultralow-field MRI. *Supercond. Sci. Technol.* **20**, S367 (2007).
30 Zotev, V. S. *et al.* Multi-channel SQUID system for MEG and ultra-low-field MRI. *IEEE Transactions on Applied Superconductivity* **17**, 839-842 (2007).
31 Zotev, V. S. *et al.* SQUID-based microtesla MRI for in vivo relaxometry of the human brain. *IEEE Transactions on Applied Superconductivity* **19**, 823-826 (2009).
32 Brown, R. W., Haacke, E. M., Cheng, Y.-C. N., Thompson, M. R. & Venkatesan, R. *Magnetic resonance imaging: physical principles and sequence design*. (John Wiley & Sons, 2014).
33 Bloch, F. Nuclear induction. *Physical review* **70**, 460 (1946).
34 Koenig, S. H. & Brown III, R. D. Determinants of proton relaxation rates in tissue. *Magnetic resonance in medicine* **1**, 437-449 (1984).
35 Stanisz, G. J. *et al.* T1, T2 relaxation and magnetization transfer in tissue at 3T. *Magnetic Resonance in Medicine: An Official Journal of the International Society for Magnetic Resonance in Medicine* **54**, 507-512 (2005).
36 Twieg, D. B. The k-trajectory formulation of the NMR imaging process with applications in analysis and synthesis of imaging methods. *Medical physics* **10**, 610-621 (1983).
37 Schultz, G. *et al.* Reconstruction of MRI data encoded with arbitrarily shaped, curvilinear, nonbijective magnetic fields. *Magnetic resonance in medicine* **64**, 1390-1403 (2010).
38 Gallichan, D. *et al.* Simultaneously driven linear and nonlinear spatial encoding fields in MRI. *Magnetic resonance in medicine* **65**, 702-714 (2011).
39 Parker, D. L. & Hadley, J. R. Multiple-region gradient arrays for extended field of view, increased performance, and reduced nerve stimulation in magnetic resonance imaging. *Magnetic resonance in medicine* **56**, 1251-1260 (2006).
40 Tam, L. K., Stockmann, J. P., Galiana, G. & Constable, R. T. Null space imaging: nonlinear magnetic encoding fields designed complementary to receiver coil sensitivities for improved acceleration in parallel imaging. *Magnetic resonance in medicine* **68**, 1166-1175 (2012).
41 Wang, Y., Xin, X., Liu, F. & Crozier, S. Spiral Gradient Coil Design for Use in Cylindrical MRI Systems. *IEEE Transactions on Biomedical Engineering* **65**, 911-920 (2018).
42 Prado, P. J. Single sided imaging sensor. *Magnetic Resonance Imaging* **21**, 397-400 (2003).
43 Perlo, J., Casanova, F. & Blümich, B. 3D imaging with a single-sided sensor: an open tomograph. *Journal of Magnetic Resonance* **166**, 228-235 (2004).
44 Herman, G. T. & Lent, A. Iterative reconstruction algorithms. *Computers in biology and medicine* **6**, 273-294 (1976).
45 Posse, S., Otazo, R., Dager, S. R. & Alger, J. MR spectroscopic imaging: principles and recent advances. *Journal of Magnetic Resonance Imaging* **37**, 1301-1325 (2013).
46 Sarracanie, M. *et al.* Low-cost high-performance MRI. *Scientific reports* **5**, 15177 (2015).
47 Vesanen, P. T. *et al.* Hybrid ultra-low-field MRI and magnetoencephalography system based on a commercial whole-head neuromagnetometer. *Magnetic Resonance in Medicine* **69**, 1795-1804 (2013).
48 Blümich, B., Kölker, C., Casanova, F., Perlo, J. & Felder, J. Ein mobiler und offener Kernspintomograph: Kernspintomographie für Medizin und Materialforschung. *Physik in unserer Zeit* **36**, 236-242 (2005).
49 Casanova, F. & Blümich, B. Two-dimensional imaging with a single-sided NMR probe. *Journal of Magnetic Resonance* **163**, 38-45 (2003).
50 Chang, W.-H., Chen, J.-H. & Hwang, L.-P. Single-sided mobile NMR with a Halbach magnet. *Magnetic resonance imaging* **24**, 1095-1102 (2006).

51 García-Naranjo, J. C., Mastikhin, I. V., Colpitts, B. G. & Balcom, B. J. A unilateral magnet with an extended constant magnetic field gradient. *Journal of Magnetic Resonance* **207**, 337-344 (2010).
52 Kato, H. *et al.* A design of permanent magnet array for unilateral NMR device. *Concepts in Magnetic Resonance Part B: Magnetic Resonance Engineering* **33**, 201-208 (2008).
53 Marble, A. E., Mastikhin, I. V., Colpitts, B. G. & Balcom, B. J. A constant gradient unilateral magnet for near-surface MRI profiling. *Journal of Magnetic Resonance* **183**, 228-234 (2006).
54 Paulsen, J. L., Bouchard, L. S., Graziani, D., Blümich, B. & Pines, A. Volume-selective magnetic resonance imaging using an adjustable, single-sided, portable sensor. *Proceedings of the National Academy of Sciences* **105**, 20601-20604 (2008).
55 Sakellariou, D. *et al.* Portable MRI Magnets and Spinning Micro-Detectors.
56 Yongliang, J., Wei, H. & Xiaolong, H. Optimization and Construction of Single-side Nuclear Magnetic Resonance Magnet. *Indonesian Journal of Electrical Engineering and Computer Science* **11**, 6017-6024 (2013).
57 Perlo, J., Casanova, F. & Blümich, B. Ex situ NMR in highly homogeneous fields: 1H spectroscopy. *Science* **315**, 1110-1112 (2007).
58 Prado, P. J., Blümich, B. & Schmitz, U. One-dimensional imaging with a palm-size probe. *Journal of Magnetic Resonance* **144**, 200-206 (2000).
59 Halbach, K. Design of permanent multipole magnets with oriented rare earth cobalt material. *Nuclear instruments and methods* **169**, 1-10 (1980).
60 Cooley, C. Z., Stockmann, J. P., Sarracanie, M., Rosen, M. S. & Wald, L. L. in *Intl Soc Mag Res Med.* 4192.
61 Tayler, M. C. & Sakellariou, D. Low-cost, pseudo-Halbach dipole magnets for NMR. *Journal of Magnetic Resonance* **277**, 143-148 (2017).
62 Raich, H. & Blümler, P. Design and construction of a dipolar Halbach array with a homogeneous field from identical bar magnets: NMR Mandhalas. *Concepts in Magnetic Resonance Part B: Magnetic Resonance Engineering* **23**, 16-25 (2004).
63 Windt, C. W., Soltner, H., Dusschoten, D. v. & Blümler, P. A portable Halbach magnet that can be opened and closed without force: The NMR-CUFF. *Journal of Magnetic Resonance* **208**, 27-33, doi:https://doi.org/10.1016/j.jmr.2010.09.020 (2011).
64 Manz, B., Benecke, M. & Volke, F. A simple, small and low cost permanent magnet design to produce homogeneous magnetic fields. *Journal of magnetic resonance* **192**, 131-138 (2008).
65 Hugon, C., D'Amico, F., Aubert, G. & Sakellariou, D. Design of arbitrarily homogeneous permanent magnet systems for NMR and MRI: Theory and experimental developments of a simple portable magnet. *Journal of Magnetic Resonance* **205**, 75-85 (2010).
66 Hills, B., Wright, K. & Gillies, D. A low-field, low-cost Halbach magnet array for open-access NMR. *Journal of Magnetic Resonance* **175**, 336-339 (2005).
67 Blümler, P. Permanent Magnet System for MRI with Constant Gradient mechanically adjustable in Direction and Strength. *arXiv preprint arXiv:1510.02772* (2015).
68 Winter, L., Barghoorn, A., Blümler, P. & Niendorf, T. in *ISMRM.*
69 Purcell, E. M., Torrey, H. C. & Pound, R. V. Resonance Absorption by Nuclear Magnetic Moments in a Solid. *Physical Review* **69**, 37-38 (1946).
70 Rollin, B. V. Nuclear paramagnetism. *Reports on Progress in Physics* **12**, 22 (1949).
71 Blümich, B. Stochastic NMR imaging. *Journal of Magnetic Resonance (1969)* **60**, 37-45 (1984).
72 Ernst, R. R., Bodenhausen, G. & Wokaun, A. *Principles of nuclear magnetic resonance in one and two dimensions*. Vol. 14 (Clarendon Press Oxford, 1987).
73 Ernst, R. R. & Anderson, W. A. Application of Fourier transform spectroscopy to magnetic resonance. *Review of Scientific Instruments* **37**, 93-102 (1966).
74 Hutchinson, M. & Raff, U. Fast MRI data acquisition using multiple detectors. *Magnetic resonance in Medicine* **6**, 87-91 (1988).
75 Roemer, P. B., Edelstein, W. A., Hayes, C. E., Souza, S. P. & Mueller, O. The NMR phased array. *Magnetic resonance in medicine* **16**, 192-225 (1990).
76 Pruessmann, K. P., Weiger, M., Scheidegger, M. B. & Boesiger, P. SENSE: sensitivity encoding for fast MRI. *Magnetic resonance in medicine* **42**, 952-962 (1999).

77 Griswold, M. A. *et al.* Generalized autocalibrating partially parallel acquisitions (GRAPPA). *Magnetic resonance in medicine* **47**, 1202-1210 (2002).
78 Sotgiu, A. & Hyde, J. S. High-order coils as transmitters for NMR imaging. *Magnetic resonance in medicine* **3**, 55-62 (1986).
79 Katscher, U. & Börnert, P. Parallel RF transmission in MRI. *NMR in Biomedicine* **19**, 393-400 (2006).
80 Rigla, J. *et al.* in *Nuclear Science Symposium and Medical Imaging Conference (NSS/MIC), 2014 IEEE.* 1-4 (IEEE).
81 Sharp, J. C. & King, S. B. MRI using radiofrequency magnetic field phase gradients. *Magnetic resonance in medicine* **63**, 151-161 (2010).
82 Baun, O. & Blümler, P. Permanent magnet system to guide superparamagnetic particles. *Journal of Magnetism and Magnetic Materials* **439**, 294-304 (2017).
83 Meriles, C. A., Sakellariou, D., Trabesinger, A. H., Demas, V. & Pines, A. Zero-to low-field MRI with averaging of concomitant gradient fields. *Proceedings of the National Academy of Sciences of the United States of America* **102**, 1840-1842 (2005).
84 Volegov, P., Mosher, J., Espy, M. & Kraus Jr, R. On concomitant gradients in low-field MRI. *Journal of Magnetic Resonance* **175**, 103-113 (2005).
85 Yablonskiy, D. A., Sukstanskii, A. L. & Ackerman, J. J. Image artifacts in very low magnetic field MRI: the role of concomitant gradients. *Journal of Magnetic Resonance* **174**, 279-286 (2005).
86 Norris, D. G. & Hutchison, J. M. Concomitant magnetic field gradients and their effects on imaging at low magnetic field strengths. *Magnetic resonance imaging* **8**, 33-37 (1990).
87 Nieminen, J. O. & Ilmoniemi, R. J. Solving the problem of concomitant gradients in ultra-low-field MRI. *Journal of Magnetic Resonance* **207**, 213-219 (2010).
88 Hoult, D. The principle of reciprocity in signal strength calculations—a mathematical guide. *Concepts in Magnetic Resonance Part A* **12**, 173-187 (2000).
89 Breneman, B. C., Purcell, J. R. & Burnett, S. C. (1990).
90 Mandal, S., Utsuzawa, S. & Song, Y.-Q. An extremely broadband low-frequency MR system. *Microporous and Mesoporous Materials* **178**, 53-55 (2013).
91 Bode, H. W. Network analysis and feedback amplifier design. (1945).
92 Fano, R. M. Theoretical limitations on the broadband matching of arbitrary impedances. *Journal of the Franklin Institute* **249**, 57-83 (1950).
93 Youla, D. A new theory of broad-band matching. *IEEE Transactions on Circuit Theory* **11**, 30-50 (1964).
94 Hoult, D. Fast recovery, high sensitivity NMR probe and preamplifier for low frequencies. *Review of Scientific Instruments* **50**, 193-200 (1979).
95 Brunner, D. O. *et al.* Symmetrically biased T/R switches for NMR and MRI with microsecond dead time. *Journal of Magnetic Resonance* **263**, 147-155 (2016).
96 Andrew, E. & Jurga, K. NMR probe with short recovery time. *Journal of Magnetic Resonance (1969)* **73**, 268-276 (1987).
97 Hoult, D. I. Receiver design for MR. *eMagRes* (2011).
98 Lowe, I. & Tarr, C. A fast recovery probe and receiver for pulsed nuclear magnetic resonance spectroscopy. *Journal of Physics E: Scientific Instruments* **1**, 320 (1968).
99 Grannell, P., Orchard, M., Mansfield, P., Garroway, A. & Stalker, D. A FET analogue switch for pulsed NMR receivers. *Journal of Physics E: Scientific Instruments* **6**, 1202 (1973).
100 Zhen, J., O'Neill, K., Fridjonsson, E., Stanwix, P. & Johns, M. A resistive Q-switch for low-field NMR systems. *Journal of Magnetic Resonance* **287**, 33-40 (2018).
101 Papoutsis, K., Li, L., Near, J., Payne, S. & Jezzard, P. A purpose-built neck coil for black-blood DANTE-prepared carotid artery imaging at 7T. *Magnetic Resonance Imaging* **40**, 53-61, doi:https://doi.org/10.1016/j.mri.2017.04.011 (2017).
102 Savukov, I., Karaulanov, T., Wurden, C. & Schultz, L. Non-cryogenic ultra-low field MRI of wrist–forearm area. *Journal of Magnetic Resonance* **233**, 103-106 (2013).
103 Savukov, I., Seltzer, S. & Romalis, M. Detection of NMR signals with a radio-frequency atomic magnetometer. *Journal of Magnetic Resonance* **185**, 214-220 (2007).
104 Sergeeva-Chollet, N. *et al.* Low field MRI with magnetoresistive mixed sensors. *Journal of Physics: Conference Series* **303**, 012055 (2011).

105 Pannetier, M., Fermon, C., Le Goff, G., Simola, J. & Kerr, E. Femtotesla magnetic field measurement with magnetoresistive sensors. *Science* **304**, 1648-1650 (2004).
106 Varpula, T. & Poutanen, T. Magnetic field fluctuations arising from thermal motion of electric charge in conductors. *Journal of applied physics* **55**, 4015-4021 (1984).
107 Gabriel, S., Lau, R. & Gabriel, C. The dielectric properties of biological tissues: II. Measurements in the frequency range 10 Hz to 20 GHz. *Physics in medicine & biology* **41**, 2251 (1996).
108 Gadian, D. & Robinson, F. Radiofrequency losses in NMR experiments on electrically conducting samples. *Journal of Magnetic Resonance (1969)* **34**, 449-455 (1979).
109 Redpath, T. W. & Hutchison, J. Estimating patient dielectric losses in NMR imagers. *Magnetic resonance imaging* **2**, 295-300 (1984).
110 Murphy-Boesch, J. & Koretsky, A. P. An in vivo NMR probe circuit for improved sensitivity. *Journal of Magnetic Resonance (1969)* **54**, 526-532 (1983).
111 Hoult, D. & Lauterbur, P. C. The sensitivity of the zeugmatographic experiment involving human samples. *Journal of Magnetic Resonance (1969)* **34**, 425-433 (1979).
112 Hoult, D. & Chen, C. Biomedical magnetic resonance technology. *Bristol and New York: IOP Publishing*, 168-170 (1989).
113 Suits, B., Garroway, A. & Miller, J. Surface and gradiometer coils near a conducting body: the lift-off effect. *Journal of magnetic Resonance* **135**, 373-379 (1998).
114 Mispelter, J., Lupu, M. & Briguet, A. *NMR probeheads for biophysical and biomedical experiments theoretical principles & practical guidelines / Joël Mispelter, Mihaela Lupu, André Briguet*. 2nd ed.. edn, (London : Imperial College Press ; Hackensack, NJ : Distributed by World Scientific, 2015).
115 Giovannetti, G. & De Marchi, D. Capacitors Quality Effect in Magnetic Resonance Radiofrequency Coils. *Journal of Medical and Biological Engineering* **37**, 639-643 (2017).
116 Cao, X. *et al.* The noise factor of receiver coil matching networks in MRI. *Magnetic resonance imaging* **37**, 252-259 (2017).
117 Petrova, P. D. in *Telecommunications in Modern Satellite, Cable and Broadcasting Service, 2003. TELSIKS 2003. 6th International Conference on.* 577-580 (IEEE).
118 Levinzon, F. A. Noise of the JFET amplifier. *IEEE Transactions on Circuits and Systems I: Fundamental Theory and Applications* **47**, 981-985 (2000).
119 Horowitz, P. & Hill, W. *The art of electronics / Paul Horowitz, Harvard University, Winfield Hill, Rowland Institute*. Third edition.. edn, (New York, NY : Cambridge University Press, 2015).
120 Leach, W. M. Fundamentals of low-noise analog circuit design. *Proceedings of the IEEE* **82**, 1515-1538 (1994).
121 Miller, J. M. *Dependence of the input impedance of a three-electrode vacuum tube upon the load in the plate circuit*. Vol. 351 (Government Printing Office, 1919).
122 Fujifilm Sonosite, I. (2017).
123 Netzer, Y. The design of low-noise amplifiers. *Proceedings of the IEEE* **69**, 728-741 (1981).
124 Erdi, G. Amplifier techniques for combining low noise, precision, and high-speed performance. *IEEE Journal of Solid-State Circuits* **16**, 653-661 (1981).
125 Friis, H. T. Noise figures of radio receivers. *Proceedings of the IRE* **32**, 419-422 (1944).
126 Bianchi, C. & Meloni, A. Natural and man-made terrestrial electromagnetic noise: an outlook. *Annals of geophysics* **50**, 435-445 (2007).
127 Vaseghi, S. V. *Advanced digital signal processing and noise reduction*. (John Wiley & Sons, 2008).
128 Fraser-Smith, A. C. Low-frequency radio noise. *Handbook of atmospheric electrodynamics* **1**, 297-310 (1995).
129 Tsai, L., Mair, R., Rosen, M., Patz, S. & Walsworth, R. An open-access, very-low-field MRI system for posture-dependent 3He human lung imaging. *Journal of Magnetic Resonance* **193**, 274-285 (2008).
130 Ishiyama, A., Hondoh, M., Ishida, N. & Onuki, T. Optimal design of MRI magnets with magnetic shielding. *IEEE Transactions on Magnetics* **25**, 1885-1888 (1989).
131 Zevenhoven, K. C. *et al.* Conductive shield for ultra-low-field magnetic resonance imaging: Theory and measurements of eddy currents. *Journal of applied physics* **115**, 103902 (2014).

132 Dong, H. *et al.* Ultra-low field magnetic resonance imaging detection with gradient tensor compensation in urban unshielded environment. *Applied Physics Letters* **102**, 102602 (2013).
133 Liu, C. *et al.* Effect of magnetic field fluctuation on ultra-low field MRI measurements in the unshielded laboratory environment. *Journal of magnetic resonance* **257**, 8-14 (2015).
134 Della Penna, S. *et al.* Biomagnetic systems for clinical use. *Philosophical Magazine B* **80**, 937-948 (2000).
135 Edelstein, W., Glover, G., Hardy, C. & Redington, R. The intrinsic signal-to-noise ratio in NMR imaging. *Magnetic resonance in medicine* **3**, 604-618 (1986).
136 Parra-Robles, J., Cross, A. R. & Santyr, G. E. Theoretical signal-to-noise ratio and spatial resolution dependence on the magnetic field strength for hyperpolarized noble gas magnetic resonance imaging of human lungs. *Medical physics* **32**, 221-229 (2005).
137 Kastler, A. & Brossel, J. La détection de la résonance magnétique des niveaux excités: L'effet de dépolarisation des radiations de résonance optique et de fluorescence. *Comp. Rend* **229**, 1213 (1949).
138 Haake, M., Natterer, J. & Bargon, J. Efficient NMR pulse sequences to transfer the parahydrogen-induced polarization to hetero nuclei. *Journal of the American Chemical Society* **118**, 8688-8691 (1996).
139 Goldman, M. Spin temperature and nuclear magnetic resonance in solids. (1970).
140 Halse, M. E. & Callaghan, P. T. A dynamic nuclear polarization strategy for multi-dimensional Earth's field NMR spectroscopy. *Journal of Magnetic Resonance* **195**, 162-168 (2008).
141 Ardenkjær-Larsen, J. H. *et al.* Increase in signal-to-noise ratio of> 10,000 times in liquid-state NMR. *Proceedings of the National Academy of Sciences* **100**, 10158-10163 (2003).
142 Kovacs, H., Moskau, D. & Spraul, M. Cryogenically cooled probes—a leap in NMR technology. *Progress in Nuclear Magnetic Resonance Spectroscopy* **46**, 131-155 (2005).
143 Fujiwara, T. & Ramamoorthy, A. in *Annual Reports on NMR Spectroscopy* Vol. 58 155-175 (Elsevier, 2006).
144 Packard, M. & Varian, R. Proton gyromagnetic ratio. *Phys. Rev* **93**, 941 (1954).
145 Bloom, A. & Mansir, D. in *Physical Review.* 941-941 (AMERICAN PHYSICAL SOC ONE PHYSICS ELLIPSE, COLLEGE PK, MD 20740-3844 USA).
146 Fite, W. & Redfield, A. G. Nuclear Spin Relaxation in Superconducting Mixed-State Vanadium. *Physical Review* **162**, 358-366 (1967).
147 Körber, R. *et al.* An advanced phantom study assessing the feasibility of neuronal current imaging by ultra-low-field NMR. *Journal of Magnetic Resonance* **237**, 182-190 (2013).
148 Blanchard, J. W. & Budker, D. Zero-to Ultralow-Field NMR. *eMagRes* (2016).
149 Wróblewski, P., Szyszko, J. & Smolik, W. T. in *Imaging Systems and Techniques (IST), 2011 IEEE International Conference on.* 248-252 (IEEE).
150 Abragam, A. *The Principles of Nuclear Magnetism*. (Clarendon Press, 1961).
151 Haake, E., Brown, R., Thompson, M. & Venkatesan, R. *Magnetic Resonance Imaging: Physical Principles and Sequence Design*. (Wiley, New York, 1999).
152 Keeler, J. *Understanding NMR spectroscopy*. (John Wiley & Sons, 2013).
153 McDermott, R. *et al.* Liquid-state NMR and scalar couplings in microtesla magnetic fields. *Science* **295**, 2247-2249 (2002).
154 Burghoff, M., Hartwig, S., Trahms, L. & Bernarding, J. Nuclear magnetic resonance in the nanoTesla range. *Appl. Phys. Lett.* **87**, 054103 (2005).
155 Espy, M. *et al.* Applications of Ultra-Low Field Magnetic Resonance for Imaging and Materials Studies. *IEEE Trans. Appl. Supercond.* **19**, 835-838 (2009).
156 Macovski, A. & Conolly, S. Novel approaches to low-cost MRI. *Magn Reson Med* **30**, 221-230 (1993).
157 Ledbetter, M. *et al.* Near-zero-field nuclear magnetic resonance. *Phys. Rev. lett.* **107**, 107601 (2011).
158 Vogel, M. W., Vegh, V. & Reutens, D. C. Numerical study of ultra-low field nuclear magnetic resonance relaxometry utilizing a single axis magnetometer for signal detection. *Med. Phys.* **40**, 052301 (2013).

159 Zalesskiy, S. S., Danieli, E., Blümich, B. & Ananikov, V. P. Miniaturization of NMR systems: Desktop spectrometers, microcoil spectroscopy, and “NMR on a chip” for chemistry, biochemistry, and industry. *Chem. Rev.* **114**, 5641-5694 (2014).
160 Bjørk, R., Bahl, C. R. H., Smith, A. & Pryds, N. Comparison of adjustable permanent magnetic field sources. *J. Magn. Magn. Mater.* **322**, 3664-3671 (2010).
161 Zhu, Z. & Howe, D. Halbach permanent magnet machines and applications: a review. *IEE Proc.-Electr. Power Appl.* **148**, 299-308 (2001).
162 Moresi, G. & Magin, R. Miniature permanent magnet for table-top NMR. *Concepts Magn. Reson. Part B* **19**, 35-43 (2003).
163 Nan, S. *et al.* Palm NMR and 1-Chip NMR. *IEEE J. Solid-State Circuit* **46**, 342-352 (2011).
164 Volegov, P. *et al.* in *17th International Conference on Biomagnetism Advances in Biomagnetism – Biomag2010* Vol. 28 *IFMBE Proceedings* (eds Selma Supek & Ana Sušac) Ch. 15, 82-87 (Springer Berlin Heidelberg, 2010).
165 Barroso, V. C., Raich, H., Blümler, P., Spiess, H. W. & Wilhelm, M. Nested dipolar Halbach arrays for the determination of magnetorheological properties at variable magnetic field. *Rheologica acta* **50**, 441 (2011).
166 Bauer, C., Raich, H., Jeschke, G. & Blümler, P. Design of a permanent magnet with a mechanical sweep suitable for variable-temperature continuous-wave and pulsed EPR spectroscopy. *Journal of magnetic resonance* **198**, 222-227 (2009).
167 http://www.rotomation.com/product-list/rotary-actuators/.
168 Soltner, H. & Blümler, P. Dipolar Halbach magnet stacks made from identically shaped permanent magnets for magnetic resonance. *Concepts Magn. Reson. Part A* **36**, 211-222 (2010).
169 Hennig, J. *et al.* Parallel imaging in non-bijective, curvilinear magnetic field gradients: a concept study. *Magn. Reson. Mat. Phys. Biol. Med.* **21**, 5-14 (2008).
170 Brown, R. W., Cheng, Y.-C. N., Haacke, E. M., Thompson, M. R. & Venkatesan, R. *Magnetic resonance imaging: physical principles and sequence design*. (John Wiley & Sons, 2014).
171 Brown, M. A. & Semelka, R. C. *MRI: basic principles and applications*. (John Wiley & Sons, 2011).
172 Vogel, M. W., Giorni, A., Vegh, V., Pellicer-Guridi, R. & Reutens, D. C. Rotatable Small Permanent Magnet Array for Ultra-Low Field Nuclear Magnetic Resonance Instrumentation: A Concept Study. *PloS one* **11**, e0157040 (2016).
173 Zotev, V. S. *et al.* Parallel MRI at microtesla fields. *Journal of Magnetic Resonance* **192**, 197-208 (2008).
174 Pyrhonen, J., Jokinen, T. & Hrabovcova, V. *Design of rotating electrical machines*. (John Wiley & Sons, 2013).
175 Press, W. H. *Numerical recipes 3rd edition: The art of scientific computing*. (Cambridge university press, 2007).
176 Meyer, C. D. *Matrix analysis and applied linear algebra*. Vol. 71 (Siam, 2000).
177 Cheng, D. K. *Field and wave electromagnetics*. (Addison-Wesley, 1989).
178 Pellicer-Guridi, R., Vogel, M. W., Reutens, D. C. & Vegh, V. Towards ultimate low frequency air-core magnetometer sensitivity. *Scientific reports* **7**, 2269 (2017).
179 Tumanski, S. Induction coil sensors—A review. *Measurement Science and Technology* **18**, R31 (2007).
180 Zakaria, Z. *et al.* Advancements in transmitters and sensors for biological tissue imaging in magnetic induction tomography. *Sensors* **12**, 7126-7156 (2012).
181 Estola, K.-P. & Malmivuo, J. Air-core induction-coil magnetometer design. *Journal of Physics E: Scientific Instruments* **15**, 1110 (1982).
182 Grosz, A. & Paperno, E. Analytical optimization of low-frequency search coil magnetometers. *IEEE Sensors Journal* **12**, 2719-2723 (2012).
183 Lukoschus, D. G. Optimization theory for induction-coil magnetometers at higher frequencies. *IEEE Transactions on geoscience electronics* **17**, 56-63 (1979).
184 Nourmohammadi, A., Asteraki, M. H., Feiz, S. M. H. & Habibi, M. A Generalized Study of Coil-Core-Aspect Ratio Optimization for Noise Reduction and SNR Enhancement in Search Coil Magnetometers at Low Frequencies. *IEEE Sensors Journal* **15**, 6454-6459 (2015).

185 Zelinka, I., Snasel, V. & Abraham, A. *Handbook of optimization: from classical to modern approach*. Vol. 38 (Springer Science & Business Media, 2012).
186 Chen, C., Liu, F., Lin, J. & Wang, Y. Investigation and Optimization of the Performance of an Air-Coil Sensor with a Differential Structure Suited to Helicopter TEM Exploration. *Sensors* **15**, 23325-23340 (2015).
187 Lin, T. *et al.* High-sensitivity cooled coil system for nuclear magnetic resonance in kHz range. *Review of scientific instruments* **85**, 114708 (2014).
188 Tashiro, K. Optimal design of an air-core induction magnetometer for detecting low-frequency fields of less than 1 pT. *Journal of the Magnetics Society of Japan* **30**, 439-442, doi:10.3379/jmsjmag.30.439 (2006).
189 Timofeeva, M., Allègre, G., Robbes, D. & Flament, S. Differential search coils based magnetometers: conditioning, magnetic sensitivity, spatial resolution. *Sensors & Transducers Journal* **14**, 16 (2012).
190 Yan, B., Zhu, W., Liu, L., Liu, K. & Fang, G. An optimization method for induction magnetometer of 0.1 mHz to 1 kHz. *IEEE Transactions on Magnetics* **49**, 5294-5300 (2013).
191 Yan, B., Zhu, W., Liu, L., Liu, K. & Fang, G. Design of induction magnetometer receiving sensor for through-the-earth communications. *IEEE Sensors Journal* **15**, 1139-1144 (2015).
192 Tashiro, K., Inoue, S.-i. & Wakiwaka, H. Sensitivity limits of a magnetometer with an air-core pickup coil. *Sensors & Transducers* **9**, 171 (2010).
193 Martinez, J. L., Babic, S. & Akyel, C. On Evaluation of Inductance, DC Resistance, and Capacitance of Coaxial Inductors at Low Frequencies. *Magnetics, IEEE Transactions on* **50**, 1-12 (2014).
194 Bowick, C. *RF circuit design*. (Newnes, 2011).
195 Halse, M. E. *et al.* A practical and flexible implementation of 3D MRI in the Earth's magnetic field. *Journal of Magnetic Resonance* **182**, 75-83 (2006).
196 Savukov, I. *et al.* Non-cryogenic anatomical imaging in ultra-low field regime: Hand MRI demonstration. *Journal of Magnetic Resonance* **211**, 101-108 (2011).
197 Suefke, M., Liebisch, A., Blümich, B. & Appelt, S. External high-quality-factor resonator tunes up nuclear magnetic resonance. *Nature physics* **11**, 767 (2015).
198 Pollak, V. & Slater, R. Input circuits for pulsed NMR. *Review of Scientific Instruments* **37**, 268-272 (1966).
199 Fujita, H., Zheng, T., Yang, X., Finnerty, M. J. & Handa, S. RF surface receive array coils: the art of an LC circuit. *Journal of magnetic resonance imaging* **38**, 12-25 (2013).
200 Cao, X. *et al.* Design of a 3T preamplifier which stability is insensitive to coil loading. *Journal of Magnetic Resonance* **265**, 215-223 (2016).
201 Kabel, M. A. Ultra-Low Noise Amplifier Design for Magnetic Resonance Imaging systems. *arXiv preprint arXiv:1706.03507* (2017).
202 Robinson, F. A sensitive nuclear quadrupole resonance spectrometer for 2-60 MHz. *Journal of Physics E: Scientific Instruments* **15**, 814 (1982).
203 Liu, K., Zhu, W., Yan, B., Liu, L. & Fang, G. Ultralow noise preamplifier and optimization method for induction magnetometers. *IEEE Sensors Journal* **15**, 3293-3300 (2015).
204 Shi, H., Wang, Y. & Lin, J. Optimal Design of Low-Noise Induction Magnetometer in 1 mHz–10 kHz Utilizing Paralleled Dual-JFET Differential Pre-Amplifier. *IEEE Sensors Journal* **16**, 3580-3586 (2016).
205 Pallottino, G. & Vannaroni, G. A low-noise low-input conductance preamplifier for gravitational research. *IEEE transactions on instrumentation and measurement* **34**, 676-680 (1985).
206 Evangelisti, F. Low-noise FET input amplifier for applications in the audio and subaudio frequency ranges. *IEEE Transactions on Audio and Electroacoustics* **20**, 164-171 (1972).
207 Mathur, R., Knepper, R. W. & O'Connor, P. B. A low-noise, wideband preamplifier for a Fourier-transform ion cyclotron resonance mass spectrometer. *Journal of the American Society for Mass Spectrometry* **18**, 2233-2241 (2007).
208 Ribov, B. Y. in *Scientific Conference Electronics (ET), International.* 1-4 (IEEE).
209 Borbely, E. JFETs: The new frontiers. *Audio Electronics*, 16-20 (1999).

210 Levinzon, F. A. Ultra-low-noise high-input impedance amplifier for low-frequency measurement applications. *IEEE Transactions on Circuits and Systems I: Regular Papers* **55**, 1815-1822 (2008).
211 Jefferts, S. R. & Walls, F. A very low-noise FET input amplifier. *Review of Scientific Instruments* **60**, 1194-1196 (1989).
212 Xiao, Y., Zhao, Z., Qian, Z. & Zhou, H. A high isolation switching unit for MRI system. *Procedia Engineering* **7**, 265-269 (2010).
213 Caverly, R. H., Doherty, W. E. & Watkins, R. D. in *Microwave Symposium Digest (MTT), 2011 IEEE MTT-S International.* 1-4 (IEEE).
214 Michal, C. A. A low-cost spectrometer for NMR measurements in the Earth's magnetic field. *Measurement Science and Technology* **21**, 105902 (2010).
215 Peshkovsky, A., Forguez, J., Cerioni, L. & Pusiol, D. RF probe recovery time reduction with a novel active ringing suppression circuit. *Journal of Magnetic Resonance* **177**, 67-73 (2005).
216 Payne, N. R., Broche, L. & Lurie, D. J. A Q-switch system for an MRI RF coil operating at 2.5 MHz. (2016).
217 Sullivan, N., Deschamps, P., Neel, P. & Vaissiere, J. Efficient fast-recovery scheme for NMR pulse spectrometers. *Revue de Physique Appliquée* **18**, 253-261 (1983).
218 Hoult, D. Fast recovery with a conventional probe. *Journal of Magnetic Resonance (1969)* **57**, 394-403 (1984).
219 Takeda, K., Tabuchi, Y., Negoro, M. & Kitagawa, M. Active compensation of rf-pulse transients. *Journal of Magnetic Resonance* **197**, 242-244 (2009).
220 Stejskal, E. & Schaefer, J. Removal of artifacts from cross-polarization NMR experiments. *Journal of Magnetic Resonance (1969)* **18**, 560-563 (1975).
221 Canet, D., Brondeau, J., Marchal, J. & Robin-Lherbier, B. A convenient method of observing relatively broad nuclear magnetic resonances in the Fourier transform mode. *Magnetic Resonance in Chemistry* **20**, 51-53 (1982).
222 Gerothanassis, I. P. Simple reference baseline subtraction–90° pulse sequence for acoustic ringing elimination in pulsed fourier transform NMR spectroscopy. *Magnetic resonance in chemistry* **24**, 428-433 (1986).
223 Zhu, G. & Bax, A. Improved linear prediction of damped NMR signals using modified "forward-backward" linear prediction. *Journal of Magnetic Resonance (1969)* **100**, 202-207 (1992).
224 Hoult, D. The principle of reciprocity. *Journal of Magnetic Resonance* **213**, 344-346 (2011).
225 Simpson, J. C., Lane, J. E., Immer, C. D. & Youngquist, R. C. Simple analytic expressions for the magnetic field of a circular current loop. (2001).
226 Hoult, D. I. & Richards, R. The signal-to-noise ratio of the nuclear magnetic resonance experiment. *Journal of magnetic resonance* **213**, 329-343 (1976).
227 Fukushima, E. *Experimental pulse NMR: a nuts and bolts approach*. (CRC Press, 2018).
228 Coleman, T., Branch, M. A. & Grace, A. Optimization toolbox. *For Use with MATLAB. User's Guide for MATLAB 5, Version 2, Relaese II* (1999).
229 Kartäusch, R. *et al.* Spatial phase encoding exploiting the Bloch–Siegert shift effect. *Magnetic Resonance Materials in Physics, Biology and Medicine* **27**, 363-371 (2014).
230 Ridgway, J. P. in *Cardiovascular MR Manual* 77-80 (Springer, 2015).
231 Zhu, B., Liu, J. Z., Cauley, S. F., Rosen, B. R. & Rosen, M. S. Image reconstruction by domain-transform manifold learning. *Nature* **555**, 487 (2018).
232 Carey, A. *et al.* Ambient Electromagnetic Noise Reduction for Ultra-Low Field NMR. *ESMRMB conference* (2017).
233 Espy, M. *et al.* Applications of ultra-low field magnetic resonance for imaging and materials studies. *IEEE Transactions on Applied Superconductivity* **19**, 835-838 (2009).
234 Riegler, J. *et al.* Superparamagnetic iron oxide nanoparticle targeting of MSCs in vascular injury. *Biomaterials* **34**, 1987-1994 (2013).